Neutron and X-ray Scattering Study of Magnetic Manganites

Graeme Eoin Johnstone

A Thesis submitted for the Degree of Doctor of Philosophy

Mansfield College

University of Oxford

Trinity 2012

Neutron and X-ray Scattering Study of Magnetic Manganites

Graeme Eoin Johnstone, Mansfield College, University of Oxford
A Thesis submitted for the Degree of Doctor of Philosophy
Trinity 2012

This thesis presents three investigations of the magnetic and electronic properties of manganese oxide materials. The investigations are performed using a variety of neutron scattering and x-ray scattering techniques.

The electronic ground-state of $\mathrm{Pr(Sr_{0.1}Ca_{0.9})_2Mn_2O_7}$ an antiferromagnet with CE-type ordering, is determined using neutron spectroscopy, as opposed to the more usual approach of using diffraction. The Zener polaron model of the electronic ground state of the CE-type magnetic phase is shown to be unsuitable for this material. The ground-state is shown to agree well with the electronic ground state proposed by Goodenough in the 1950's, but without significant $\mathrm{Mn^{3+}/Mn^{4+}}$ disproportionation.

The distribution of the magnetisation density within the unit cell of the CE-type antiferromagnet $\mathrm{La_{0.5}Sr_{1.5}MnO_4}$ is determined from a polarised neutron diffraction experiment by analysing the results with the maximum entropy method. The majority of the magnetisation density is found to be located at the Mn site. The investigation shows tentative evidence of a small magnetic moment on the in-plane O site. However, a larger moment is observed at both the La/Sr site and the out-of-plane O site.

The magnetic structure of the magnetoelectric multiferroic $\mathrm{DyMn_2O_5}$ is investigated using resonant magnetic x-ray scattering. The magnetic structure is shown to be similar to other members of the $\mathrm{RMn_2O_5}$ series of multiferroics, but with the key difference that the magnetic moments are closely aligned parallel with the crystallographic *b*-axis, in contrast to the usual observation of the moments being close to parallel with the *a*-axis. This study also shows evidence that the electrical polarisation has a significant contribution from the valence electrons of the O ions, agreeing with previous work.

Acknowledgments

There are a great many people who I would like to thank for their contributions and for the support they have given me over the years I have been working on this thesis. Andrew Boothroyd, my supervisor, has been very supportive since the day he agreed to let me have a go at being a DPhil student. He has been a font of advice, excellent insight and, of course, good humour on the gloomy days when this project seemed never-ending. I must also thank Prabhakaran Dharmalingham for providing the samples used for these studies, without his skill in the dark arts of crystal growth there wouldn't be many experiments conducted in this thesis.

A significant portion of the work on $Pr(Sr_{0.1}Ca_{0.9})_2Mn_2O_7$ would have been impossible without the help, advice and late nights aligning crystals that accompany working with the elusive Toby Perring. I'd also like to thank Olga Sikora for providing the spin wave models that were used in this study.

I am grateful to Martin Rotter for his assistance and enthusiasm on experiments regardless of whether they were successful or beset by problems. His assistance with the investigation of $La_{0.5}Sr_{1.5}MnO_4$ is of particular importance for the work presented in this thesis. I must also thank Bachir Ouladdiaf and especially Anne Stunault for being extremely helpful instrument scientists. Their expertise on crystallography was essential for us to get such high quality data. My thanks also go Anders Markvaardsen for providing the maxent program for analysing the results of the polarised neutron scattering experiment.

There are a large number of people who assisted with the study of $DyMn_2O_5$. Russell Ewings was of great assistance at all times during this investigation, on both experiments and at all stages of the analysis. Roger Johnson must be given

particular credit for the FDMNES analysis and I really appreciate his willingness to go to the pub at every possible opportunity. My thanks goes to the instrument scientists that I worked with on both experiments, Claudio Mazzoli at ESRF and Paul Steadman at Diamond. The experiments were assisted by a number of other people, Helen Walker and Jon Payne during the ESRF experiment and Peter Hatton, Tom Beale and Stuart Wilkins during the Diamond experiment.

I must mention the good people that worked beside me in the Clarendon over the years, my thanks for your great help and for the good times. My office mates over the years (a few of whom have already been mentioned) deserve the greatest thanks mainly for just putting up with me, but I have thoroughly enjoyed working with Heather Lewtas (a calming influence in stressful days, unless she was the one getting stressed), Rhiannon Jones (for the fighting fish), Alice Taylor (for never being short of an opinion), Ivelisse Cabrera (and temporary office mate Natalia) and Stephen 'GAW' Gaw (for being gawesome). There are so many other people with whom I've shared tea times and various misadventures with over the years that I can't mention everyone, but I can at least start with Andrew Steele, Isabel Franke, Jack Wright and Danielle Kaminski. Of all my colleagues over the years, one man stands above all others, literally according to the office door. A great deal of thanks goes to Peter 'Babbers' Babkevich. He has always been there with great tips (usually given with a sigh and a shake of the head) and some of the most entertaining moments of my time at Oxford have involved him, even if he wasn't always aware of it (apparently he only looks up once a month).

I would like to thank all of my friends that have been such a great source of joy and support over the last few years, in both Oxford and beyond. Completing my thesis would have been very difficult without the help of Simon Fairclough, Julia Shanks and Chris Duffy, and a very special thank you to Ricardo Engel and Katie

Moore for their kindness and patience. This thesis would have been impossible without my family. My brother has been a great friend throughout my time in Oxford and for a very long time before that. I cannot thank my parents enough for the love and support they have given me that has brought me this far. Finally, thanks to Susanne, who has made this last year in Oxford happier than I thought possible.

Contents

Chapter 1

Introduction to the Physics of Manganites

Many of the challenges of human society seem to be easily solvable, if only there were an unlimited variety of materials that could display any physical property required of them. Materials with zero resistivity could help solve the world's energy needs. Materials with certain magnetic memory properties could revolutionise the computer industry. Incredibly light weight, but extremely strong materials would open up many new possibilities for construction and transportation. Although these materials may not currently exist in any commercially viable manner at the moment, all of the properties mentioned have been observed in real materials.[1, 2, 3]

Understanding the physics of the systems that do show some of the aforementioned properties, is the most logical way to develop new materials that work under normal conditions. The case of superconductivity is perhaps the best documented. Before the mid-1980's, superconductivity was thought to be an interesting physical phenomenon, but the extremely low temperatures (< 20K) that were required to reach the superconducting state meant that it could only have very limited practical applications. The discovery of the superconducting cuprates,[4] where the superconducting state exists above the boiling point of liquid nitrogen (77K), altered that outlook. Although superconductivity has still not been observed at a normal temperature for an environment on earth or in any material that is easy to manufacture, the progress that has been made by studying the physics of superconductors has made the goal of one day having zero resistance electricity transfer seem more attainable.[5]

All of the effects listed above arise from unusual quantum mechanical effects. The study of materials that display these effects is the study of the quantum mechanics of systems with large numbers of electrons and nuclei. For example, although magnetic materials have been known since ancient times,[6] the quantum mechanics that lead to magnetic effects are not understood for all materials. Magnetism plays a role in the daily life of many people, in their computer's memory or in the credit cards in their wallets. Developing the understanding of magnetism in materials could open new technologies that can be part of everyday life in the future.

Complicated magnetic systems are some of the most interesting materials for future applications.[2, 7] The complexity of these systems is due to competing quantum mechanical interactions. One particularly interesting group of materials is the manganese oxides, or manganites. These materials have been the source of some important discoveries in condensed matter physics since,[8] but a true understanding of the quantum mechanics of these systems has still not been attained. All of these reasons mean that magnetic manganites are a fascinating area of research. The long history of manganite research has left many unanswered questions, meaning there is interesting physics still to be discovered and perhaps even technological benefits in the not too distant future.

1.1 Why Manganites?

Interest in manganites goes back at least 24,000 years when paleolithic humans used MnO_2 as a pigment in cave paintings.[9] The same cave paintings also contained the ferromagnetic material hematite (Fe_2O_3), so it might be argued that correlated electron physics has been a relevant subject to mankind since at least the last ice age. In the field of condensed matter physics, manganites tends to refer to complicated crystals containing manganese ions, often in a magnetic state. The manganese sites are usually linked by oxygen ions, with other cations, such as alkaline earth ions or rare earth ions filling in the gaps in the Mn-O structure.

In modern physics, manganites are probably most famous for the subset of materials showing colossal magnetoresistance,[10] which manifests as a very large reduction in the resistance of a material when a magnetic field is applied. Beyond this important discovery, the number of concepts that find there origins in manganites is impressive. The Jahn-Teller polaron,[11, 12] Zener double-exchange[13, 14] and even the naming system for cubic antiferromagnetic structures[15] all originate from work on manganite materials. More recently, there was a resurgence in the field of magnetoelectric multiferroics when a large coupling between the magnetic ordering and electronic ordering was observed in $TbMnO_3$.[16]

A trait of Mn that helps enable all of the aforementioned effects is its ability to exist in a range of chemical states, with compounds observed with Mn ions in any valence state from $3-$ to $7+$, but of particular importance are the Mn^{3+} and Mn^{4+} ions. The majority of these ionic states contain unpaired electrons in the d-orbitals, meaning that Mn ions usually have a large magnetic moment. The variety of d-orbital occupancy also means that the different valence ions have different electron distributions. Materials where more than one type of Mn valence exists, where the

Mn ions are surrounded by a variety of O environments results in a huge range of complicated and connected electronic and magnetic states.[15, 17] These can be manipulated in such a way that small environmental changes can have large effects on the physical properties of the materials.[10]

The complexity of these materials and the fact that many of the features of manganites are not yet fully understood, means that there are a large number of unanswered questions. The aim of this thesis is to explore a few of these questions. The main investigative work described is on three separate problems in the field of correlated electron manganites. Firstly, what is the electronic state of the complicated CE-type antiferromagnetic phase? This magnetic phase is seen in many manganese oxides, particularly ones related to the colossal magnetoresistance manganites. Secondly, what is the role of the oxygen ion in the CE-type antiferromagnetic phase? In particular, the magnetic state of the O ions was investigated. The third investigation is on the poorly understood magnetic structure of a multiferroic manganite that shows a particularly large electrical polarisation.

These three investigations are presented in chapters 3-5. Chapter 2 covers the theoretical and technical aspects of the main experimental techniques used in the work, namely neutron scattering and resonant magnetic x-ray scattering. The present chapter offers a brief introduction to some of the concepts of condensed matter physics that have particular relevance to the work presented here.

1.2 Chemical Environments and Crystal Fields

The three projects presented in this work are on different manganese oxide materials, with a variety of structures, but they all have some common features. In each, the positively charged Mn ions are surrounded by negatively charged O ions. The crystal structure is completed by rare-earth ions (RE) with a charge of 3+ (La,Pr,Dy), alkaline earth (AE) ions with a charge of 2+ (Ca,Sr) or a mixture of the two. Although the RE/AE ions are not thought to contribute directly to the magnetism in the Mn ions, changing the ratio of RE to AE has a significant effect on the charge of the Mn site. For example, in the frequently studied perovskite-structured material $\mathrm{LaMnO_3}$ the Mn ion has a charge of +3, but as the material is chemically altered to $\mathrm{La}_{1-x}\mathrm{Ca}_x\mathrm{MnO}_3$ the positive charge on the Mn increases until at $x = 1$ and the Mn ion has a charge of +4.

It should be noted at this point that in many cases it is difficult to attribute a truly integer charge to any ion in a manganite, with the most challenging often being the Mn. Transition metal oxides often show a degree of covalency in the nature of the bonds between ions. However, for simplification the charges are often presented as having integer values in discussions of the physics of these types of materials. This will also be the case in this work, unless otherwise stated.

The precise arrangement of the O ions and interactions between the Mn and O ions has a significant effect on the charge of the Mn, the orbital arrangement of the Mn and subsequently the magnetic interactions between Mn ions. At the simplest level, in a material such as $\mathrm{DyMn_2O_5}$ where the average charge for the Mn ions is +3.5, (see chapter 5) half of the Mn ions are surrounded by an octahedron of 6 O^{2-} ions at the vertices and the other half are surrounded by a square-based pyramid with 5 O^{2-} at the vertices. The Mn ions on the two different sites show a different valence, the Mn in the octahedra is in a 4+ state and the Mn in the square-based pyramid is in a 3+ state.

The situation is more complicated when all of the ions have the same environment, for example when all of the Mn ions are surrounded by an O octahedron, such as in perovskites. To develop the idea of the effect the environment has on the

Mn ions, a basic discussion of crystal fields is useful. A combination of the magnetic properties of the Mn ions and the crystal fields can lead to the Jahn-Teller effect, which is observed in the manganites studied in chapters 3 and 4.

1.2.1 Crystal Fields

Crystal field theory describes the effect a local environment has on the energy-levels in an ion. The most simple way to explain the concept is to illustrate the effect on an ion in a simple environment. The energy levels of a transition metal ion, such as Mn, are altered when the ion is surrounded by an octahedron of O^{2-} ions, see Fig. 1.1(a). The five different *d*-orbital energy levels vary in shape and lose their degeneracy in such an environment. The main reason for this is the electrostatic force. Occupied transition metal 3*d*-orbitals are negatively charged, as are the surrounding O^{2-} ions, therefore the energy of the system is reduced when the *d*-orbital electrons are as far from the O ions as possible. For this example, the energy of the d_{xy}, d_{xz} and d_{yz} are all reduced, because the orbitals lie between the O^{2-} ions, whereas the energy of the $d_{3z^2-r^2}$ and $d_{x^2-y^2}$ is increased because of their proximity to the O^{2-}. This is illustrated in Fig. 1.1(b) with the d_{xy} and $d_{x^2-y^2}$ orbitals as an example. In the diagram it is clear that the negatively charged lobes are kept further apart for the d_{xy} orbitals. The three low energy states are called the t_{2g} states and the two high energy states are the e_g states. These labels represent the symmetry of the different states.

This is a simplified example of crystal fields, but it is useful to illustrate the point of how a local environment can effect the energy levels of an ion. An introduction to crystal fields is presented by Blundell.[18] This can be generalised to many other systems, by a mathematical treatment using the Stevens operators.[19]

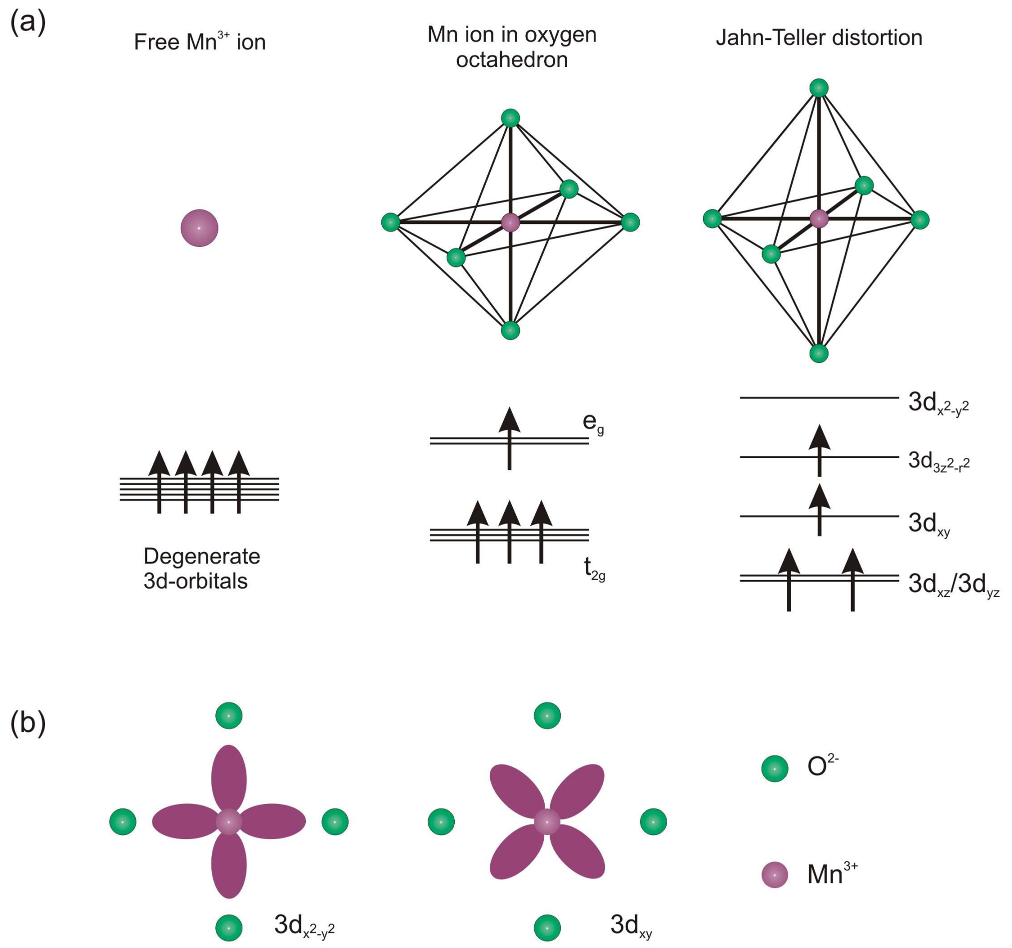

Figure 1.1: (a) A qualitative energy level diagram of the d-orbital states for a Mn^{3+} ion in different environments (also illustrated). (b) An example of the crystal field effect for the d_{xy} and $d_{x^2-y^2}$ orbitals in an MnO_6 octahedra, viewed along the z-direction.

1.2.2 Jahn-Teller Effect

The occupation of the d-orbitals of the transition metal ion can affect the ions local environment. Again using the simple model of the Mn ion surrounded by an O^{2-} octahedra, it is possible to consider a large number of different d-orbital occupations. Mn can exist in a number of ionic states and the ion Mn^{3+} is of particular interest in this case. There are four d-orbital electrons in Mn^{3+} and these are placed into the energy levels according to Hund's rules, one electron in each of the three lower energy t_{2g} and one in the higher energy e_g levels. In this configuration, the energy of the whole MnO_6 structure can be reduced if the octahedron becomes distorted. The distortion reduces the energy of one e_g orbital and raises the energy of the other, but since only one of these is occupied, the energy of the entire system is decreased. This is known as the Jahn-Teller effect[20] and it is effectively a trade-off between the electrostatic energy and the elastic energy of the crystal structure. The Jahn-Teller process is illustrated in Fig. 1.1(a), showing a distortion causing an elongation of the octahedron along the z-direction, which reduces the energy of the $d_{3z^2-r^2}$ orbital and raises the energy of $d_{x^2-y^2}$ orbital.

Mn^{3+} can be described as a Jahn-Teller ion and this characteristic of Mn^{3+} is important in some of the effects discussed later in this chapter and throughout this thesis.

1.3 Charge Ordering

The scenario described earlier for $DyMn_2O_5$ could be described as charge ordering, with Mn^{3+} and Mn^{4+} both being present in a crystal but located on different sites in a regular arrangement. However, for the purposes of this thesis, charge ordering will be considered as an effect where Mn ions on sites that are symmetrically equivalent at one temperature, are in different valence states after going through a phase transition. Of particular relevance is the case of Mn^{3+} and Mn^{4+} charge ordering in a two-dimensional square lattice, connected by O ions.

1.3.1 Charge Order in Manganites

In certain manganese oxide systems, there exists two dimensional planes of MnO_2. A square lattice of Mn ions is shown in Fig. 1.2(a); the O ions lie halfway between

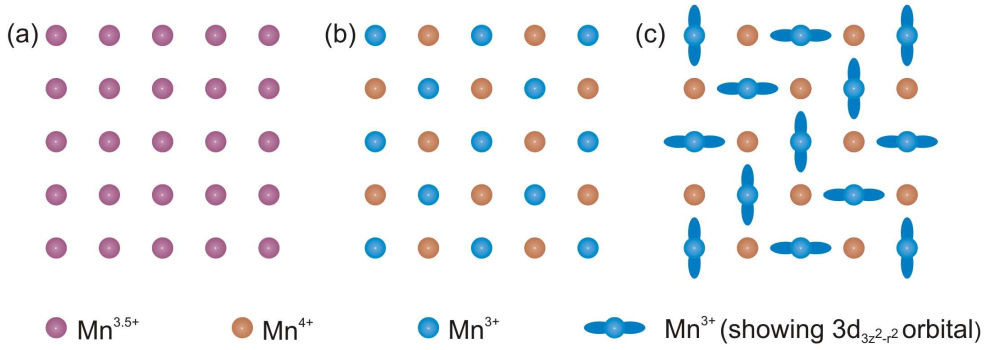

Figure 1.2: (a) A diagram of the 2D lattice of only the $Mn^{3.5+}$ ions in a MnO_2 plane of a half-doped manganite. The O ions would lie between the nearest neighbour Mn ions. (b) The charge ordered phase in the half doped manganite and (c) the orbital ordered phase, showing the alignment of the $d_{3z^2-r^2}$ orbitals in the crystal MnO_2 plane.

each nearest neighbour Mn ion, but are not shown for simplicity. If the system is chemically doped in such a way that there is a non-integer number of electrons per Mn ion, the system finds the lowest energy solution to distribute these electrons. The case of 3.5 electrons per Mn site is simple to illustrate and is often referred to as half-doping. At high temperatures in a system such as $La_{0.5}Sr_{1.5}MnO_4$ each Mn site in the MnO_2 plane has the same charge, averaging out to $Mn^{3.5+}$. However, as the temperature is lowered a phase transition occurs such that the charge on each Mn ion becomes ideally integer, with half of the sites being Mn^{3+} and the other half being Mn^{4+}.[21] In this particular case each ion of one charge is surrounded by ions of the other charge, shown in Fig. 1.2(b).

As mentioned earlier, there is an uncertainty over the degree of charge ordering that exists in half-doped manganites, i.e. whether the ions become strictly Mn^{3+} and Mn^{4+} or if it is some other mixture of $Mn^{+3.5+\delta}$ and $Mn^{+3.5-\delta}$. However, for the purposes of this introduction it will be assumed that the charge ordering has $\delta = 0.5$.

This is a very simple illustration of charge ordering. Much more complicated charge-ordered systems exist in other materials, for example in copper oxides. Charge ordering also happens in systems that have a different doping from the one presented here and therefore a different number of electrons per site, resulting in much more complicated ordering patterns.[22]

1.3.2 Orbital Order in Manganites

In the case of the charge-ordered MnO_2 plane, with Mn^{3+} and Mn^{4+} ions, the Jahn-Teller effect must be considered. In half-doped materials, the Jahn-Teller effect causes the $3d_{3z^2-r^2}$ orbital be an energetically favourable state for the e_g electrons in Mn^{3+} ions. These occupied $3d_{3z^2-r^2}$ orbitals can arrange their orientation into an ordered super-structure, which of course implies an ordering of the Jahn-Teller distortions. In this case, the ordering of the $3d_{3z^2-r^2}$ orbitals on Mn^{3+} ions is in the herring bone pattern,[23] illustrated in Fig. 1.2(c).

Orbital effects can go far beyond ordering patterns and a discussion of many aspects of orbital physics is presented in the article by Tokura and Nagaosa.[24]

1.4 Magnetic Interactions

In the materials discussed in this thesis, the magnetic effects are not those of magnetic ions isolated from each other within the crystal structure. The macroscopic magnetic effects observed are a result of interactions between magnetic moments and in some cases competing interactions on similar energy scales that mean small external influences can have a large effect on the properties of the material. However, the interactions normally observed do not have a purely magnetic origin. The magnetic dipole interactions are far too weak to account for magnetic ordering in systems that order at any temperature higher than a few Kelvin. A general introduction to magnetic interactions is presented by Blundell.[18]

1.4.1 Exchange Interactions

Magnetic ordering at temperatures higher than a few Kelvin finds its origin in electrostatic interactions at a quantum mechanical level. An exchange between two magnetic ions with spin $\mathbf{S}_i$ and $\mathbf{S}_j$ is usually described using the Hamiltonian,

$$\hat{H} = -\sum_{ij} J_{ij}\mathbf{S}_i.\mathbf{S}_j \tag{1.1}$$

where J_{ij} is known as the magnetic exchange constant between the spins of ion i and ion j. The magnetic exchange constant represents the strength of the magnetic interaction. A material with strong magnetic interactions usually displays magnetic ordering at higher temperatures. The sign of J describes whether an exchange favours a parallel alignment of two spins, a ferromagnetic exchange ($J > 0$), or an anti-parallel alignment of two spins, an antiferromagnetic exchange ($J < 0$).

Two types of magnetic interaction are particularly important for this thesis, superexchange and double exchange. These are described in the following two sections. These two exchanges are known as indirect exchanges because the two magnetic ions concerned do not interact with each other directly, instead the interaction is mediated by a non-magnetic ion. In addition to indirect exchange, there is direct exchange, where the magnetic ions do interact with each other, but this is not a particularly strong effect in the materials discussed here.

1.4.2 Superexchange

Superexchange usually leads to antiferromagnetic ordering. This interaction between two magnetic ions is mediated by a non-magnetic ion lying directly between

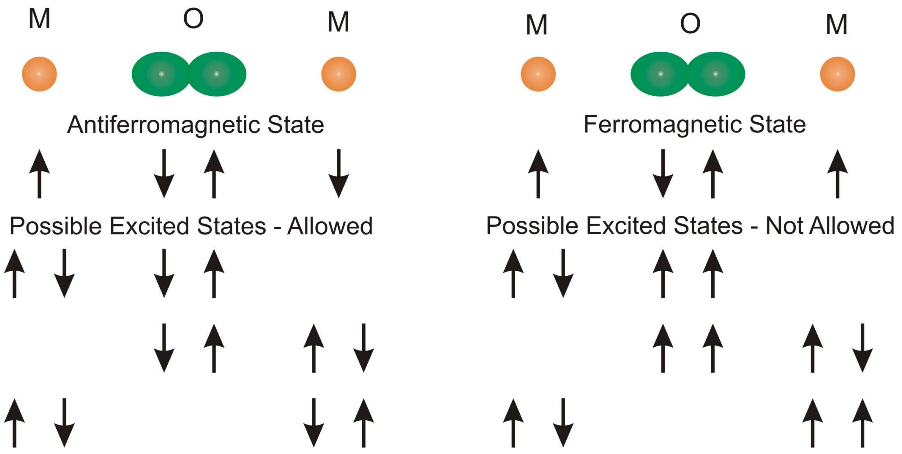

Figure 1.3: A diagram of the superexchange interaction for two single electron magnetic ions (M) separated by an O^{2-} ion. The excited states of the antiferromagnetic arrangement are allowed, but the excited states of the ferromagnetic state are not allowed by the Pauli exclusion principle.

the two. Superexchange leads to antiferromagnetism due to a simple kinetic energy argument,[18] illustrated in Fig. 1.3 for a single electron magnetic ion. If the moments on the magnetic ions (M) are parallel to each other (ferromagnetic), then the possible excited states of this system break the Pauli exclusion principle, with two electrons in the same state having the same spin. However, the excited states of the antiferromagnetic state are allowed. Therefore, if the two magnetic ions are aligned antiferromagnetically, the electrons on all three sites are less confined. It is clear from the Heisenberg uncertainty principle that if the electrons are less confined spatially they will have a lower kinetic energy, meaning that antiferromagnetism is energetically favourable in such a system.

1.4.3 Double Exchange

Double exchange is an interaction most relevant in mixed valence materials, such as manganites that contain both Mn^{3+} and Mn^{4+} ions. A particularly relevant example is to consider Mn^{3+} and Mn^{4+} ions surrounded by oxygen octahedra, as

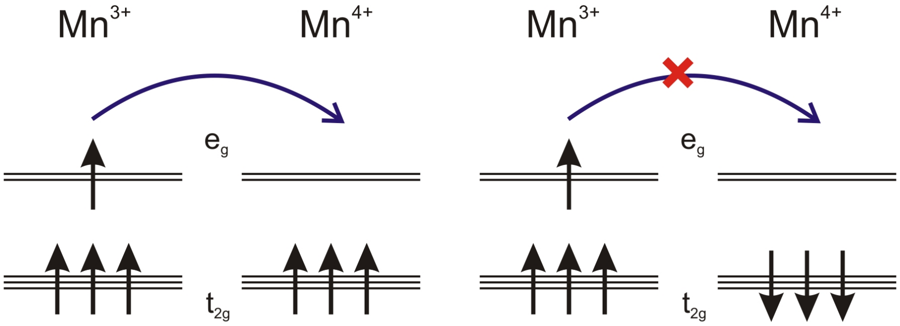

Figure 1.4: For mixed valence materials the double exchange mechanism can be important. Ferromagnetism is favoured in such a system because the e_g electrons can only hop to neighbouring sites if they are ferromagnetically aligned, due to Hund's rules. The antiferromagnetic arrangement would break Hund's rules if such hopping occurred.

discussed earlier. In such an arrangement, the crystal field causes the d-levels to split into the e_g and t_{2g} levels. The lone electron in an e_g level may move into the e_g levels of the neighbouring ion, only if the two sites are ferromagnetically aligned in accordance with Hund's rules, see Fig. 1.4. If the sites were antiferromagnetically aligned, the electron could only transfer sites if the spin of the electron was flipped, otherwise Hund's rules are broken, costing energy. Therefore, the less spatially confined state that allows for a lower kinetic energy, is for the two neighbouring ions to be aligned ferromagnetically.

1.5 Magnetic Order

All materials show one of three types of magnetic behaviour when a magnetic field is applied. Every material is diamagnetic, meaning that when a magnetic field is applied the electrons move in such a way as to set up a field that opposes the applied field. Diamagnetism is a very weak effect and in some materials it cannot be observed due to a much stronger type of magnetism. One of the other types is paramagnetism, which occurs in materials that have unpaired electrons with magnetic moments that interact too weakly to order. When a magnetic field is applied to such a material the magnetic moments align with the applied field. Finally, the third type of behaviour is magnetic ordering.

1.5.1 Types of Magnetic Order

There are a number of types of magnetic ordering that occur in materials. Simplest to describe is ferromagnetism, in which all of the magnetic moments in the material point in the same direction, giving the entire material a net magnetic moment (this is not always apparent due to magnetic domains, which are not discussed here). In antiferromagnetic materials the alignment of the magnetic moments is ordered, but in such a way that all of the moments cancel each other out and there is zero net magnetic moment. A ferrimagnet is similar to an antiferromagnet in that not all of the spins point the same direction, but the net moment of all of the spins is not zero. A simple ferrimagnet can be though of in the same way as an antiferromagnet, but with the oppositely aligned moments having a different magnitude. More complex types of magnetic order can occur, such as helical order, where layers of magnetic moments are rotated from each other, with a constant angle of rotation between the layers.

1.5.2 Antiferromagnetic Structures

All of the materials discussed in this work are antiferromagnets. There are a number of different types of antiferromagnetic structure and some of these will be discussed later in this thesis. Some examples of structures that can exist on a simple cubic lattice are shown in the upper half of Fig. 1.5.[15] The only structure where there is an anti-parallel alignment between every ion is the G-type magnetic structure. The A-type structure has ferromagnetic layers that are coupled antiferromagnetically,

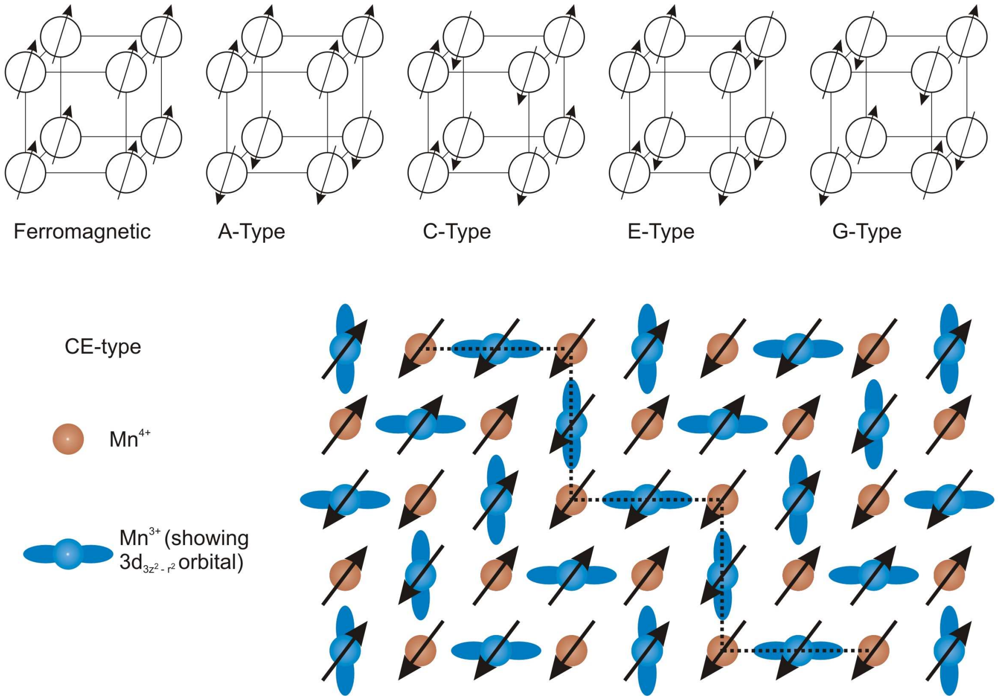

Figure 1.5: Some examples of magnetic structures. All of these were originally observed in a cubic lattice by Wollan and Koehler.[15] Only one layer of a CE-type magnetic structure is shown. The magnetic structure is super imposed on the charge-orbital structure discussed earlier. The dotted line marks one of the ferromagnetic zigzag chains that runs through the CE-type structure.

while C-type was ferromagnetic rods that are coupled antiferromagnetically. Also shown is the ferromagnetic structure, which was referred to as B-type in the original work by Wollan and Koehler.[15]

Much more complicated antiferromagnetic structures do exist. One with particular relevance is the CE-type magnetic structure. This structure appears in MnO_2 layers of half-doped manganites. In a system that displays the charge-ordered/orbital-ordered shown in Fig. 1.2, ferromagnetic double exchange occurs along the zig-zags of the ordered $3d_{3z^2-r^2}$, while antiferromagnetic superexchange occurs between the zigzags. This CE-type structure is shown in lower part of Fig. 1.5.

1.6 Magnetic Excitations

At non-zero temperatures, magnetic structures have excitations. These are analogous to the excitations of a crystal lattice, i.e. phonons. The excitations of the lattice propagate through the crystal obeying a material dependent dispersion relationship. In magnetic structures, the excitation is a magnon, a magnetic spin reorientation that moves through the lattice as a spin wave.

1.6.1 Spin Waves

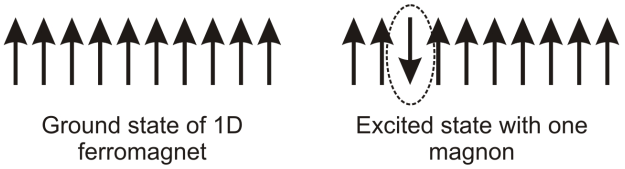

Figure 1.6: The left panel shows an example of a one-dimensional ferromagnet and the right shows a magnon in this system (circled).

Quantum mechanically, a spin wave is a flipped spin in the magnetic lattice, shown in Fig. 1.6 for a simple 1D ferromagnet. This spin can disperse throughout the lattice from its original position. The energy to cause this excitation is related to the magnetic exchange constant J in equation 1.1. If the entire spin wave dispersion of a magnetic structure can be measured, it is possible to determine the strength of the magnetic interactions present in the material. A discussion of spin waves in both ferromagnets and antiferromagnets is given by Kittel. [25]

1.7 Colossal Magnetoresistance

The most dramatic effect in the physical properties of manganites is known as colossal magnetoresistance (CMR). Magnetoresistance is the change in the resistance of a material when a magnetic field is applied, but is usually quite a small effect, changing the resistance of the material by a few percent. However, the complex magnetic and electronic properties of doped perovskite-structured manganites creates an environment in which a much larger magnetoresistance effect can be observed. In the complex magnetic phases observed in materials with intermediate doping, an applied magnetic field forces all of the magnetic moments to align. This forces the interactions between neighbouring magnetic ions to favour aligning with each other, meaning that double exchange is now the energetically favoured exchange interaction. As discussed earlier, double exchange allows for increased electron mobility and therefore a lower resistance. When CMR is observed in manganites, what is occurring is a phase change from an antiferromagnetic insulator to a ferromagnetic metal. The two states are energetically similar and the applied magnetic field is enough to shift the balance between the two.

The problem is not quite as simple as this for a number of reasons. The charge carriers in these materials are not simple electrons. When an electron transfers between two Mn sites in CMR manganites, it can change an Mn^{4+} ion to an Mn^{3+} ion. As mentioned earlier, Mn^{3+} ions are Jahn-Teller ions and therefore, when an electron moves in the material, a lattice distortion moves with in. This combination of an electron and lattice distortion moving together through a material is usually referred to as a polaron, and it is the polaron that complicates the understanding of the electronic properties of the material. The complexity of the antiferromagnetic insulating phase is not entirely understood and it is not clear how valid double exchange is for describing the metallic state. These key components of the theory of CMR manganites means that this is still an important topic of research. There are many reviews on CMR which give summaries of the experimental[7, 8] and theoretical[26, 27] discoveries so far, as well as the many outlying questions in this field.[10]

1.8 Multiferroics

Multiferroics are a class of material that exist with more than one type of ferroic ordering. Typically this refers to a material being both magnetically ordered and spontaneously electrically polarised, the latter of which is called ferroelectric. There are other types of ferroic ordering, such as ferroelasticity, but these are not relevant to this discussion. The field of multiferroics has been of much interest recently, due the discovery of materials that display a much higher degree of interaction between the magnetic and electronic ordering than had been previously observed.[16, 28]

Multiferroics are usually categorised by their ferroelectric properties, usually being classified as proper or improper ferroelectrics.[2] Proper ferroelectrics are materials where the electrically polarised state is energetically favourable and the main driving force for the ferroelectric state to occur. Most known proper ferroelectrics are not magnetic (therefore not multiferroic). The polarisation mechanism in a proper ferroelectric material such as $BaTiO_3$ is due to the non magnetic Ti ion's empty d-orbitals bonding with neighbouring O ions. This causes the Ti to shift in the crystal structure, leading to a polarisation. This mechanism does not allow for any magnetism in the system, as it only occurs because the d-orbitals are empty. An example of a multiferroic material that is a proper ferroelectric is $BiMnO_3$, but here the ferroelectricity is caused by a displacement of the Bi $6s$ electrons, whilst the magnetism appears on the Mn sites. Therefore, in materials such as $BiMnO_3$, the magnetism and electrical polarisation are effectively decoupled physical effects occurring at different locations in the structure.

Multiferroics that are improper ferroelectrics tend to display a much higher connection between the magnetism and ferroelectricity. An improper ferroelectric is one that polarises as a secondary effect of another feature in the system. An introduction to the most important of these is discussed in the review articles by Cheong et al.[28] and Khomskii.[2] One such effect that can lead to an improper ferroelectric is a structural transition that induces a polarisation (such as in hexagonal $RMnO_3$)[29] or a charge-ordering transition, where the charges order in a non-symmetric fashion, inducing an electrical polarisation in a material, as propoesd for $LuFe_2O_4$.[30]

One other class of improper ferroelectric multiferroic is one where the electrical polarisation is induced by the magnetic ordering.[16] The discovery of this class of multiferroic has stimulated the recent resurgence of research in this field. One type of magnetic ordering that can lead to an electrical polarisation is a magnetic spiral or cycloidical state. In such states, the inverse Dzyaloshinskii-Moriya interaction between two neighbouring spins can cause a slight displacement to a neighbouring O ion, inducing a polarisation.[31] Another magnetic interaction that can induce polarisation is exchange-striction.[32] In complicated magnetic structures, it is possible for the exchange interaction to cause a displacement of the magnetic ions, if it will reduce the energy of the system. This displacement of ions in a non-symmetric way again leads to the electrical polarisation in the materials.

It is for multiferroics in which the magnetism induces the ferroelectric ordering that the largest coupling between these two degrees of freedom is observed. Regardless of the precise mechanism that causes the polarisation, it is clear that this phenomenon only exist in materials with a very complicated magnetic structure, and so it is essential to have a good understanding of the magnetic properties of these materials in order to establish the interactions that lead to the multiferroic behaviour.

1.9 Structure of the Remainder of this Thesis

This thesis contains three separate studies into materials that are connected to the physical effects mentioned in this chapter. The experimental techniques used in the course of these projects are introduced in chapter 2. This covers the basic theory and important experimental considerations of neutron scattering and resonant magnetic x-ray scattering, the two techniques that were used for the majority of the experimental work in this thesis.

The first of the three studies is presented in chapter 3 and is a neutron scattering investigation of the bilayered-manganite $\mathrm{Pr(Sr_{0.1}Ca_{0.9})_2Mn_2O_7}$. This material shows the CE-type magnetic structure that is observed in many half doped manganites. A number of theories exist as to what is the true electronic ground-state of the CE-type magnetic structure. Theoretically, the different electronic structures give different spin wave spectra, therefore the full inelastic neutron scattering spectrum for $\mathrm{Pr(Sr_{0.1}Ca_{0.9})_2Mn_2O_7}$ was measured and analysed to determine which electronic ground state is present in the CE-type magnetic structure of this material.

In chapter 4 a polarised neutron scattering study of a half-doped single layered manganite is presented. This investigation explores a slightly different aspect of the electronic and magnetic structure of the CE-type magnetic phase, whether the O site within the $\mathrm{MnO_2}$ layer is magnetic, which would imply that the O ions do not have the expected charge of -2. A detailed study of the determination of the crystal structure of two samples of $\mathrm{La}_x\mathrm{Sr}_{2-x}\mathrm{MnO}_4$ is presented, the results of which are used to investigate the magnetic structure factor of the samples. The magnetic structure factor was determined using the method of flipping ratios. The results of the experiment were analysed using the maximum entropy method to determine the magnetisation distribution in the samples of $\mathrm{La}_x\mathrm{Sr}_{2-x}\mathrm{MnO}_4$.

The final chapter of this thesis presents a study of the magnetic structure of the multiferroic $DyMn_2O_5$ using resonant magnetic x-ray scattering. $DyMn_2O_5$ shows a particularly large electrical polarisation for a magnetoelectric multiferroic material, the largest observed in a manganite, but the magnetic structure of this material in the ferroelectric phase is poorly understood. Therefore two resonant magnetic x-ray scattering experiments, one using hard x-rays and the other using soft x-rays, were performed to examine this magnetic structure.

CHAPTER 2

Experimental Techniques - Neutron Scattering, Resonant Magnetic X-ray Scattering and Bulk Property Measurements

---

The range of experimental techniques used in studies of condensed matter physics is large and ever expanding. A selection of these techniques were used in the research presented in this thesis. The majority of the experiments in chapters 3 and 4 of this thesis use neutron scattering, a now very well developed and well understood technique that has many applications within and outside of correlated electron physics.[33, 34] Therefore, a significant part of this chapter is an introduction to the important aspects of neutron scattering that are relevant for the rest of this thesis. A newer technique was used as the main part of the final chapter in this thesis, resonant magnetic x-ray scattering. X-ray scattering has been used in a variety of fields for some time, but only relatively recently has it been used to directly research magnetism [35]. The interaction between x-rays and magnetic moments is very weak, but new techniques involving both energy resonances in the magnetic materials and intense x-ray sources have made studying magnetism with x-rays a reasonable alternative to neutron scattering. The second part of this chapter will cover the important aspects of x-ray scattering, including resonant magnetic x-ray scattering. Finally a number of measurements have been made of the bulk properties of the materials studied in this thesis and the techniques used for bulk measurements are explained in the final part of this chapter.

2.1 Introduction to Neutron Scattering Theory

The neutron was discovered by James Chadwick in 1932 [36] and as early as 1936 it was shown [37, 38] that thermal neutrons had a wavelength similar to that of interatomic distances in condensed matter. Large numbers of free neutrons were being produced in the world's first nuclear reactor by 1942 and the earliest neutron scattering experiments, usually by crystallographers, were being performed on research reactors not long after this.[34] Neutron sources dedicated to providing neutrons for scattering experiments were later built as it was realised how many different useful measurements could be performed using this technique.

Neutron scattering as a technique is dependent on the way that a neutron interacts with matter and there are a number of properties of neutrons that make it a useful particle for such scattering experiments.[33] Neutrons traveling at the velocities used in the experiments described in this thesis tend to have a wavelength similar to that of the interatomic spacing meaning it is well suited to detecting these features. Neutrons, as suggested by their name, are electrically neutral, meaning that neutrons will not interact with the electrons or the electrical charge of nuclei when they are passing through a solid, allowing them to penetrate quite far into a material. This means that neutron scattering is a probe of the bulk of a material, instead of just the surface, as is the case in an electron diffraction experiment. However, the neutron does have a magnetic moment. This means the neutron has two ways of interacting with matter, via the strong nuclear force when it comes close to nuclei or by the electromagnetic force when the neutron interacts with a magnetic moment within the material, such as that arising from the spin of an unpaired electron. The magnetic moment of the neutron is what makes it a vital tool in understanding the magnetic characteristics of materials at the atomic scale.

To characterise the interaction between a neutron and what it is scattering from, it is important to understand the concept of the scattering cross-section. There are three important cross-sections. The first is known as the total scattering cross-section, defined as

$$\sigma_{\mathbf{tot}} = \frac{\text{(total number of neutrons scattered per second in all directions)}}{\mathbf{\Phi_0}} \tag{2.1}$$

where Φ_0 is the flux of the incident neutrons. It is useful to know the number of neutrons incident in a certain angular direction and this is characterised by the differential cross-section

$$\frac{d\sigma}{d\Omega} = \frac{\text{(total number of neutrons scattered per second into } d\Omega \text{ in the direction } \theta,\, \phi\text{)}}{\Phi d\Omega} \tag{2.2}$$

where $d\Omega$ is the solid angle in the direction θ, ϕ, the spherical polar coordinates. This is the cross-section that is usually measured in elastic neutron scattering (where the neutron does not change energy during the scattering process). The final cross section takes into account the energy of the scattered neutrons in a certain direction.

This is called the partial differential cross-section,

$$\frac{d\sigma}{d\Omega dE_f} = \frac{\begin{pmatrix} \text{Total number of neutrons scattered} \\ \text{per second into d}\Omega\text{ in the direction } \theta \\ \phi \text{ with an energy between } E_f \text{ and } E_f + dE_f \end{pmatrix}}{\Phi d\Omega dE_f} \tag{2.3}$$

where E_f is the final energy of the neutron after it has scattered. This cross-section is usually measured in inelastic neutron scattering, where the neutron does change energy during the scattering process. The calculation of these cross-sections is essential in the analysis of data from neutron scattering experiments and the theory of neutron scattering has accounted for these terms for every type of experiment.

Another important term in neutron scattering is known as the scattering length. A neutron is thought of as a plane wave with the wave function,

$$\psi_i = e^{ikz} \tag{2.4}$$

where the neutron's wavenumber k is related to its wavelength λ by $k = 2\pi/\lambda$. After the neutron interacts with a nucleus via the strong nuclear force, its wave function becomes a spherical wave in addition to the incident wave,

$$\psi_f \simeq -b\frac{e^{ikz}}{r} + e^{ikz} \tag{2.5}$$

where r is the distance from the nucleus and b is the scattering length. There is a negative sign in this equation so that the majority of scattering lengths for the different elemental nuclei have a positive value of b. The scattering length cannot be calculated without a complete theory of the strong nuclear force, so it has to be determined empirically. If the scattering length is complex, this means the nucleus can absorb neutrons. It should be noted that different isotopes of the same element can have completely different values for b. This idea can be expanded to include magnetic scattering, which arises from the interaction between the magnetic moment of the neutron and the magnetic moment distribution of an unpaired electron, giving a magnetic scattering length.

When a neutron undergoes a scattering event, the energy and momentum of the scattering system must remain the same. The energy transferred from the neutron to the scatterer, sometimes given as the angular frequency ω,

$$E_T = \hbar\omega = E_i - E_f \tag{2.6}$$

and momentum (p) transferred (expressed here as the wavevector i.e. $k = p/\hbar$),

$$k_T = \mathbf{Q} = k_i - k_f \tag{2.7}$$

where i refers to the initial state of the neutron and f its final state. The momentum transferred is usually denoted, $\mathbf{Q}$ and referred to as the scattering vector. Scattering can be classified as one of two types depending on whether $E_{\mathrm{T}} = 0$, when E_{T} equals zero there is elastic scattering and when E_{T} is non-zero there is inelastic neutron scattering.

2.1.1 Elastic Neutron Scattering

In elastic neutron scattering, $\mid \mathbf{k_i} \mid = \mid \mathbf{k_f} \mid$ and the scattering vector $\mathbf{Q}$ has to be equal to a reciprocal lattice vector of the sample, $\mathbf{H}$ for constructive interference in a perfect crystal. The reciprocal lattice vector is often defined in terms of the Miller indices h, k and l such that, $\mathbf{H} = h\mathbf{a}^* + k\mathbf{b}^* + l\mathbf{c}^*$, where $\mathbf{a}^*$, $\mathbf{b}^*$ and $\mathbf{c}^*$ are the unit vectors of the reciprocal lattice. It can be shown that,[33]

$$|\mathbf{Q}| = 2|\mathbf{k_i}|\sin\theta \tag{2.8}$$

where 2θ is the scattering angle. This is most commonly known as Bragg's Law and can also be expressed in the familiar form,

$$n\lambda = 2d\sin\theta \tag{2.9}$$

where n is an integer, λ the neutron wavelength and d the distance between two atomic layers in the material ($d = 2\pi/|\mathbf{Q}|$).

The total cross-section for elastic scattering, of all types, can be expressed as a sum of the intensities,[39]

$$\sigma = I_{nuclear} + I_{magnetic} + I_{interference} + I_{chiral} \tag{2.10}$$

where the first term is the contribution from a lattice of nuclei, the second term is from the magnetic moment distribution in the lattice, the third term is the magnetic-nuclear interference term and the final term is known as the chiral term, which is only non-zero for certain complicated magnetic structure, *e.g.* a helicoidal magnetic structure. The third and fourth terms are only relevant in polarised neutron scattering experiments and the third term will be discussed in a later section. The fourth term is outside the scope of this thesis as no chiral magnetic structures have been studied.

2.1.2 Elastic Nuclear Scattering

In equation 2.10, the nuclear term only refers to the coherent scattering from a nucleus and it is this term that is of interest in a measurement of the crystal structure of a material. The neutron can also scatter incoherently giving rise to an isotropic background in the data. For some nuclei the incoherent term can be very large giving a high background. One such example is vanadium, where the scattering is almost entirely incoherent, giving a nearly isotropic elastic scattering signal. This makes it useful for calibrating detectors.

Coherent elastic scattering in crystals only occurs when the scattering vector is equal to a reciprocal lattice vector, as this is the requirement for constructive interference in the scattering. The coherent nuclear elastic differential cross-section for a given scattering vector is,

$$\frac{d\sigma}{d\Omega} = N_0 \frac{(2\pi)^3}{V_0} \sum_H \delta(\mathbf{Q} - \mathbf{H}) |F_N(\mathbf{Q})|^2 \tag{2.11}$$

where N_0 is the number of unit cells the neutrons interact with, V_0 is the volume of a unit cell and the nuclear structure factor,

$$F_N(\mathbf{Q}) = \sum_j b_j e^{i\mathbf{Q}.\mathbf{r_j}} e^{-W_j(\mathbf{Q},T)} \tag{2.12}$$

which sums over all the atoms j in the unit cell, with $\mathbf{r_j}$ the position of atom j, b_j the scattering length of atom j and $e^{-W_j(\mathbf{Q},T)}$ the Debye-Waller factor of the atom j. The Debye-Waller factor is a function of temperature and scattering vector and it takes into account the small thermal fluctuations in the position of an atom. The Debye-Waller factor represents the probability that the atom will be in its equilibrium position during the scattering process. Derivations and further discussion on these equations is given in many books on neutron scattering.[33]

2.1.3 Elastic Magnetic Scattering

The second term in equation 2.10 is due to the interaction of the magnetic moment of the neutron with the magnetic moment arising from unpaired electrons in the sample. Since the magnetic ions form a lattice superimposed on the nuclear lattice, there are a number of similarities between the two cross-sections. The main differences arises from the fact that the magnetic moment of an electron in a material has a large distribution of its scattering potential, unlike a nucleus which only scatters when the neutron is very close to it. Another difference is that a neutron only scatters from a magnetic moment when that moment is aligned perpendicular to the scattering vector **Q**. The differential cross-section for elastic magnetic scattering is written as,

$$\frac{d\sigma}{d\Omega} = N_m \frac{(2\pi)^3}{V_0} \sum_H \delta(\mathbf{Q} - \mathbf{H}) |\mathbf{F}_{M\perp}(\mathbf{Q})|^2 \tag{2.13}$$

where N_m is the number of magnetic ions, V_0 the volume of the sample, the delta function is zero unless the scattering vector **Q** is equal to a reciprocal lattice vector of the magnetic lattice **H** and,

$$\mathbf{F}_{M\perp} = \hat{\mathbf{Q}} \times \mathbf{F}_M \times \hat{\mathbf{Q}} \tag{2.14}$$

where $\mathbf{F}_M$ is the magnetic structure factor, which in the dipole approximation is,

$$\mathbf{F}_M = \gamma r_0 \sum_j f_j(\mathbf{Q}) \mu_j e^{i\mathbf{Q}.\mathbf{r}_j} e^{-W_j(\mathbf{Q},T)} \tag{2.15}$$

with $\gamma = 1.9132$ the gyromagnetic ratio, $r_0 = 2.8 \times 10^{-15}$m the classical radius of the electron and μ_j the magnetic moment of the j^{th} ion. These two equations demonstrate that scattering from a magnetic ion only occurs when there is a component of the magnetic moment perpendicular to the scattering vector.

The magnetic structure factor is the Fourier transform of the magnetisation density ($\mathbf{M}$) in a unit cell.

$$\mathbf{F}_M(\mathbf{Q}) = \int \mathbf{M}(\mathbf{r}) e^{i\mathbf{Q}.\mathbf{r}} d\mathbf{r} \tag{2.16}$$

with the integral performed over the entire magnetic unit cell. This means that at $\mathbf{Q} = 0$, $\mathbf{F}(0) = \int \mathbf{M}(\mathbf{r}) d\mathbf{r}$, the total magnetic moment of the unit cell.

2.1.4 Polarised Neutron Scattering

Elastic polarised neutron scattering can be used to measure magnetic densities with better accuracy than normal methods. The polarisation of a neutron is defined as the direction that the neutron spin is pointing. If a neutron beam has a mixture of n_+ neutrons in a spin up state and n_- neutrons in a spin down state, then the polarisation of the beam is given as,

$$P = \frac{n_+ - n_-}{n_+ + n_-} \tag{2.17}$$

Therefore, for a fully polarised beam $P = \pm 1$, whereas for an unpolarised beam $P = 0$. This definition of P is only meaningful in an experiment where there is only one polarisation axis. Experiments can be performed with polarisation in all three cartesian directions, but this is outside the scope of this thesis.

High accuracy measurements of ferromagnetic ordering can be performed with just one polarisation axis by the method of measuring flipping ratios. Magnetic Bragg peaks from ferromagnetic structures appear at the same scattering vector as nuclear peaks; this means the intensity of these features is the sum of the nuclear scattering intensity, magnetic scattering intensity and the nuclear-magnetic interference term, or simply the first, second and third terms from equation 2.10. The fourth term, the chiral term, is also relevant for certain magnetic structures, but no such structure was studied in this thesis and this term is ignored.

If the incident beam is fully polarised, $P_i = \pm 1$, for example, along the z-axis, then the flipping ratio, or the ratio of the intensity of scattering for incoming positively polarised neutrons to the intensity of scattering for incoming negatively polarised neutrons,[40]

$$R = \frac{I_{+z}}{I_{-z}} = \frac{F_N F_N^* + \mathbf{F}_{M\perp}.\mathbf{F}_{M\perp}^* + (F_N F_{M\perp z}^* + F_N^* F_{M\perp z})}{F_N F_N^* + \mathbf{F}_{M\perp}.\mathbf{F}_{M\perp}^* - (F_N F_{M\perp z}^* + F_N^* F_{M\perp z})} \tag{2.18}$$

Here $F_{M\perp z}$ is the component of $\mathbf{F}_{M\perp}$ parallel to the z-axis. This can be simplified under the following conditions, both of which are relevant for this thesis. Firstly, if the crystal structure is centrosymmetric then all of the terms of equation 2.18 are real. Secondly, if the magnetisation (and therefore $\mathbf{F}_M$) is fully aligned along the z-axis then $\mathbf{F}_{M\perp}$, $F_{M\perp z}$ and $\mathbf{F}_M$ are connected by the angle α between the scattering vector and the $z - axis$ by the equations,

$$F_{M\perp z} = F_M \sin^2 \alpha, \tag{2.19}$$

$$|\mathbf{F}_{M\perp}|^2 = |\mathbf{F}_M|^2 \sin^2 \alpha. \tag{2.20}$$

These results mean that,

$$R = \frac{F_N^2 + 2F_N F_M \sin^2 \alpha + F_M^2 \sin^2 \alpha}{F_N^2 - 2F_N F_M \sin^2 \alpha + F_M^2 \sin^2 \alpha}. \tag{2.21}$$

Measurements made in this thesis are all obtained with $\alpha \sim 90°$, which leads to further simplification and R can be written as

$$R = \frac{(F_N + F_M)^2}{(F_N - F_M)^2}. \tag{2.22}$$

It is now very easy to see the advantage of this method of measuring F_M in a ferromagnet with a known F_N. There is a much higher sensitivity to F_M using polarised neutrons compared to a measurement with unpolarised neutrons. For example, if $F_M = 0.1F_N$ and a measurement of F_M is performed using unpolarised neutrons,

$$I = F_N^2 + F_M^2 = F_N^2 + (0.1 \times F_N)^2 = 1.01F_N^2. \tag{2.23}$$

However, measuring the flipping ratio with polarised neutrons gives,

$$R = \frac{(F_N + 0.1F_N)^2}{(F_N - 0.1F_N)^2} = \frac{1.21F_N^2}{0.81F_N^2}. \tag{2.24}$$

This means the difference in measured signal between F_M being present or not in the unpolarised neutron measurement is 1%, but using polarised neutrons to measure the flipping ratio the difference is 49%.

This method only works for ferromagnets, where there is interference between the magnetic and nuclear scattering. However, it is possible to induce a ferromagnetic moment on an antiferromagnetic or paramagnetic material by applying a large magnetic field, allowing this method to be used to study the magnetisation distribution in these types of materials.

2.1.5 Inelastic Neutron Scattering

It is possible for scattering to occur such that $E_T \neq 0$ and this is known as inelastic scattering. One possible mechanism for this is for the neutron to exchange energy into the crystal lattice and create a quantum of vibrational energy, known as the phonon. It is also possible for the neutron to absorb a phonon and therefore take energy from the lattice. However, the process of neutron absorbing a phonon is much less likely than the process of it creating one; this is due to the number of phonons of energy ω,

$$n_j(\omega) = \frac{1}{e^{\beta\hbar\omega_j} - 1}, \tag{2.25}$$

where $\beta = \frac{1}{k_{\mathrm{B}}T}$, being low for any experimentally realistic temperature.

2.1.6 Magnetic Inelastic Neutron Scattering

A neutron can also cause an excitation to an ordered magnetic lattice, called a magnon. In this case the neutron generates a magnetic excitation, such as one of the spins in the lattice to flip, see section 1.6. The number of magnons in the ground state at low temperatures, by the same reasoning as equation 2.25, means that the neutron almost always loses energy to create a magnetic excitation, rather than to absorb energy from one. Mapping out the excitations of the magnetic structure gives important information on the strength of the interactions between two magnetic ions. Magnons typically have an excitation energy similar to the energy of a thermal neutron (although this can vary), meaning neutron scattering is a suitable tool for measuring the excitation spectrum of a magnetic lattice.

The partial differential cross-section for magnetic inelastic scattering may be written in the dipole approximation as,

$$\frac{d\sigma^2}{d\Omega dE} = (\frac{\gamma r_0}{2})^2 f^2(\mathbf{Q}) e^{-2W(\mathbf{Q},T)} \frac{k_i}{k_f} S(\mathbf{Q},\omega) \tag{2.26}$$

where $S(\mathbf{Q},\omega)$ is known as the response function, which is given by,

$$S(\mathbf{Q},\omega) = \sum_{\alpha\beta}(\delta_{\alpha,\beta} - \hat{Q}_\alpha \hat{Q}_\beta) S^{\alpha\beta}(\mathbf{Q},\omega) \tag{2.27}$$

where α and β refer to two of the cartesian axes x, y and z, and $S^{\alpha\beta}(\mathbf{Q},\omega)$ the space and time Fourier transforms of the time-dependent spin correlation function. The time-dependent spin correlation function is simplified when only the excitations created are considered, it can be expressed as,

$$S^{\alpha\beta}(\mathbf{Q},\omega) = \sum_{\lambda} \langle 0|S^{\alpha\dagger}(\mathbf{Q})|\lambda\rangle\langle\lambda|S^{\beta}(\mathbf{Q})|0\rangle\delta(\hbar\omega - E_0 - E_\lambda) \tag{2.28}$$

where $|0\rangle$ is the ground state of the system, with energy E_0, the sum is over all possible eigenstates $|\lambda\rangle$, with energy E_λ and $S^{\alpha}(\mathbf{Q})$ is the Fourier transform of the α-component of the spin S_j^{α}. It is the response function that contains the information of the spin wave model of the system.

2.1.7 Absorption

Measuring the intensity of the neutrons reaching the detector does not necessarily give an accurate measurement of intensity of the neutron scattering. Before or after a neutron has scattered it is possible for it to be either absorbed by a nucleus or for it to incoherently scatter, thus reducing the intensity of the scattered beam.[34] These two effects have a similar effect on the diffracted signal and are usually referred to as the absorption. Absorption is characterised by the equation,

$$I = I_0 e^{-\mu r} \tag{2.29}$$

where I is the intensity of the neutrons that have passed through a material with absorption coefficient μ, for a length r and I_0 the beam intensity at $r = 0$. The absorption coefficient for a sample containing n different elements is,

$$\mu = N \sum_{i=1}^{n} c_i \sigma_{ai} \tag{2.30}$$

where N is the number of atoms per unit volume, c_i is the fraction of the i^{th} element and σ_{ai} is the sum of the absorption cross-section of the element i and the cross-section of the absorption due to incoherent scattering.

In practice the absorption is usually determined when fitting the data from a diffraction experiment. For small crystals, usually less than 1mm, absorption can generally be ignored.

2.1.8 Extinction

Extinction is another effect which can cause the reduction of the measured neutron beam intensity.[34] The mechanism causing extinction and the effect it has on diffraction patterns are quite different from those due to absorption. Extinction is caused by the beam being more intense in the part of the crystal closest to the beam source, because neutrons will be scattered from the first few atomic planes. Therefore, further into the crystal, there is a lower intensity of neutrons that can scatter from the crystal. Extinction is most noticeable on very strong peaks, where a large percentage of the beam will be diffracted in the first few atomic layers of the crystal, meaning the rest of the crystal has a shortage of neutrons with which diffraction can occur. Similarly to absorption, extinction has to be treated empirically and accounted for when fitting data.

2.2 Neutron Scattering Experiments

To conduct neutron scattering experiments, the first thing that is required is a beam of neutrons with the correct characteristics for the experiment. An overview of all of these topics can be found in the book by Willis and Carlile.[34] More detailed accounts can be found in a large number of other sources.

There are currently two main ways of producing neutron beams suitable for neutron scattering. These are; the creation of excess neutrons during a nuclear fission chain reaction or by the spallation of high energy protons interacting with nuclei of heavy elements. Neutrons from these reactions have a wide range of energies, whereas for many experiments it is better to have the majority of neutrons to have an energy within a certain band. To achieve this, a neutron moderator can be used to get all of the neutrons into the required temperature range. For some experiments only one value of neutron energy is required, this can be set by a monochromator crystal or a chopper, depending on the instrument. Another characteristic of the neutron beam that can be modified is the polarisation of the beam. Finally, the beam has to be measured using a detector to get information about the experiment.

2.2.1 Neutrons from Nuclear Reactors

Nuclear reactors produce neutrons from the nuclear fission of a fissile material. An equation for a common reaction in modern research reactors would be,

$$^{235}U + n = 2.4n + \text{fission fragments} + 192.9\text{MeV} \tag{2.31}$$

where a combination of ^{235}U (a fissile isotope) and a neutron n, gives excess neutrons out, as well as unwanted radioactive products of lower mass and a significant amount of energy. The excess neutrons can cause further fission events or can escape the reactor. In a research reactor designed to maximise the neutron flux, the reactor is configured to allow as many neutrons as possible to leave the reactor whilst maintaining a chain reaction. Reactor sources have been in use for many years and their neutron output has long since been optimised. Reactors give a reliable and steady flux of neutrons to experiments. The reactor source used for work in this thesis is at the Institut Laue-Langevin (ILL) in Grenoble.

2.2.2 Neutrons from Spallation Sources

Spallation sources are newer than reactor sources and have the long term potential to produce higher neutron fluxes. The mechanism for producing neutrons involves a high energy proton entering a target made of a heavy metal. The proton interacts with nuclei in the target by going through a cascade reaction, where it briefly joins a nucleus and is then ejected and able to interact with more nuclei in the same way. After the proton has left the nucleus, the nucleus is in an excited state and to return to its ground state it undergoes neutron evaporation, where low energy neutrons leave the nucleus. A single incident proton can produce 20-40 neutrons through a series of cascade and evaporation events.

There are number of methods that can be used to create the high energy protons used in spallation. The experiments in this thesis that were performed at a spallation source, were all conducted at the ISIS facility at the Rutherford-Appleton Laboratory in Oxfordshire, so the method used here will be described in further detail. An ion source produces H^- ions, which are accelerated in a linear accelerator injector towards an alumina foil, where the ions are stripped of their two electrons, leaving a proton. The protons are then injected into a synchrotron, where they rotate in pulses. Protons are extracted from this ring and directed towards the target, a series of tantalum discs, where the spallation occurs. The protons are produced in short, intense pulses at 50Hz, allowing time of flight measurements to be made between pulses.

Alternatively, by using a cyclotron instead of a synchrotron (such as at SINQ, at the Paul Scherrer Institute in Switzerland), a constant stream of protons can be produced, meaning the spallation occurs continuously and resulting in a constant neutron beam for the experiment.

2.2.3 Moderators

Typical energies of neutrons leaving a neutron source tend to be in the range of 1MeV, whereas for most experiments they should have an energy around 0.1 to 100meV. to achieve this a neutron moderator must be used. A moderator is maintained at a constant temperature and neutrons enter thermal equilibrium with the moderator as they pass through it. Typical experiments are performed with moderators at room temperature, around 300K. However, to access longer wavelengths, it is preferable to use a cold moderator, such as liquid hydrogen kept at 20K. For shorter wavelengths a hot moderator can be used, such as a block of graphite kept at 2400K.

2.2.4 Monochromators

The simplest method of getting a monochromatic beam is simply to diffract the polychromatic neutron beam from a single crystal sample at an angle θ, such that only wavelengths that satisfy the Bragg equation $n\lambda = 2d\sin(\theta)$ will diffract. This can leave multiple orders of wavelengths satisfying different values of n and diffraction orders other than the required one must be suppressed, such as by use of resonant absorbers.

2.2.5 Choppers

There are a number of different types of choppers used at neutron sources around the world, but of most relevance in this work is the Fermi chopper, which were used during experiments performed at ISIS. These choppers are useful on pulsed neutron sources, because neutrons of different energies within a pulse travel at different velocities. A Fermi chopper is a cylinder of neutron absorbing material with slots of neutron transmitting material running through it. The chopper spins around its cylindrical axis, perpendicularly to the neutron beam. When the transmitting slots are parallel to the beam, neutrons are let through. As the chopper is spinning very quickly, only neutrons in a narrow velocity band can actual go through the slots while they are open, resulting in an essentially monochromatic pulse of neutrons.

2.2.6 Polarising Neutrons

Neutron beams can be polarised by using Bragg peaks in ferromagnetic crystals where the nuclear scattering has the same strength as the magnetic scattering. Usually a magnetic field is applied to ensure that all of the material is ferromagnetic, overcoming domains in the sample. Using the first three terms in equation 2.10 and the condition that $F_N = F_M$ for the Bragg peaks being used to polarise, the scattering cross-section

$$\sigma = F_N^2 + F_M^2 - 2P_i F_N F_M \tag{2.32}$$

Therefore any neutrons which have $P_i = 1$ have a scattering cross-section $\sigma = 0$ and are not diffracted. Only neutrons with $P_i = -1$ are scattered, resulting in a fully polarised beam.

Once a polarised neutron beam has been created, it can be manipulated to change the polarisation direction of the neutrons. A small magnetic field, called the guide field, must be applied to keep the neutrons polarised along the whole flight path. If the guide field is varied adiabatically the magnetic moment of the polarised neutrons can be altered. A device known as a spin flipper reverses a neutron's polarisation; this is useful in an experiment that measures the flipping ratio of neutrons.

2.2.7 Neutron Detectors

One of the advantages of neutrons as a probe is their ability to penetrate deeply into most materials due to their weak interaction with matter. This has the side-effect of making them quite difficult to detect directly. One common type of detector is a gas detector. These detectors work by having a gas containing nuclei that readily undergoes neutron capture reaction. One suitable nucleus is the increasingly hard to come by ^{3}He, which combines with a neutron to form tritium and a proton. The electrical signal from the proton can be easily detected if the gas is confined to a cell with proton detection electronics inside it.

Alternatively a scintillator can be used. When a neutron capture event occurs in ^{6}Li it emits a burst of light which causes ionizing secondary particles to be formed which are easily detected.

Beam monitors are a special type of detector designed to interact with a small percentage of the total beam, typically $< 1\%$. These pick up the intensity of the incoming beam, which is important for getting accurate intensities of peaks. Beam monitors can be a sparse medium of ^{235}U ions that undergo fission when they interact with a neutron and the fission products can be easily detected. Another typical monitor is a low efficiency gas detector. A well designed monitor must let most of the neutrons pass, or else it will decrease the intensity of the beam falling on the sample.

2.3 Neutron Instruments

Neutrons are a very versatile tool for probing matter, so many different types of instruments have been developed for the variety of experiments that can be performed. In this section the most relevant instruments to this thesis will discussed. Much of the information about the instruments can be found in references about the example instruments mentioned in this chapter. The book by Willis and Carlile,[34] covers a number of the instrument types discussed here.

2.3.1 Two-Axis Diffractometer

A very simple diffractometer that is suitable for some measurements is a two axis diffractometer.The sample must be mounted with the scattering plane to be investigated in the plane of the neutron beam and detector. The first axis controls then incoming wavelength and the second axis controls the scattering angle by changing θ (sample rotation) and 2θ (the scattering angle). A diffractometer similar to this is D3 at the ILL, which has a large magnet mounted around the sample axis. The only difference is that the detector on D3 can be lifted out of the scattering plane by a small amount, this means that the detector position in the plane of the experiment is not actually 2θ. Two new angles are introduced, ω, the angular position of the detector to the experimental plane and γ, the angle the detector is lifted out of the plane. A diagram showing D3 is shown in Fig. 2.1

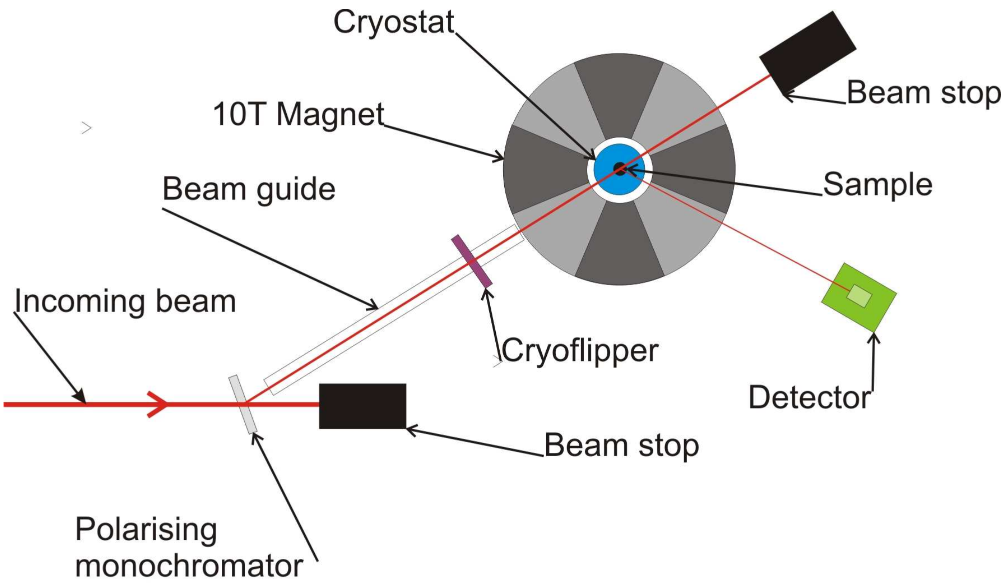

Figure 2.1: An overhead plan of the instrument D3 at the ILL. This instrument is designed to provide beam of polarised neutrons incident on the sample. In this set up the sample is inserted in a cryostat and a large magnetic field can also be applied.

2.3.2 Four-Circle Diffractometer

A standard instrument for monochromatic diffraction experiments is the four-circle diffractometer. As the name suggests these instruments have four different axes of rotation, shown in Fig. 2.2. The three rotations θ, χ and ϕ are coupled, with ϕ sitting on χ, which in turn sits on θ. Together these three angle form an Eulerian cradle. The angle 2θ is the diffraction angle and is independent from the other three rotations, usually it is the position of the detector. By manipulation of the sample alignment using the first three angles it is possible to measure diffraction peaks in most of reciprocal space.

Two four-circle neutron diffraction instruments were used in the course of this study, instruments D9 and D10 at the ILL. The only small variation on these instruments from the standard four-circle diffractometer is that they have a small two-dimensional detector. This has the advantage of making peaks slightly easier

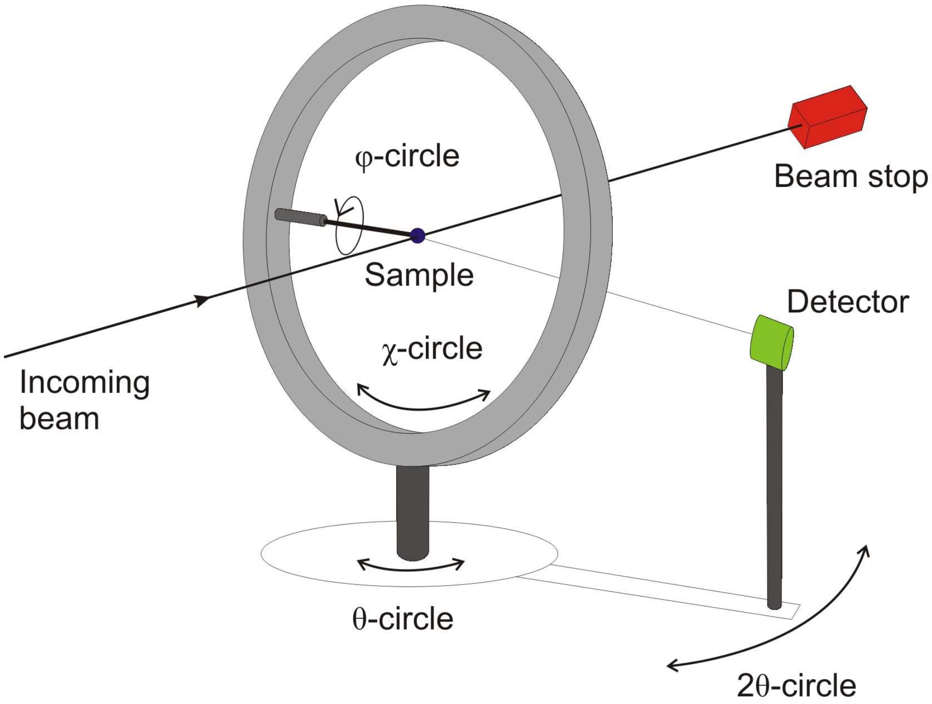

Figure 2.2: A sketch of a typical four circle diffractometer, showing the four rotations available. These are the ϕ, χ, θ and 2θ rotations.

to find and the ability to measure a true integrated intensity of the entire peak as opposed to measuring a line across the maximum intensity.

2.3.3 Time-of-Flight Diffractometer

A different way of measuring a diffraction signal can be used at a pulsed neutron source, making use of the fact that neutrons of different energies travel at different velocities. The crystal is mounted such that the scattering plane to be investigated is in the same plane as the beam and the detector. When a pulse of white neutrons is incident upon the crystal, neutrons can scatter from every possible scattering wave vector. This is similar to a simple Laue method experiment, with the main difference that the time of arrival of the neutron at the detector gives information on the neutron wavelength. Since the neutron position and wavelength are known, a full picture of the scattering plane can be constructed easily. This technique can be used to observe scattering vectors that are not observed at Bragg positions. With the previous methods, it is hard to build up a picture of the whole scattering-plane using a point detector or a small area detector. An instrument of this type used for neutron diffraction in this way for work in this thesis is the now decommissioned, PRISMA at ISIS.

2.3.4 Time-of-Flight Spectrometer

A time-of-flight spectrometer can also be used to measure the energy spectrum of excitations in crystals. These instruments work by measuring the time of arrival of a neutron at the detector after a pulse has interacted with the sample. An incoming pulse of white neutrons is made monochromatic by use of a Fermi chopper. The monochromatic pulse of neutrons then interacts with the sample and the neutrons are scattered. Any neutrons that cause an excitation in the sample, such as a phonon or magnon, will have lost energy and therefore travels more slowly. By measuring the time and position that a neutron reaches a detector, the energy and the momentum of the excitation it caused can be calculated.

Normally spectrometers meeting this description, such as MAPS at ISIS (shown in figure 2.3), are built with very large detector banks so that large parts of reciprocal space can be measured simultaneously. This is important because the neutron flux at the detectors is quite low; therefore it is advantageous to run the experiment for a relatively long counting time and map out a large part of reciprocal space.

2.3.5 Alignment Instruments

In laboratories such as the ILL and ISIS there are alignment instruments where crystals can be looked at on a simple instrument to check the crystal orientation

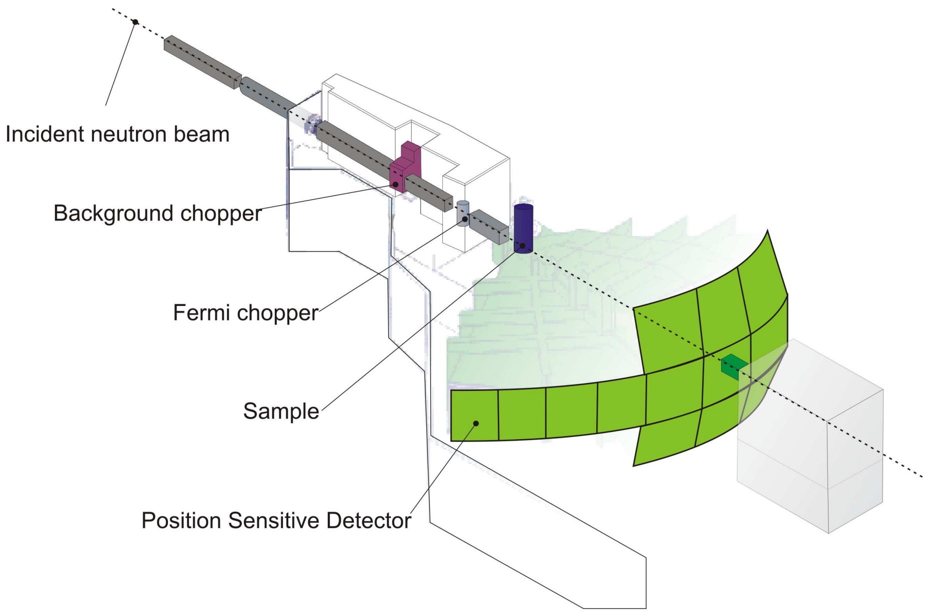

Figure 2.3: A sketch of the MAPS spectrometer at ISIS with some of the most important components labeled.

or to co-align a few crystals for an experiment. At ISIS the alignment instrument is ALF. Crystals can be mounted on an Eulerian cradle for orientation and the white-beam is diffracted into a two dimensional detector bank.

Another advantage of alignment instruments (for example the neutron Laue instrument at the ILL, Orient Express) is that they can be used to check the quality of samples that are thought to be single crystals. It is often hard to know for sure whether a sample does have more than one crystal grain in it, since most lab based procedures to test this involve x-rays, which only probes the surface of the sample.

2.4 X-ray Scattering

X-ray scattering and neutron scattering share many similarities, the goal of any experiment is still to measure intensity of x-rays scattered into a solid angle, therefore the definition of the differential cross section is the same as in equation 2.2.

X-rays, as a form of electromagnetic radiation, mainly interact with the charge of the electrons in a material, but can also weakly interact with the magnetic moment of any unpaired electrons. The first part of this section will cover the normal interaction between x-rays and crystals. A good introduction to this and many parts of the theory of x-ray physics is given in the book by Als-Neilsen and McMorrow.[35] The second part of this section covers, the anomalous scattering due to resonance effects when the energy of an x-ray is equal to that of an atomic transition, which can enhance the intensity of magnetic features in a crystal. A good theoretical introduction to this technique can be found in the paper by Altarelli.[41]

2.4.1 X-ray Scattering Theory

When an x-ray phonon interacts with a charged particle, its plane wave electric field causes the particle to oscillate. The oscillating particle can then act as a source for the emission of another x-ray. The strength of the emission is polarisation dependent. If the emission is in a plane parallel to the polarisation of the incoming x-ray, then the intensity of the emitted x-rays is reduced, the full oscillation of the charged particle is not observed from the scattering point. In this case the intensity is reduced by a factor of $\sin(\Psi)$ in this type of scattering, where Ψ is the angle from the direction of the charged particle oscillation to the scattering direction. However, if scattering is in a plane perpendicular to the polarisation of the x-ray, then the full oscillation of the particle can always be observed.

In a similar argument for an incoming plane wave of neutrons being scattered into a spherical wave with a scattering length b, the ability of a charged object to scatter an x-ray is usually expressed in terms of the scattering length r. For a charged particle, the scattering length,

$$r = \frac{Q^2}{4\pi\varepsilon_0 mc^2} \tag{2.33}$$

where Q is the charge of the particle, m is the mass, ε_0 the permittivity of free space and c the speed of light. For electrons the scattering length is known as the Thomson scattering length $r_0 = 2.82 \times 10^{-15}$m. It is clear from this equation that scattering from electrons will always be much stronger than that from protons or nuclei, since the mass of an electron is orders of magnitude smaller than that of a proton or nuclei. For a more complex arrangement of charges, such as the electrons in an atom, the distribution of the electron density $\rho(\mathbf{r})$ has to be considered to determine the total scattering length of the atom, known as the atomic form factor,

$$f^0(\mathbf{Q}) = \int \rho(\mathbf{r}) e^{i\mathbf{Q}.\mathbf{r}} d\mathbf{r} \tag{2.34}$$

where the contribution from the volume element $d\mathbf{r}$ at position $\mathbf{r}$ contributes to the scattering with a phase factor $e^{i\mathbf{Q}.\mathbf{r}}$, for scattering wavevector $\mathbf{Q}$.

Equation 2.34 is the classical atomic form factor, but of course the electrons in an atom behave quantum mechanically and sit in discrete energy levels. One effect of this is that the oscillation of the electrons might be restricted in their response to the incoming field, reducing the scattering length by $f'(\hbar\omega)$. This is mainly an energy dependent phenomenon and if the x-ray photon energy is much higher than the binding energy then f' is taken to be zero. There is also a phase lag between the incoming x-ray and the emitted one from the oscillating electron, this gives rise to another energy dependent component to the form factor if'' and this gives the full atomic form factor as,

$$f(\mathbf{Q}, \hbar\omega) = f^0(\mathbf{Q}) + f'(\hbar\omega) + if''(\hbar\omega) \tag{2.35}$$

Further expanding these ideas from an atomic level to a crystal structure, the structure factor away from an energy resonance is written,

$$F(\mathbf{Q}) = -r_0 f_D \sum_{\mathbf{r}_j} f_j(\mathbf{Q}) e^{i\mathbf{Q}.\mathbf{r}_j} \sum_{\mathbf{R}_n} e^{i\mathbf{Q}.\mathbf{R}_n} \tag{2.36}$$

The first sum is over the unit cell of the lattice containing atoms j and the second term is the sum over the whole lattice and only has a meaningful value if $\mathbf{Q}.\mathbf{R}_n = 2\pi \times \text{integer}$, where $\mathbf{R}_n$ is a lattice vector. The term f_D is the Debye-Waller factor, which has the same meaning for x-rays as it does for neutrons.

It is possible to directly observe magnetic scattering using x-rays, but the amplitude of magnetic scattering is reduced by a factor of $\hbar\omega/mc^2$ compared to the Thomson scattering length, making it a very weak effect. Magnetic x-ray scattering was first observed in 1972 [42] using lab based x-ray apparatus and very long counting times, it is now much simpler to measure magnetic peaks due to the very high intensity x-ray sources provided by a synchrotron. This appears in the full expansion of the term f^0 in 2.35 and is given by Blume et al.[43].

$$f^{magnetic}_{non-res} = ir_0(\frac{\hbar\omega}{mc^2}) f_D[\frac{1}{2}\mathbf{L}(\mathbf{Q}).\mathbf{A} + \mathbf{S}(\mathbf{Q}).\mathbf{B}] \tag{2.37}$$

with $\mathbf{L}$ and $\mathbf{S}$ the orbital and spin magnetic densities respectively. The terms $\mathbf{A}$ and $\mathbf{B}$ are complicated terms involving the incoming and scattered wavevectors and polarisation vectors,[44]

$$\mathbf{A} = 2(1 - \hat{\mathbf{k}}.\hat{\mathbf{k}}')(\hat{\varepsilon}' \times \hat{\varepsilon}) - (\hat{\mathbf{k}} \times \hat{\varepsilon})(\hat{\mathbf{k}}.\hat{\varepsilon}') + (\hat{\mathbf{k}}'.\hat{\varepsilon}')(\hat{\mathbf{k}}'.\hat{\varepsilon}) \tag{2.38}$$

$$\mathbf{B} = (\hat{\varepsilon}' \times \hat{\varepsilon}) + (\hat{\mathbf{k}}' \times \hat{\varepsilon}')(\hat{\mathbf{k}}'.\hat{\varepsilon}) - (\hat{\mathbf{k}} \times \hat{\varepsilon})(\hat{\mathbf{k}}.\hat{\varepsilon}') - (\hat{\mathbf{k}}'.\hat{\varepsilon}') \times (\hat{\mathbf{k}}.\hat{\varepsilon}) \tag{2.39}$$

where $\mathbf{k}$ and $\mathbf{k}'$ are the incoming and scattered wave vectors respectively and ε and

ε' are the incoming and scattered polarisations respectively, with hats denoting unit vectors.

2.4.2 Resonant X-ray Scattering

Resonant x-ray scattering occurs when the energy of the x-rays approaches that of the electronic transitions in atoms. There is an enhancement to the magnetic signal, which can be considered similar to the classical damped, driven simple oscillator, where there is an increase in the amplitude of the oscillation when the driving frequency is close to the natural frequency of the oscillator. Quantum mechanically, resonance features are understood by the second order perturbation of the full x-ray and matter interaction Hamiltonian, the details of which are given in the paper by Altarelli.[41]

Before continuing with the discussion of resonant x-rays, it is worth mentioning the notation used to describe the electronic transitions that resonant x-ray experiments probe. The principle quantum number, $n = 1$, 2, 3 and 4 is usually expressed as a shell denoted by the letter K, L, M and N respectively. The l (orbital) and s (spin) quantum numbers give the total magnetic quantum number $j = l + s$. The l and j quantum numbers can be denoted l_j and are then designated by numbers, for example $s_{1/2} = 1$, $p_{1/2} = 2$, $p_{3/2} = 3$, *etc.*(often this number is written in Roman numerals). Thus the transition from the quantum state $2p_{1/2}$ can be written as L_2. The transitions are named after the state that they are being excited from, therefore a K-edge transition is from the $1s$ core level and an $\mathrm{L}_{2,3}$-edge is from the $2p$. The level which they excite into is dependent on what sort of transition they undergo. An electric dipole transition (which is the most common), excites an electron into a state with $l = \pm 1$ and a quadrupole transition is with $l = \pm 2$. The upper state denoted by this will be the lowest available state of its type. In Mn, a K-edge transition excites an electron from the 1s state into the 4p and in a rare earth ion a L$_{III}$-edge is the transition from the 2p-orbital to the 5d-orbital. It should be made clear that the transitions discussed are not true atomic excitations and should be considered as a virtual process with instantaneous absorption and emission of the x-ray.

At an energy resonance, the terms in the x-ray atomic form factor, equation 2.35, f' and f'' become more significant. The details of these terms depends on what the relevant atomic transition is, for the work in this thesis only the electric dipole transitions will be considered, these are the $l = \pm 1$ transitions. The form factor for an electric dipole becomes,[44]

$$f_{res} = (\hat{\varepsilon}.\hat{\varepsilon}')G^0 - i((\hat{\varepsilon}' \times \hat{\varepsilon})).\hat{\mu}_{\mathbf{j}}G^1 + (\hat{\varepsilon}'.\mu_{\mathbf{j}})(\hat{\varepsilon}.\mu_{\mathbf{j}})G^2 \tag{2.40}$$

where $\mu_{\mathbf{j}}$ is the magnetic moment of ion j, ε and ε' are the incoming and outgoing polarisations, respectively, and the G terms are factors containing details about the spherical harmonics of the transitions which can be considered to be constants. The first term in this equation is just a resonant enhancement to the diffraction peaks due to Thomson scattering. The second term is a true magnetic term being dependent on the on the moment $\mu_{\mathbf{j}}$ and this creates the first magnetic satellite peaks in a resonance experiment. The final term is also magnetic and can generate second harmonic magnetic satellites. The second term in the equation is the most relevant for work in this thesis. It is possible to work at quadrupole transitions ($l = \pm 2$) and even higher multipoles, but this thesis will be restricted to dipole transitions.

From equation 2.40, it is clear that the polarisation of the incoming and outgoing x-rays is important for understanding magnetic resonant x-ray scattering.

Although the x-rays can be linearly polarised in any direction, or circularly and elliptically polarised, there are two types of linear polarisation which are of particular importance, these are denoted as σ and π for the incoming x-ray and σ' and π' for the outgoing x-ray. For σ polarisation the x-ray is polarised orthogonally to the scattering plane and therefore $\sigma = \sigma'$. For π polarised light, the x-ray is polarised within the scattering plane, therefore $\pi \neq \pi'$. The angular difference between π and π' is 2θ, the scattering angle. These polarisation states are illustrated in Fig. 2.4.

For resonant x-ray scattering coming from the second term in 2.40, it can be shown that scattering of $\sigma \to \sigma'$ is forbidden, so strong magnetic signals are found in the $\sigma \to \pi'$ and $\pi \to \sigma'$ channels and as well as the $\pi \to \pi'$. One way of writing this is in a matrix representation for the second term in 2.40,

$$f_{res} = -iG^1 \begin{vmatrix} \sigma \to \sigma' & \pi \to \sigma' \\ \sigma \to \pi' & \pi \to \pi' \end{vmatrix} = \begin{vmatrix} 0 & \mu_1 \cos\theta + \mu_3 \sin\theta \\ \mu_3 \sin\theta - \mu_1 \cos\theta & -\mu_2 \sin\theta \end{vmatrix} \tag{2.41}$$

where θ is the scattering angle and (μ_1, μ_2, μ_3) is the magnetic moment lying in the cartesian direction $\hat{U}_1$, $\hat{U}_2$ and $\hat{U}_3$, which are defined by the experimental geometry. The definition of the directions are, $\hat{U}_3 = -\hat{\mathbf{Q}}$, where $\hat{\mathbf{Q}}$ is the unit scattering vector, $\hat{U}_2$ is perpendicular to the scattering plane and $\hat{U}_1$ is perpendicular to $\hat{U}_3$, but in the scattering plane. These directions are also illustrated in Fig. 2.4.

One advantage of resonant x-rays is that it is a somewhat element specific probe. When probing the magnetic moment μ, it should be possible to excite electrons directly in to the atomic shell containing the unpaired electrons and the signal measured comes almost entirely from those electrons. However, due to a number of reasons, it is not always possible to find a resonance that meets this requirement, for example the correct energy might not be available on the instrument being used. It

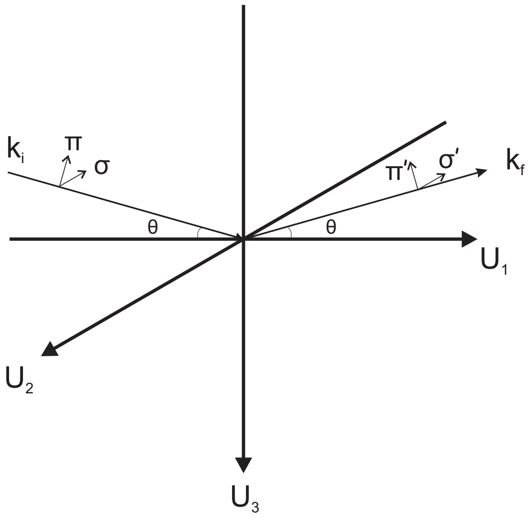

Figure 2.4: The polarisation and the axes labeling for the scattering in a polarised x-ray experiment. The lines marked k_i and k_f show the directions of incoming and outgoing x-rays, respectively. These are shown on the axes U_1, U_2 and U_3 which are defined in the text. Incoming σ or scattered σ' polarised light are both polarised parallel to U_2 and the polarisation direction for both are equal. The incoming π and outgoing π' polarised light have different directions of polarisation, but both direction lie in the scattering plane. The scattering angle θ is also marked.

is still possible to observe a magnetic signal from resonance into a different energy level. All of the states that are available for an electron to be excited into are at a similar energy and there is expected to be some hybridisation of these states. This means that the magnetism is still apparent at resonances other than the one that would excite an electron into the magnetic state. If there is more than one species of magnetic ion in the unit cell, then they will all contribute to the resonant x-ray signal with varying amounts. It is also important to consider the type of orbital that the magnetic electrons are sitting in, for example a d-orbital is spatially quite spread out and it could be expected that it overlaps with orbitals in other ions, but an f-orbital tends to be spatially confined and less likely to have an overlap. These points are discussed in the work by Johnson et al.[45] where, during a similar study on $TbMn_2O_5$, it was observed that there was contribution from the manganese Mn^{4+} magnetic structure at the Dy L_{III}-edge.

2.4.3 Azimuthal Scans

One type of experiment that can exploit the polarisation relationships to investigate the magnetic structure of a material is a scan of the azimuthal dependence of the scattering. This type of scan is carried out in the $\sigma\pi'$ polarisation channel and therefore the μ_1 and μ_3 components of the magnetic structure can be investigated. To perform the scan the intensity of a magnetic scattering vector $\mathbf{Q}$ is measured. The crystal is then rotated around the scattering vector, with scans of the peak intensity being measured at regular intervals. As the crystal is rotated, the experimental axes $\hat{U}_n$ $(n = 1, 2, 3)$ remain the same, but different components of the magnetic moments in the crystal are investigated. The change in scattering intensity as the azimuthal angle is altered can be fit to a magnetic structure. Azimuthal scans have been used on a number of materials to investigate magnetic structures.[46, 47]

2.4.4 Full Linear Polarisation Analysis

Although equation 2.40 can be simplified to give equation 2.41 to just consider the σ, π and π' polarisation channels, it can be generalised to any polarisation,[43, 44, 45] which allows another type of measurement of the magnetic structure, called a full linear polarisation analysis (FLPA). For this type of measurement the incoming x-rays are linearly polarised at an angle χ, with $\chi = 0°$ being the same as σ polarised light and $\chi = 90°$ being equal to π polarised light. At each value of χ in the scan, a full analysis of the linear polarisation of the intensity of scattered light from a magnetic reflection is performed. This is achieved by measuring the intensity of the x-rays scattered with a linear polarisation of η, where $\eta = 0°$ and $\eta = 90°$ being the same as σ' and π' polarised light respectively. By measuring at a range of values of

η for each incoming polarisation angle χ, the relationship

$$I = \frac{I_0}{2}(1 + P_1 \cos 2\eta + P_2 \sin 2\eta) \tag{2.42}$$

can be mapped out. The parameters P_1 and P_2 are the first two Stokes parameters and describe the polarisation of the light (see, for example, the book, Optics by Hecht [48]). In particular, P_1 is related to the linear polarisation in the σ and π directions and P_2 is related to the linear polarisation in the intermediate ±45° directions.

It is shown elsewhere that P_1 and P_2 can be defined for magnetic peaks by using the second term in equation 2.40, which is now termed $f_{res}^{mag}(\hat{\varepsilon}', \hat{\varepsilon}, \hat{\mu}_j, \hat{\mathbf{k}}', \hat{\mathbf{k}}) = -i((\hat{\varepsilon}' \times \hat{\varepsilon})).\hat{\mu_{\mathbf{n}}} G^1$. This gives the following formulae,

$$P_1 = \frac{|\sum_j f_{res}^{mag}(\hat{\varepsilon}'_\sigma, \hat{\varepsilon}, \hat{\mu}_j, \hat{\mathbf{k}}', \hat{\mathbf{k}}) e^{i\mathbf{Q}.\mathbf{r_j}}|^2 - |\sum_j f_{res}^{mag}(\hat{\varepsilon}'_\pi, \hat{\varepsilon}, \hat{\mu}_j, \hat{\mathbf{k}}', \hat{\mathbf{k}}) e^{i\mathbf{Q}.\mathbf{r_j}}|^2}{|\sum_j f_{res}^{mag}(\hat{\varepsilon}'_\sigma, \hat{\varepsilon}, \hat{\mu}_j, \hat{\mathbf{k}}', \hat{\mathbf{k}}) e^{i\mathbf{Q}.\mathbf{r_j}}|^2 + |\sum_j f_{res}^{mag}(\hat{\varepsilon}'_\pi, \hat{\varepsilon}, \hat{\mu}_j, \hat{\mathbf{k}}', \hat{\mathbf{k}}) e^{i\mathbf{Q}.\mathbf{r_j}}|^2} \tag{2.43}$$

$$P_2 = \frac{|\sum_j f_{res}^{mag}(\hat{\varepsilon}'_{+45^\circ}, \hat{\varepsilon}, \hat{\mu}_j, \hat{\mathbf{k}}', \hat{\mathbf{k}}) e^{i\mathbf{Q}.\mathbf{r_j}}|^2 - |\sum_j f_{res}^{mag}(\hat{\varepsilon}'_{-45^\circ}, \hat{\varepsilon}, \hat{\mu}_j, \hat{\mathbf{k}}', \hat{\mathbf{k}}) e^{i\mathbf{Q}.\mathbf{r_j}}|^2}{|\sum_j f_{res}^{mag}(\hat{\varepsilon}'_{+45^\circ}, \hat{\varepsilon}, \hat{\mu}_j, \hat{\mathbf{k}}', \hat{\mathbf{k}}) e^{i\mathbf{Q}.\mathbf{r_j}}|^2 + |\sum_j f_{res}^{mag}(\hat{\varepsilon}'_{-45^\circ}, \hat{\varepsilon}, \hat{\mu}_j, \hat{\mathbf{k}}', \hat{\mathbf{k}}) e^{i\mathbf{Q}.\mathbf{r_j}}|^2} \tag{2.44}$$

where,

$$\hat{\varepsilon}'_\sigma = \hat{\mathbf{U}}_2, \tag{2.45}$$

$$\hat{\varepsilon}'_\pi = -\sin\theta \hat{\mathbf{U}}_1 - \cos\theta \hat{\mathbf{U}}_3, \tag{2.46}$$

$$\hat{\varepsilon}'_{+45^\circ} = \frac{1}{\sqrt{2}}(-\sin\theta \hat{\mathbf{U}}_1 + \hat{\mathbf{U}}_2 - \cos\theta \hat{\mathbf{U}}_3), \tag{2.47}$$

$$\hat{\varepsilon}'_{-45^\circ} = \frac{1}{\sqrt{2}}(\sin\theta \hat{\mathbf{U}}_1 + \hat{\mathbf{U}}_2 + \cos\theta \hat{\mathbf{U}}_3), \tag{2.48}$$

$$\hat{\varepsilon} = \sin\chi \sin\theta \hat{\mathbf{U}}_1 + \cos\chi \hat{\mathbf{U}}_2 - \sin\chi \hat{\mathbf{U}}_3, \tag{2.49}$$

$$\hat{\mathbf{k}}' = \cos\theta \hat{\mathbf{U}}_1 - \sin\theta \hat{\mathbf{U}}_3, \tag{2.50}$$

$$\hat{\mathbf{k}} = \cos\theta \hat{\mathbf{U}}_1 + \sin\theta \hat{\mathbf{U}}_3. \tag{2.51}$$

Using these equations and conducting a full outgoing polarisation analysis to obtain the Stokes parameters for a series of incoming polarisations, it is possible to fit a magnetic structure to the values of the Stokes parameters

2.5 X-ray Sources and Techniques

For many years x-rays were produced from small anode sources that could only produce a relatively low intensity beam of x-rays. These are still useful for many lab based experiments, but when it was realised that the synchrotron radiation that was being produced at many nuclear physics experiments could provide a much higher intensity x-ray beam a number of dedicated storage ring sources were built with the purpose of producing intense x-ray beams. This section will cover the production of x-rays and an introduction to the kinds of instruments used for x-ray diffraction experiments. The final part of this section will look at the technique of producing and analysing polarised x-rays.

2.5.1 X-ray Sources

This section will cover the production of x-rays at storage ring sources such as ESRF, in Grenoble and Diamond Light Source, in Oxfordshire. All of the synchrotron x-ray experiments discussed in this thesis were performed at these two institutions. The idea of this technique is to produce radiation from an electron orbiting at relativistic speeds around a storage ring. Electrons are accelerated to these speeds in smaller particle accelerators, usually inside the circumference of the storage ring, and then injected into the storage ring itself. The book by Als-Nielsen and McMorrow provides an introduction to the x-ray scattering experiments at modern synchrotrons.[35]

The storage ring consists of long straight sections with magnets at the end of each section. The magnets bend the electrons into the next straight section. It is this bending of the electron beam that causes the beam to emit light as x-rays. The bending magnet itself is simply a large static magnetic field, causing the electrons to bend due to the Lorentz force. X-rays are emitted in the forward direction of the electron beam with a small angular divergence. Instruments at storage ring x-ray sources often make use of bending magnets as a source of x-rays. Light emitted at a bending magnet varies considerably in the energy of the photon emitted, so a full range of wavelength are available at bending magnets

An alternative way to get x-rays from the electron beam is to use an insertion device. Insertion devices are found on the straight sections of storage rings, but also rely on the bending of the electron beam to produce x-rays. There are two important types of insertion device, wigglers and undulators. Both of them have a similar design, a series of magnets with the field applied perpendicularly to the plane of the synchrotron, but the outgoing x-rays have different properties. A wiggler is similar to a number of bending magnets one after the other, with the electron being bent one way then the opposite direction a number of times. Therefore the light emitted by a wiggler is similar to that of a bending magnet in that a wide range of wavelengths are available, but it is much more intense.

An undulator looks very similar to a wiggler, but is designed so that an x-ray of a certain wavelength emitted at one of the oscillations in the undulator will be in phase with an x-ray of the same wavelength emitted at the next oscillation. This means that for a certain wavelength of light, the undulator creates a high intensity, almost monochromatic beam. Higher harmonics of the fundamental wavelength are also produced because the constructive interference condition that the undulator relies upon will also be met by any wavelength that is an integer times the fundamental wavelength. All of the x-ray instruments discussed in this thesis were on undulator insertion devices.

2.5.2 X-ray Instruments

The instruments used in this thesis were both variations on the four circle diffractometer described in section 2.3.2, with the four circles defined identically to those for a neutron scattering instrument. However, one of the x-ray instruments only had a very limited χ circle. The difference between the two instruments is the wavelength of x-rays that they are designed to use. The first, ID20 at the ESRF, is a hard x-ray instrument meaning the x-rays are in the shorter wavelength regime of the x-ray part of the electromagnetic spectrum. Hard x-rays penetrate quite far into materials and have suitable wavelengths for resonance such as the 3d transition metal K-edges and the lanthanide L-edges. They also allow for an Ewald sphere over a large part of reciprocal space.

The other instrument used is RASOR on the I10 beamline at Diamond Light Source. RASOR is designed for use in the soft x-ray regime. These are x-rays of longer wavelengths and lower energies (typically around one keV). Soft x-rays are very easily absorbed by any matter, including air, so the entire diffractometer must be kept at ultra-high vacuum. The vacuum chamber is the main reason that the χ-range is limited on an instrument like RASOR, it would be very difficult to have a vacuum large enough to allow a full χ circle. Soft x-rays are suitable for measuring resonances such as the 3d transition metal L-edges and the lanthanide

M-edges, which are useful since these resonances directly probe the magnetism in the relevant shells. The longer wavelengths involved in these instruments result in there being quite a small Ewald sphere, often not containing any Bragg peaks from the lattice, meaning crystal alignment often depends on finding super-lattice peaks.

2.5.3 Polarisation

Synchrotrons produce polarised x-rays, which are linearly polarised in the plane of the synchrotron [49]. This is because the electron acceleration is always in the plane of the synchrotron. Above and below this plane the light becomes circularly polarised, with a different handedness on either side of the plane. In the case of linear polarisation, a half-wave plate made from diamond can be used into rotate the light to any arbitrary polarisation, giving all possible incoming linearly polarised lights, including σ and π polarisations mentioned earlier.

Polarisation analysis makes use of Brewster's angle in a crystal for x-rays. An analyser crystal is chosen for the experimental set up that diffracts at 45°, therefore only one linear polarisation will be diffracted. The reasons for this can be thought of in terms of electrons oscillating. When an electron is excited by an electric field it emits photons in the same plane as it was excited in and none perpendicularly to that plane. Therefore when vertically and horizontally polarised light are incident on an analyser crystal with a scattering angle of $\theta = 45°$, the light that causes an electron to oscillate in the scattering plane diffracts, whereas the light that causes the electron to oscillate out of the scattering plane does not. By rotating the analyser crystal around the incoming beam it is therefore possible to detect any incoming polarisation.

2.6 Bulk Property Measurements

Measurements were made of two bulk physical properties of materials during the course of this project. Magnetisation was measured using two techniques, firstly using a superconducting quantum interference device (SQUID) and secondly by simply using detection coils. The electrical polarisation of a multiferroic material was by measuring the pyroelectric current.

2.6.1 Magnetisation Measurements

A SQUID measures the magnetisation of a sample by detecting the voltage imbalance across a Josephson junction in a ring of superconducting material. When a magnetised sample passes through a detection coil connected to the ring it induces a current in the superconductor proportional to the size of the magnetisation of the sample. If the current becomes great enough, it exceeds the critical current of the Josephson junction, inducing a voltage that can be detected. The direction the induced current flows changes for every half value of the magnetic flux quantum that goes through the detection coil. This means the SQUID is an extremely sensitive way of measuring the magnetisation in a sample.

2.6.2 Electrical Polarisation Measurements

A measurement of the pyroelectric current flowing to or from a material is a method that can accurately determine the temperature dependance of the electrical polarisation of a material. This measurement is conducted using the following process. An electric field is applied across the sample, parallel to the direction of the polarisation that is to be measured. The electric field is applied in the paraelectric phase of the sample. The sample is then cooled into the ferroelectric phase, with the field still applied. The temperature is lowered to the desired starting temperature for the measurement, which must still be in a ferroelectric phase and not in a lower temperature paraelectric phase. The electric field is then removed. The sample is then heated and the current flowing in to and out of the sample is measured. If the detected current is integrated over the temperature range of the measurement, then the polarisation of the ferroelectric phase can be determined.

Chapter 3

Determination of the Electronic Ground State of $Pr(Sr_{0.1}Ca_{0.9})_2Mn_2O_7$ Using neutron Scattering

---

3.1 Introduction

The family of manganite materials with the generic formula $R_{n+1}Mn_nO_{3n+1}$, where n is an integer, has been of interest for many years due to the strong interactions between the structure, charge, orbital and magnetic degrees of freedom in these systems.[17, 15, 10] Materials with this generic formula are referred to as the Ruddlesden-Popper series of perovskites.[50, 51] The most studied compounds in this series for manganites are the $n = 1, 2$ and ∞ members of the series, which are commonly referred to as the (single-)layered, bi-layered and cubic (or infinite layered) perovskite, respectively, see Fig. 3.1. These compounds became widely studied after the rediscovery of colossal magnetoresistance (CMR) in 1989 [52], which is an extreme example of the interaction of the different degrees of freedom. The details of CMR are covered in a number of good reviews [10] and an overview is given in section 1.7.

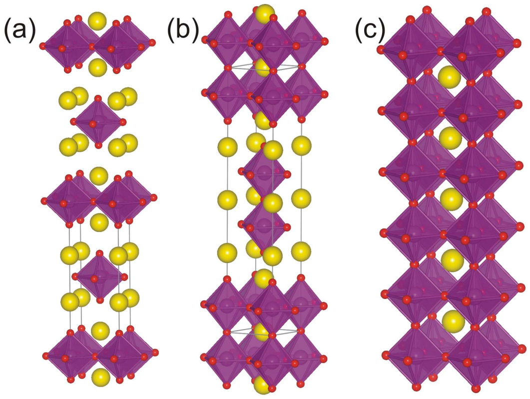

Figure 3.1: The single-layer, bilayer and infinite layer or cubic perovskite manganites. Mn ions are at the centre of the purple octahedra, the O ions are red and the yellow are the RE/AE ions.

CMR emerges from a number of competing magnetic and electronic interactions within the manganese oxide layers in these systems. Another interesting case of competing interactions is in the half-doped manganites (discussed in section 1.3)with some half-doped systems form the complicated CE-type antiferromagnetic phase [15] below T_N, see Fig. 3.2.

The magnetic structure of the CE phase throughout the Ruddlesden-Popper series is well established,[15, 21, 23] however, there are unanswered question about the nature of the electronic structure of the ground state. There are two main proposals for an electronic ground state that would lead to a CE-type magnetic structure. The first is the historic CE-phase model predicted by the Goodenough-Kanamori-Anderson rules for magnetic superexchange.[17, 53] This model will be referred to as the Goodenough (GE) model in this thesis. The alternative model is the Zener polaron (ZP) model, where two nearest neighbour manganite sites share an extra electron in an e_g orbital between the two sites, via the mechanism of the Zener double exchange [13] discussed in section 1.4.1. This forces the two manganese ions to act as one magnetic unit due to the strength of the double exchange between them and that two manganese ions share the charge evenly. This leads to the magnetism being located in the centre of the bond between two Mn ions. The existence of Zener polarons may result in a ferroelectric phase in half-doped manganites.[54]

In recent years there has been an effort to establish the best model for the electronic ground state, but so far the results have been inconclusive. Initial observations of half-doped manganites using neutron scattering [55] and resonant x-ray scattering [56] suggested that the GE model is correct and that charge ordering exists in the half-doped manganites. However, later experiments cast some doubt on the degree of the charge ordering,[57, 58] suggesting that there was not an integer splitting of charge. Other neutron and synchrotron x-ray diffraction experiments suggest the ZP model is more suitable,[59, 60] which is also supported by later x-ray diffraction [61] and electron diffraction.[62] Theoretical calculations have also predicted that the ZP model may be more suitable.[63, 54, 64] In recent years, new experiments have observed little evidence of Zener polarons, such as neutron spectroscopy [65] and soft resonant x-ray,[66] but observations of electrical polarisation in $Pr(Sr_{0.1}Ca_{0.9})_2Mn_2O_7$ are typically explained using Zener polarons.[23]

These difficulties in distinguishing between the two models arise from their magnetic similarity and from the difficulty in observing (the degree of) charge ordering in the systems directly. The magnetic similarity of the two systems can be seen by comparing figures 3.2 (a) and (b). The two models both have identical magnetic unit cells, with the majority of the magnetic moment located in the 3d orbitals of the Mn moments. The ZP model does predict that some of the moment will be found between the two Mn moments, near the oxygen site. However, this would be small and is therefore difficult to measure, see Chapter 4. Observing the degree of charge ordering has also proven to be difficult, with experiments offering a full range of results from true charge ordering of Mn^{3+} and Mn^{4+}, to a system of all $Mn^{3.5+}$ and seemingly any $Mn^{3.5+\delta}/Mn^{3.5-\delta}$ in between.

Neutron spectroscopy offers a method that can distinguish between the two models without having to face the difficulties outlined in the previous paragraph. The GE and ZP models have very different predicted spin wave dispersions.[67] In the ZP model the individual magnetic moments for the spin wave calculation are thought of as arising from the two Mn sites together, with the moment centered at the O-site between the two Mn's in each polaron. This results in a different set of magnetic exchange parameters for the two models. The charge ordering issue is also incorporated into the exchange parameters as will be demonstrated later in this chapter. The aim of the work presented here is to establish a suitable spin wave model for the excitations in $Pr(Sr_{0.1}Ca_{0.9})_2Mn_2O_7$ and to measure the strength of the magnetic interactions in the CE-type phase of a magnetic material, and to use this model to determine the electronic ground state of a CE-phase magnetic structure.

The CE magnetic phase has a complex structure within a single layer of MnO_2 in the sample and there is an advantage to not using the true perovskite material in which the CE phase was originally observed.[15] The infinite-layered perovskite allows for the orbital ordering and therefore the CE-type phase to exist in 3 directions within a sample, along the x-, y- and z-directions. This is due to samples not being true single crystals and different domains within the samples have the CE-phase forming perpendicularly to the CE-phase in other domains. However, in a layered material, the long axis always points in the same direction within a sample, meaning that the layers always lie parallel to each other and that the collected data will therefore be easier to interpret. Another important requirement for

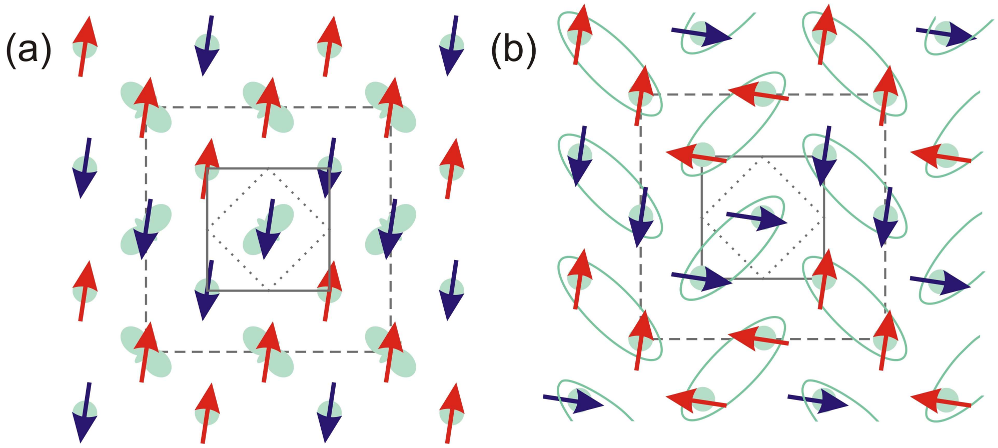

Figure 3.2: (a) The CE-structure magnetic structure for in an Mn-O plane. (b) The Zener polaron structure in the Mn-O plane. The ellipses show the neighbouring Mn ions that act as one magnetic moment in this structure. In both figures the dotted square shows the structural unit cell in the plane for an undistorted perovskite, the solid line is the in-plane unit cell in $Pr(Sr_{0.1}Ca_{0.9})_2Mn_2O_7$, which corresponds to the charge-ordered unit cell and the dashed-line the unit cell of the CE magnetic phase.

inelastic neutron scattering is to have the largest possible samples available. This is because the inelastic neutron scattering process produces quite a weak signal at the detector, so maximising the size of the sample will increase the signal, as long as sample quality is not compromised. For these reasons, the bilayer manganite material $Pr(Sr_{0.1}Ca_{0.9})_2Mn_2O_7$ was chosen for this experiment. The ratio of Pr to Sr/Ca, gives a Mn valency of +3.5 and the Sr to Ca ratio in this composition allows for large crystals to be grown.

3.2 Physical Properties of $Pr(Sr_{0.1}Ca_{0.9})_2Mn_2O_7$

The bilayer manganite $Pr(Sr_{0.1}Ca_{0.9})_2Mn_2O_7$ is studied here due to the CE-type magnetic phase that exist at low temperatures in this system. However, this material also goes through a number of phase transitions as a function of temperature, showing different types of structural, charge, orbital and magnetic ordering. All of the structural information in this section can be found in the previous work by Tokunaga et al.[23, 68, 69] At high temperature (> 370K), $Pr(Sr_{0.1}Ca_{0.9})_2Mn_2O_7$ exists in its purely structural ordered phase, described by the orthorhombic space group *Amam*, with lattice parameters a=5.410Å, b=5.462Å and c=19.277Å (at 405K). The unit cell within one plane is shown in both Fig. 3.2, showing that this structure contains more than one Mn-O square.

Below the first charge-order/orbital-order transition temperature, $T_{CO1} = 370$K, there appears to be a charge disproportionation between neighbouring Mn sites, towards Mn^{3+} and Mn^{4+}; the degree of this disproportionation is debated and important to the outcome of this and similar studies, but for simplicity, this short description of the structure shall assume that there is complete charge disproportionation of Mn^{3+} and Mn^{4+} ions. As the Mn^{3+} ion is a Jahn-Teller ion, the oxygen octahedron becomes distorted and the $3d_{3z^2-r^2}$ orbital becomes energetically favourable for the highest energy electron in the e_g orbitals, shown section 1.2.2. This creates the first charge-ordered/orbital-ordered phase in this material, shown in Fig. 3.3(a). In this phase the material takes on the orthorhombic space group *Pbnm*, with lattice parameters a=5.412Å, b=10.921Å and c=19.234Å (at 330K) and the unit cell has effectively doubled along the zigzag direction of the orbital ordering.

Unusually for this type of material, $Pr(Sr_{0.1}Ca_{0.9})_2Mn_2O_7$ undergoes a second charge-ordered/orbital-ordered transition, where the orbital ordering zigzag through the structure appears to rotate by 90°, shown in Fig. 3.3(b). This transition occurs at $T_{CO2} = 315$K when cooling ($T_{CO2} = 300$K when heating). The transition involves a change in space group to the orthorhombic *Am2m*, with lattice parameters a=10.812Å, b=5.475Å and c=19.203Å (at 295K). The crystallographic a and b axes have effectively been switched around, with the longer one still being in the direc-

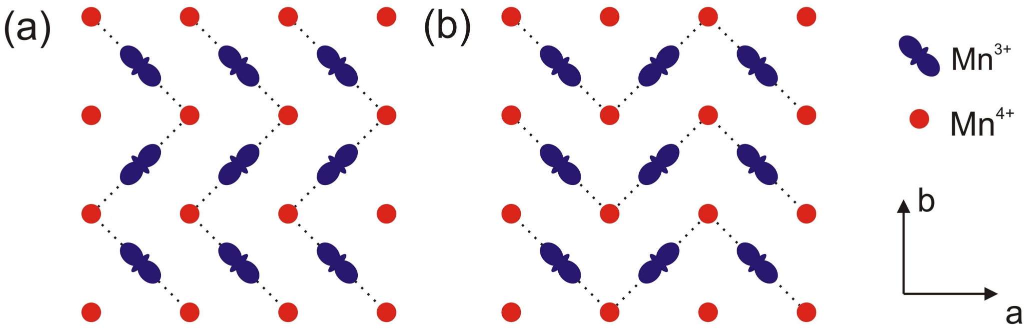

Figure 3.3: Showing the two charge-ordered/orbital-ordered phases in a single layer of Pr(Sr$_{0.1}$Ca$_{0.9}$)$_2$Mn$_2$O$_7$. The charge order is shown by colour and the orientation of the 3d$_{3z^2-r^2}$ is shown for the Mn^{3+} ions. The direction of the orbital ordering zigzags in two phases is also shown as a black dotted line. (a) The first charge-ordered/orbital-ordered phase showing the orbital ordering zigzag running parallel to the b-axis. (b) The lower temperature, second charge-ordered/orbital-ordered phase showing the orbital ordered zigzags parallel to the a-axis.

tion of the orbital ordering zigzag. This unusual rotation of the orbital ordering has been reported in a number of papers,[23, 68, 70, 71, 72] using a variety of methods to detect the rotation.

Below the Néel temperature $T_N = 153$K, the material is magnetically ordered in the CE-type magnetic structure. Along the orbital ordered zigzags, the Mn moments are aligned ferromagnetically, with adjacent zigzags aligned antiferromagnetically, this is shown in Fig. 3.2. The magnetic easy axis is along the *b*-axis, suggesting that the magnetic moments lie in the plane and also shows that there is some magnetic anisotrpy in the system. The structure in the second charge-ordered/orbital-ordered phase is maintained upon the magnetic transition, with the magnetic unit cell being doubled along the *b*-axis, when compared to the orbital ordered unit cell.

There is another structural transition at T$_S$=90K, where the system undergoes a structural distortion to become monoclinic. This phase has not been fully characterised as yet, but does not appear to effect the charge, orbital or magnetic ordering phases already present above 90K. However, a small rotation of the MnO_6 octahedra occurs at this transition.

3.3 Elastic Neutron Scattering - Experimental Details

Before performing the experiments to study the magnetic excitations, a diffraction experiment was performed in order to confirm the nature of the magnetic phases in the crystal and to determine the ordering temperatures. Performing a diffraction experiment under suitable conditions can also give information on diffuse scattering, a magnetic feature of the system. Diffuse scattering is typically observed between Bragg peaks, therefore an instrument that can measure large areas of reciprocal space is well suited to an investigation of diffuse scattering and provide diffraction data for checking sample quality. For these purposes, the high resolution diffractometer PRISMA at the ISIS Facility at the Rutherford Appleton Laboratory was used, see section 2.3.3 for more details of the instrument. PRISMA was particularly suited to studying magnetic phenomena due to the high intensity of long wavelength neutrons available.

Large single crystals of $Pr(Sr_{0.1}Ca_{0.9})_2Mn_2O_7$ were grown by D. Prabhakaran in the Clarendon Laboratory using the floating zone method, described by Prabhakaran et al.[73] The largest such crystal has a mass of 2.41g, with a number of other smaller crystals ranging from 0.5g to 1.5g. The largest crystal of $Pr(Sr_{0.1}Ca_{0.9})_2Mn_2O_7$ was aligned on ALF, the alignment facility at the ISIS, where it was found to be of high quality, and was then transferred to PRISMA. PRISMA was used in diffraction mode for this experiment. In this mode it is possible to measure a large area of reciprocal space, over a wide range of neutron wavevectors during one measurement.

The first part of the experiment was to measure scattering planes that are relevant to the charge-ordered/orbital-ordered phases and to the expected magnetic structure. The scattering plane that was measured was the $(h, 0, l)$ plane. The ferromagnetic zigzags are expected to lie in this plane. This scattering plane was measured in two different Q-ranges, a small Q range of 0.5Å^{-1} to 7Å^{-1} and a large Q range of 1.5Å^{-1} to 10.5Å^{-1}. The small Q range is suited to the measurement of the magnetic scattering, due to the magnetic form factor, whilst the large Q-range is more suited to investigating the structure of the sample. These two measurements of this scattering plane were performed at 5 temperatures, 380K ($T > T_{\text{CO1}}$), 310K ($T_{\text{CO1}} > T > T_{\text{CO2}}$), 225K ($T_{\text{CO2}} > T > T_{\text{N}}$), 175K ($T_{\text{CO2}} > T > T_{\text{N}}$, just above T_{N}, where diffuse scattering might be expected) and 9K ($T \ll T_N$). A second scattering plane was also studied, (h, h, l), which is related to the $(h, 0, l)$ direction by a 45° rotation around the *c*-axis. This scattering plane was only studied in the small Q range and only at the temperatures 9K, 175K and 225K.

The second part of the experiment was to measure the temperature dependence of a number of important Bragg peaks, characteristic of the different types of ordering expected in this material. Temperature scans were made for peaks in both scattering planes over a range of 9K to 330K.

3.4 Elastic Neutron Scattering - Results

The neutron scattering data for the $(h, 0, l)$ plane are plotted below in figures 3.4-3.13. The figures are in pairs with each pair corresponding to the sample temperature. The first figure of each pair shows the measured scattering plane at the small Q-range measurements (0.5Å^{-1} to 7Å^{-1}) and the second figure of each pair shows the large Q-range measurements (1.5Å^{-1} to 10.5Å^{-1}). The pairs are at the tem-

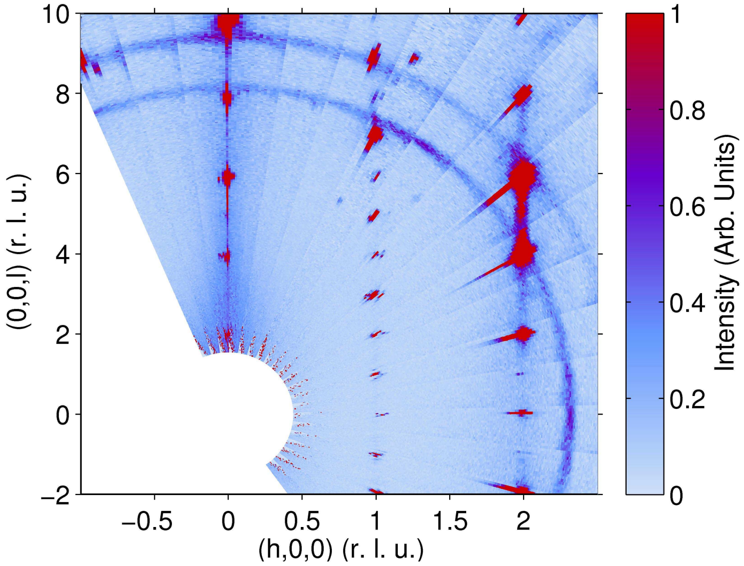

Figure 3.4: Diffraction data from the (h,0,l) plane at 380K with scattering at low Q (0.5Å^{-1} to 7Å^{-1})

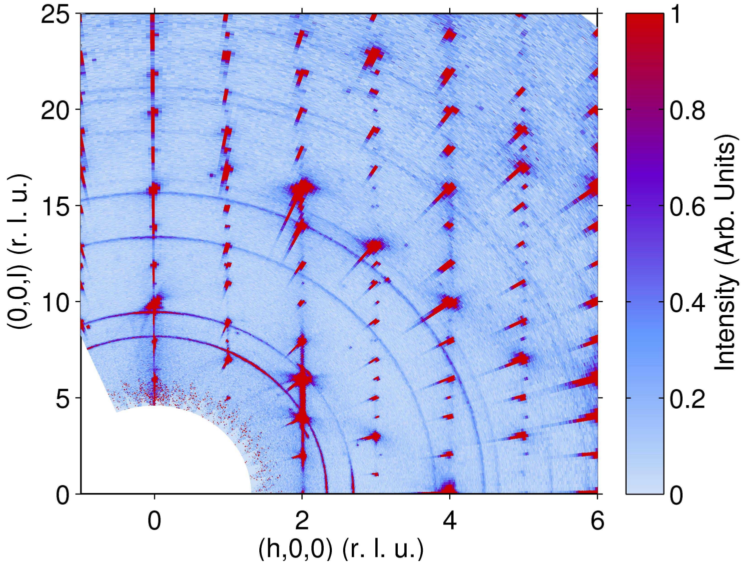

Figure 3.5: Diffraction data from the (h,0,l) plane at 380K with scattering at high Q (1.5Å^{-1} to 10.5Å^{-1})

peratures, 380K (Fig. 3.4 and Fig. 3.5), 310K (Fig. 3.6 and Fig. 3.7), 225K (Fig. 3.8 and Fig. 3.9), 175K (Fig. 3.10 and Fig. 3.11) and 9K (Fig. 3.12 and Fig. 3.13). The large circular features in all of these images are due to powder rings from the Al used in the cryostat and are not relevant to the sample.

The 380K data, above any charge-ordered/orbital-ordered or magnetic transition temperatures, shows the diffraction pattern due to the crystal structure in this scattering plane. This fundamental structure remains the same upon cooling through the various transitions, the different phases only ever cause slight distortions to the structure. If the crystal structure was tetragonal and the fundamental unit cell was just one Mn-O square, the dotted box in Fig. 3.2, then the peaks in the line $(2, 0, l)$ would be the fundamental structural peaks. However the distortion to an orthorhombic structure in this material doubles this unit cell in the Mn-O plane and the fundamental structural peaks are the weaker series along the line $(1, 0, l)$.

When cooled down to 310K, the data shows that the structure has changed, with the new lines of peaks at $(n + 1/2, 0, l)$ (where n is an integer). This sample was now in the first charge-ordered/orbital-ordered phase so these peaks can be attributed to the structural distortions arising from this transition and the new larger unit cell. Although the characteristic peaks of the CE-type magnetic order also appear in these positions, the peaks observed at this temperature are due to structural distortions. This is apparent because the intensity of these peaks remains strong at larger scattering vectors and because the temperature dependence of the peak intensity shows that 310K is above T_N, see figures 3.15 and 3.16. A series of peaks due to a magnetic structure would be expected to have lower intensity at larger wavevectors, as the magnetic form factor tends to zero with longer scattering vectors.

Upon further cooling down to 225K, there has been another small change to the

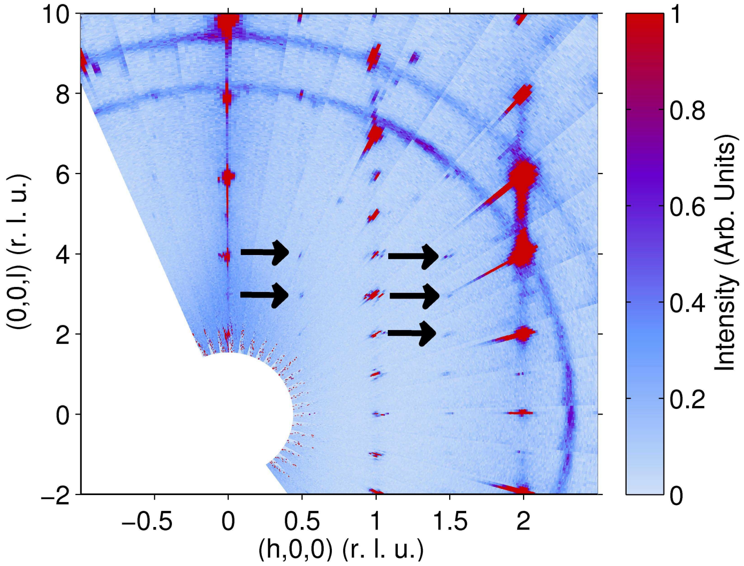

Figure 3.6: Diffraction data from the (h,0,l) plane at 310K with scattering at low Q (0.5Å^{-1} to 7Å^{-1}). Arrows indicate some of the weak orbital ordering peaks.

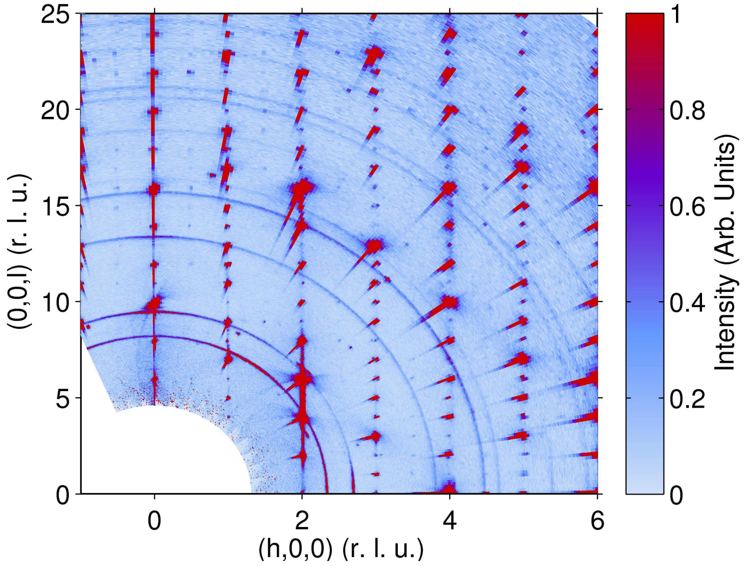

Figure 3.7: Diffraction data from the (h,0,l) plane at 310K with scattering at high Q (1.5Å^{-1} to 10.5Å^{-1})

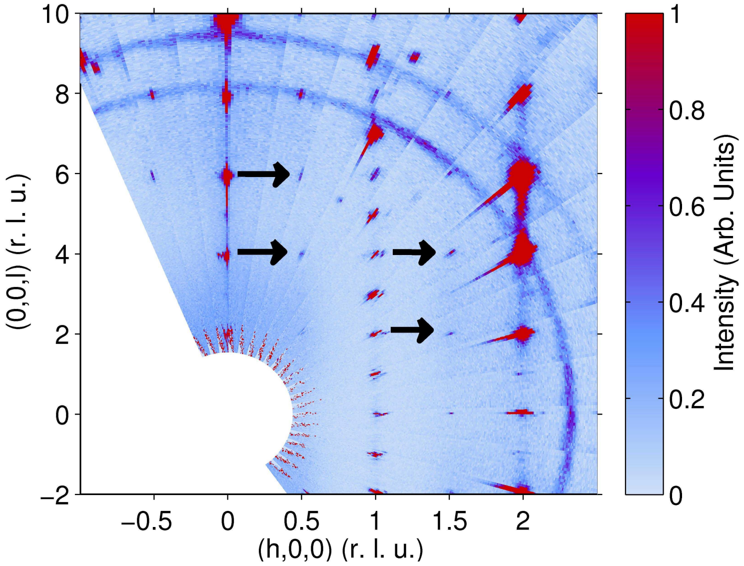

Figure 3.8: Diffraction data from the (h,0,l) plane at 225K with scattering at low Q (0.5Å^{-1} to 7Å^{-1}). Arrows indicate some of the weak orbital ordering peaks.

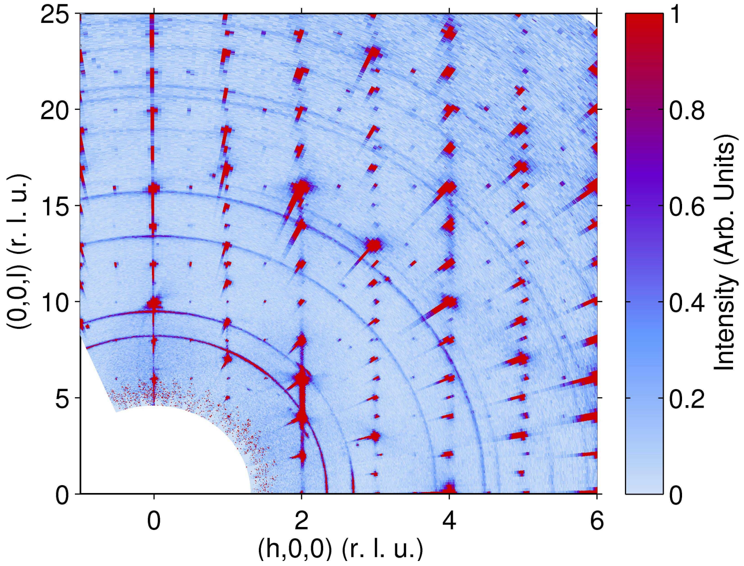

Figure 3.9: Diffraction data from the (h,0,l) plane at 225K with scattering at high Q (1.5Å^{-1} to 10.5Å^{-1})

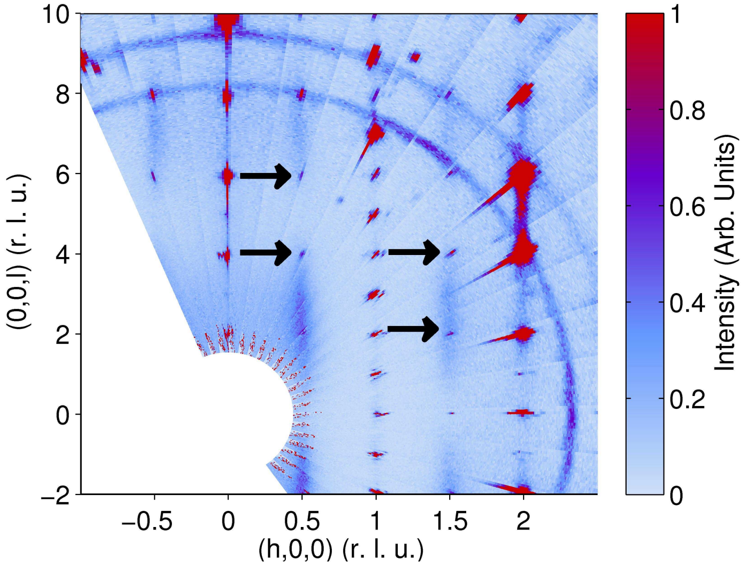

Figure 3.10: Diffraction data from the (h,0,l) plane at 175K with scattering at low Q ($0.5Å^{-1}$ to $7Å^{-1}$). Arrows indicate some of the weak orbital ordering peaks.

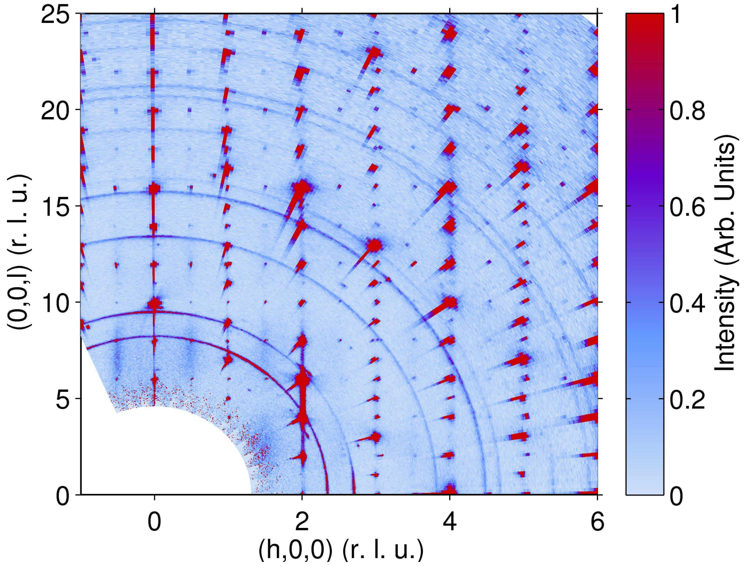

Figure 3.11: Diffraction data from the (h,0,l) plane at 175K with scattering at high Q ($1.5Å^{-1}$ to $10.5Å^{-1}$)

structure, seen in the $(n+1/2,0,l)$ lines of peaks, where now there are only peaks for even values of l. This is an indication of the second charge-ordered/orbital-ordered phase. If the sample were not twinned, a series of peaks in the $(n+1/2,0,l)$ line would not be observed in both charge-ordered/orbital-ordered phases, but the twinning means that both the $(h,0,l)$ and $(0,k,l)$ planes are observed simultaneously, so peaks appear in this series in both charge-ordered/orbital-ordered phases. It is important to understand the twinning of the sample for inelastic neutron scattering, as discussed later.

At 175K the sample is in the same phase, however there are now patches of diffuse scattering centred along the lines $(n+1/2,0,l)$ (where n is an integer). The patches are most intense around the points $l=\pm 2.5, 7.5$ etc. These patches are most intense at low wavevector which is an indication that they have a magnetic origin. Although this is above $\mathrm{T_N}$, this suggests that there is some CE-type magnetic ordering already in the MnO_2 planes (since this is the correct wavevector for CE-type magnetic ordering), but only existing over a small cluster size.[74]

After cooling to 9K, $T \ll T_N$, the magnetic Bragg peaks are now clearly visible at the $(n+1/2,0,l)$ positions. The intensity of the peaks is highest at low wavevector, confirming these are magnetic peaks. Examining peaks in this series at higher wavevector shows that the intensity does not drop off completely. This is attributed to the structural distortion into a monoclinic phase reported by Tokunaga et al. [23]. It appears that the magnetic peaks are almost non-existent when l is a multiple of 5, which is particularly apparent when taking a cut along the $(0.75,0.75,l)$ line, shown in Fig. 3.14. The interbilayer distance $d \sim 3.8$Å, is close to 1/5 of the c-axis dimension of the unit cell at low temperatures $c = \sim 19.2$Å. The 3.8Å separation of the bilayer is the reason for the modulation in peak strength along this line. The fact that the minimum values for the peak are at l=0, $\pm 5, \pm 10$,

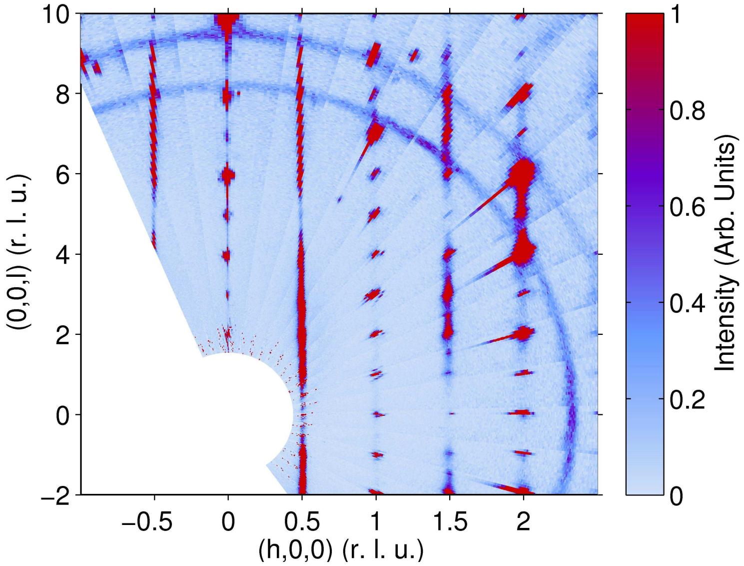

Figure 3.12: Diffraction data from the (h,0,l) plane at 9K with scattering at low Q ($0.5Å^{-1}$ to $7Å^{-1}$). There are peaks along the line $(1/2, 0, l)$, but these are obscured by the intense background feature, the nature of the peaks is similar to those shown in the cut in Fig. 3.14.

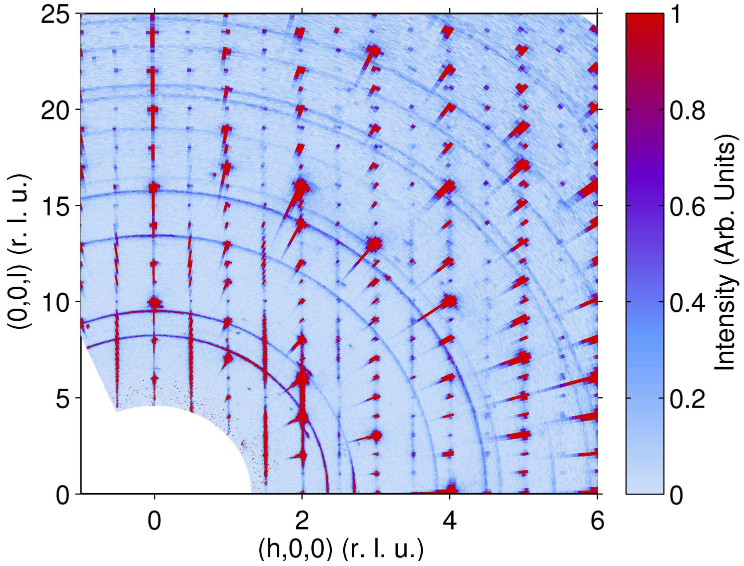

Figure 3.13: Diffraction data from the (h,0,l) plane at 9K with scattering at high Q ($1.5Å^{-1}$ to $10.5Å^{-1}$). There are peaks along the line $(1/2, 0, l)$, but these are obscured by the intense background feature, the nature of the peaks is similar to those shown in the cut in Fig. 3.14.

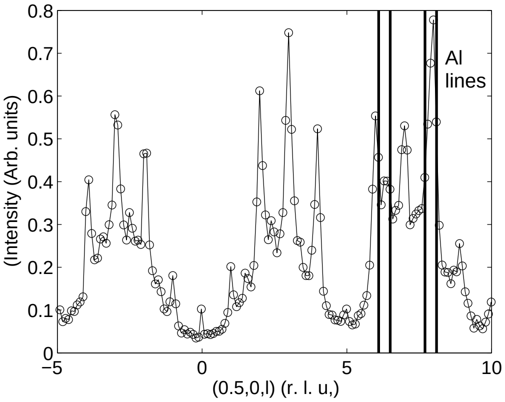

Figure 3.14: Cut along the line $(0.75, 0.75, l)$, with a width of 0.1 r. l. u. The cut is taken from the data at 9K. The area marked in the two rectangles should be ignored due to it overlapping with Al powder lines arising from the cryostat.

etc, as is obvious from the cut along $(0.75, 0.75, l)$ shown in Fig. 3.14, suggests that there is an antiferromagnetic interaction between the two layers in a bilayer, a ferromagnetic interaction would have maximum values at the aforementioned values of l.

There is still some diffuse scattering at this temperature, in the form of long bars in the background of the signal in Fig. 3.12 or the bumps in Fig. 3.14. These are modulated along l with the same periodicity as the Bragg peaks and they get weaker at higher Q. This suggests that these rods also arise from the magnetic interaction along the c-direction, perhaps an indication that there is a short correlation length along the c-axis and a weak interaction between bilayers.

Looking ahead to the spin wave model, it is useful to know that the interaction between two layers in a bilayer is antiferromagnetic. Also, with these results indicating that the interaction between bilayers is weak, we can therefore assume that this exchange is relatively insignificant and discard it from the model. This weak interbilayer interaction also has implications in aligning the crystal for the inelastic neutron experiment which will be discussed later in the chapter.

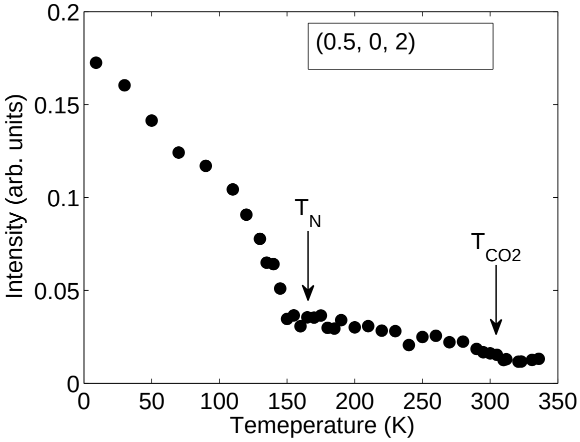

Figure 3.15: Temperature dependency of the scattering intensity of the (0.5,0,2) diffraction peak. The main transition temperatures in this temperature range are marked.

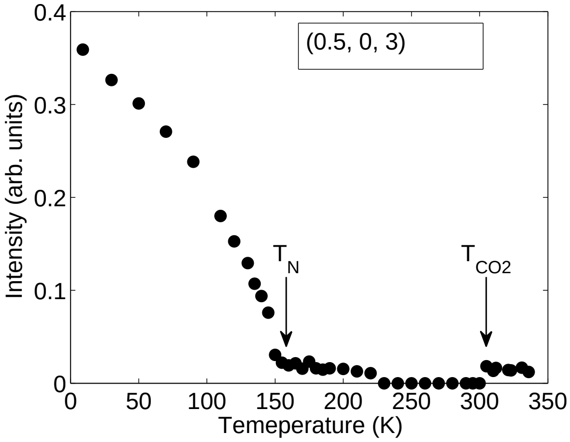

Figure 3.16: Temperature dependency of the scattering intensity of the (0.5,0,3) diffraction peak. The main transition temperatures in this temperature range are marked.

A measurement of the temperature dependence of the intensity of some of the most important peaks is presented in Fig. 3.15, showing the $(0.5, 0, 2)$ peak, and Fig. 3.16, showing the $(0.5, 0, 3)$ peak. The intensity at the $(0.5, 0, 3)$ goes to zero below T_{CO2}, with the intensity only slowly recovering as the magnetism becomes prevalent at this point. The magnetic ordering temperature is clearly marked by a large increase in the intensity measured at around 155K. These main transition temperatures are clearly visible in these plots and agree well with the established transition temperatures reported elsewhere [68]. This confirms that this sample is a high quality crystal of $Pr(Sr_{0.1}Ca_{0.9})_2Mn_2O_7$.

The data that was obtained in the (h, h, l) scattering plane contains the other propagation vector of the CE-type magnetic phase. However, the results of the measurements in the (h, h, l) scattering plane does not provide any information relevant to this study that was not already observed in the $(h, 0, l)$ scattering plane.

3.5 Inelastic Neutron Scattering - Experimental Detail

The inelastic neutron scattering part of this study, was designed to determine the nature of the electronic ground state of a CE-type magnetic material, by measuring the spin wave dispersion of $Pr(Sr_{0.1}Ca_{0.9})_2Mn_2O_7$. The measurements were also performed at the ISIS facility of the Rutherford Appleton Laboratory. The instrument used was the time-of-flight spectrometer MAPS, which has a large area detector designed to measure a large part of the spin wave dispersion in each measurement.

To perform a successful inelastic neutron scattering experiment, the largest possible mass of high quality crystal should be used. This is due to the scattering process for inelastic magnetic neutron scattering being relatively weak. To use the largest possible mass of $Pr(Sr_{0.1}Ca_{0.9})_2Mn_2O_7$, it was decided that it would be best to co-align an array of crystals so that the scattering from the whole array would be similar to that from one larger crystal. Five crystals ranging in mass from 0.79g to 2.41g (the largest mass crystal is the same one that was used in the elastic neutron diffraction experiment) were aligned on ALF at ISIS. To have this many crystals in the beam at one time a special sample mount had to be manufactured, shown in Fig. 3.17, with crystals attached to it in the final alignment for the neutron

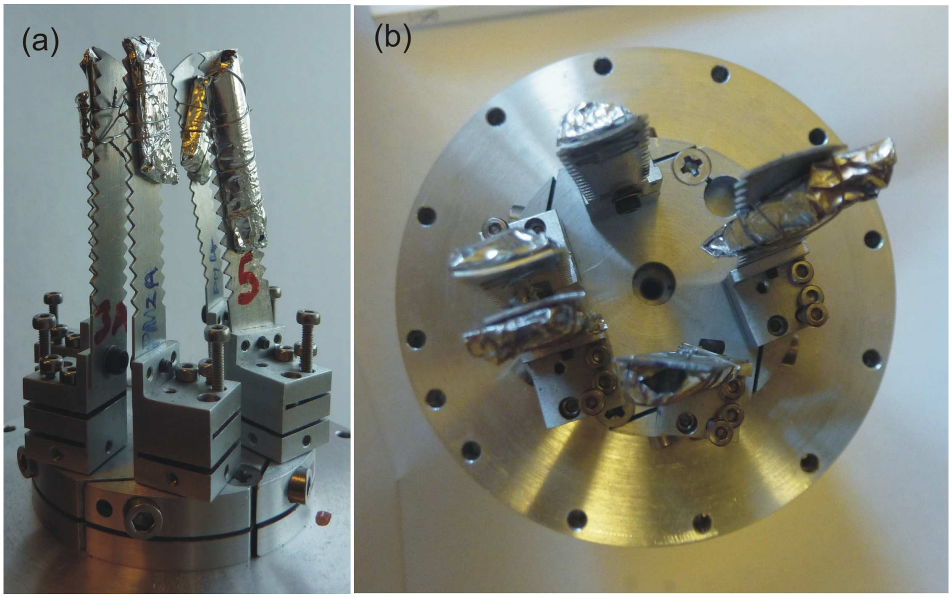

Figure 3.17: The 5 crystals, mounted on Al mounts and wrapped in Al foil. The crystals are co-aligned so that the crystallographic axis are in the same direction for each crystal. This is the sample arrangement that was inserted into the MAPS spectrometer. The crystal on the mount marked 5 in panel (a) is the one closest to the bottom of the image in panel (b), this crystal was studied in the elastic neutron scattering part of this experiment.

spectroscopy experiment.

The process of alignment was as follows. The largest crystal was aligned in the desired orientation, as close to the centre of the array as possible. The process becomes more complicated at this point as the crystals must be aligned to have precisely overlapping Bragg reflections. Each crystal must fit in to the array without getting in each others way or altering their alignment, so the problem of aligning the crystals in reciprocal space becomes a problem in real-space as well. It is beneficial for the crystals to be as close as possible to the centre of mass and centre of rotation of the sample mount. A smaller sample volume has two benefits, it allows the instrument's beam defining aperture to be as small as possible. This means that the highest percentage of neutrons are incident on the sample, reducing the background. The second reason is to minimise the effects of the resolution arising from the sample, which will be discussed later in the chapter.

After the alignment was completed, each of the samples had the crystallographic c-axis and the (twinned) ab-axes orientated in the same direction. The sample array is shown in Fig. 3.17. The mosaic spread of a diffraction peak of the array was 1.6°, which compares favourably with the mosaic of each single crystal which was typically around 1.2°. The total mass of the coaligned sample was 7.0g.

With the crystals coaligned on the sample mount, they were placed into the cryostat for the MAPS experiment. In a time-of-flight neutron spectroscopy experiment such as the one described here, the objective is to measure the magnetic excitation spectrum over as large a part of reciprocal space as possible. In a single crystal experiment (here the coaligned crystals are treated as a single crystal), the spectrum is a function of energy (ω) and three components of momentum (Q_x, Q_y, Q_z). The scattered neutrons are recorded as a function of flight time and position on the detector, and which can be converted to energy and momentum transfer through a transformation. As only three characteristics of the neutron are detected, only three of the parameters (ω and the three components of momentum), can be obtained independently. The fourth variable is determined by the other three.

If the three momentum components are set to be parallel to the three crystallographic directions in $\mathrm{Pr(Sr_{0.1}Ca_{0.9})_2Mn_2O_7}$, there is a choice of which of these three is dependent on the other parameters. In this experiment Q_a, Q_b and ω were set to be the three independent variables and Q_c was determined from these. This is convenient in a quasi-two dimensional material such as $\mathrm{Pr(Sr_{0.1}Ca_{0.9})_2Mn_2O_7}$, where there is almost no magnetic coupling between bilayers, as seen in the elastic neutron experiment described earlier. There is a variation in the neutron scattering intensity with Q_c, a sinusoidal modulation due to the bilayer structure (discussed earlier), but this variation can be taken into account in a spin wave model, which will be covered later.

With the crystals coaligned and the c-axis aligned with the incident neutron beam, the sample was cooled to ~ 3.5K. At this temperature, the entire spectrum was measured at a number of different neutron incident energies from 18meV to 200meV, with suitable chopper frequencies for each incident energy. There are a number of reasons for choosing to measure over so many different energies. It is important to check that the entire magnon dispersion is measured, so it is necessary to check over a wide range of incident energies for any features. High incident energies can map the entire magnon dispersion. However, increasing the incident energy decreases the resolution, so to study the lower parts of the dispersion accurately, low incident energy measurements must also be made. MAPS is designed with some gaps between detector banks, therefore it is necessary to take some overlapping energy ranges to ensure that interesting parts of the dispersion are not hidden by an unfortunate coincidence with a detector gap at that position and energy. As only three independent parameters are measured, the fourth parameter (Q_c) becomes dependant upon the incident energy of the neutrons, affecting the intensity of the neutrons at different parts of the dispersion. Measuring a number of incident energies ensures that the effect of Q_c on the intensity can be accurately determined.

Long measurements of $4000-7000\mu$A hr (the microamp hour is the measurement of the total charge of protons that are accelerated at ISIS and is therefore proportional to the number of neutrons available during a scattering experiment) were taken at most of these incident energies at this temperature, ensuring that there were adequate counts to perform a meaningful analysis. Shorter measurements of around 2000μA hr were made at higher temperatures. These were at 260K and 317K, both of which were only measured at an incident energy of 140meV and a chopper frequency of 400Hz.

3.6 Inelastic Neutron Scattering - Results

The spin wave dispersion measured on MAPS at $\sim$ 3.5K, is shown in Fig. 3.18, which are slices through reciprocal space. The slices are taken along the direction $(h, 0)$, demonstrated by the rectangle shown in Fig. 3.19. The two slices show different energy ranges but both are along the same direction, parallel to the magnetic zigzag. The constant momentum slices are made from sections with varying incident energies, as marked in the relevant sections of each slice.

A few data handling techniques have been used to aid in visualisation of the dispersion in Fig. 3.18 and in the later figure, Fig. 3.37. Like the diffraction sample, the array of samples is twinned and therefore the measured signal has four-fold rotational symmetry around the (0,0,l) axis, as seen in the elastic energy cut Fig. 3.19(a). Therefore the dispersion could be symmetrised, i. e. all of the data was folded into one quarter of reciprocal space, Fig. 3.19(b), this improves the counting statistics. Although the signal has four-fold symmetry, the detector does not, but this is taken into account in the calculation. In both panels of Fig. 3.19, the large rings towards the edge of the images are aluminium powder rings from the cryostat and sample mount. The data has also been corrected for an energy dependent background, with the background always calculated in a part of the spectrum where no magnetic scattering is expected or measured. For the purposes of these plots, the measured intensity of each pixel has been multiplied by a factor tending to the energy transfer at high energy transfers. This is purely for visualisation and compensates for the reduction of intensity in the higher energy transfer parts of the spectrum. The multiplication factor f for a given energy transfer E is,

$$f(E) = \frac{E/E_0}{1 - e^{-E/E_0}} \tag{3.1}$$

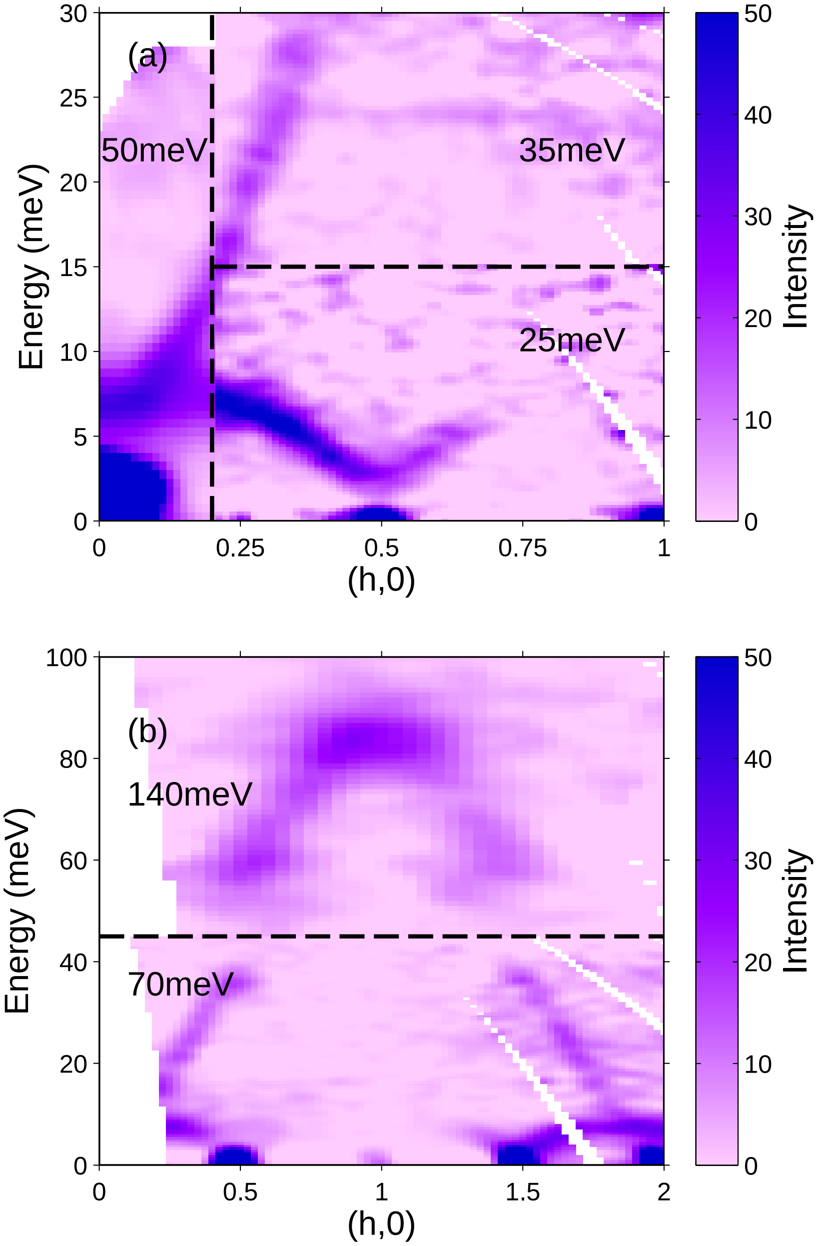

Figure 3.18: The neutron spectrum measured as a slice along the (h,0) direction. This images are composed of sections taken from different neutron incident energy runs. The incident energies of each section are marked on the corresponding parts of the figure. (a) Shows the detail of the low energy part of the dispersion . (b) Shows the full bandwidth of the dispersion.

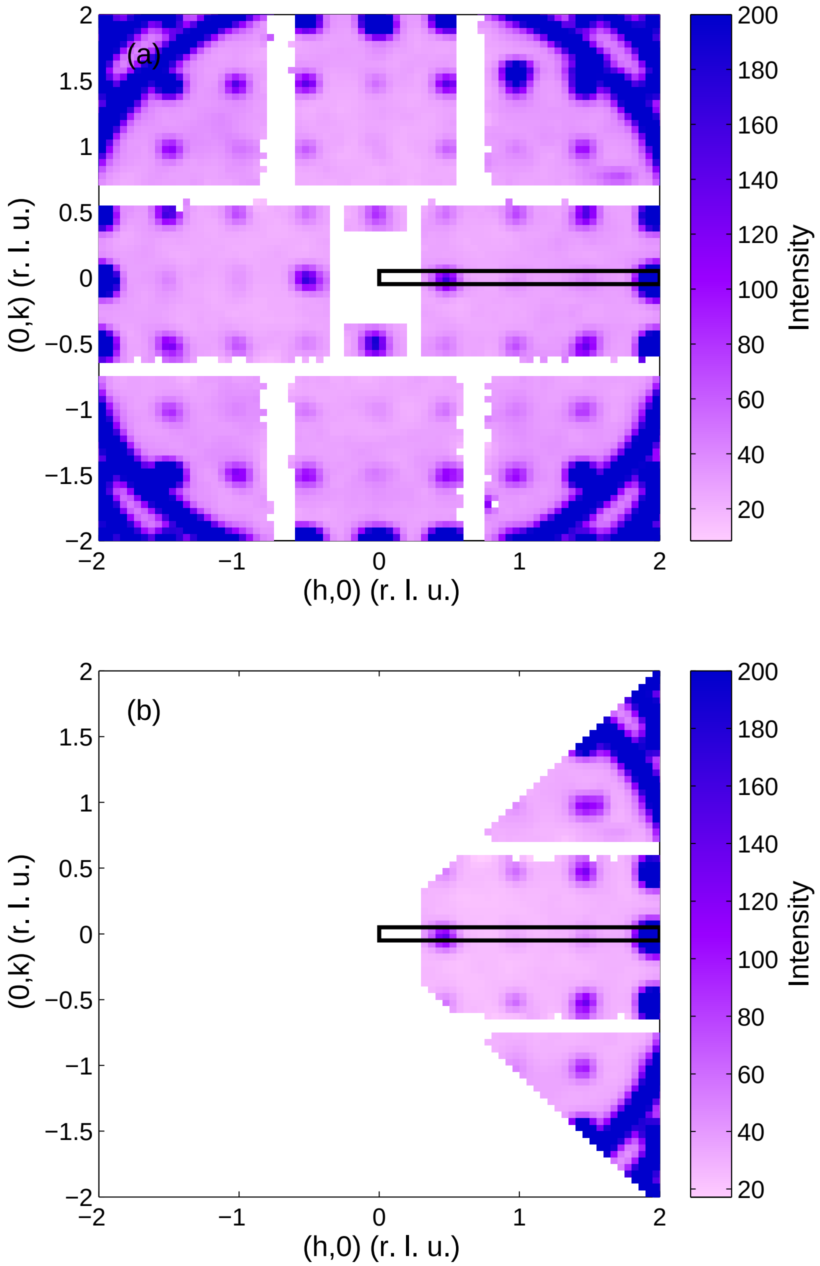

Figure 3.19: Elastic scattering from PCSMO, measured on MAPS at 3.5K, (a) The full data, (b) the data symmetrised into one quarter. In both figures the black rectangle shows the direction of the energy slices presented in Fig. 3.18

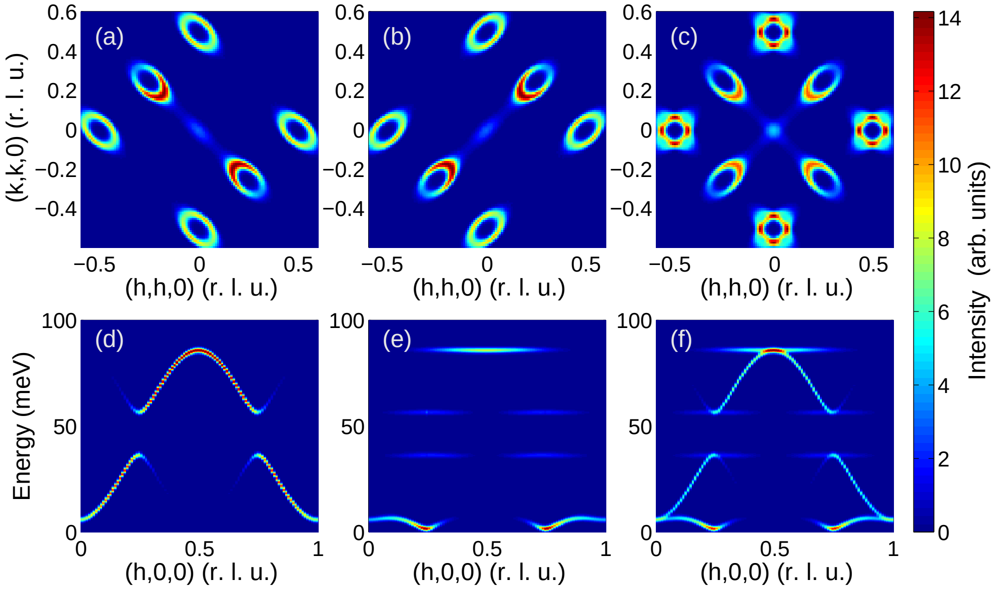

Figure 3.20: Simulations of the neutron scattering spectrum using the GE model with some test parameters. The test parameters were similar to the final best fit parameters. Panels (a), (b) and (c) show a constant energy slice through the spectrum at 2 meV, while panels (d), (e) and (f) all show a slice along the $(h, 0)$ direction. (a) and (d) show the spectrum from twin 1, (b) and (e) the spectrum from twin 2 and, (c) and (f) the two twins plotted together.

where $E_0 = 10$meV. This means that $f(E) \rightarrow 1$ for $E \ll E_0$ and $f(E) \rightarrow E/E_0$ for $E \gg E_0$. All neutron intensities in this chapter, unless explicitly stated otherwise, have the units of millibarn per steradian per millielectronvolt per Mn ion multiplied by $f(E)$ (mb sr^{-1} meV^{-1} Mn^{-1} $\times f(E)$).

These slices are meant to give an overview of the data, but also contain many of the important features of the spectrum, which had to be accounted for in the spin wave models used to describe these results. The following can all be read with reference to Fig. 3.18. There is a low energy band emerging from the magnetic Bragg peak at $(0.5, 0)$, with a maximum energy of 7 meV at $(0, 0)$. An upper band disperses from $(0, 0)$ point at 7 meV and reaches a maximum energy at 85 meV. The upper band has an energy gap between 35 and 55 meV, that extends throughout the entire dispersion. The intense features near the elastic line are Bragg peaks and are also observed in Fig. 3.19. The high intensity around the point $(0, 0)$ in Fig. 3.18 (a), is from the $(1, 1)$ Bragg peak; this part of the dispersion has been folded into the first Brillouin zone.

Although the cut is in the direction of the magnetic zigzag, twinning results in some of the data in this section arising from the direction perpendicular to the zigzag, demonstrated in Fig. 3.20(a-c). Preliminary analysis with the GE spin wave model (discussed in the following section) showed that the low energy band emerging from the magnetic Bragg peak at (0.5,0) and meeting (0,0) at about 7 meV is from the direction perpendicular to the FM zigzag. All of the dispersion over 7 meV is in the same direction as the FM zigzag. This is shown in Fig. (3.20) (d-f), where (d) shows one twin, (e) the other and (f) both together.

Figure 3.21 shows some examples of shows cuts through the spectrum at constant **Q**, along the energy axis, showing the intensity. The cuts are made at a number of different **Q** values and each cut is taken from an appropriate neutron incident energy. Figures 3.21(a)–(c) contain data on the lower band, and (c)–(f) on the upper band. Cut (a) shows that there is a small energy gap of about 2 meV at $(0.5, 0)$, (d) and (e) show the lower and upper limits of the gap in the upper band, and (f) is a cut through the top of the dispersion at $(1, 0)$. The small gap at the magnetic Bragg peak (0.5,0) (Fig. (3.21)(a)), is an indication of anisotropy in the system. This is also apparent in the magnetisation data, which show that the b-direction is the magnetic easy axis.[23]

At an early stage in the data analysis, it became apparent that the resolution was an important factor in understanding this data. Not only does the resolution broaden the signal, but in extreme cases it can significantly change the position and shape of the peaks in the data. In the case of $Pr(Sr_{0.1}Ca_{0.9})_2Mn_2O_7$, resolution was particularly important when dealing with low energy transfer features (relative

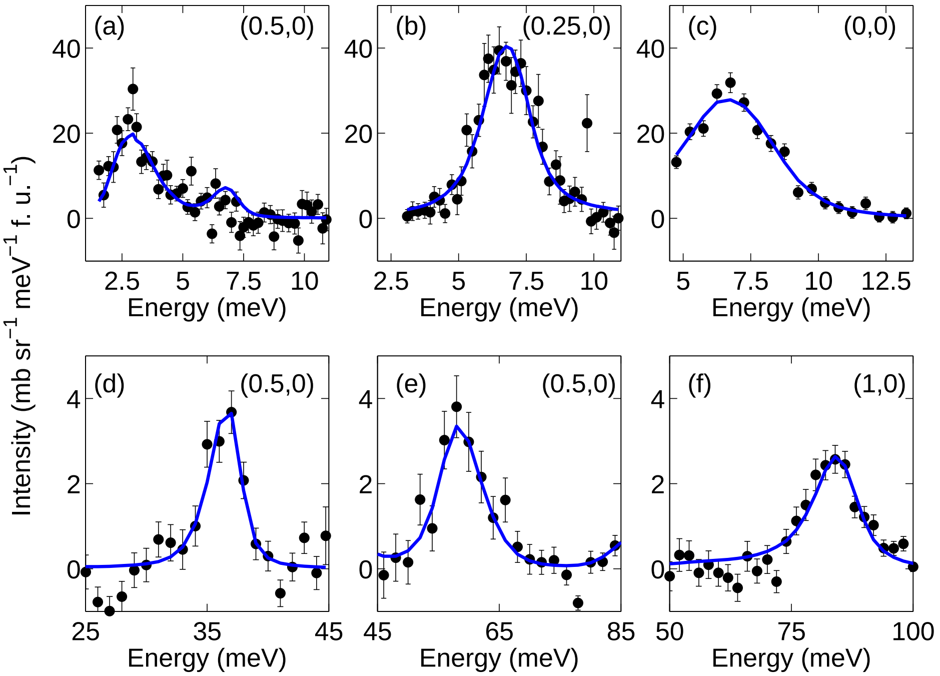

Figure 3.21: These constant **Q** cuts are shown as an example of the type of cuts used to find the dispersion, by the method described in the main body of the text. They also contain some of the most important points in the dispersion and their position is indicated in each panel; (a) the minimum of the dispersion, (b) half way along the lower dispersion, (c) the dispersion at (0,0), (d) the bottom of the gap in the dispersion, (e) the top of the gap in the dispersion, (f) the maximum of the dispersion. In each figure, the solid line shows the preliminary fit with the GE model.

to the incident energy of the neutrons). Since measurements were made at many incident energies, most of the dispersion could be measured with good resolution and only the very low energy parts of the dispersion were strongly affected.

To resolve the resolution issue at low energy transfers and to fit the data to a model a suitable correction for the resolution had to be made. This was achieved by using the program Tobyfit, from the ISIS facility, which is designed to fit spin wave models with resolution considered for the spectrometers at ISIS. There are various sources of resolution broadening on MAPS. The moderator and the chopper, used as a monochromator, both result in an energy broadening of the neutron energy at the sample. As both the moderator and the chopper are finite in size, there is also a spatial consideration for the resolution, related to which part of these components the neutrons travel through. Sample size is also important, especially in the case of a co-aligned array of samples such as $Pr(Sr_{0.1}Ca_{0.9})_2Mn_2O_7$, where neutrons are scattering from different parts of the large volume of the sample. On top of this, beam divergence must also be considered. All of these effects must be accounted for in any good resolution correction. These effects and others are all taken into account in Tobyfit.

It is possible to use Tobyfit to fit a model spectrum to an entire data set, simultaneously with inclusion of resolution. However, this is impractical in this case as the amount of computational time required is far too much for the resources available. Each pixel in the data is fitted for resolution individually and an entire spectrum includes a vast number of pixels (> 40000) taken over 2000 time steps. Instead, an alternative scheme to fit the data was adopted, which is described below.

In summary the process is as follows; a number of constant energy and constant momentum cuts (> 50 in this study) are made through the observed spectrum. A preliminary model for the magnetic spectrum is then chosen and fitted to each cut separately. The purpose of this is simply to obtain an approximate description of the dispersion in the vicinity of the cut. The effects of resolution could then be quantified by fitting each cut in Tobyfit, which folds the spectrometer resolution function with the model dispersion. From the fit parameters for these cuts, each cut can now be simulated, resulting in a simulated cut that is resolution-corrected. Finally, these resolution-corrected peak positions from each cut are plotted as a dispersion and can be used to test various spin wave models.

This procedure was conducted as follows for $Pr(Sr_{0.1}Ca_{0.9})_2Mn_2O_7$. The Goodenough model (the model described in detail in the following section) was used as the preliminary model for $Pr(Sr_{0.1}Ca_{0.9})_2Mn_2O_7$ and, after some trial simulations, this

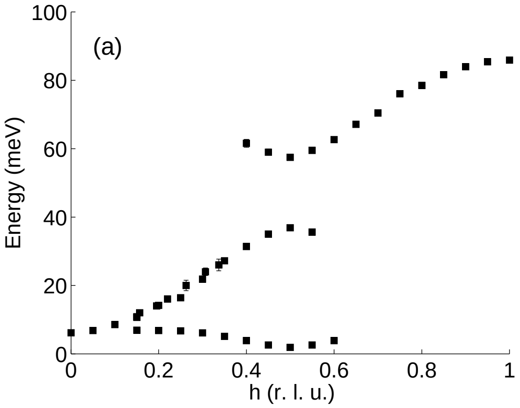

Figure 3.22: The dispersion found by analysing cuts through the neutron spectrum, each point represents a fit to one cut. This dispersion is in both the direction parallel to and perpendicular to the ferromagnetic zigzag in the sample, due to the nature of the twinning. The error bars are only shown if they are larger than the marker.

model was found to give a good qualitative description of the measured spectrum. To constrain the parameters of the Goodenough model, the model was fitted to cuts taken at 6 key symmetry points (those shown in Fig. 3.21) using the parameters of Senff et al. [65] which gave a reasonable overall description of the spectrum. The model dispersion was then refined for each of the $>$ 50 cuts separately, by allowing the dominant exchange parameter to vary while fixing the ratios of smaller parameters to the dominant one. The other free parameters were an independent amplitude and width for each cut and, where necessary, a constant background.

By taking the parameters of each independent fit and simulating them separately, the peak position can for each of the individual cuts can now be obtained, giving a dispersion with the resolution accounted for. The dispersion obtained in this manner for $Pr(Sr_{0.1}Ca_{0.9})_2Mn_2O_7$ is shown in Fig. 3.22. One way to test how suitable the Goodenough model is as a preliminary model is to examine the fitted amplitudes of the peaks. The peak amplitudes are determined in the model by a pre-factor in the spin wave cross section. If the model fits the data well the prefactor should be the same for each individual cut. The prefactors determined from the fits are shown in Fig. 3.23 as a function of energy transfer. The pre-factor is relatively constant, with perhaps a small decrease at high energy transfers. Another test of the quality of the fit of the Goodenough model is to examine the peak width. If the resolution is being dealt with correctly by the program, the intrinsic peak width should be proportional to the energy transfer of the neutrons. The peak width is plotted against the energy of the cut in Fig. 3.24. These two plots confirm that the Goodenough model was a suitable model for retrieving the resolution corrected dispersion from the data and that it should be a suitable model for the whole dispersion.

The resolution-corrected dispersion, shown in Fig. 3.22, has been obtained as described above using the Goodenough model as the means to correct for the resolution. However, any model that correctly describes the dispersion in the vicinity of each cut would have been able to produce the same resolution-corrected dispersion from the data, though only a model that provides a reasonable description of the whole dispersion would have a constant pre-factor for the intensity, as found here for the Goodenough model, see Fig. 3.23.

The dispersion is now corrected for resolution and completely independent of the preliminary model used to obtain it. The experimental dispersion can now be fitted to any model one wishes to test. The models tested in this study are described in the next section, along with the results of the fits to these models.

It is useful to compare the dispersion measured here to the one measured for $La_{0.5}Sr_{1.5}MnO_4$ by Senff et al.[65] Both materials are CE-type antiferromagnets, the main difference being the $La_{0.5}Sr_{1.5}MnO_4$ has a single Mn-O layer and $Pr(Sr_{0.1}Ca_{0.9})_2Mn_2O_7$ has bilayers. The two dispersions do show some similarities. Below 40meV the dispersions are very similar, however, there is no gap in the dispersion measured by Senff et al. and the upper part of the dispersion is entirely different. It is possible that there is a gap and a higher energy part of the dispersion in $La_{0.5}Sr_{1.5}MnO_4$ and it has not been shown in the previous work.

3.6.1 High Temperature Results

In figures 3.25 and 3.26, the spin wave spectrum parallel to the ferromagnetic zigzags is measured above T_N at 260K (in the second charge-ordered/orbital-ordered phase) and at 317K (in the first charge-ordered/orbital-ordered phase), respectively. Both measurements were made at an incident energy of 140 meV. The same display techniques are used here as were used for the low temperature spectrum, such as symmetrising the data and multiplying by the intensity by the incident energy. The high temperature dispersion shows a similar overall shape to the low temperature dispersion with the same periodicity and rising to a peak at roughly the same energy of around 80 meV. However, there is no indication of the low energy dispersion or of the gap in the dispersion. Instead the dispersion is characteristic of a simple ferromagnet. As this is above the magnetic ordering temperature, this suggests that only a nearest neighbour ferromagnetic interaction is important at these temperatures. This is in general agreement with the work of Senff et al.[74], whose measurement show signs of magnetic clusters forming in $La_{0.5}Sr_{1.5}MnO_4$.

3.7 Spin Wave Models

Initially two spin wave models were considered in relation to the measured dispersion. These were the aforementioned Goodenough (GE) model and the Zener Polaron (ZP) model. A model that is best thought of as a hybrid model of these two models, termed the Dimer (DI) model, was developed after testing of the first two models. The three models were written by Olga Sikora and Toby Perring. All three

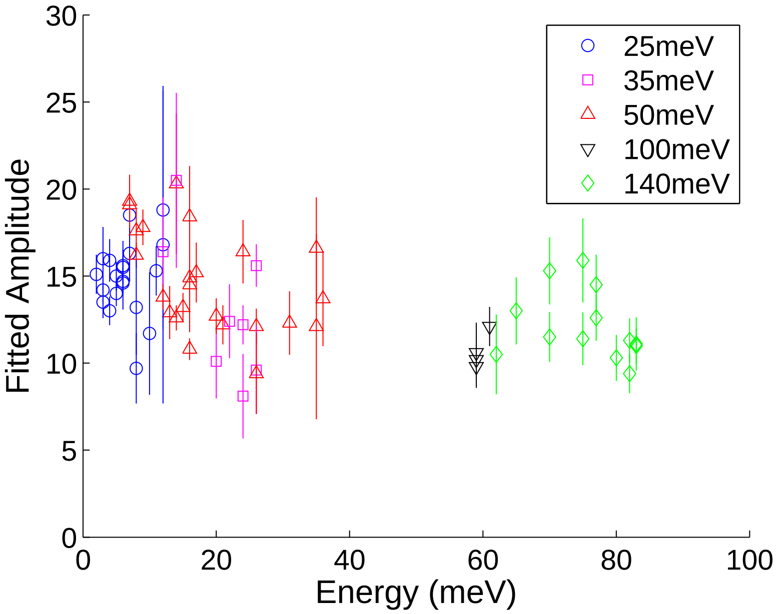

Figure 3.23: The fitted amplitude (i.e. intensity pre-factor) for the spin-wave cross-section obtained from fits to each cut. The colour represents the incident energy of the neutrons for the cuts.

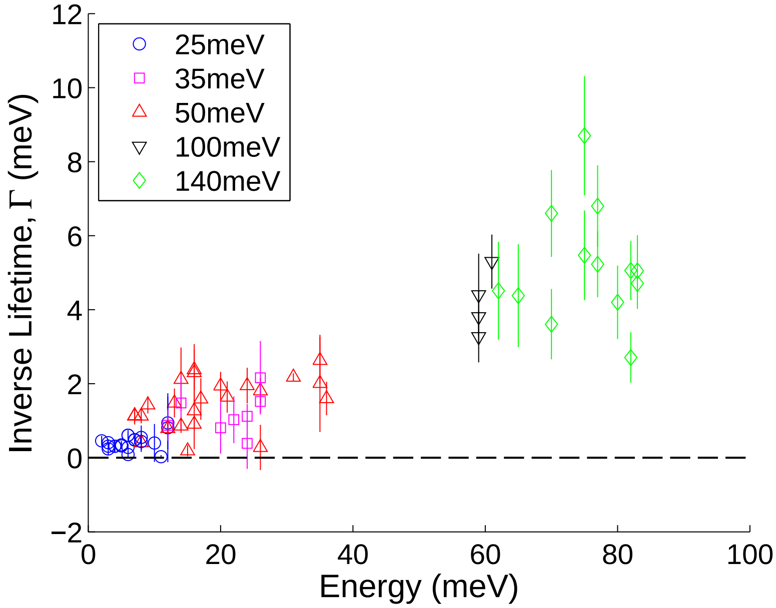

Figure 3.24: The fitted inverse lifetime for each cut. The colour determines the incident energy of the neutrons for that cut.

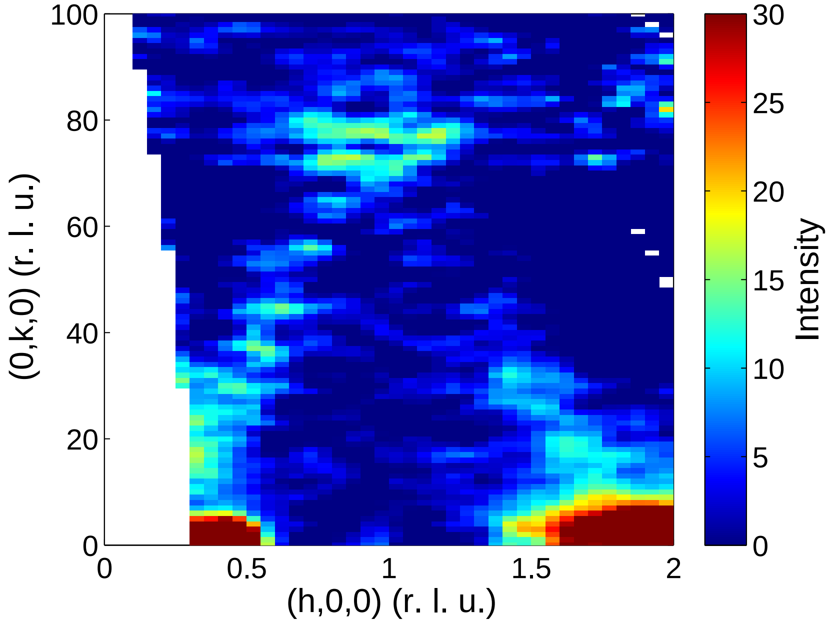

Figure 3.25: The dispersion parallel to the ferromagnetic zigzag at 260K, in the second charge-ordered/orbital-ordered phase.

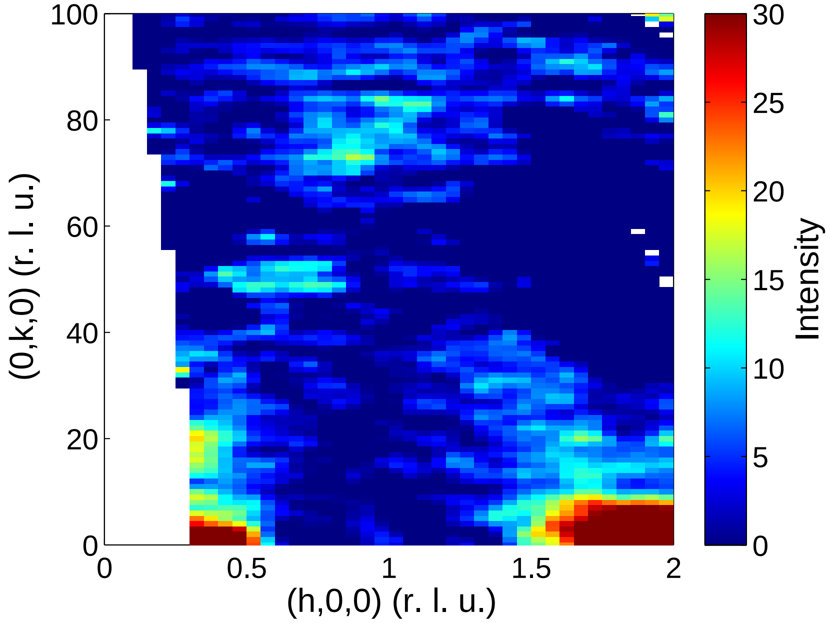

Figure 3.26: The dispersion parallel to the ferromagnetic zigzag at 317K, in the first charge-ordered/orbital-ordered phase.

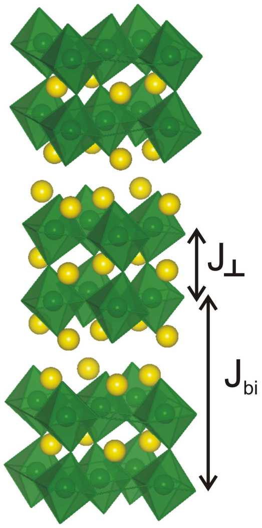

Figure 3.27: Out of plane exchanges considered in all of the spin wave models discussed here. These are the interbilayer interaction, J_{bi} and the intrabilayer interaction, $J_{\perp}$. J_{bi} is at least an order of magnitude smaller than $J_{\perp}$.

spin wave models are constructed from the Heisenberg Hamiltonian for the interaction between two spins at sites i and j, $H = -\sum_{\langle i,j \rangle} J_{i,j} \mathbf{S_i} \cdot \mathbf{S_j}$. The three models differ in the in-plane interactions, all three have the same out of plane interactions, shown in Fig. 3.27. In each case J_{bi} is assumed to be zero, since it is believed to be negligible. This is implied in the diffraction data and the diffuse scattering observed parallel to the *ab*-plane in the elastic scattering results already presented. Using these models the partial differential cross-section for neutron scattering can then be calculated and fitted to the measured spectrum by use of linear spin wave theorem, see section 1.6. The following subsections give the results of the fits for each model separately and a discussion of the results for each fit.

3.7.1 The Goodenough Model

The GE model is similar to the model described by Senff et al.[65] and is based on the principles of charge-ordered antiferromagnetic superexchange proposed by Goodenough [17] and Kanamori [53]. The spin wave model is based on the magnetic

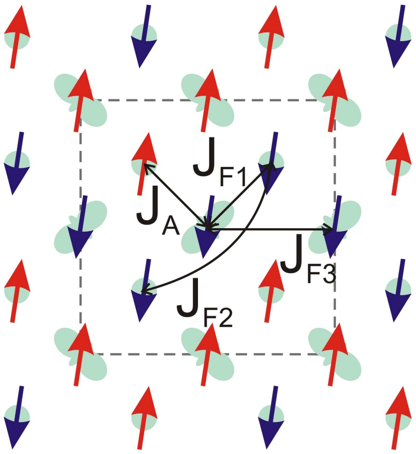

Figure 3.28: The magnetic interactions in a single MnO_2 layer for the GE model. The dashed box shows the magnetic unit cell.

interaction between ions ($\mathbf{S_{i,j}}$) arranged in the CE-phase magnetic structure. The exchanges within the MnO_2 layer are shown in Fig. 3.28 and the out of plane exchange parameters are shown in Fig. 3.27. The 4 in plane exchanges are the nearest neighbour (nn) ferromagnetic (FM) interaction J_{F1}, the nn-AFM interaction J_A, the next nearest neighbour (nnn) FM interaction between two Mn^{4+} sites J_{F2} and the nnn-FM interaction between two Mn^{3+} sites J_{F3}. There is also the nn-AFM interaction to the next layer in a bilayer $J_\perp$. A single ion anisotropy ($D\sum_i(S_i^z)^2$) is added to the Hamiltonian to account for the gap observed between the dispersion and $E_T = 0$. The magnitude of the spin on each Mn site is assumed to be the same.

It became apparent early in the analysis process that the GE model would be suitable for describing the dispersion, hence it was used to obtain the resolution corrected dispersion described in the previous section. Therefore it came as no surprise that a good fit of this model to the measured dispersion was achieved, shown in Fig. 3.29. The exchange parameters found from this fit were as follows, $J_{F1} = 11.39 \pm 0.05$meV, $J_A = -1.50 \pm 0.02$meV, $J_{F2} = 1.35 \pm 0.07$meV, $J_{F3} = -1.50 \pm 0.05$meV, $J_\perp = -0.88 \pm 0.03$meV and an anisotropy $= 0.073 \pm 0.001$.

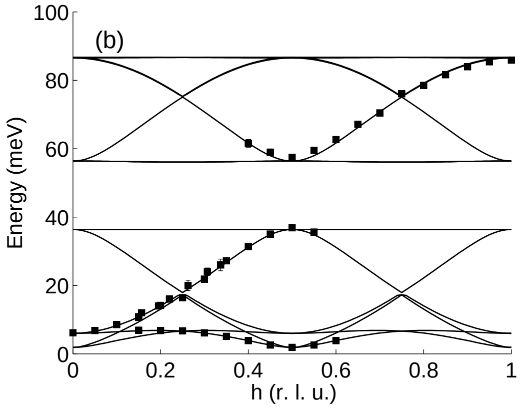

Figure 3.29: The complete dispersion fitted using the GE model, in the direction parallel to the ferromagnetic zigzag, showing all modes.

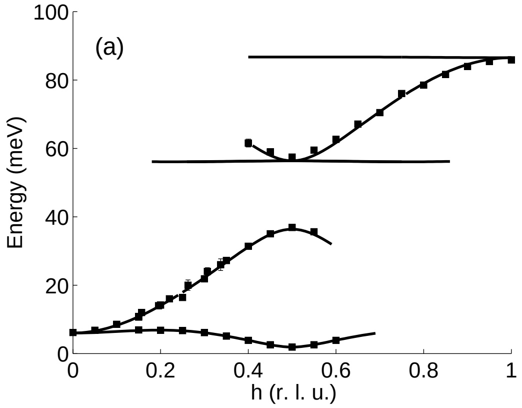

Figure 3.30: The dispersion fitted using the GE model, showing only the modes with an intensity greater than 10% of the maximum calculated intensity. This is dispersion in the direction parallel to the ferromagnetic zigzag.

Although there are 32 magnetic ions in the true magnetic unit cell, for the purposes of the model, this could be reduced to 8, the number of ions in one layer. Therefore there are 8 modes calculated in this model (which are degenerate with the three other sets of 8 that would exist in the true 32 mode dispersion). The structure factor for the dispersion is also calculated, so to make the picture clearer, only the modes that have an intensity $>$ 10% of the maximum calculated intensity are plotted in Fig 3.30.

The striking feature of this fit is the dominance of the nn-FM interaction, almost an order of magnitude larger than any other exchange. One unusual feature of the

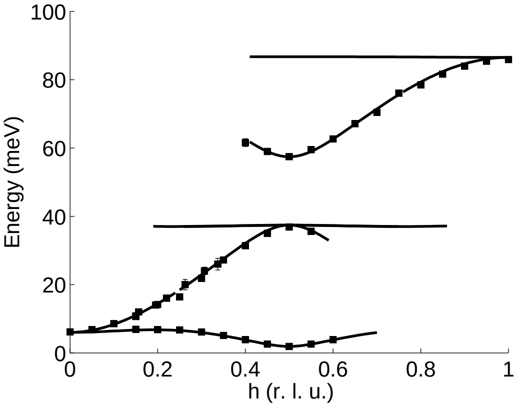

Figure 3.31: The dispersion fitted using the alternative GE model discussed in the text, showing only the modes with an intensity greater than 10% of the maximum intensity calculated. This is dispersion in the direction parallel to the ferromagnetic zigzag.

fit is that one of the nnn-FM interactions fits as an AFM interaction, suggesting that for this model to be correct there must be some frustration in the magnetic ground state.

It is possible for either J_{F2} or J_{F3} to be the AFM interaction, the two numbers can simply be swapped to get an equally good fit ($J_{F2} = -1.50$meV and $J_{F3} = 1.35$meV), giving two models that seemingly indistinguishable in the fit. The dispersion found by the alternative set of exchange parameters is shown in Fig. 3.31 for comparison. The only difference observed is the dispersionless mode apparent at the top of gap in Fig. 3.30, appears at the bottom of the gap in Fig. 3.31. This difference is due to the a change in the structure factor of these mode between the two models. The dispersionless mode is not clearly observed at either of the these positions, see Fig. 3.18(b). For the remainder of this chapter the original GE model ($J_{F2} > J_{F3}$) will be referred to simply as the GE model and the second GE model ($J_{F3} > J_{F2}$) as the alternative GE model.

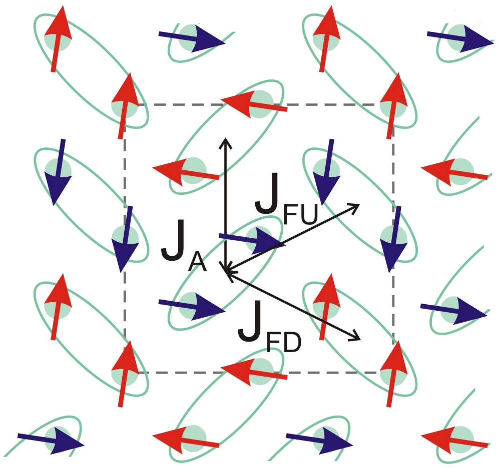

Figure 3.32: The magnetic interactions in a single MnO_2 layer for the ZP model. The dashed box represents the magnetic unit cell.

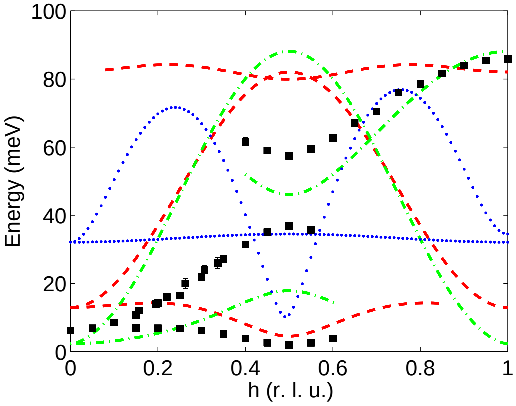

Figure 3.33: The complete dispersion modeled with the ZP model. The black squares show the data and the three coloured lines show the different test models that are discussed in the text, showing only parts of the calculated dispersion that have an intensity greater than 10% of the maximum calculated intensity.

3.7.2 The Zener Polaron Model

In the case of the Zener polaron model, the same Hamiltonian is used except the spins $(\mathbf{S_i}, \mathbf{S_j})$ in the Hamiltonian refer to the Zener polaron, rather than an individual Mn ion. The Zener polaron describes two magnetic moments that are effectively bound together by the Zener double exchange to such an extent that they are treated as one magnetic moment spread out over two Mn sites and centred at the point exactly between them. Treating the moment as being evenly distributed around the central point is a simplification, as most of the moment should still reside near the Mn sites. However, it is useful to consider this extreme case of the ZP model. This results in a model with only three in-plane magnetic exchanges, the nn-AFM interaction between two dimers, J_A and two nn exchanges reflecting the zigzag structure, labeled J_{FU} and J_{FD}. These three exchanges are illustrated in Fig. 3.32. The out of plane exchange $J_\perp$ shown in Fig. 3.27 is again fitted in this model.

The spin wave model used here does not correctly handle the magnetic form factor for the Zener polaron system, which relates to how the model considers the distribution of the magnetic moment. In the model there is assumed to be a distribution of the moment around the central point between the two Mn sites, however, in reality the majority of the moment will still be located on the Mn site, with only a small fraction delocalised. This issue is not important in this discussion as the magnetic form factor only affects the intensity of the neutron scattering, it does not change the dispersion. In this work, only the dispersion of the Zener polaron model has been calculated, not the entire spectrum.

In previous work by Sikora et al.[67, 75] it was shown that there are three stable models for the magnetic exchanges. These three models are described as either one dominant ferromagnetic exchange, two ferromagnetic exchanges stronger than the antiferromagnetic exchange or a dominant antiferromagnetic exchange. The dispersions predicted by these three models are shown in Fig. 3.33 and are described by the following exchange parameters: the dominant single ferromagnetic exchange model, shown in red (dashed line), has the exchange parameters $J_{FU} = 5$meV, $J_{FD} = 1$meV, $J_A = -2.5$meV and $J_\perp = -1$meV; the model with two higher ferromagnetic exchanges shown in green (dot-dash line), has the exchange parameters $J_{FU} = 4$meV, $J_{FD} = 2$meV, $J_A = -1$meV and $J_\perp = -1$meV; the antiferromagnetic dominant model (blue, dotted line), has the exchange parameters $J_{FU} = 0.5$meV,

$J_{FD} = 0.5$meV, $J_A = -10$meV and $J_\perp = -1$meV. In each case, only parts of the dispersion that have an intensity greater than 10% of the maximum calculated intensity are plotted. These exchange parameters all represent simulations describing the models, these are not fits. These sets of parameters were chosen to reproduce the observed magnon bandwidth and to be representative of each class of Zener polaron model. Many other models are obviously possible, but all the physically meaningful ones fall into one of the three classes described here. Each of these three classes can be shown to be unsuitable for fitting the dispersion, as described in the following paragraph.

As with the GE model, the plots only show the dispersion when the calculated intensity is $> 10\%$ of the maximum calculated intensity of the dispersion. It is clear from the plots that these three models are unable to describe the measured dispersion. The Zener polaron has no mechanism to create a complete gap in the dispersion in the 35 meV to 55 meV range, as observed experimentally. The Zener polaron model does not have the correct periodicity for the dispersion along the direction of the ferromagnetic zigzags. This is because the distance between two magnetic moments in this direction is larger than the distance between two magnetic ions. The periodicity of the dispersion suggests that the strongest ferromagnetic interaction must be between nearest-neighbour Mn ions, not between two nearest-neighbour pairs of Mn ions, as the Zener polaron model requires. As a further check, a large part of parameter space was also tested for suitability as a spin wave model for $Pr(Sr_{0.1}Ca_{0.9})_2Mn_2O_7$ and none were able to replicate the observed dispersion. The Zener polaron model is therefore unsuitable for describing the spin wave dispersion in $Pr(Sr_{0.1}Ca_{0.9})_2Mn_2O_7$ and this casts doubt on its viability as an electronic groundstate in CE-phase manganites.

3.7.3 The Dimer Model

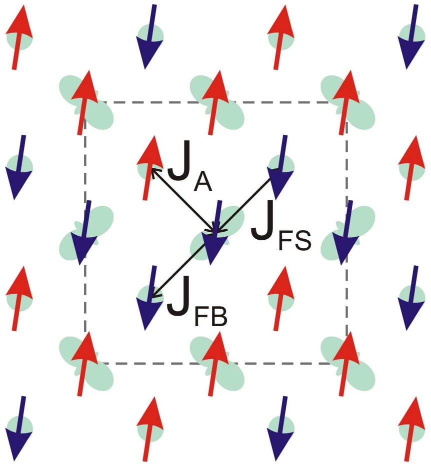

Figure 3.34: The magnetic interactions in a single MnO_2 layer for the DI model. The dashed square represents the magnetic unit cell.

The DI model is similar to the GE model in that the spins in the Hamiltonian arise from individual manganese sites, but it allows two different values for nn-ferromagnetic interaction. Therefore, a Mn^{3+} site can have a stronger interaction to one nn-FM Mn^{4+} site than it does to the other one. This allows for the effect of a double exchange between a Mn^{3+} and a Mn^{4+}, without implementing the Zener polaron idea of the two ions acting as one magnetic moment. The exchange parameters involved in this model are shown in Fig. 3.34. The important interactions in this case are the two nn-FM interactions J_{FB} and J_{FS}, the nn-AFM interaction J_A and yet again the intrabilayer interaction $J_\perp$.

The fit of this model to the measured dispersion is shown in Fig. 3.35. The fitted parameters are $J_{FB} = 14.2 \pm 0.08$meV, $J_{FS} = 8.43 \pm 0.06$meV, $J_A = -1.52 \pm 0.01$meV, $J_\perp = -0.92 \pm 0.03$meV and a fitted anisotropy $= 0.073 \pm 0.001$. The fit of the DI model is also shown in Fig. 3.36 where only the modes with intensity greater than 10% of the maximum calculated intensity are displayed. The Dimer model fits the dispersion very well. It is obvious when comparing the two dispersions, that the

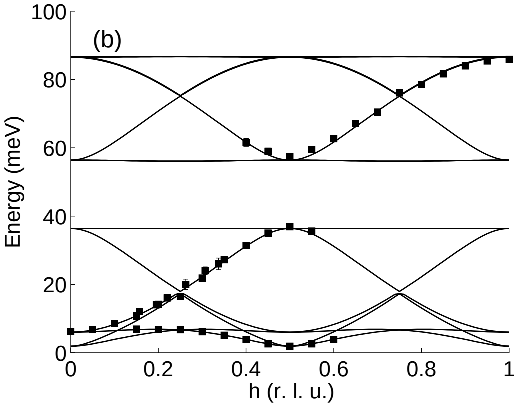

Figure 3.35: The complete dispersion fitted using the DI model, in the direction parallel to the ferromagnetic zigzag.

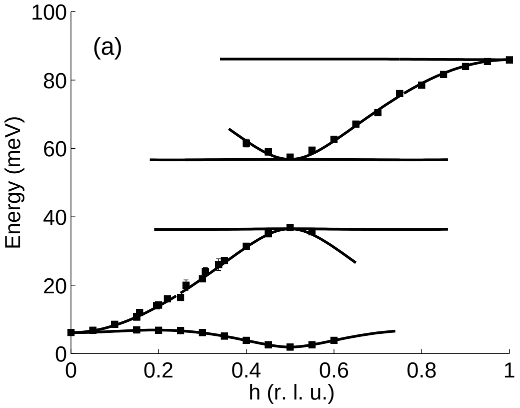

Figure 3.36: The dispersion fitted using the DI model, showing only the modes with an intensity greater than 10% of the maximum intensity calculated. This is dispersion in the direction parallel to the ferromagnetic zigzag.

GE and DI models fit an almost identical dispersion, the only difference being that the dimer model predicts a dispersionless band at both the bottom and the top of the energy gap in the dispersion.

3.8 Determining the Best Model

One of the key reasons for ruling out the ZP model is that there is no mechanism for creating a gap throughout the dispersion between ∼35meV and ∼55meV. When considering the Dimer and the Goodenough models, there are three possible mechanisms that allow for the creation of this large gap in the dispersion. One of the mechanisms is charge disproportionation, i.e. how many electrons are on the Mn^{3+} and Mn^{4+} sites. As mentioned, all of the fits were conducted with an equal spin/charge on each site. Assuming that the charge state of the Mn ions is proportional to the spin, with $S = 2$ associated with Mn^{3+} and $S = 3/2$ with Mn^{4+}, the calculated the spin wave spectrum for the GE model requires the charge states of $Mn^{2.84+}$ and $Mn^{4.16+}$, which is unrealistic in the context of previous experiments.[57, 58]

The two other mechanisms are intrinsic properties of the Goodenough and dimer spin models. In the Goodenough model, the gap appears when the values of the next-nearest-neighbour interactions J_{F2} and J_{F3} are non-zero. To get the size of gap correct, the two exchanges must have opposite interactions. Considering that the these two interactions exist between moments which are ferromagnetically aligned means that a degree of frustration must exist for the GE model to correctly describe the system. In the dimer model the gap merely originates from the difference in magnitude between the nearest-neighbour FM interactions J_{FB} and J_{FS}, neither of which have to be frustrated. By this argument the dimer model seems to present the more elegant solution and requires fewer parameters to achieve an equally good fit. The dimer model, allowing for a broken symmetry between the interaction of the two nearest neighbour manganese ions in a ferromagnetic chain, incorporates the effects observed in other experiments in this regard, without imposing the need for complete charge and spin sharing between two nearest neighbour Mn ions implied by the Zener polaron model.

The high temperature data, Fig. 3.25 and Fig. 3.26, can give some insight to the behaviour of the system. The high temperature data show a spectrum with a similar shape to the $T \sim 3$K data presented elsewhere in this chapter, but without a gap in the dispersion. This means that the dominant nn-FM term is still apparent at this temperature, but the mechanism for creating the gap is not strong enough to affect the dispersion here. This means, that in the GE scenario, the nnn terms are too incoherent to allow for a magnetic excitation or in the DI scenario, that the inequality of the two nn Mn ions in the FM zigzags is non existent in this phase. In the latter case this could go against this model, because both of the high temperature datasets are below T_{COO1} and therefore any imbalance due to the charge ordering or orbital ordering would already be present and the gap would start forming.

None of these arguments offer a definitive answer as to which is the best model and it is hard to distinguish between the Goodenough model and the Dimer model using only the dispersion. Both are able to fit the measured dispersion equally well. To try to overcome this problem the full neutron scattering spectrum was calculated using both models. This is shown in the series of figures from Fig. 3.37 to Fig. 3.43. These figures show simulations of various slices through the data, described in the following paragraph.

The energy versus wavevector slices shown in Fig. 3.18 are plotted again in Fig. 3.37 (a) and (b) respectively. Below each of these is a simulation using the GE model, (c) and (d), and the DI model, (e) and (f) at the same part in the dispersion. The neutron incident energy is shown for plots (a) and (b) in each marked section, and the plots directly below these two have the same composition of incident energies. The next six figures are all constant energy slices through the spectrum; (a) is the data (with a constant background subtracted), (b) the GE model simulation and (c) the DI model simulation. Each figure is at a different energy transfer E_T and neutron incident energy E_i. The figures are at the following energies; for Fig. 3.38 $E_T = 5$meV with $E_i = 25$meV, for Fig. 3.39 $E_T = 11$meV with $E_i = 25$meV, for Fig. 3.40 $E_T = 17$meV with $E_i = 50$meV, for Fig. 3.41

$E_T = 35$meV with $E_i = 70$meV, for Fig. 3.42 $E_T = 60$meV with $E_i = 100$meV and for Fig. 3.43 $E_T = 75$meV with $E_i = 140$meV.

Both simulations are very similar to the observed spectrum and both give excellent fits to the dispersion. When comparing the two models, the intensity predicted by both is almost identical in all the slices presented. There is a slight difference in both Fig. 3.41 at $E_T = 35$meV and Fig. 3.42 at $E_T = 60$meV, which are located just below and just above the gap in the dispersion, respectively. In these slices, the GE model gives a better simulation of the data than the DI model. This is the most convincing evidence available and the conclusion must be made that the GE model is a superior model of the spin wave spectrum than the DI model.

There are, however, two competing GE models, depending on which of J_{F2} and J$_{F3}$ is negative and which is positive. Examining constant energy simulations just above and below the gap in the dispersion rules out the alternative GE model. Fig. 3.44 shows the data and simulations for constant energy slices at 35 meV (panels (a)-(c))and 60 meV (panels (d)-(f)). The data has been corrected for a constant background. The simulations allow a comparison of the two GE models, calcuations using the GE model (panels (b) and (e)) show an excellent agreement with the data, where as those performed with the alternative GE model (panels (c) and (f)), do not describe the data well. It is clear that the original GE model provides the better simulation of the data and the alternative GE model may be discarded.

3.9 Conclusion

This measurement of the spin wave dispersion of Pr(Sr$_{0.1}$Ca$_{0.9}$)$_2$Mn$_2$O$_7$, clearly demonstrates that the Zener polaron model is not a suitable candidate for the electronic ground state in CE-type magnetic phase of this system. The dispersion can

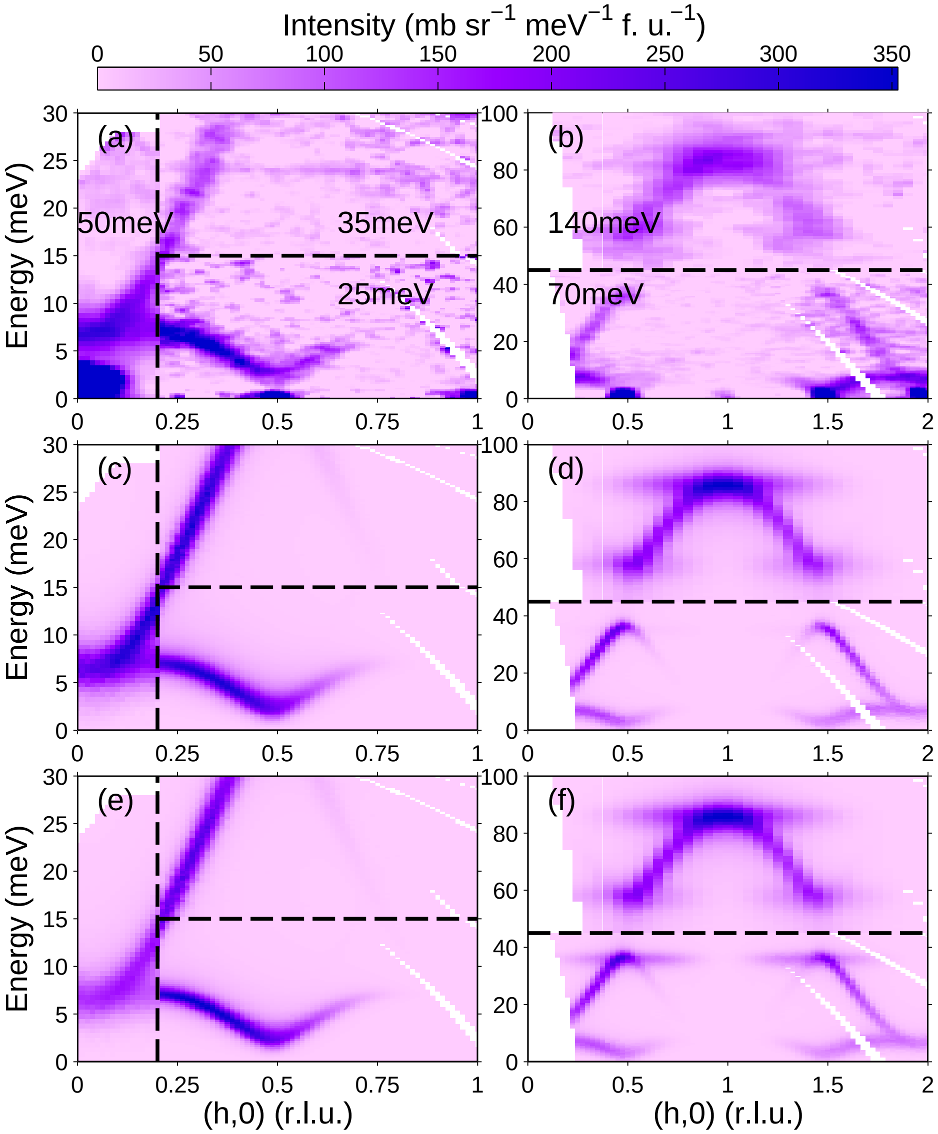

Figure 3.37: Spin wave dispersion in $Pr(Sr_{0.1}Ca_{0.9})_2Mn_2O_7$ showing energy slices are along the $(h, 0, l)$ direction. parallel to the ferromagnetic zigzag. Each plot is split in to sections depending on the incident neutron energy for that section, the values of the incident energy are shown in (a) and (b) and remain the same for the figures directly below in each column. (a) The low energy dispersion data (b) the high energy dispersion data (c) the low energy simulation with the DI model (d) the high energy simulation with the DI model (e) the low energy dispersion of the GE model (f) the high energy simulation of the GE model.

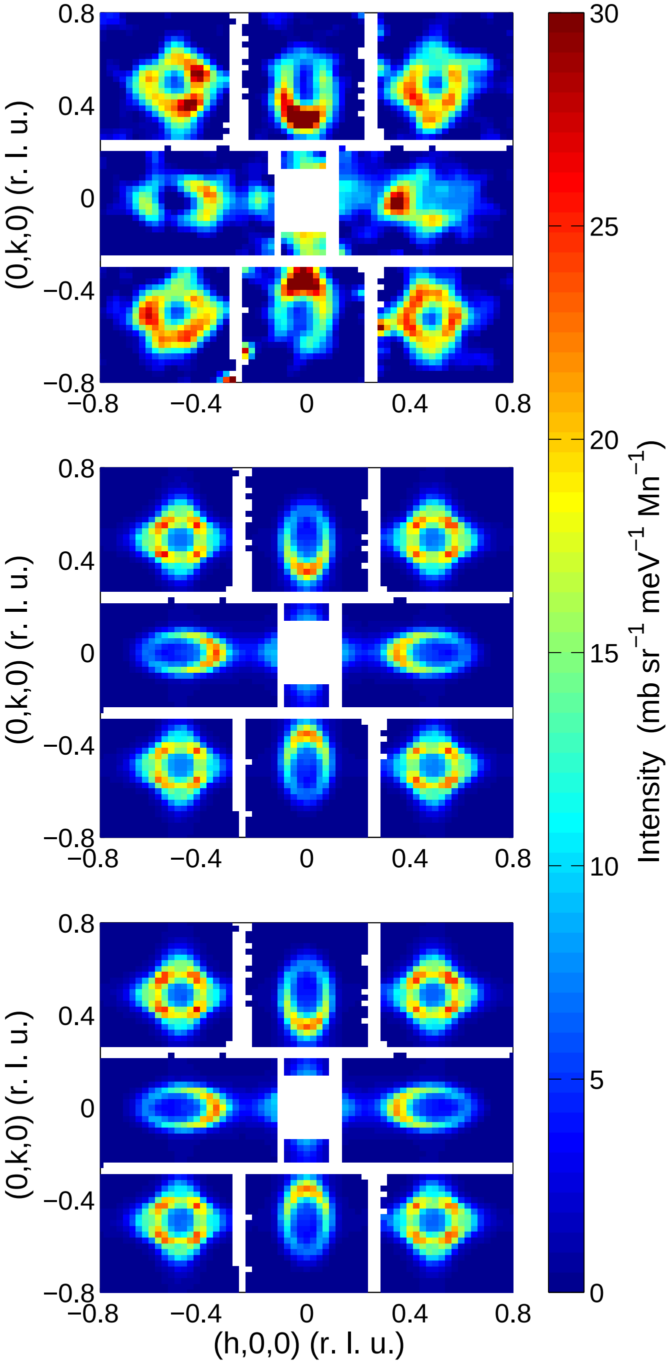

Figure 3.38: A constant energy slice through the dispersion between 4.5 and 5.5 meV taken at an incident energy of 25 meV. (a) A slice of the measured spectrum (b) the spectrum simulated using the GE model (c) The slice simulated using the DI model.

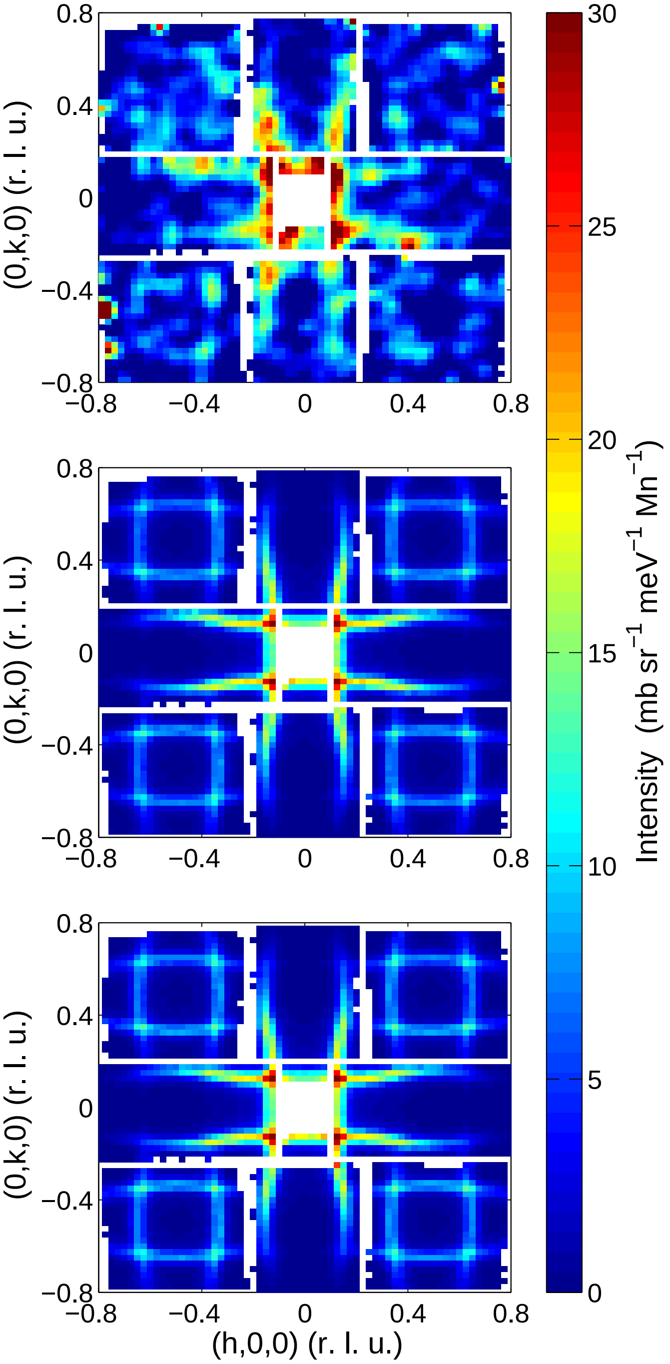

Figure 3.39: A constant energy slice through the dispersion between 10.5 and 11.5 meV taken at an incident energy of 25 meV. (a) A slice of the measured spectrum (b) the spectrum simulated using the GE model (c) The slice simulated using the DI model.

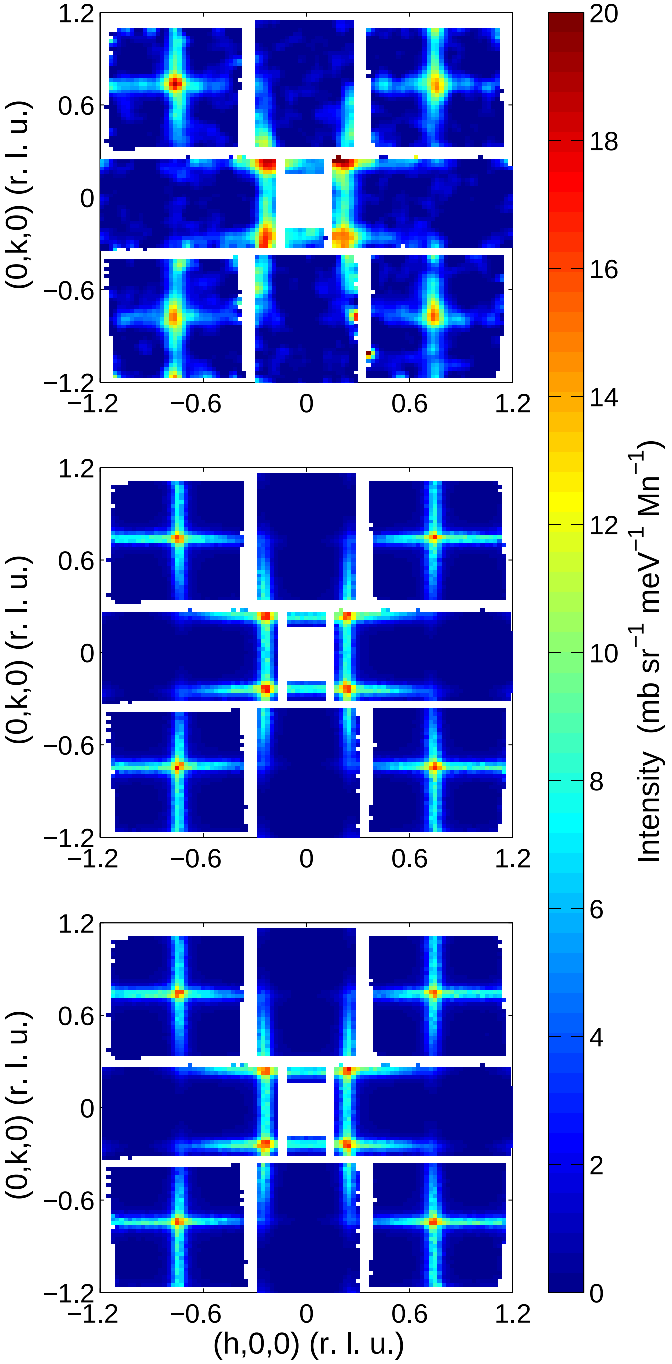

Figure 3.40: A constant energy slice through the dispersion between 16 and 18 meV taken at an incident energy of 50 meV. (a) A slice of the measured spectrum (b) the spectrum simulated using the GE model (c) The slice simulated using the DI model.

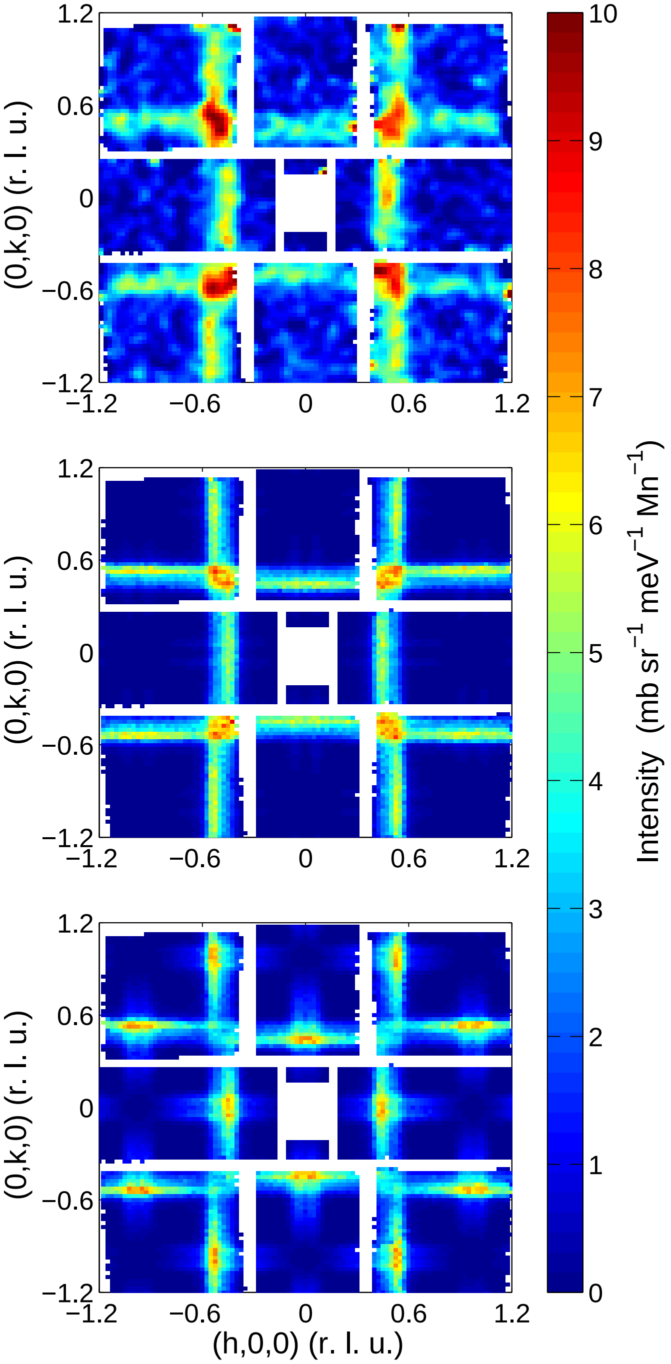

Figure 3.41: A constant energy slice through the dispersion between 34 and 36 meV taken at an incident energy of 70 meV. (a) A slice of the measured spectrum (b) the spectrum simulated using the GE model (c) The slice simulated using the DI model.

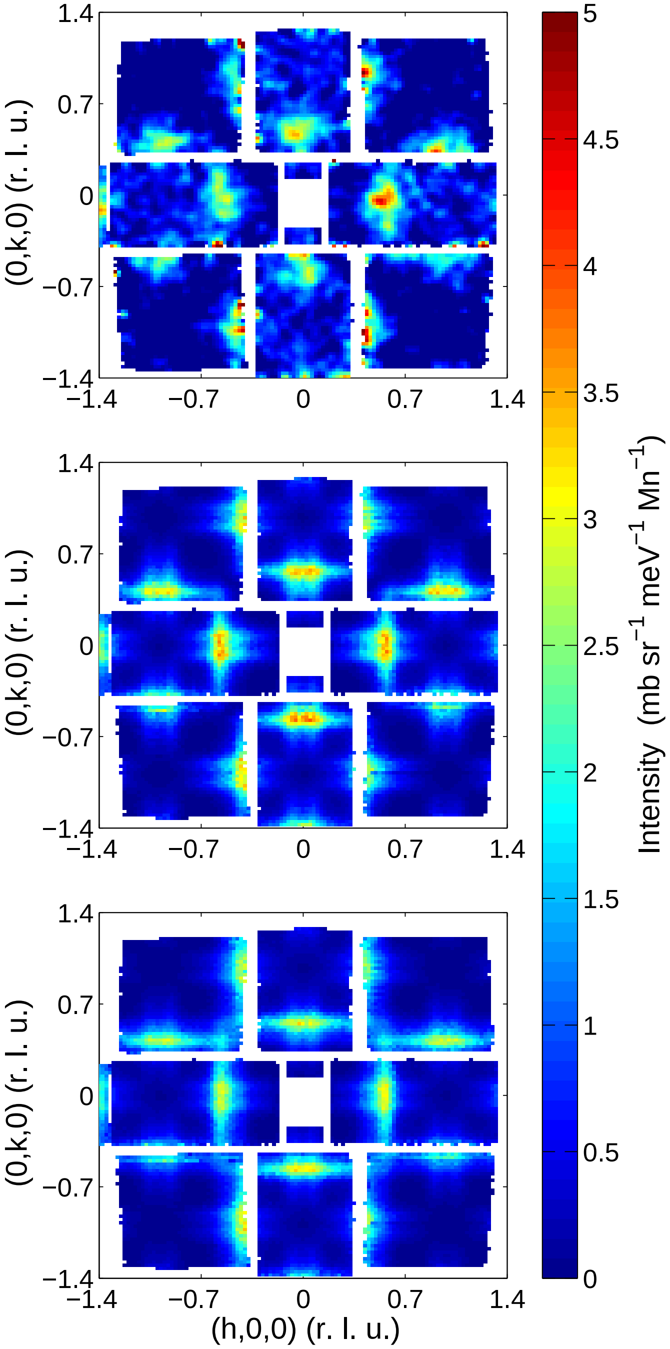

Figure 3.42: A constant energy slice through the dispersion between 58 and 62 meV taken at an incident energy of 100 meV. (a) A slice of the measured spectrum (b) the spectrum simulated using the GE model (c) The slice simulated using the DI model.

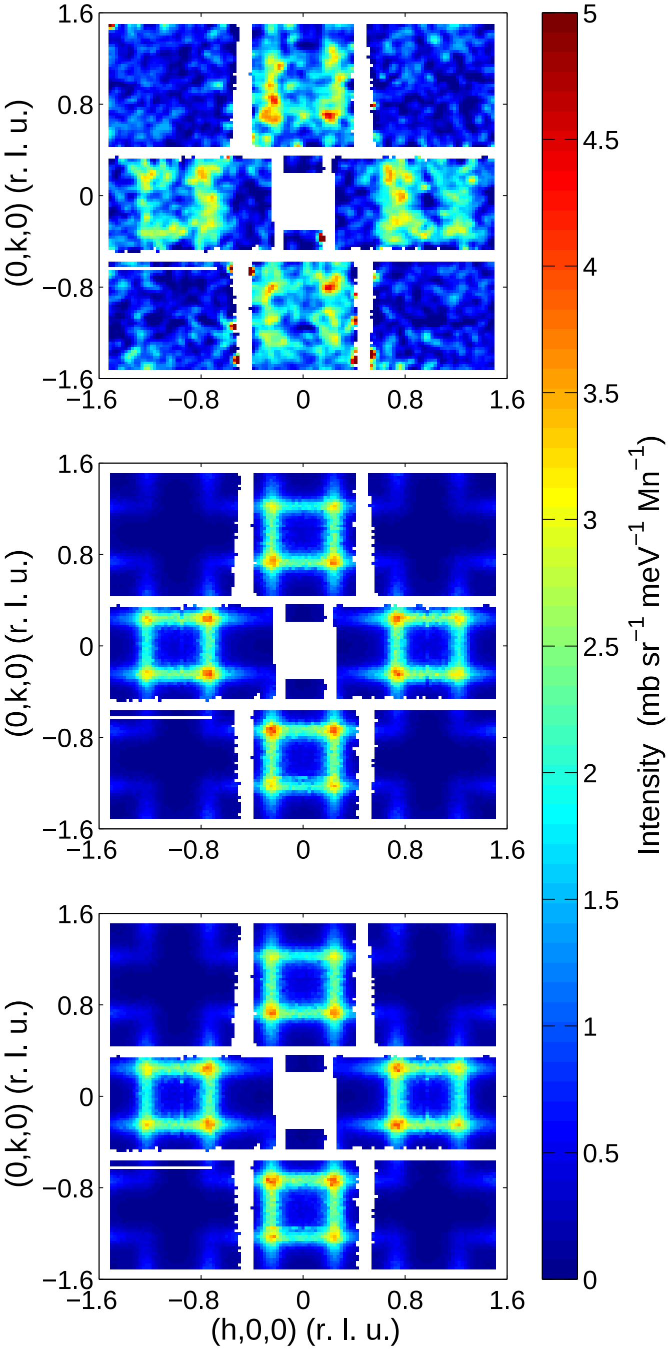

Figure 3.43: A constant energy slice through the dispersion between 73 and 77 meV taken at an incident energy of 140 meV. (a) A slice of the measured spectrum (b) the spectrum simulated using the GE model (c) The slice simulated using the DI model.

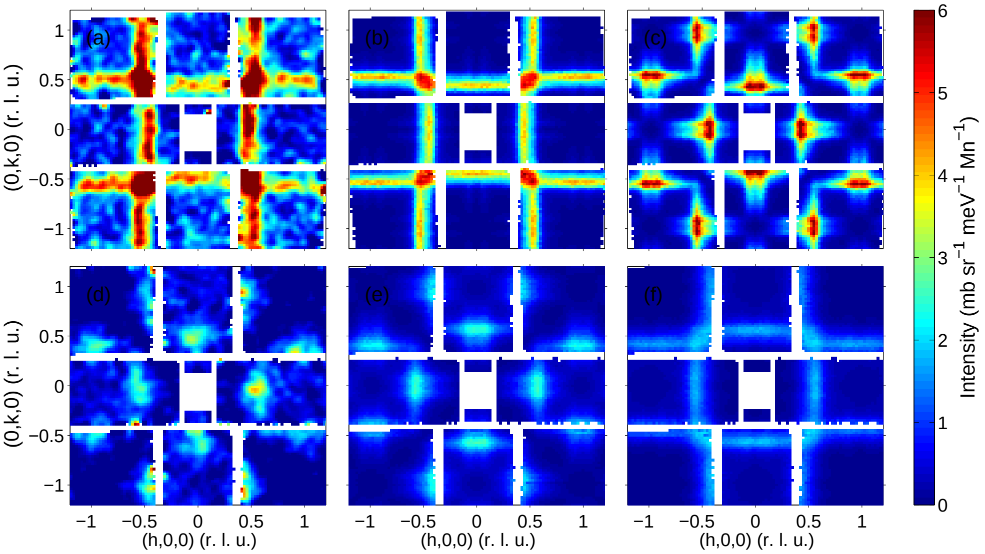

Figure 3.44: A series of constant energy slices. The top row of panels show slices at 35 meV, with (a) showing the data, (b) a slice using the GE model and (c) a slice using the alternative GE model. The bottom row shows slices at 60 meV, with (d) showing the data, (e) a slice using the GE model and (f) a slice using the alternative GE model

be described by the traditional CE-type electronic ground state originally proposed by Goodenough, even without any significant charge ordering. However, this does require some frustration within the ferromagnetic chain. The dispersion can also be described by a dimer model, somewhat similar to the Goodenough model, but having a broken symmetry in the nn-FM interaction within the FM chain. The DI model and an alternative version of the GE model can both be ruled out by simulations of the neutron scattering spectrum, leaving the GE model with J_{F2} positive and J_{F3} negative as the only model that describes the observed neutron scattering spectrum. It is demonstrated that the electronic ground state can produce this spin wave dispersion, even with equal charges on the Mn sites.

The values for the exchange parameters found as a result of the fit with the GE model, such as the nn-FM interactions, agree well with work on similar manganites which shows A-type antiferromagnetism, like the bilayer manganite $La_{2-2x}Sr_{1+2x}Mn_2O_7$.[76]

The dominance of the FM term being almost an order of magnitude greater than the other interactions, shows that this material is close to having a magnetic structure with ferromagnetic layers, agreeing with the traditional view of colossal magnetoresistance.

Chapter 4

The Magnetisation Distribution in $La_{0.5}Sr_{1.5}MnO_4$

4.1 Introduction

One of the most striking phenomena in manganites is the wide variety of magnetic phases that can exist with relatively small changes in the chemical composition, particularly changes in R in the generic formula $R_{n+1}Mn_nO_{3n+1}$. In the $La_{1-x}Sr_xMnO_3$ at least five different magnetic ordering regimes are present as the material is doped from $x = 1$ to $x = 0$.[77] The most complex of these phases is perhaps the charge-exchange (CE) magnetic phase, shown in Fig. 4.1.[15, 17] The exact composition of the electronic ground state in the CE phase has long been debated, as discussed in the previous chapter.

Theories explaining the different types of magnetic ordering observed in $RMnO_3$ materials have mainly focused on the Jahn-Teller effect and the consequent appearance of orbital ordering.[17, 78] The orientation of the ordered orbitals in relation to each other determines the dominant magnetic exchanges between Mn ions, mediated by O ions in a Mn-O-Mn configuration. However, these explanations have always relied on charge ordering of the Mn sites into Mn^{3+} and Mn^{4+} ions, a picture that is not entirely consistent with experimental results.[59, 60]

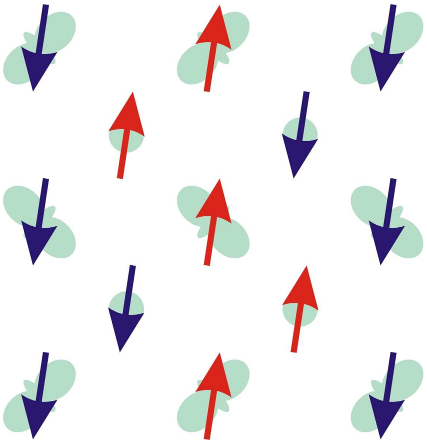

Figure 4.1: The CE-type magnetic structure superimposed upon conventional picture of the orbital ordering.

A measurement of the O K-edge electron energy loss spectra,[79] indicated that the charge carriers in $La_{1-x}Sr_xMnO_3$ had the character of O p-orbitals. This is in contrast to the earlier theoretical work, which assume that oxygen was in an unpolarised O^{2-} state. Ferrari et al conducted an *ab initio* electronic structure calculation of the cubic manganite $La_{0.5}Ca_{0.5}MnO_3$,[63] and the results suggested that there was magnetic polarisation on the oxygen site, in the Mn-O-Mn bond in a layer of the CE-magnetic phase. The results of this calculation are reproduced in Fig. 4.2 and demonstrates the electronic ordering expected on the oxygen site in this material. Also shown is the expected magnetic polarisation of the O site, antiferromagnetic to the nearest neighbour Mn ions.

A number of studies have since investigated the electronic state of the O ion in $La_{0.5}Ca_{0.5}MnO_3$ and closely related materials.[80, 81, 82, 83] There is a reasonable but not conclusive agreement that the charge of the O-site is not strictly 2−. However, only the study by Grenier et al.[80] has tested the magnetism of O site, using resonant x-ray scattering at the O K-edge, but that measurement was not performed on a half-doped material. Therefore the prediction of Ferrari et al.[63] that the O is antiferromagnetically aligned with the neighbouring Mn ions is as yet

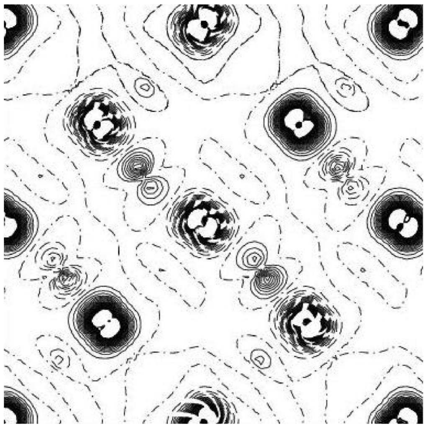

Figure 4.2: Magnetisation density distribution within a layer of $La_{0.5}Ca_{0.5}MnO_3$. This figure is adapted from the work presented by Ferrari et al.[63] Positive density is represented by full lines and negative density is represented by broken lines. Reprinted figure with permission from Ferrari et al.[63] Copyright (2003) by the American Physical Society.

untested for the CE-type magnetic phase.

This investigation examines the magnetisation distribution in the unit cell of the CE-phase in the manganite material $La_{0.5}Sr_{1.5}MnO_4$ using a measurement of the flipping ratios in a polarised neutron scattering experiment to determine the magnetic form factor. The magnetisation distribution is found from the magnetic structure factor using the maximum entropy method.[84]

This study is performed on the single-layered material $La_{0.5}Sr_{1.5}MnO_4$, instead of a cubic perovskite, for a number of important reasons. $La_{0.5}Sr_{1.5}MnO_4$ is the $n = 1$ member of the Ruddlesden-Popper series and has a similar chemical composition to $La_{0.5}Ca_{0.5}MnO_3$. In particular the number of electrons per Mn ion is the same in both materials, giving an average Mn valency of +3.5. It has been shown in a number of previous studies that $La_{0.5}Sr_{1.5}MnO_4$ shows the same magnetic CE phase at low temperatures that $La_{0.5}Ca_{0.5}MnO_3$ displays and that this magnetic structure seems to be induced by the same charge order/orbital order.[21] These orderings are also observed in the $n = 2$ member of the series, including one discussed in Chapter

3.

One advantage of $La_{0.5}Sr_{1.5}MnO_4$ over $La_{0.5}Ca_{0.5}MnO_3$ in a single crystal neutron experiment is the relative simplicity of the twinning problem in the layered material (twins in this case are the possible energy equivalent arrangements of the MnO_2 planes in the CE-type magnetic phase). In $La_{0.5}Ca_{0.5}MnO_3$ the planes of the CE phase can have six possible orientations, two twins (rotated 90° from each other) in each of the three crystallographic directions. In $La_{0.5}Sr_{1.5}MnO_4$ there is only one orientation of the MnO layers and therefore only two twins for the CE-phase, making the experimental results much easier to interpret.

As the MnO_2 layers interact weakly, $La_{0.5}Sr_{1.5}MnO_4$ can be considered as a quasi-two-dimensional system. The single layered perovskite manganites have been shown to have very stable magnetic states within the layers, which are not altered until very high magnetic fields are applied.[85] This is essential in this study due to the large magnetic fields which are applied in the polarised neutron scattering experiment (discussed later).

4.1.1 Bulk properties of $La_xSr_{2-x}MnO_4$

The series of manganites $La_xSr_{2-x}MnO_4$ for ($0 \leq x \leq 0.6$) have the tetragonal $I4/mmm$ space group symmetry at room temperature, with $La_{0.5}Sr_{1.5}MnO_4$ having the lattice parameters $a = 3.86$Å and $c = 12.42$Å at room temperature (precise values of a and c vary with x).[86] At all temperatures, $La_{0.5}Sr_{1.5}MnO_4$ displays a crystal structure that is close to having the same $I4/mmm$ symmetry and for convenience all scattering vectors discussed in this chapter are referenced in this unit cell. The crystal structure of a unit cell of $La_xSr_{2-x}MnO_4$ is shown in Fig. 4.3, showing the MnO layers in purple with La/Sr site in between these layers, in yellow and the room temperature unit cell shown by the black box.

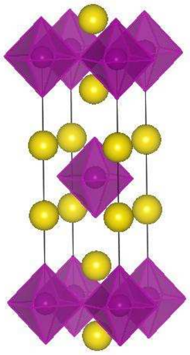

Figure 4.3: The $I4/mmm$ crystal structure of $La_xSr_{2-x}MnO_4$ purple circle are Mn ions, which are surrounded by an octahedron of O ions. The yellow circles are the La/Sr sites. The black lines show the crystallographic unit cell.

On cooling $La_{0.5}Sr_{1.5}MnO_4$ goes through two significant phase transitions. There is a charge-order/orbital-order transition at $T_{CO-OO} = 217$K.[21] The charge-order/orbital-order phase results in a small distortion to the crystal structure, with structural superlattice Bragg peaks appearing at $(h + 1/2, k + 1/2, l)$ positions. $La_{0.5}Sr_{1.5}MnO_4$ undergoes a magnetic transition at $T_N = 110$K, below which CE-phase antiferromagnetism is observed. The magnetic unit cell is rotated 45° around the c-axis from the structural unit cell and has the dimensions $2\sqrt{2}a \times 2\sqrt{2}a \times 2c$.[21]

Measurements of the magnetisation of the $La_xSr_{2-x}MnO_4$ materials are important for this study both for sample characterisation and for determining the magnetic form factor. For this reason it is convenient to compare this work with the previous work of Morimoto et al.[87] shown in Fig. 4.4, where measurements of magnetisation versus temperature on samples with doings from $0 \leq x \leq 0.7$ is shown. However, it is thought that the measurement of the sample at $x = 0.5$ in Fig. 4.4 is unreliable (this is the crucial value for this experiment). Later measurements for $x = 0.5$ have been produced by Senff et al.[74] (shown in Fig. 4.5) and Arao et al.[88] which agree with each other and disagree with Moritomo et al. These later

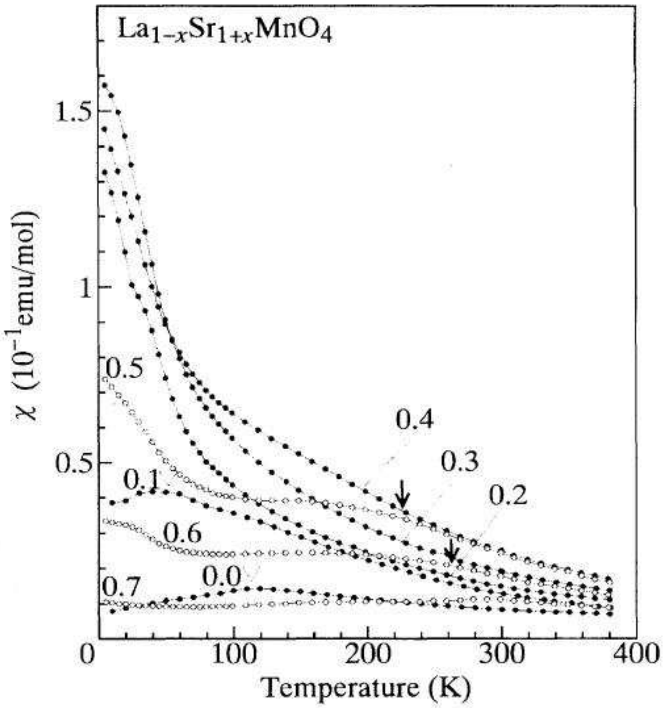

Figure 4.4: The magnetisation temperature dependencies of various compositions of $La_xSr_{2-x}MnO_4$ with a magnetic field of 1T applied parallel to the c-axis. Reprinted figure with permission, from Morimoto et al.[87]. Copyright (1995) by the American Physical Society.

results are thought to be more reliable for the $x = 0.5$ sample.

4.2 Experimental Overview

The aim of this study was to determine the distribution of the magnetic moment within a unit cell of $La_{0.5}Sr_{1.5}MnO_4$ and in particular that of the moment localised on the oxygen site within an MnO_2 layer. To determine this, a measurement of the flipping ratios in a polarised neutron diffraction experiment was used to find the magnetic form factor. The details of this technique are discussed in section 2.1.4. The method of flipping ratios is used to determine a ferromagnetic magnetisation. Since $La_{0.5}Sr_{1.5}MnO_4$ is an antiferromagnet, a large magnetic field (around

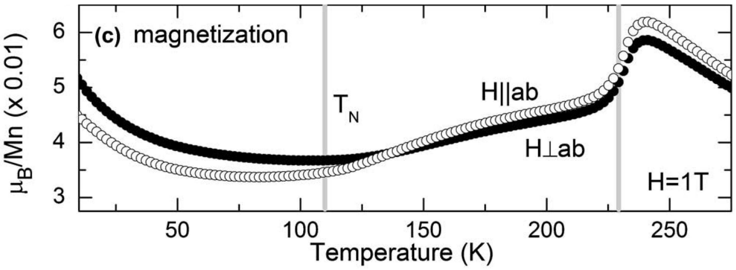

Figure 4.5: The magnetisation temperature dependence of $La_{0.5}Sr_{1.5}MnO_4$, Reprinted figure with permission from Senff et al.[74] Copyright (2008) by the American Physical Society.

9T) was applied to induce a ferromagnetic moment in the sample. To accurately determine the distribution of magnetic moment within the unit cell in a sample of $La_{0.5}Sr_{1.5}MnO_4$ by use of this method, an analysis technique known as the maximum entropy method [84, 40] was used to convert the magnetic form factor into a real space distribution of the magnetic moment. This a multiple step process and will be presented as such over the following sections.

All of the samples used in this study were grown in the Clarendon Laboratory by D. Prabhakaran. High quality single crystals were grown using the floating zone method.[89] Two samples were found to be of suitable quality to allow for the determination of the distribution of the magnetic moment. A similar experimental procedure has been carried out for each sample. Both samples were characterised using a number of experimental methods, to determine both the quality of the sample and its precise composition. These measurements are presented in section 4.3.

To determine the magnetic structure factor using this method, the nuclear structure factor needs to be modeled accurately. The determination of the crystal structure of the samples used in this study is presented in section 4.4. As part of the crystal structure determination, it is essential to have characterisation of the neutron absorption and extinction of the sample. These values are sample dependent and are considered as part of the crystal structure determination.

The final experiment is the actual measurement of the flipping ratios and the determination of the detailed magnetic form factor of the samples. This was again performed for both samples and is presented in section 4.5.

4.3 Sample Characterisation and Bulk Properties

The physical properties of $La_{0.5}Sr_{1.5}MnO_4$ are well known through a number of studies.[87, 21, 86, 74] For this study, a high quality sample of a material with the correct stoichiometry is required. A number of samples were available for these experiments, and the procedures described in this section allowed the best ones to be chosen for the measurement of the magnetic structure factor of $La_{0.5}Sr_{1.5}MnO_4$.

4.3.1 Experiments

Growing high quality single crystals of $La_{0.5}Sr_{1.5}MnO_4$ with the precise stoichiometry is a difficult procedure. It was important to perform a series of checks on samples to ensure the best possible quality and to find the samples that are closest to being half doped, i. e. when $x = 0.5$ in $La_xSr_{2-x}MnO_4$. If the stoichiometry is correct ($x = 0.5$), then the sample should be in the CE-type magnetic phase below T_N and testing for this magnetic phase is a good indication of the sample composition.

Crystal quality was examined using a x-ray Laue system at the Clarendon Laboratory at the University of Oxford. A number of the crystals were shown to have multiple crystalline grains, with important Bragg peaks overlapping. This makes the crystal unusable when precise measurements of peak intensities are necessary. X-rays do not probe the bulk of the material, whereas neutrons do; therefore suitable crystals were also scanned on the neutron Laue instrument, Orient Express, at the ILL, Grenoble. Some crystals that appeared to be of high quality on the x-ray Laue were shown to have multiple grains on the neutron Laue.

To determine the crystal composition, and to get an accurate value for x in $\mathrm{La}_x\mathrm{Sr}_{2-x}\mathrm{MnO}_4$ for the available samples, magnetisation measurements were made using a Superconducting Quantum Interference Device (SQUID), described in section 2.6.1, in a Quantum Designs Magnetic Properties Measurement System (MPMS). The magnetisation of samples was measured with a magnetic field of 1000 Oe (0.1T) applied parallel to the crystallographic c-axis and was measured over a range of temperatures, $2 \leq T \leq 300$K.

High quality samples were examined using neutron diffraction on the four-circle diffractometers D9 (hot neutrons) and D10 (thermal neutrons), at the ILL, Grenoble. The samples were glued to an aluminium pin and were mounted in a He cryostat allowing a wide range of temperatures, from $10 < T < 300$K. On D10 measurements were made using a graphite monochromator and a wavelength of $\lambda = 2.3587$Å. The instrument D9 also used a graphite monochromator, with a wavelength of $\lambda = 0.837$Å. The other orders of λ are suppressed by the guide mirrors on both instruments. A variety of measurements were made on these instruments, checking for such phenomena as charge ordering, orbital ordering and magnetic ordering (particularly the CE-type antiferromagnetic ordering) in a number of samples and checking the temperature dependence of some important peaks.

Both D9 and D10 use an area detector for measuring the intensity of the scattered beam; this allows the true integrated intensity of the peaks to be measured. The peak is aligned in the detector and then a θ-scan is performed through the peak. The peak intensities were found using Racer,[90] a program specifically designed to accurately determine peak intensities on 2D multidetectors.

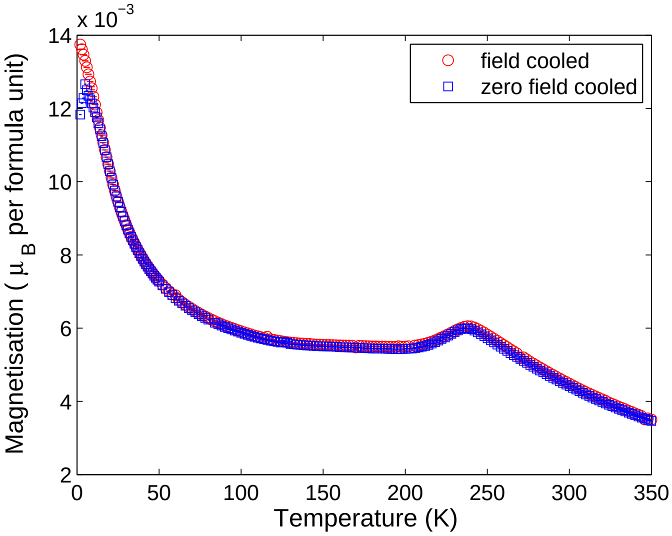

Figure 4.6: The magnetisation vs temperature of crystal A (identified as being close to $La_{0.5}Sr_{1.5}MnO_4$). The red circles show the field cooled measurement and the blue squares the zero field cooled measurement. A magnetic field is 0.1T was applied parallel to the *c*-axis.

4.3.2 Results and Discussion

After running all of the characterisation experiments, it was found that two of the crystals were of higher quality than the other samples; these will be referred to as crystal A and crystal B. These two samples were both shown to be high quality single crystals when examined by both neutron and x-ray Laue diffraction.

Magnetisation temperature dependencies of the two high quality samples is presented in Fig. 4.6 and Fig. 4.7. Both crystals are shown with a field cooled and a zero field cooled measurement. These can be compared to previous work on $La_xSr_{2-x}MnO_4$, shown in Fig. 4.4 and Fig. 4.5 [87, 74], although it should be noted that these figures both show measurements made at 1T, 10 times higher than the measurements made in this study. Nonetheless, the measurements can be used to get an estimate for the sample composition.

Although crystal A shows a local maximum at 240K, roughly T_{CO}, a characteristic of the half-doped, CE-type magnetic phase observed by Senff et al. and

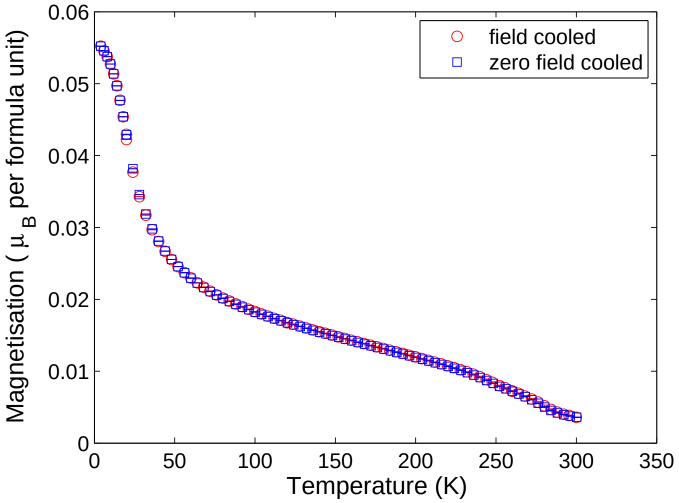

Figure 4.7: The magnetisation vs temperature of crystal B. The red circles show the field cooled measurement and the blue squares the zero field cooled measurement. A magnetic field is 0.1T was applied parallel to the *c*-axis.

shown in Fig. 4.5,[74] the low temperature maximum is much higher than would be expected in an $x = 0.5$ sample of $\mathrm{La}_x\mathrm{Sr}_{2-x}\mathrm{MnO}_4$. The fact that characteristic features of both an $x = 0.5$ crystal and an $x < 0.5$ crystal, are apparent in the same sample suggests that the doping level throughout the sample is inhomogeneous. This probably means that part of the sample is $\mathrm{La}_{0.5}\mathrm{Sr}_{1.5}\mathrm{MnO}_4$ and another part has a slightly lower value of x. This sample is the highest quality single crystal available that has a composition close to $x = 0.5$.

The magnetisation temperature dependence of crystal B, Fig. 4.7, shows a constant increase of magnetisation with decreasing temperature. There is a slight bump between 200K and 250K and below 100K the magnetisation curve gets much steeper. When comparing these features of the magnetisation of crystal B, with the previous magnetisation measurements on $\mathrm{La}_x\mathrm{Sr}_{2-x}\mathrm{MnO}_4$ in Fig. 4.4, the steep increase in magnetisation on cooling below 100K is similar to materials with $x = 0.2, 0.3$ or 0.4, although the measurement on crystal B shows a steeper slope. The larger magnitude of the rate of change of the magnetisation with temperature apparent in the crystal B results might be due to the fact that it was measured with a lower applied magnetic field. The bump near 200K is most similar to the $x = 0.5$ composition. As mentioned earlier, it is believed that the $x = 0.5$ crystal measured by Moritomo et al.[87], probably had a true value of slightly less than $x = 0.5$.

Both samples were examined on D10 as a further test of the chemical composition of each. Crystal B was tested for the characteristic diffraction peaks expected with the CE-type magnetic phase at 20K, which should be well below T_N, such as the $(h + 1/4, k + 1/4, l/2)$ peaks. A detailed diffraction experiment on $La_{0.5}Sr_{1.5}MnO_4$ is presented by Sternlieb et al.[21], where a list of the characteristic Bragg peaks in this material is presented. No evidence of CE-type ordering was observed in this experiment on crystal B, a further indication that the composition of this sample does not allow for the existence of the CE phase. The magnetisation data available suggests that crystal B has a character similar to that of $La_{0.4}Sr_{1.6}MnO_4$; however, this might not be due to an incorrect La/Sr ratio, a similar effect could arise from having too much oxygen in the system. Either one of these issues would increase the electron content of MnO_2 layer, resulting in a material similar to $La_{0.4}Sr_{1.6}MnO_4$.

The same checks for the characteristic Bragg peaks found by Sternlieb et al.[21] were performed on crystal A and all of the peaks expected in the CE magnetic phase were present at 20K, below T_N. A full temperature dependence of the intensity of a characteristic magnetic- and orbital-ordered peak, as well as a structural peak was performed on this sample on D9. The three temperature dependencies are shown in Fig. 4.8. The wavevectors examined are the $(0.75, -0.25, 0.5)$ for the magnetic CE-phase, $(0.25, 1.75, 0)$ for the orbital ordering and $(0, 2, 0)$ for the main structural peak. The two temperatures marked in Fig 4.8 were established in the previous study by Sternlieb et al.[21] and the results measured here agree well with this previous study. The charge-order/orbital-order in crystal A does appear to exist

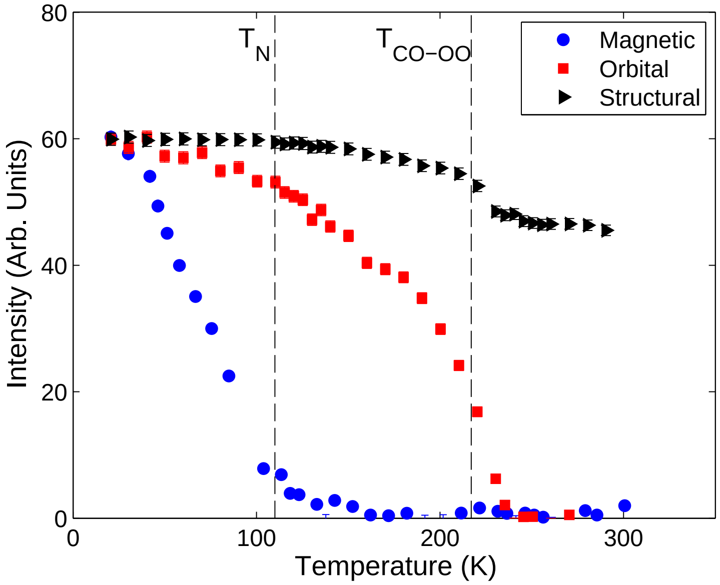

Figure 4.8: Temperature dependence of the integrated intensity of Bragg peaks that are indicative of different ordering phases in crystal A. The blue circles represent the $(0.75, -0.25, 0.5)$ magnetic peak, the red squares represent the $(0.25, 1.75, 0)$ orbital ordering peak and the black triangles represent the $(0, 2, 0)$ structural peak, showing a transition at the charge ordering temperature. All of the intensities have been normalised to the maximum intensity of the charge ordering reflections. The temperatures marked are the previously measured values for the Neel temperature and the charge-order/orbital-order transition.[21]

to a slightly higher temperature than expected, but the difference is quite small. Therefore it can be confirmed that at least part of crystal A has the composition $La_{0.5}Sr_{1.5}MnO_4$.

These two high quality single crystals, with slight differences in their composition are good candidates for measuring the magnetisation distribution within a unit cell. The two different doping levels available allow for a wider study than was initially hoped for and should improve the sensitivity of the analysis to any unique features of the antiferromagnetic CE-phase. The rest of this chapter concerns the measurement of the magnetisation distribution in the unit cell in these two crystals of $La_xSr_{2-x}MnO_4$, crystal A and crystal B.

4.4 The Crystal Structure $La_xSr_{2-x}MnO_4$

To measure the magnetic form factor of the two samples of $La_xSr_{2-x}MnO_4$ using polarised neutron diffraction, it is important that the intensity of the diffraction signal can be accurately measured for all peaks, requiring the nuclear structure factor to be determined. It is particularly important to get accurate extinction and absorption corrections for the samples under the same condition that they will be subjected to in the polarised neutron experiment. Neutron absorption and extinction are described in sections 2.1.7 and 2.1.8, respectively. Ideally the samples would have a isotropic extinction for all Bragg peaks, which requires a spherical sample. Both of the samples used were too small to allow such shaping, as the mass would have to be reduced below a practical level for the experimental time frame. This section describes the experiments conducted to get an accurate model of the structure of the two samples, as well as good absorption and extinction corrections for both samples. All scattering reflections are referred to in the $I4/mmm$ reciprocal space units discussed in the first section of this chapter.

4.4.1 Experiment

The two samples of $La_xSr_{2-x}MnO_4$ were measured by a neutron diffraction experiment on D9, at ILL, Grenoble. D9 is a hot neutron four circle diffractometer that allows the same neutron wavelength and sample temperature conditions that are available at the polarised neutron measurement used in this study (D3, also at ILL). Hot neutrons also allow for a short wavelength and a large Ewald sphere, which gives access to many Bragg peaks. Measuring a large number of peaks will enable a better fit to the data to be achieved and therefore more accurate measurements of the extinction and absorption. Both samples were glued to aluminium pins and then mounted in a He cryostat. As mentioned in the previous section, D9 has an area detector and peak intensities are measured using a θ-scan and then calculated using Racer.[90]

A number of measurements were made on each crystal, at various temperatures and wavelengths. For crystal A, at a wavelength of $\lambda = 0.837\text{Å}$, 747 peaks were measured at the temperatures 20K and 120K, while 558 peaks were measured at 250K. One measurement was also made at 20K with $\lambda = 0.511\text{Å}$, covering 446 peaks. With crystal B, measurements were made at 20K with 545 peaks measured for $\lambda = 0.837\text{Å}$ and 653 peaks measured with $\lambda = 0.511\text{Å}$. At higher temperatures all measurements were made with $\lambda = 0.837\text{Å}$, 683 peaks were measured at 120K and 582 peaks were measured at 250K.

4.4.2 Results

The lists of peak intensities were fitted separately for each sample, temperature and wavelength to a model of $La_{0.5}Sr_{1.5}MnO_4$ using CCSL. This work was mainly performed by Anne Stunault. The fitted model was then used to generate the calculated peak intensities, which can then be compared to the observed peak intensities. The comparison of the fitted intensities to the data for the various data sets measured are shown in figures 4.9-4.16.

The measurements on crystal A (figures 4.9-4.12) show an excellent fit to the data with most peaks having very similar observed and calculated intensities. The results of the fit are presented in table 4.1. Due to the quality of the fit (as illustrated by the low χ^2 values) for crystal A, which includes an extinction and absorption correction, it can be assumed that the structure of this crystal is well known at a range of temperatures and can be used to determine the magnetic structure factor for this crystal (as described in the following sections).

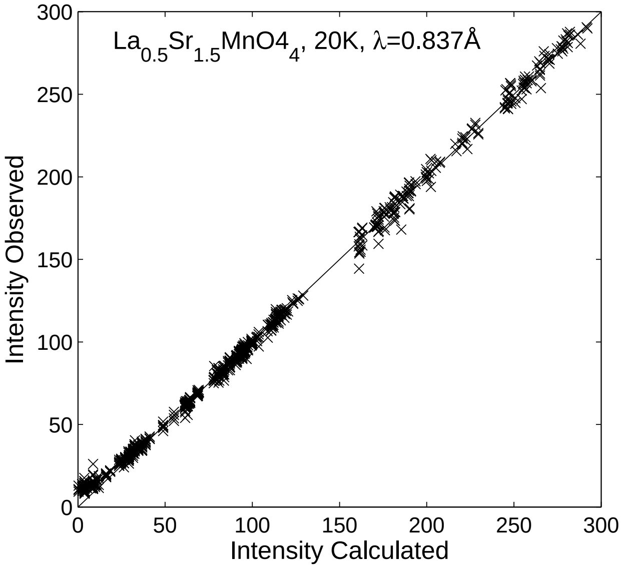

Figure 4.9: Comparison of the calculated peak intensities for crystal A (using the model described in the text) compared to the measured intensities at 20K. The wavelength used was $\lambda = 0.837$Å. Equivalent reflections are plotted separately.

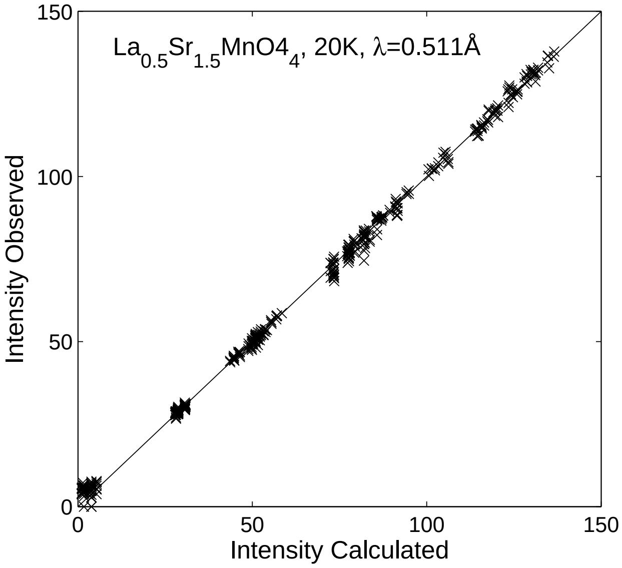

Figure 4.10: Comparison of the calculated peak intensities for crystal A (using the model described in the text) compared to the measured intensities at 20K. The wavelength used was $\lambda = 0.511$Å. Equivalent reflections are plotted separately.

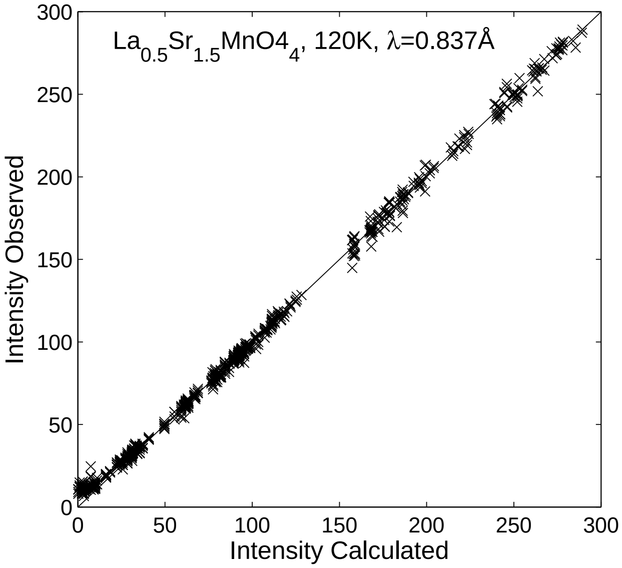

Figure 4.11: Comparison of the calculated peak intensities for crystal A (using the model described in the text) compared to the measured intensities at 120K. The wavelength used was $\lambda = 0.837$Å. Equivalent reflections are plotted separately.

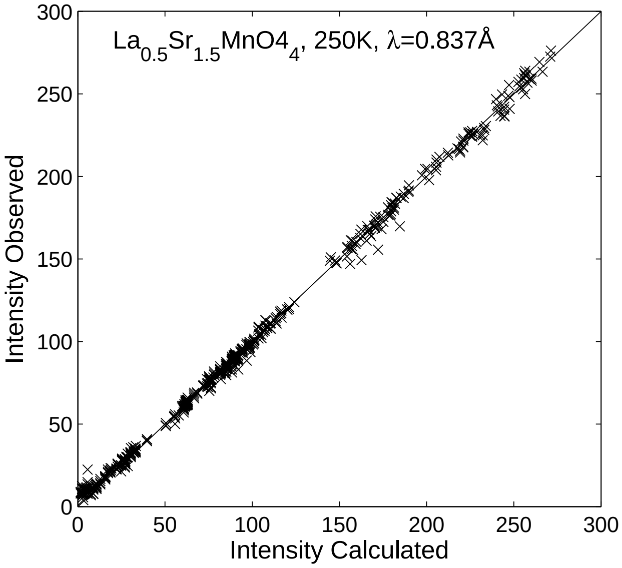

Figure 4.12: Comparison of the calculated peak intensities for crystal A (using the model described in the text) compared to the measured intensities at 250K. The wavelength used was $\lambda = 0.837$Å. Equivalent reflections are plotted separately.

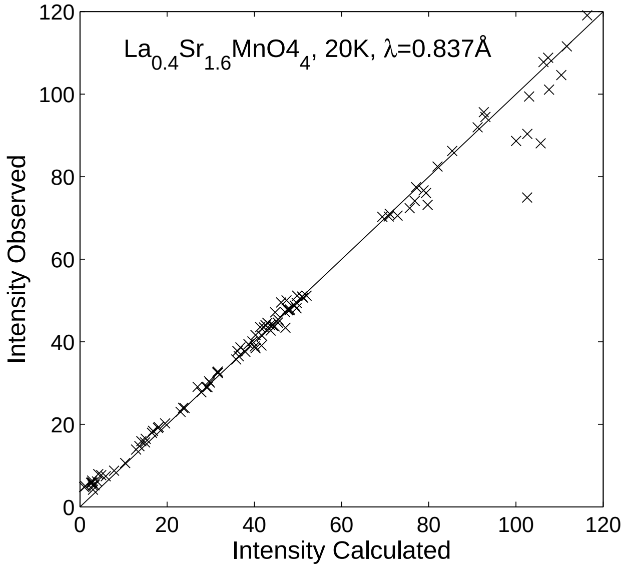

Figure 4.13: Comparison of the calculated peak intensities for crystal B (using the model described in the text) compared to the measured intensities at 20K. The wavelength used was $\lambda = 0.837$Å. Equivalent reflections are plotted together.

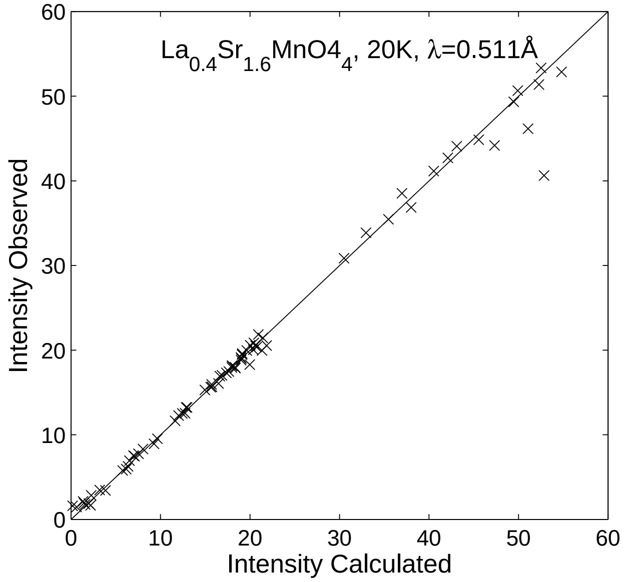

Figure 4.14: Comparison of the calculated peak intensities for crystal B (using the model described in the text) compared to the measured intensities at 20K. The wavelength used was $\lambda = 0.511$Å. Equivalent reflections are plotted together.

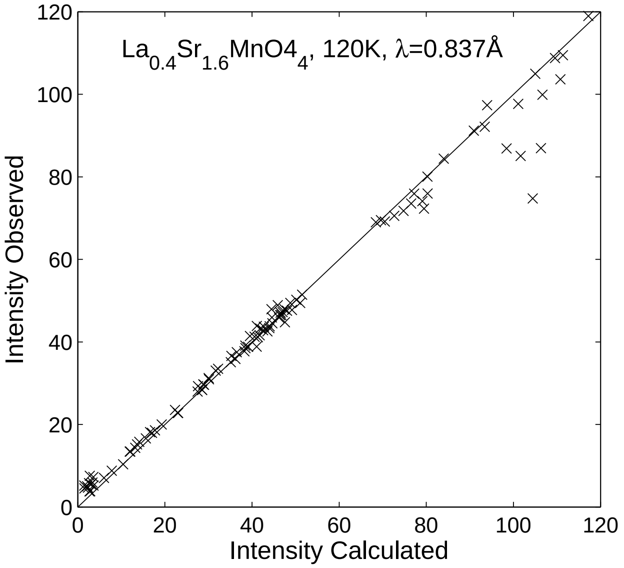

Figure 4.15: Comparison of the calculated peak intensities for crystal B (using the model described in the text) compared to the measured intensities at 120K. The wavelength used was $\lambda = 0.837$Å. Equivalent reflections are plotted together.

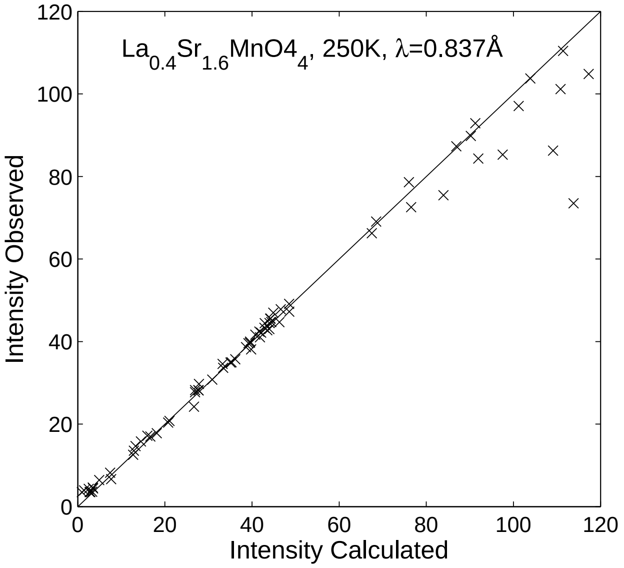

Figure 4.16: Comparison of the calculated peak intensities for crystal B (using the model described in the text) compared to the measured intensities at 250K. The wavelength used was $\lambda = 0.511$Å. Equivalent reflections are plotted together.

Table 4.1: The structural parameters for crystal A with $\lambda = 0.837$Å at 20K, 120K and 250K, presented in the tetragonal $I4/mmm$ space group. The lattice parameters are given in Å, U_{ab} are the anisotropic temperature factors and the z-position of the Sr/La and O(2) sites are presented as a fractional length along the c-axis of the unit cell. Absorption, μ,is given as an inverse distance, representing the exponential decay of the intensity. The extinction is determined using the Becker and Coppens Lorentzian model[91] with domain radius given in Å and mosaic in 1/radians.

		20K	120K	250K
$a = b$	(Å)	3.8652	3.8652	3.8615
c	(Å)	12.4611	12.4611	12.4615
Mn	$U_{11/22}$ (10^{-4}Å^2)	17.8(1.4)	13.5(1.9)	16.6(3.4)
	U_{33} (10^{-4}Å^2)	47.3(3.1)	20.4(2.5)	50.9(5.3)
La/Sr	z-position	0.3581(1)	0.3581(1)	0.3581(1)
	$U_{11/22}$ (10^{-4}Å^2)	55.3(1.2)	36.5(1.3)	57.7(1.6)
	U_{33} (10^{-4}Å^2)	69.0(1.8)	34.2(1.5)	49.2(2.4)
O(1)	U_{11} (10^{-4}Å^2)	81.9(1.5)	64.2(2.2)	81.5(2.8)
	U_{22} (10^{-4}Å^2)	84.6(1.0)	84.9(2.1)	84.2(2.9)
	U_{33} (10^{-4}Å^2)	79.5(1.5)	64.1(2.2)	82.3(3.03)
O(2)	z-position	0.1607(1)	0.1607(1)	0.1607(1)
	$U_{11/22}$ (10^{-4}Å^2)	116.9(1.0)	88.3(1.5)	115.8(2.2)
	U_{33} (10^{-4}Å^2)	90.7(1.4)	78.8(2.4)	91.3(3.0)
Absorption	μ (mm^{-1})	0.00986	0.00986	0.00986
Extinction	Domain (nm)	500	500	500
	Mosaic (rad^{-1})	10.08(0.17)	10.22(0.30)	16.07(0.46)
χ^2		13.7	43.6	40.5

The measurements on crystal B (figures 4.13-4.16), do not show a good agreement between calculated and observed intensities, with particularly severe problems at high intensity peaks. The results of the fit are presented in table 4.2. The poor quality of the fit is evident in the much higher χ^2 observed in the fits of this crystal compared to those for crystal A.

The reasons for the poor fit with crystal B are not well understood, but may be linked to an observation of double peaks at some of the reflections, meaning two scattering peaks were observed in the area detector at the same time separated by an angle smaller that expected for $La_{0.5}Sr_{1.5}MnO_4$. This could be a problem with a

Table 4.2: The structural parameters for crystal B with $\lambda = 0.837$Å at 20K, 120K and 250K, presented in the tetragonal $I4/mmm$ space group. The lattice parameters are given in Å, U_{ab} are the anisotropic temperature factors and the z-position of the Sr/La and O(2) sites are presented as a fractional length along the c-axis of the unit cell. Absorption, μ,is given as an inverse distance, representing the exponential decay of the intensity. The extinction is determined using the Becker and Coppens Lorentzian model[91] with domain radius given in Å and mosaic in 1/radians.

		20K	120K	250K
$a = b$	(Å)	3.8471	3.8471	3.8471
c	(Å)	12.6104	12.6104	12.6104
Mn	$U_{11/22}$ (10^{-4}Å^2)	31.7(54.3)	18.9(22.7)	46.0(24.3)
	U_{33} (10^{-4}Å^2)	40.3(69.1)	11.6(29.6)	40.2(28.9)
La/Sr	z-position	0.3583(1)	0.3583(2)	0.3583(2)
	$U_{11/22}$ (10^{-4}Å^2)	31.8(12.5)	30.1(10.9)	67.7(14.1)
	U_{33} (10^{-4}Å^2)	26.3(24.6)	32.5(55.9)	19.6(14.4)
O(1)	U_{11} (10^{-4}Å^2)	74.4(11.7)	86.2(17.7)	130.1(21.5)
	U_{22} (10^{-4}Å^2)	102.2(16.8)	100.1(17.5)	112.2(20.2)
	U_{33} (10^{-4}Å^2)	79.5(28.4)	1.4(15.4)	54.8(15.3)
O(2)	z-position	0.1645(2)	0.1647(3)	0.1643(3)
	$U_{11/22}$ (10^{-4}Å^2)	121.6(10.7)	135.9(14.0)	171.6(16.5)
	U_{33} (10^{-4}Å^2)	161.3(21.9)	104.7(18.9)	136.5(19.0)
Absorption	μ (mm^{-1})	0.00957	0.00957	0.00957
Extinction	Domain (nm)	100	100	100
	Mosaic (rad^{-1})	7.8(4.1)	12.8(2.6)	11.7(2.7)
χ^2		91.1	194	217

contamination of some other material in the sample or two crystals of the same material within the sample, aligned so that there is a small angular difference between the two. Either of these could lead to problems with measuring peak intensities due to an overlap of multiple scattering peaks. However, this does not explain why only a selection of particularly intense peaks seem to be affected. Measurements at 20K at the two different wavelengths suggest that the lower wavelength measurement gives a slightly better fit for the more intense peaks, compare figures 4.13 and 4.14, although there is almost no difference in the χ^2 of both fits ($\lambda = 0.511$Å fit is not shown). Such a wavelength dependence of the results suggests that the problem

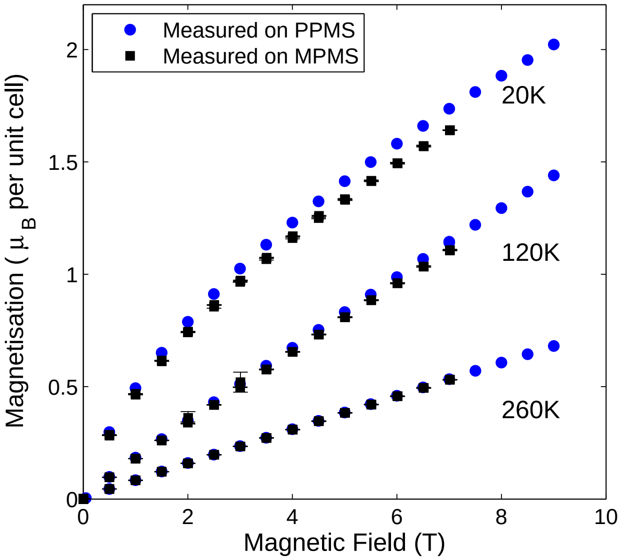

Figure 4.17: Magnetisation in Bohr magnetons per crystallographic unit cell versus applied magnetic field for crystal B at 20K, 120K and 260K measured on both the PPMS (blue circles) and MPMS (black squares).

could be extinction in the sample. Extinction tends to be most problematic in large high quality samples, but crystal B is both smaller and of worse quality that crystal A, so extinction does not seem likely in this case.

The structural data on crystal B is not perfect, but the model does describe the majority of the peaks well. Therefore polarised neutron scattering experiment to measure the flipping ratios was performed with both samples.

4.5 The Magnetic Structure Factor of $La_xSr_{2-x}MnO_4$

Measuring the magnetic structure factor for both samples of $La_xSr_{2-x}MnO_4$ used in this study required two different experimental techniques. Most of the results are obtained by use of polarised neutron scattering, and the method of measuring flipping ratios to determine the magnetic structure factor. This technique is covered in section 2.1.4 and the experiment is covered in 4.5.2. To measure the $\mathbf{Q} = 0$

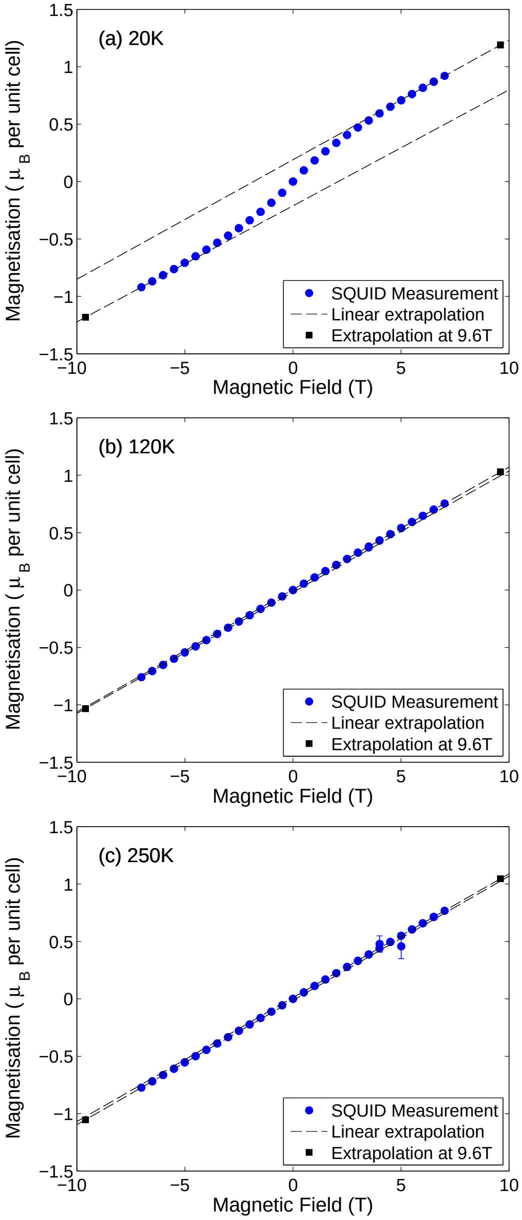

Figure 4.18: Magnetisation in Bohr magnetons per crystallographic unit cell versus applied magnetic field for crystal A at 20K (top), 120K (middle) and 250K (bottom) is shown with blue circles. The dashed lines show a linear extrapolation of the maximum (minimum) applied field measurements to 9.6T (-9.6T) marked with a black square.

point of the magnetic structure factor, a measurement of the magnetisation of the sample must be performed. The magnetic form factor can be thought of as the magnetisation of the sample under spatially varying magnetic fields and therefore a magnetisation measurement with a spatially homogenous magnetic field can be considered to be the $\mathbf{Q} = 0$ point of the magnetic form factor, this is discussed in section 2.16. These magnetisation measurements are covered in section 4.5.1. The last two parts of this section present all of the magnetic structure factor results on firstly crystal A and then crystal B.

4.5.1 Magnetisation Measurements

The magnetisation measurements used to determine the $\mathbf{Q} = 0$ point in the magnetic form factor were measured using the same Quantum Design MPMS SQUID that was discussed earlier in this chapter. This instrument has a maximum applied magnetic field of 7T, but the polarised neutron measurements were performed at 9.6T for crystal A and 9T for crystal B, applied parallel to the crystallographic *c*-axis in both cases. Therefore the data taken using the SQUID had to be extrapolated to this point, using a linear extrapolation. To confirm that a linear extrapolation was an acceptable approximation, the magnetisation of $La_{0.5}Sr_{1.5}MnO_4$ at 20K was also measured on a Quantum Design Physical Property Measurement System (PPMS). A comparison of the magnetisation measured with varying magnetic field applied parallel to the *c*-axis, for crystal B at 20K, 120K and 250K is shown in Fig. 4.17. This figure shows that the PPMS and MPMS do not give the same values of the magnetisation, but that they do show the same trend. The MPMS SQUID is regularly calibrated and thought to give the more reliable measurement of the magnetic field and therefore a linear extrapolation of the SQUID measurement to the applied field used for the polarised neutron experiment, is used instead of the PPMS

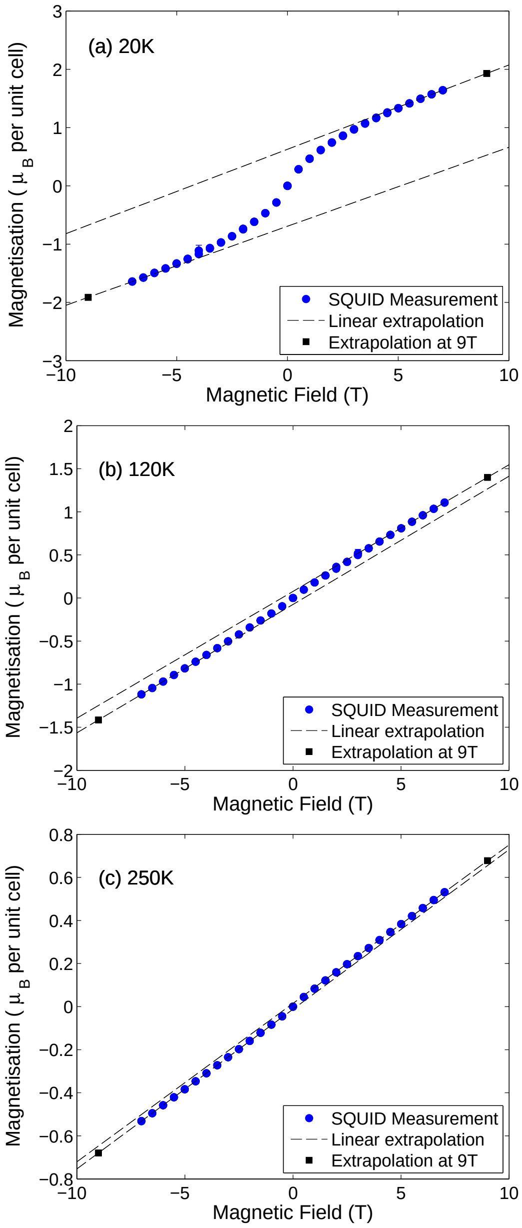

Figure 4.19: Magnetisation in Bohr magnetons per crystallographic unit cell versus applied magnetic field for crystal B at 20K (top), 120K (middle) and 250K (bottom) is shown with blue circles. The dashed lines show a linear extrapolation of the maximum (minimum) applied field measurements to 9.6T (-9.6T) marked with a black square.

measurement at the same field.

The measurement of the magnetisation in crystal A versus the magnetic field is shown for 20K, 120K and 250K in the top, middle and bottom panels, respectively, of Fig. 4.18. The equivalent measurement for crystal B are shown in Fig. 4.19. All of the figures show the linear extrapolation of the magnetic field from the maximum and minimum points in the measurement. The linear extrapolation is evaluated at the magnetic field that was applied in the polarised neutron experiment for each sample. The mean value of the magnitude of the positive and negative extrapolations is used for the results. The relevant results from these extrapolations that are to be used for the magnetic form factors are summarised in the tables 4.3 and 4.4. The results at 5T for both samples at 20K, are the average of all of the magnetisation measurement made at 5T for that sample.

Table 4.3: Summary of the magnetisation measurements on crystal A that are used as the $Q = 0$ points of the magnetic form factors presented in section 4.5.3.

Temperature (K)	Field (T)	Magnetisation (μ_B per unit cell)
20	9.6	1.185(2)
20	5.0	0.707(1)
120	9.6	1.030(2)
250	9.6	1.049(3)

Table 4.4: Summary of the magnetisation measurements on crystal B that are used as the $Q = 0$ points of the magnetic form factors presented in section 4.5.4.

Temperature (K)	Field (T)	Magnetisation (μ_B per unit cell)
20	9.0	1.921(8)
20	5.0	1.334(2)
120	9.0	1.408(3)
250	9.0	0.678(1)

4.5.2 Polarised Neutron Scattering

The polarised neutron scattering experiment was performed at the ILL, using the hot neutron diffractometer, D3. This is a two axis diffractometer and both samples were mounted on Al pins in a He-cryostat with the *c*-axis aligned parallel to the diffractometer axes. This gives a scattering plane allowing all reflections with $l = 0$. However, the detector on D3 is mounted on a lifting arm, allowing measurements to be made a few degrees above and below the $l = 0$ scattering plane. Both samples were mounted such that a magnetic field could be applied parallel to the *c*-axis. This induces a ferromagnetic moment along the c-axis and since neutrons only interact with a magnetic moment perpendicular to the scattering vector, the magnetic moment induced by the applied field is the only moment that the neutrons are sensitive to (see section 2.1.3). The instrumental setup is discussed further in section 2.3.1.

The neutrons were polarised using the (111) reflection from a Heusler crystal. The two incoming polarisation channels measured, spin up (I_+) and spin down (I_-), were set using a superconducting Nb flipper. The flipping ratio,

$$R = \frac{I_+}{I_-} = \left(\frac{F_N + F_M}{F_N - F_M}\right)^2 = \left(\frac{1+\gamma}{1-\gamma}\right)^2 \tag{4.1}$$

where F_N is the nuclear structure factor, F_M the magnetic structure factor and $\gamma = F_M/F_N$. With the detailed knowledge of F_N already obtained, F_M can calculated accurately for each peak. This is discussed in section 2.1.4.

All of the measurements were performed at a wavelength of either $\lambda = 0.825$Å or $\lambda = 0.52$Å, similar to the wavelengths used to determine the structure of both samples (precisely the same wavelengths are not available on D9 and D3). The magnetic structure factor measurements were made at three temperatures for each sample. The measurements of the magnetic phase were performed at 20K, which is below T_N and the close to maximum of the magnetisation of $La_{0.5}Sr_{1.5}MnO_4$, meaning that the magnetic moment induced parallel to the c-axis is at its maximum.

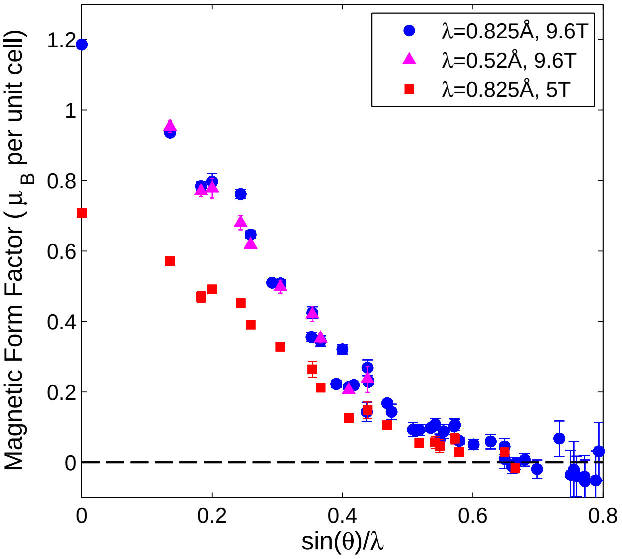

Figure 4.20: Magnetic form factor of crystal A, shown against $\sin(\theta)/\lambda$, measured at a temperature of 20K. Blue circles show the form factor measured at $\lambda = 0.825$Å with an applied magnetic field of 9.6T. Magenta triangles show the measurement at an applied magnetic field of 9.6T, but with $\lambda = 0.52$Å. The red squares show $\lambda = 0.825$Å, but with a field of 5T.

The measurements at 20K were performed at both wavelengths and at two different applied fields, 5T and 9.6T for crystal A, 5T and 9T for crystal B. By testing both values of field and wavelength, it is possible to see if the measured signal has any unexpected dependence on either one. Further measurements were performed at 120K, just above T_N, and 250K, above T_{CO-OO}. For both samples only $\lambda = 0.825$Å and an applied field of 9.6T or 9T were used at the two higher temperatures.

Peak positions are defined in $\sin(\theta)/\lambda$ and flipping ratios were only measured up to a maximum of $\sin(\theta)/\lambda = 0.8$. For each peak (h, k, l), all of the available equivalent positions $(\pm h, \pm k, \pm l)$ were measured and analysed together. The number of inequivalent peaks in each scan varies from 10 to 47.

4.5.3 The Magnetic Structure Factor for Crystal A

In total, five sets of magnetic structure factors were measured for crystal A, with the first three shown in Fig. 4.20. The blue circles in Fig. 4.20 show the full measurement of the magnetic structure factor at 9.6T and $\lambda = 0.825$Å, and in total the flipping ratios of 46 inequivalent reflections were measured. The measurement shows the expected trend for a magnetic structure factor, tending to zero at larger scattering vectors. At the largest scattering vectors $\sin(\theta)/\lambda \geq 0.7$, the quality of the measurements is quite low, due to the small values of F_M and the fact that fewer equivalent reflections were measured for these points.

It is important to check for wavelength or field dependent effects on the magnetic structure factor factor. The magenta triangles in Fig. 4.20 show the structure factor measured at 9.6T for $\lambda = 0.52$Å, where 10 inequivalent reflections were measured. It shows excellent agreement with the measurement at $\lambda = 0.825$Å, with most points matching within error bars. The only point that doesn't match is at $\sin(\theta)/\lambda = 0.244$, which corresponds to the (114) reflection. This peak was found to have very little effect on the final analysis using the maximum entropy method and was therefore left in for the final calculation. The 5T measurement (at $\lambda = 0.825$Å), with 19 inequivalent reflections, shows the same trend as the 9.6T data. It does not quite scale linearly with the 9.6T data due to the field dependence of the magnetisation, see Fig. 4.18, but there are no other remarkable features and it can be assumed that the magnitude of the magnetic field is not having any unexpected effects.

The two remaining measurements are both at 9.6T and $\lambda = 0.825$Å. The measurement at 120K, see Fig. 4.21, shows 37 inequivalent reflections and the measurement at 250K, see Fig. 4.22, shows 36 inequivalent reflections. Both sets of magnetic

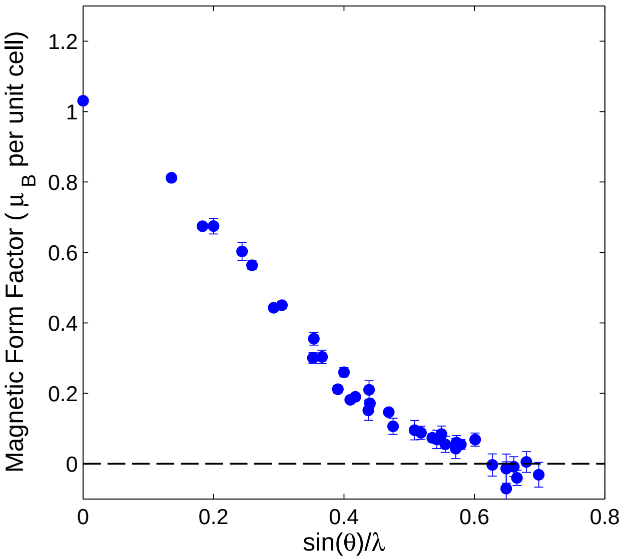

Figure 4.21: Magnetic form factor of crystal A, shown against $\sin(\theta)/\lambda$, measured with $\lambda = 0.825$Å, with an applied magnetic field of 9.6T at a temperature of 120K.

structure factors show the same expected trend, of tending to zero at large scattering vectors. At 250K, the distribution of points, particularly at low $\sin(\theta)/\lambda$, appears to be smoother, which suggests there is less variation in the structure. This is expected with $250K \gg T_N$.

4.5.4 The Magnetic Structure Factor for Crystal B

Five magnetic structure factors of crystal B have also been measured. The first three were measured at a temperature of 20K, with 47 inequivalent reflections measured with a magnetic field of 9T and a wavelength of $\lambda = 0.825$Å, 19 inequivalent reflections with a different wavelength of $\lambda = 0.52$Å and 7 inequivalent reflections with $\lambda = 0.825$Å and an applied field of 5T, all of which are shown in Fig. 4.23. Comparing the two measurements at 9T, but different wavelengths, it is clear that there is some disagreement in the results. These are all shown in Fig. 4.23. This is not surprising based on the poor structural fits that were obtained on this sample and is a further indication that this dataset is of quite low quality. The 5T data,

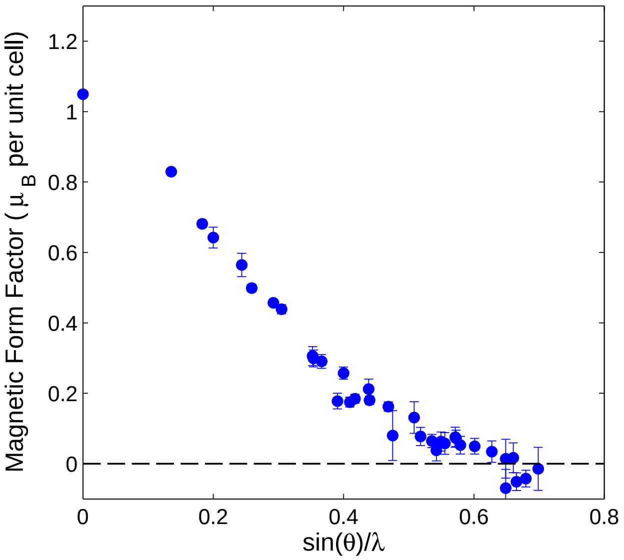

Figure 4.22: Magnetic form factor of crystal A, shown against $\sin(\theta)/\lambda$, measured with $\lambda = 0.825$Å, with an applied magnetic field of 9.6T at a temperature of 250K.

particularly at higher $\sin(\theta)/\lambda$ has an F_M that is almost as large as that from the 9T data, a surprising result given that the induced magnetisation should be larger in the 9T data. Other than this, the presented form factors all show a similar trend, tending to zero for high **Q**.

The two higher temperature measurements were both made with an applied magnetic field of 9T and a wavelength of $\lambda = 0.825$Å. The measurement at 120K has 34 inequivalent reflections (Fig. 4.24) and the measurement at 250K has 33 inequivalent reflections (Fig. 4.25). In the 250K data there is one particularly poor point that disagrees with the overall trend, at $\sin(\theta)/\lambda \sim 0.45$, this point is removed for the next stage of the analysis.

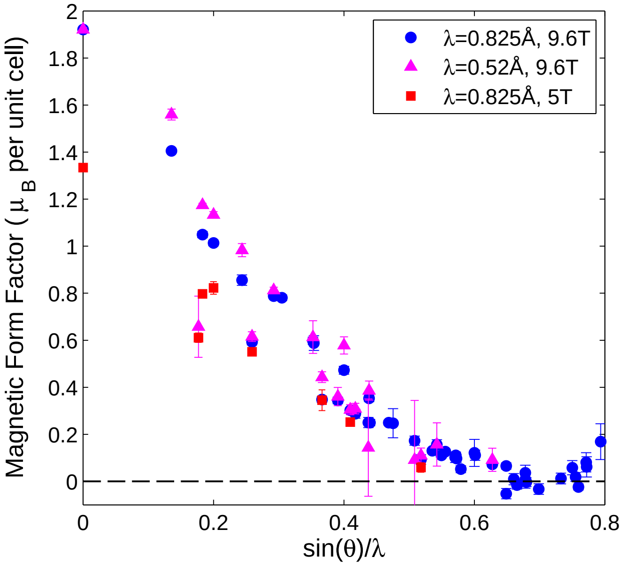

Figure 4.23: Magnetic form factor of crystal B, shown against $\sin(\theta)/\lambda$, measured at a temperature of 20K. Blue circles show the form factor measured at $\lambda = 0.825$Å with an applied magnetic field of 9.6T. Magneto triangles show the measurement at an applied magnetic field of 9.6T, but with $\lambda = 0.52$Å. The red squares show $\lambda = 0.825$Å, but with a field of 5T.

4.6 The Maximum Entropy Method for Analysing Magnetic Structure Factors in $La_xSr_{2-x}MnO_4$

To obtain the magnetisation distribution in the two samples has to be determined by analysing the results of the measurements described in the previous section. Only the $z-$component of the magnetic structure factor was measured and therefore the analysis techniques will only give the $z-$component of the magnetisation distribution.

The magnetic structure factor ($\mathbf{F_M}(\mathbf{Q})$) is the Fourier transform of the magnetisation distribution ($\mathbf{M}(\mathbf{r})$) and can be calculated directly by this method.[92] However, this method has a few problems, such as being limited to only centric structures, being unable to measure $\mathbf{F_M}$ to infinite $\mathbf{Q}$ (this leads to spurious features in the Fourier transform). Another problem is this method's poor way of

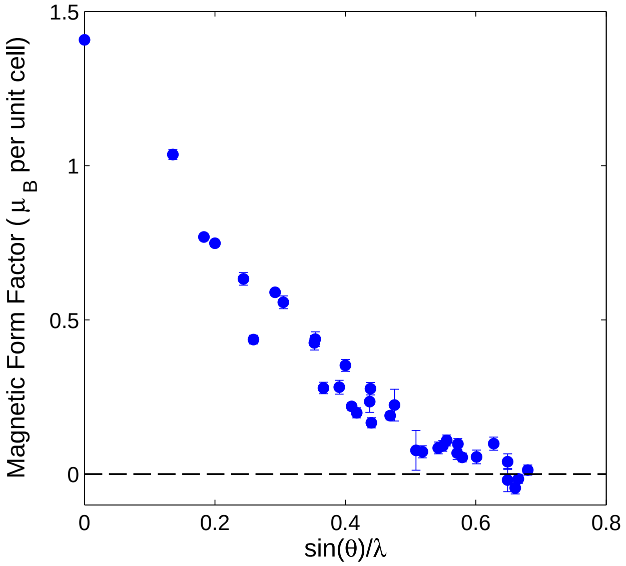

Figure 4.24: Magnetic form factor of crystal B, shown against sin(θ)/λ, measured with $\lambda = 0.825$Å, with an applied magnetic field of 9.6T at a temperature of 120K.

handling probabilities or experimental errors (the Fourier transform is direct, without any consideration of whether it is physically realistic).[40]

An alternative method that overcomes these issues is the maximum entropy method, which is often referred to as MaxEnt or MEM. This works by using Bayesian statistics to find the most probable magnetisation distribution given the data. It treats the magnetisation distribution in discrete cells in a similar way to how Boltzmann treated phase space when establishing the most likely distribution of particles. The maximum entropy method puts density in cells, labeled i, so that it maximises an entropy function $S = -\sum_i p_i ln p_i$ and suitably describes a Fourier transform of the magnetic form factor. Thus the most likely magnetisation density distribution can be found without worrying about the problems of a direct Fourier transform. An important feature of the maximum entropy method is that, like a direct Fourier transform, it is independent of the crystal structure. Therefore it places magnetic moment anywhere in the unit cell, based solely on the statistical

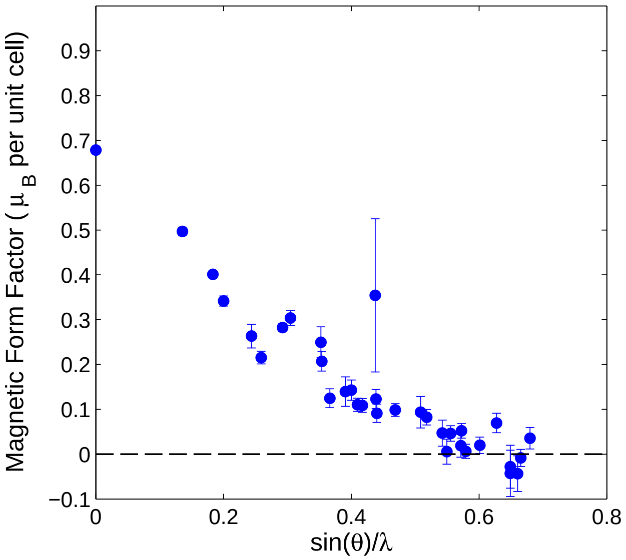

Figure 4.25: Magnetic form factor of crystal B, shown against $\sin(\theta)/\lambda$, measured with $\lambda = 0.825\text{Å}$, with an applied magnetic field of 9.6T at a temperature of 250K.

likelihood of it being there, not the physical likelihood. This method is well documented since its development for polarised neutron scattering in the early 1990's[84] and had proved to be successful in NMR spectroscopy and astronomy.[93] The precise method used in this study was developed by A. Markvardsen[94] and was used to determine the magnetisation density distribution in $PrBa_2Cu_3O_{6+x}$.[95]

Table 4.5: Summary of the important sites in the magnetisation density distribution produces by the maximum entropy method analysis. There are a number of equivalent sites based on the tetragonal body centred $I4/mmm$ symmetry of the crystal structure. The x, y and z columns give the relative distance along the a, b and c columns

Site	Ion	x	y	z
A	Mn	0	0	0
B	La/Sr	0	0	0.4
C	O(2)	0	0	0.25
D	-	0.5	0.5	0
E	O(1)	0	0.5	0

The magnetisation distribution of crystals A and B found by the maximum entropy method has some interesting and unexpected features. These features will

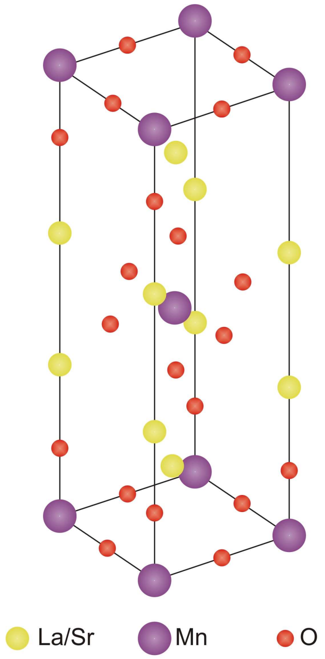

Figure 4.26: The crystal structure of $La_{0.5}Sr_{1.5}MnO_4$ showing only the positions of the ions, with the La/Sr site shown in yellow, the Mn site shown in purple and the O site in red. This is useful as a reference for analysing the results of the maximum entropy method analysis.

be discussed for each data set in the order of decreasing magnitude of magnetic moment. Sites of interest are labeled with letters for the first results analysed and then discussed for all of the results in later sections. As a summary, the sites of interest are listed in the table 4.5, along with the ion positioned closest to that point in the real unit cell. These ion position can be seen in Fig. 4.26. It is useful to compare the magnetisation distribution presented to this simple crystal structure showing the locations of the centre of the ions.

4.7 Magnetisation Distribution in $La_xSr_{2-x}MnO_4$

For each material and temperature, the maximum entropy method results are presented in two ways. Firstly, a 2D-slice of the magnetisation density in the MnO_2 plane is shown in Fig. 4.27. In these figures, blue represents positive magnetisa-

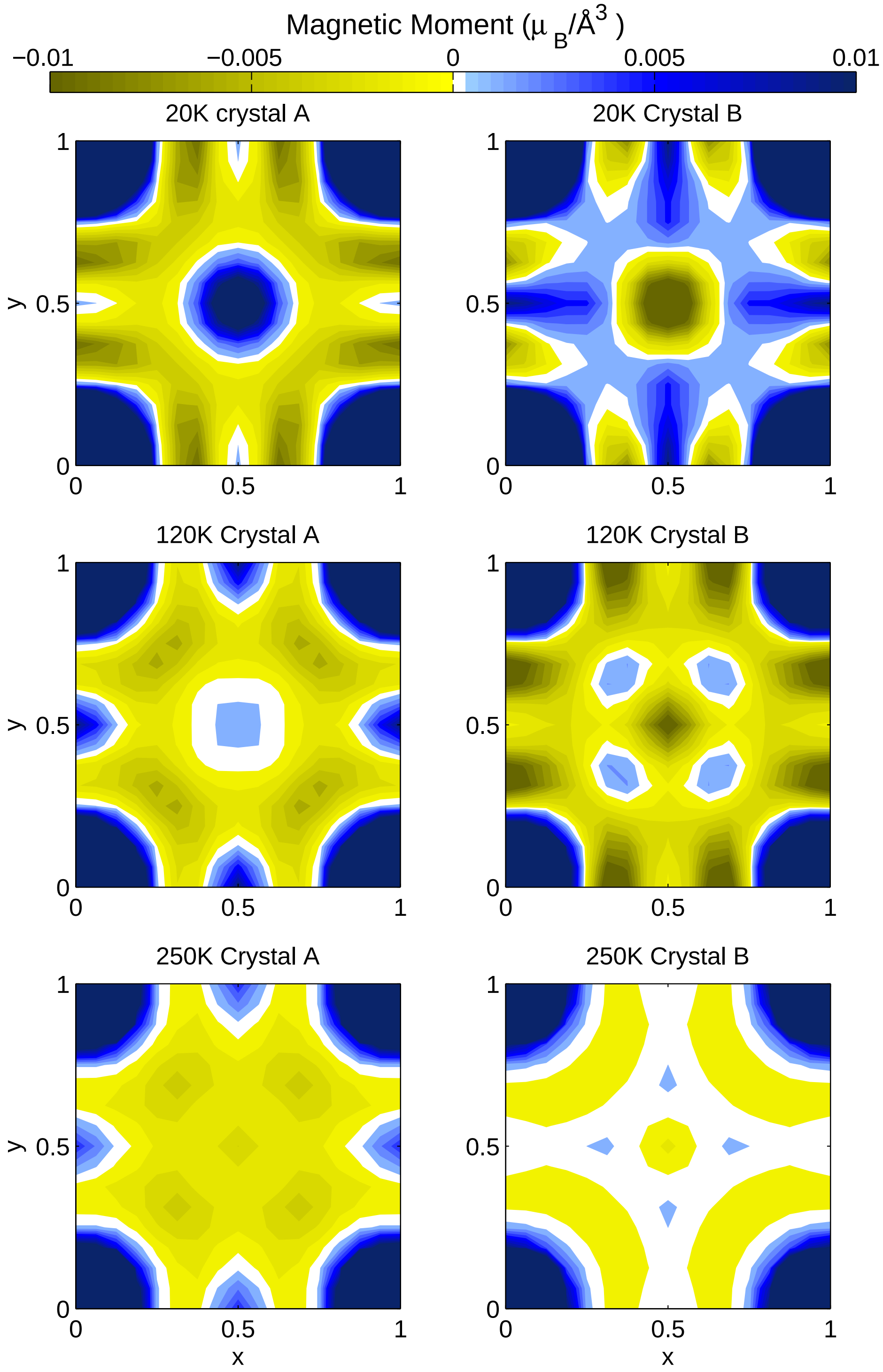

Figure 4.27: 2D contour maps of the magnetisation distribution in the MnO_2 plane for crystal A (left column) and crystal B (right column). The top row are the results at 20K, the middle shows 120K and the bottom 250K. Blue areas show positive magnetic moment, whereas yellow shows negative and white zero. The moment is largely positive in the MnO_2 plane and the most positive value shown has been capped at approximately the same magnitude as the largest negative moment. The large magnetic moments in the corners of each panel are the Mn ions and the in-plane O ion lies directly between two Mn ions, halfway along each edge of the square.

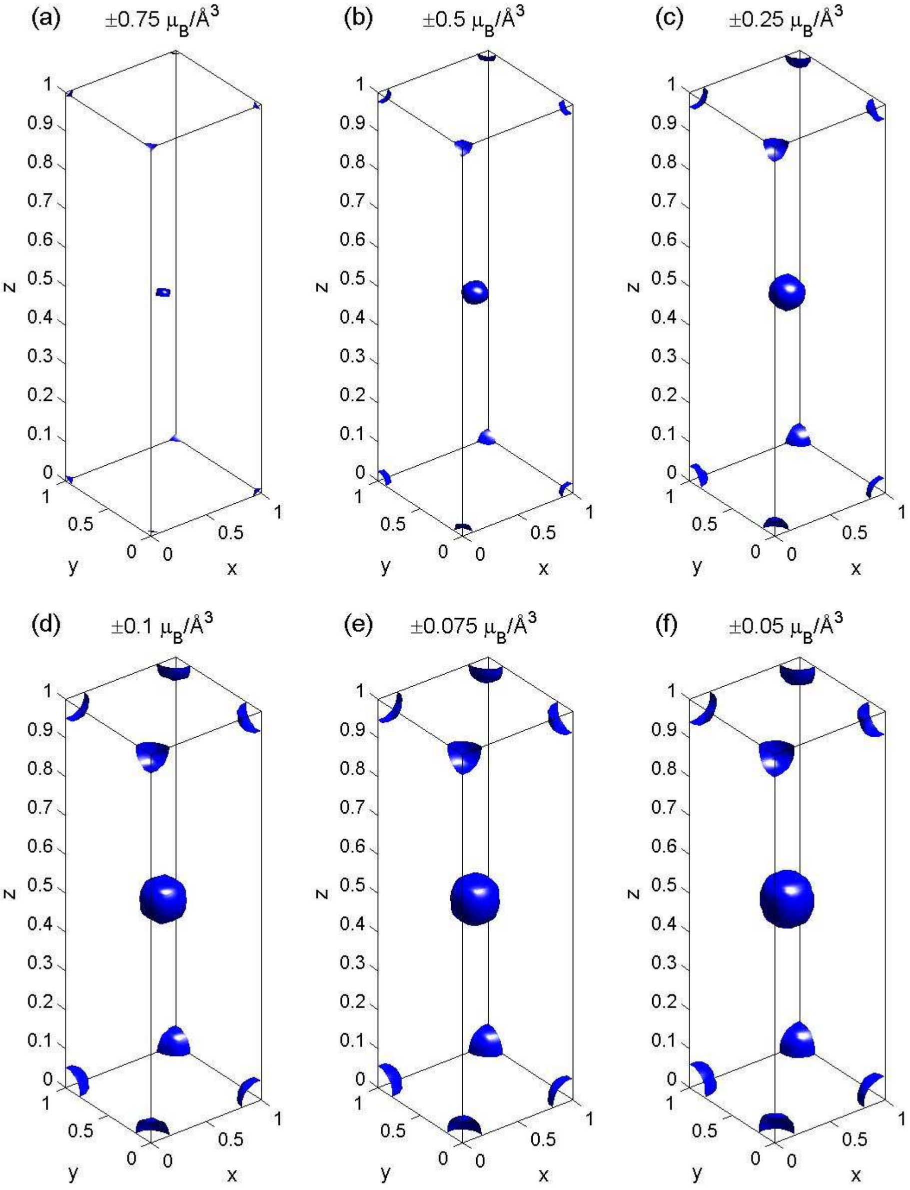

Figure 4.28: 3D contours of the magnetisation distribution in the structural unit cell of crystal A at 20K, with a magnetic field of 9.6T applied along the c-axis. The positive contour is shown in blue and the negative contour in yellow for each plot. The contours shown in each of the figures are as follows, (a) $\pm 0.75\mu_{\mathrm{B}}/\mathring{\mathrm{A}}^3$, (b) $\pm 0.5\mu_{\mathrm{B}}/\mathring{\mathrm{A}}^3$, (c) $\pm 0.25\mu_{\mathrm{B}}/\mathring{\mathrm{A}}^3$, (d) $\pm 0.1\mu_{\mathrm{B}}/\mathring{\mathrm{A}}^3$, (e) $\pm 0.075\mu_{\mathrm{B}}/\mathring{\mathrm{A}}^3$ and (f) $\pm 0.05\mu_{\mathrm{B}}/\mathring{\mathrm{A}}^3$.

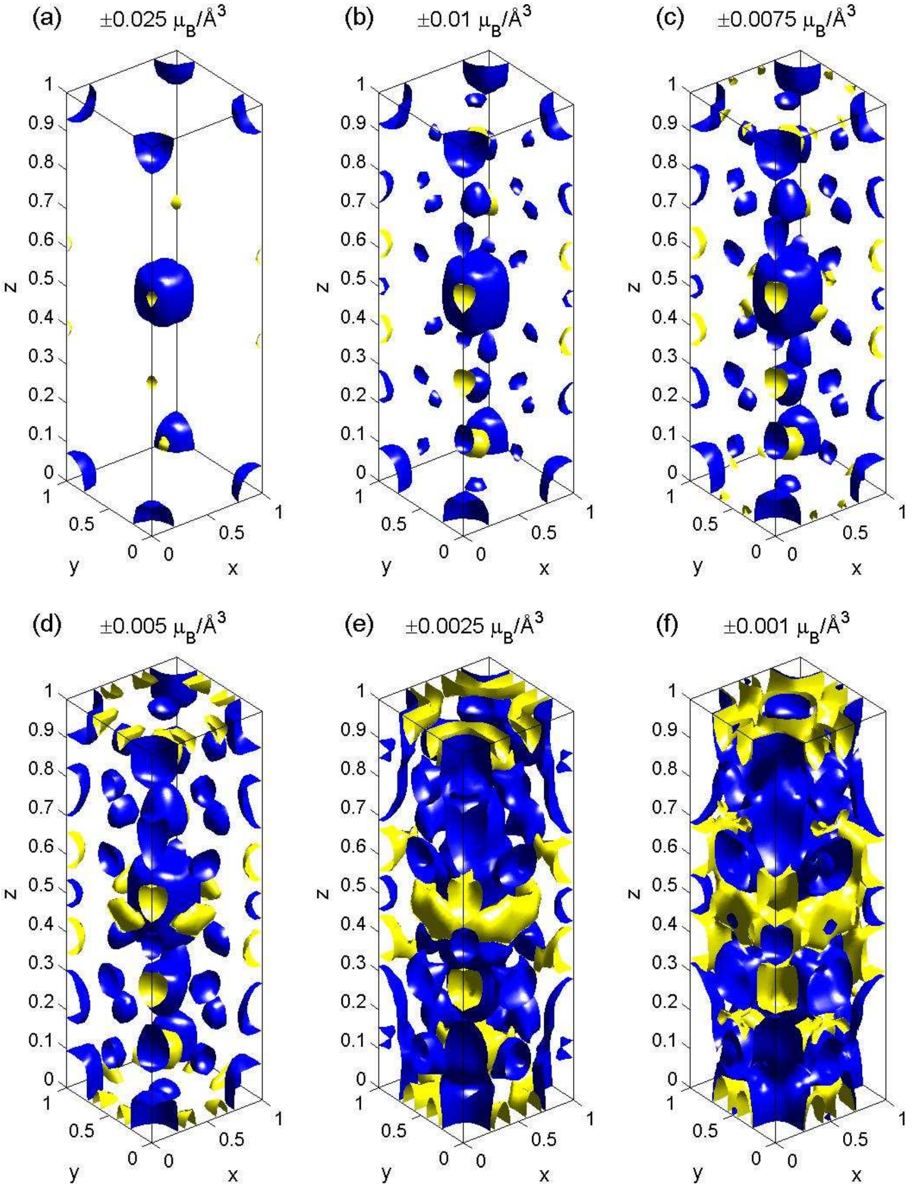

Figure 4.29: 3D contours of the magnetisation distribution in the structural unit cell of crystal A at 20K, with a magnetic field of 9.6T applied along the c-axis. The positive contour is shown in blue and the negative contour in yellow for each plot. The contours shown in each of the figures are as follows, (a) $\pm 0.025\mu_B/\text{Å}^3$, (b) $\pm 0.01\mu_B/\text{Å}^3$, (c) $\pm 0.0075\mu_B/\text{Å}^3$, (d) $\pm 0.005\mu_B/\text{Å}^3$, (e) $\pm 0.0025\mu_B/\text{Å}^3$ and (f) $\pm 0.001\mu_B/\text{Å}^3$.

tion and yellow represents negative magnetisation. Plots of the 3D magnetisation distribution are presented separately for each material and temperature in figures 4.28-4.39. Each of the images shows different pairs of contours of equal magnitude and opposite alignment, blue contours showing the positive magnetisation and the yellow contours showing the negative magnetisation. Each image shows one unit cell and the axes show the relative distance along that crystallographic direction. It is useful to refer to the crystal structure shown in Fig. 4.26 as a guide to understanding all of the 3D contour maps. The $z = 0$ plane in the 3D images corresponds to the 2D contour maps in Fig. 4.27

4.7.1 Magnetisation Distribution in Crystal A

The results at 20K, $\lambda = 0.825$Å and an applied field of 9.6T are shown with 3D contour maps of the unit cell of $La_{0.5}Sr_{1.5}MnO_4$ in figures 4.28 and 4.29. The top left panel of Fig. 4.27 shows the magnetisation in the MnO_2 plane.

The most magnetic features are the Mn ions, at $(0, 0, 0)$ and $(1/2, 1/2, 1/2)$, labeled as site A, which are the only features that show a magnetic moment greater than $\pm 0.75\mu_B/\text{Å}^3$, shown in Fig. 4.28(a). The first unexpected feature is the next strongest, which is the negative feature appearing with greater than $\pm 0.025\mu_B/\text{Å}^3$, shown in Fig. 4.29(a). This is in the location of the La/Sr ions near $(0, 0, 0.4)$ and $(0.5, 0.5, 0.1)$, labeled site B. There is no reason to expect a magnetic moment on the La/Sr site, since both ions are in a non-magnetic state, with all of the electrons being paired.

The next contour at $\pm 0.01\mu_B/\text{Å}^3$, Fig. 4.29(b) shows two features not observed in the higher contours. At approximately $(0, 0, 0.25)$ and equivalent positions, site C, there is a positive moment which is close to the site of the O ion that does not lie in the MnO_2 plane, and is the top or bottom ion in the MnO_6 octahedra. The other feature that appears in this figure cannot be attributed to any of the ions in the material. This is the $(1/2, 1/2, 0)$ position (and all of its equivalent positions), site D.

However, when examining the next contour at $\pm 0.0075\mu_B/\text{Å}^3$, Fig. 4.29(c), there is a noticeable negative magnetic moment close to the in-plane O site in the form of two small lobes centred on the $(0, 0.5, 0)$ position, site E. These are perhaps even more telling at $\pm 0.005\mu_B/\text{Å}^3$, Fig. 4.29(d), and look similar to the O *p*-orbital shape calculated by Ferrari et al.[63] and shown in Fig. 4.2. Below this contour level, the volumes of positive and negative magnetic moment merge into each other, thus creating a ring of negative moment around the Mn site, which can be observed in the 2D contour map, Fig. 4.27. It is important to remember that the magnetic unit cell has been averaged into the structural unit cell and therefore if there is a magnetic moment on the in-plane O site, it would appear at all positions in the structural unit cell.

The results for the 120K data ($\lambda = 0.825\text{Å}$ and $B = 9.6\text{T}$) are presented in the 3D contour plots shown in figures 4.30 and 4.31. The magnetic moment at site A does not appear until the $\pm 0.5\mu_B/\text{Å}^3$, Fig. 4.28(b), suggesting that it is smaller at this temperature than at 20K. The shape of the feature at site A is also different from the lower temperature data, apparent in Fig. 4.29(b), as it appears to be stretched along the c-axis. A negative moment is again observed at site B and at site C there is a positive moment, which overlaps with the one at site A.

In contrast to the 20K data, the next highest moment feature is at site E and seen in Fig. 4.29(c). Here there is a small positive moment, but this appears to be surrounded by a negative moment, see Fig. 4.29(e) and (f). It has a smaller magnitude than at 20K, but a similar shape. By comparing the 2D contour maps in Fig. 4.27 it is apparent that the strongest in-plane negative magnetic feature lies between two O sites, near the point (0.25,0.25,0). Another difference between the two different temperatures is the lack of any significant moment at site D.

Finally for crystal A, the results for the 250K data are presented in the 3D contour plots shown in figures 4.32 and 4.33. Again the positive feature at site A is the largest moment, with a similar magnitude to the feature observed at 120K. This feature is even more distorted from spherical at this temperature, than at lower temperatures. The features at site A and site C also overlap more than at the lower temperatures. The feature at site B is apparent at roughly the same magnitude as the lower temperature results. Finally, there is very little observed moment at sites D and E, as seen in Fig. 4.27.

4.7.2 Magnetisation Distribution in Crystal B

The results of the flipping ratios experiment on crystal B seemed to be unreliable, but nonetheless they have been analysed using the maximum entropy method to try to give some context to the results on crystal A, at least qualitatively. The results of this analysis for the data measured at 20K, with an applied field of 9T and $\lambda = 0.837$Å is shown in Fig. 4.34 and Fig. 4.35.

The feature with the largest magnetic moment in this case is again the Mn ion at site A (Fig. 4.34(a)), although the size of the moment is larger here, compared to that in crystal A. This is expected given the magnetisation measurements on both samples. The next feature that is apparent is the negative moment on site B (Fig. 4.35(a)), in agreement with the results on crystal A. The next most prominent feature is located along the *c*-axis from site E (Fig. 4.35(b)), where a negative moment is observed. In contrast to the crystal A results, the moment observed at site D is now observed to be negative, Fig. 4.34(b). At the lower contour levels it becomes difficult to draw any further conclusions due to the large number of

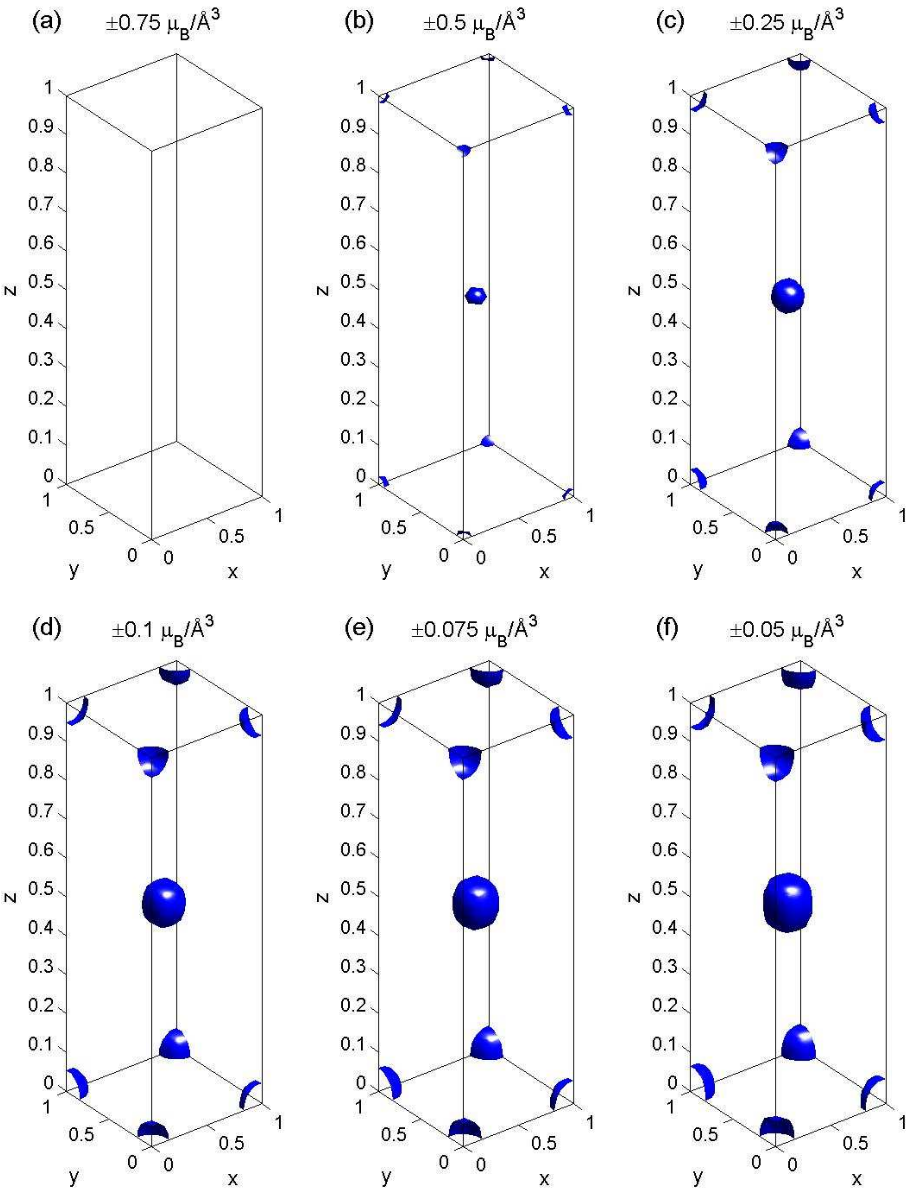

Figure 4.30: 3D contours of the magnetisation distribution in the structural unit cell of crystal A at 120K, with a magnetic field of 9.6T applied along the c-axis. The positive contour is shown in blue and the negative contour in yellow for each plot. The contours shown in each of the figures are as follows, (a) $\pm 0.75\mu_{\mathrm{B}}/\mathrm{\AA}^3$, (b) $\pm 0.5\mu_{\mathrm{B}}/\mathrm{\AA}^3$, (c) $\pm 0.25\mu_{\mathrm{B}}/\mathrm{\AA}^3$, (d) $\pm 0.1\mu_{\mathrm{B}}/\mathrm{\AA}^3$, (e) $\pm 0.075\mu_{\mathrm{B}}/\mathrm{\AA}^3$ and (f) $\pm 0.05\mu_{\mathrm{B}}/\mathrm{\AA}^3$.

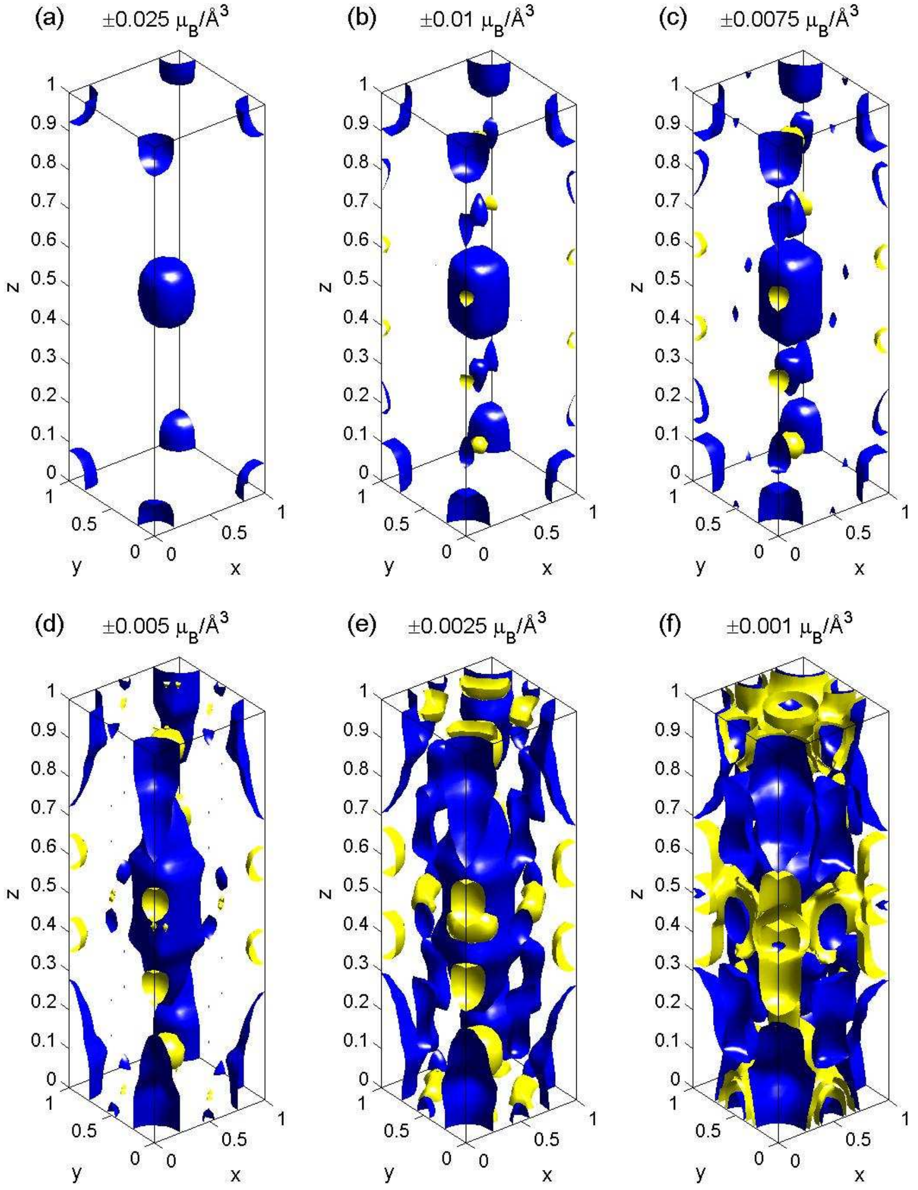

Figure 4.31: 3D contours of the magnetisation distribution in the structural unit cell of crystal A at 120K, with a magnetic field of 9.6T applied along the c-axis. The positive contour is shown in blue and the negative contour in yellow for each plot. The contours shown in each of the figures are as follows, (a) $\pm 0.025\mu_{\mathrm{B}}/\text{Å}^3$, (b) $\pm 0.01\mu_{\mathrm{B}}/\text{Å}^3$, (c) $\pm 0.0075\mu_{\mathrm{B}}/\text{Å}^3$, (d) $\pm 0.005\mu_{\mathrm{B}}/\text{Å}^3$, (e) $\pm 0.0025\mu_{\mathrm{B}}/\text{Å}^3$ and (f) $\pm 0.001\mu_{\mathrm{B}}/\text{Å}^3$.

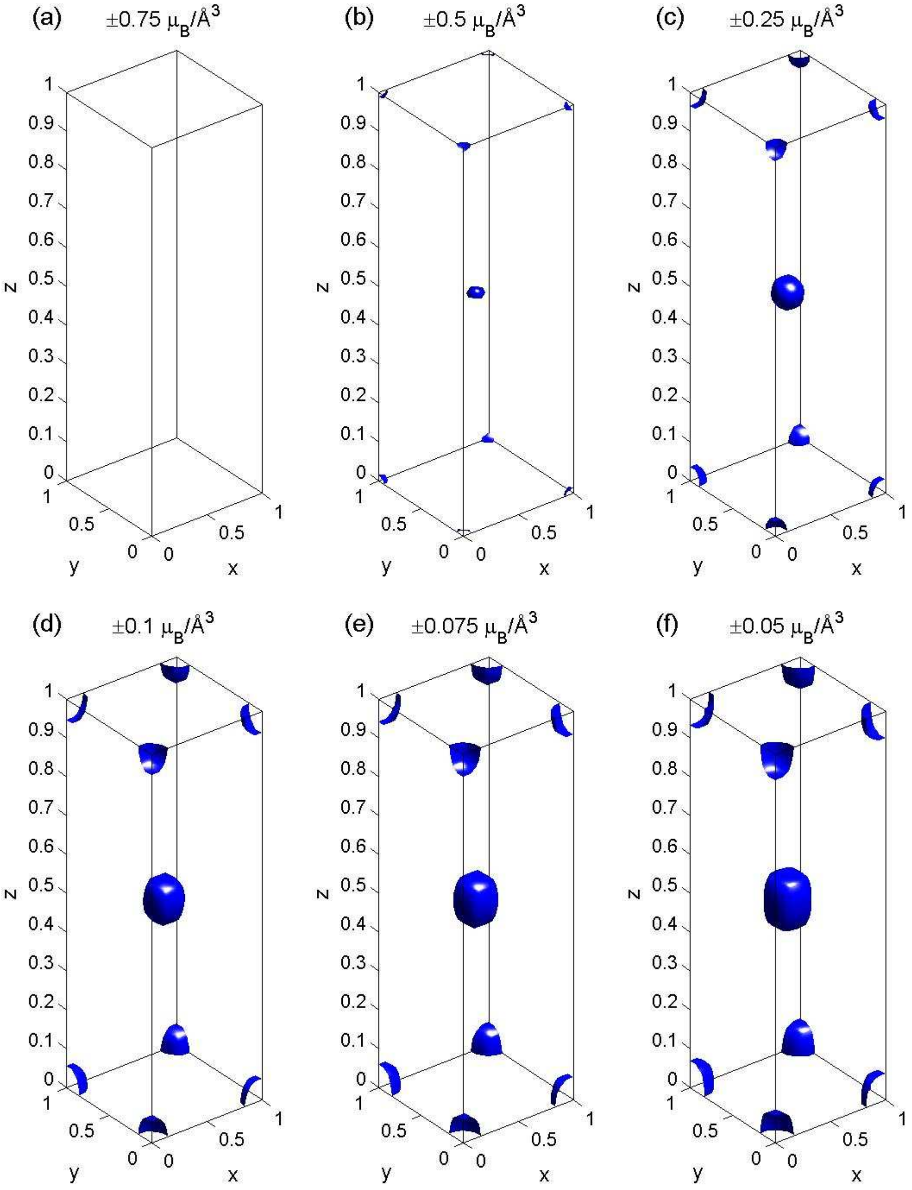

Figure 4.32: 3D contours of the magnetisation distribution in the structural unit cell of crystal A at 250K, with a magnetic field of 9.6T applied along the c-axis. The positive contour is shown in blue and the negative contour in yellow for each plot. The contours shown in each of the figures are as follows, (a) $\pm 0.75\mu_{\rm B}/\text{Å}^3$, (b) $\pm 0.5\mu_{\rm B}/\text{Å}^3$, (c) $\pm 0.25\mu_{\rm B}/\text{Å}^3$, (d) $\pm 0.1\mu_{\rm B}/\text{Å}^3$, (d) $\pm 0.075\mu_{\rm B}/\text{Å}^3$ and (f) $\pm 0.05\mu_{\rm B}/\text{Å}^3$.

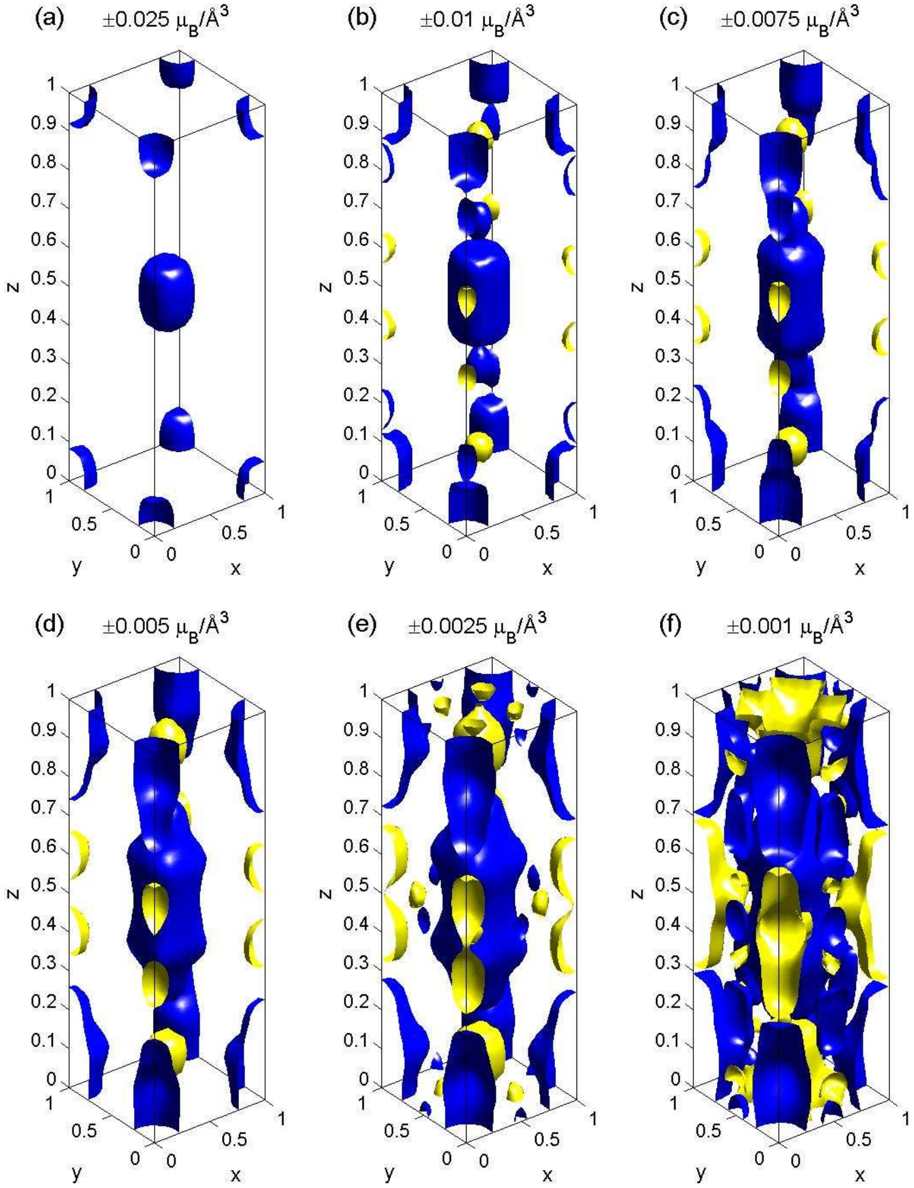

Figure 4.33: 3D contours of the magnetisation distribution in the structural unit cell of crystal A at 250K, with a magnetic field of 9.6T applied along the c-axis. The positive contour is shown in blue and the negative contour in yellow for each plot. The contours shown in each of the figures are as follows, (a) $\pm0.025\mu_B/\text{Å}^3$, (b) $\pm0.01\mu_B/\text{Å}^3$, (c) $\pm0.0075\mu_B/\text{Å}^3$, (d) $\pm0.005\mu_B/\text{Å}^3$, (e) $\pm0.0025\mu_B/\text{Å}^3$ and (f) $\pm0.001\mu_B/\text{Å}^3$.

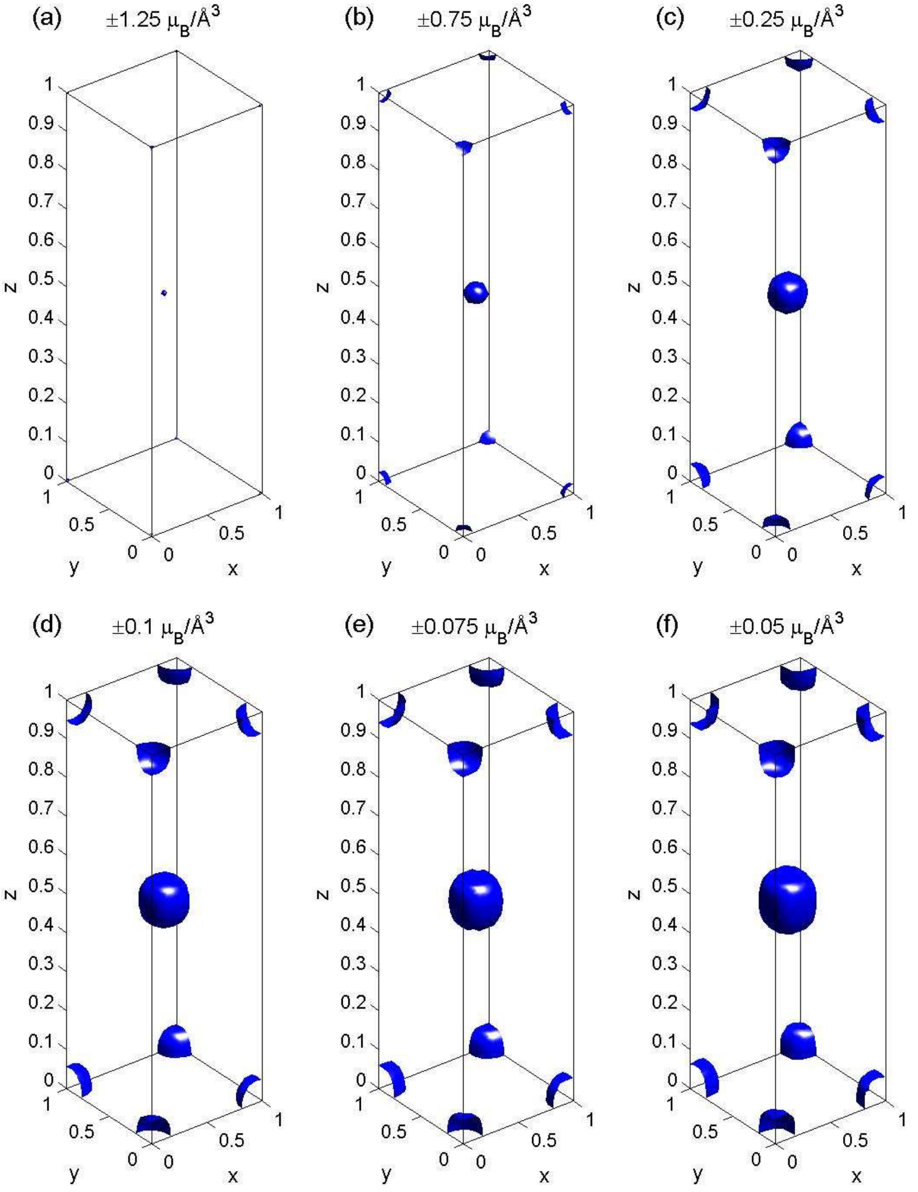

Figure 4.34: 3D contours of the magnetisation distribution in the structural unit cell of crystal B at 20K, with a magnetic field of 9T applied along the c-axis. The positive contour is shown in blue and the negative contour in yellow for each plot. The contours shown in each of the figures are as follows, (a) $\pm 1.25\mu_B/\text{Å}^3$, (b) $\pm 0.75\mu_B/\text{Å}^3$, (c) $\pm 0.25\mu_B/\text{Å}^3$, (d) $\pm 0.1\mu_B/\text{Å}^3$, (e) $\pm 0.075\mu_B/\text{Å}^3$ and (f) $\pm 0.05\mu_B/\text{Å}^3$.

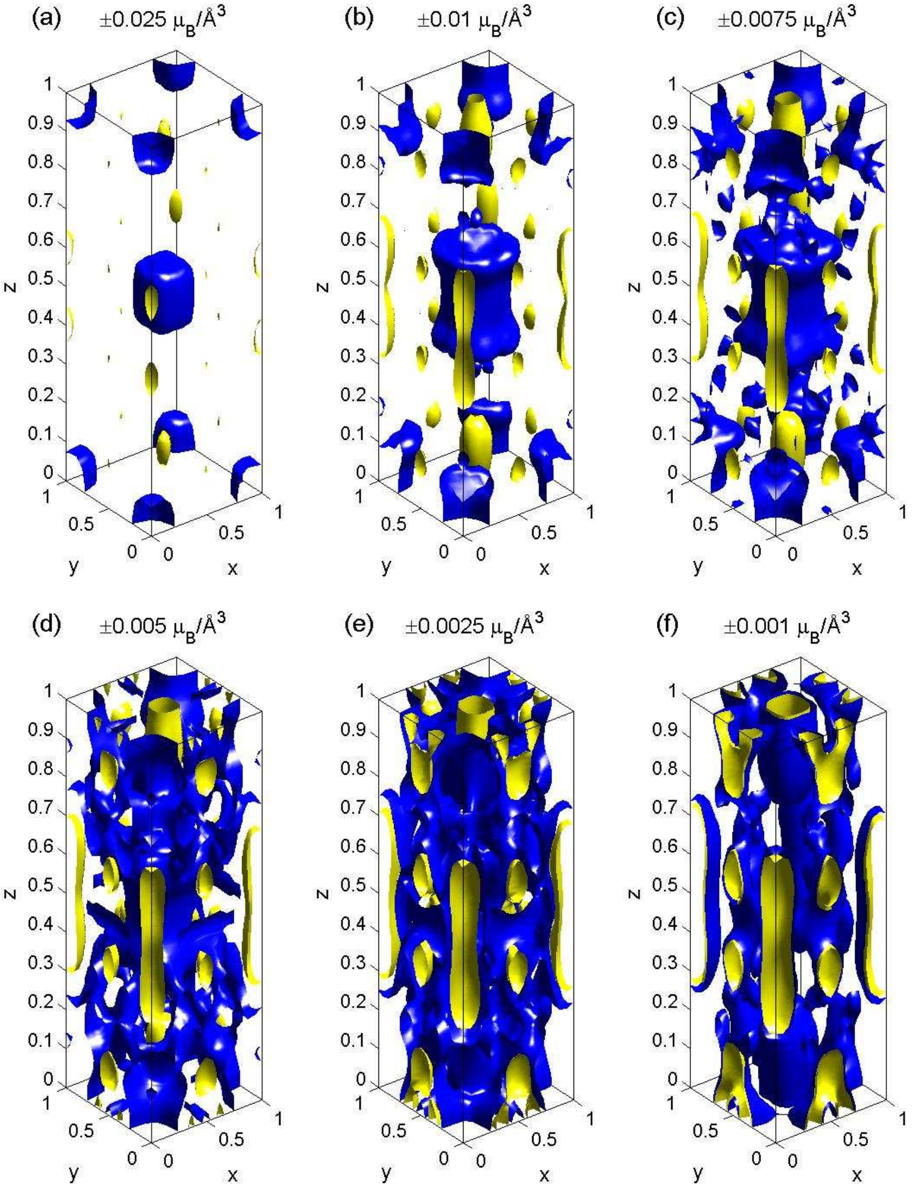

Figure 4.35: 3D contours of the magnetisation distribution in the structural unit cell of crystal B at 20K, with a magnetic field of 9T applied along the c-axis. The positive contour is shown in blue and the negative contour in yellow for each plot. The contours shown in each of the figures are as follows, (a) $\pm0.025\mu_B/\text{Å}^3$, (b) $\pm0.01\mu_B/\text{Å}^3$, (c) $\pm0.0075\mu_B/\text{Å}^3$, (d) $\pm0.005\mu_B/\text{Å}^3$, (e) $\pm0.0025\mu_B/\text{Å}^3$ and (f) $\pm0.001\mu_B/\text{Å}^3$.

features, although it can be seen that a positive moment exists at site C and that the shape of the negative feature at site E is similar to that observed in crystal A. The shape of the lobes near site E is clearly seen in 4.27.

The results of the 120K data, Fig. 4.36 and 4.37, are slightly different from the other results. The largest feature is again at the Mn site, Fig. 4.36(a), but the moment is not as large as that observed at 20K. The moment at site B seems to extend between two equivalent sites, see Fig. 4.37(b), and when looking at the smaller contours the overall character of the unit cell seems to show negative moments whereas all of the other sets of results point to a mainly positive magnetic moment within the unit cell. Overall the cell is of course positive due to the large moment on site A, but more of the pixels appear to have negative moments. The mainly negative unit cell is unexpected as it is intuitive to assume that most of the unit cell will display a magnetisation aligned with the applied magnetic field. The only positive site other than site A is site C. At site E, the moment is again negative and shows a similar shape to that observed in the other sets of results, see Fig. 4.37(e). It is clear from Fig. 4.27 that the moment at site E is stronger in these results than in any of the others, which is probably a sign of the poor quality of the data.

The final data analysed is the 250K measurement of crystal B, shown in Fig. 4.38 and 4.39. The moment at site A, is again the most prominent feature but is much smaller than in all of the other datasets, not appearing until a contour level of $0.25\mu_B/\text{Å}^3$, Fig. 4.38(c). At lower contour levels the results are qualitatively similar to those found for crystal A at 250K, compare Fig. 4.33 and Fig. 4.39. Site B is negative in both sets of results, as is the small feature above site E. Site C is also positive in both of the 250K results and displays a similar shape, although the shape is slightly smoother in the results for crystal A, perhaps an indication of the better quality data for sample A. The magnetisation in the MnO_2 plane for this set of results, see Fig. 4.27 is almost featureless away from the Mn ions, as expected above T_N/T_{CO-OO}.

4.8 Magnetic Moments in $La_xSr_{2-x}MnO_4$

The maximum entropy method code employed here gives a full 3D picture of the distribution of the magnetisation density and it is possible to use the results to determine the magnetic moment that can be attributed to each site in the unit cell. To do this, moments contained within a sphere of a suitable radii are summed. The ionic radii most commonly used in the literature are those summarised by Shannon et al.[96] with values adapted from this paper used by Tokura in the discussion of colossal magnetoresistive manganites.[10] In this study the Shannon radii are taken as follows, 0.7Å for Mn, 1.4Å for O and 1.42Å for La/Sr (this final radius is the weighted sum of the two ions' radii).

However, the maximum entropy method is thought to underestimate the moment placed on any ionic site in its attempt to create a smoothly varying distribution. As an example of this it is useful to compare the magnetic moment of a unit cell by a SQUID measurement and comparing it to the sum of all of the moments in the maximum entropy method unit cell. The SQUID measurement at 20K on crystal A gives a magnetic moment of $1.185\mu_B$, whereas the sum from the maximum entropy analysis for 20K on crystal A is $1.064\mu_B$, a significant difference indicating the degree to which the maximum entropy method underestimates the magnetisation. The Shannon radii clearly assumes a sphere, which also has two problems. It is apparent from the figures of the 3D contours that the areas of magnetic moment are not necessarily spherical. The second problem is that the spheres in some cases overlap, for example a Shannon Mn diameter plus an O diameter is greater than

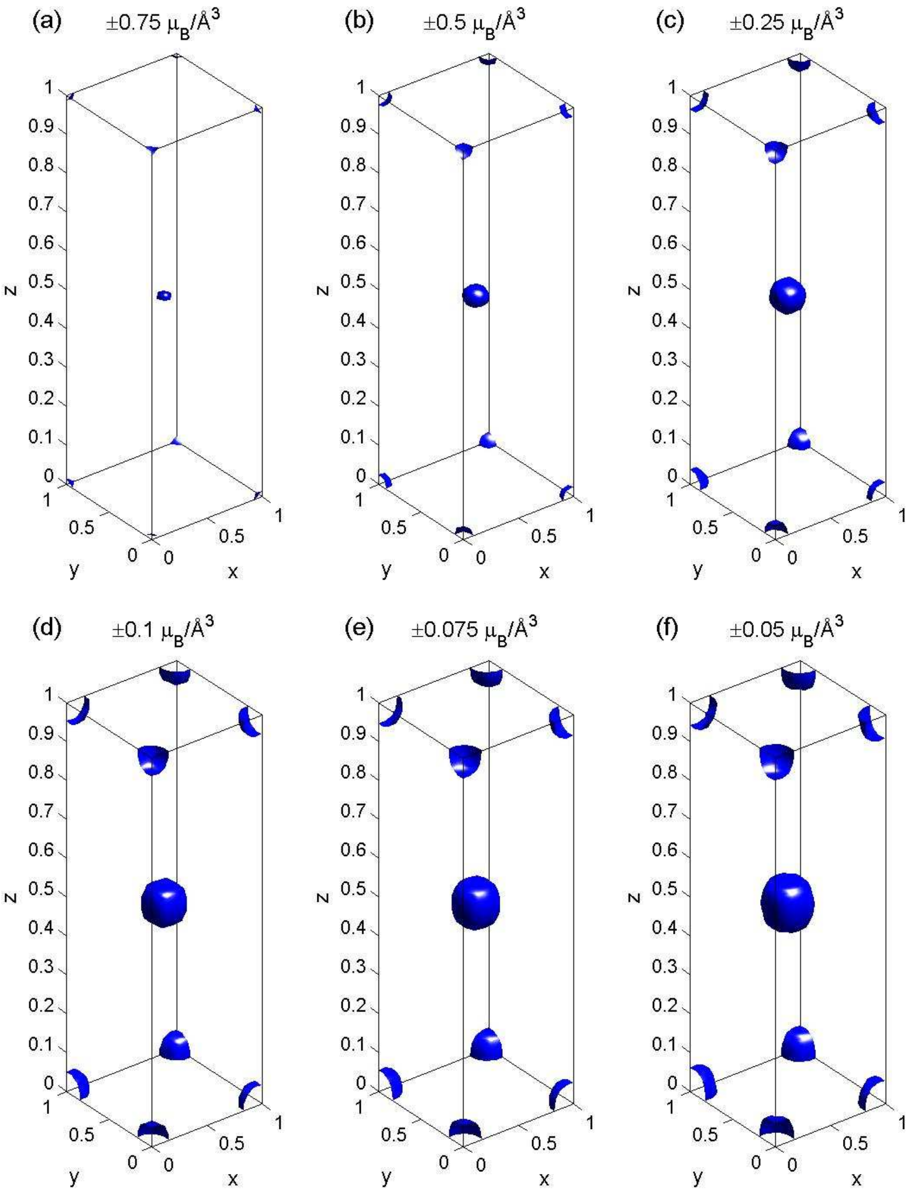

Figure 4.36: 3D contours of the magnetisation distribution in the structural unit cell of crystal B at 120K, with a magnetic field of 9T applied along the c-axis. The positive contour is shown in blue and the negative contour in yellow for each plot. The contours shown in each of the figures are as follows, (a) $\pm 0.75\mu_B/Å^3$, (b) $\pm 0.5\mu_B/Å^3$, (c) $\pm 0.25\mu_B/Å^3$, (d) $\pm 0.1\mu_B/Å^3$, (e) $\pm 0.075\mu_B/Å^3$ and (f) $\pm 0.05\mu_B/Å^3$.

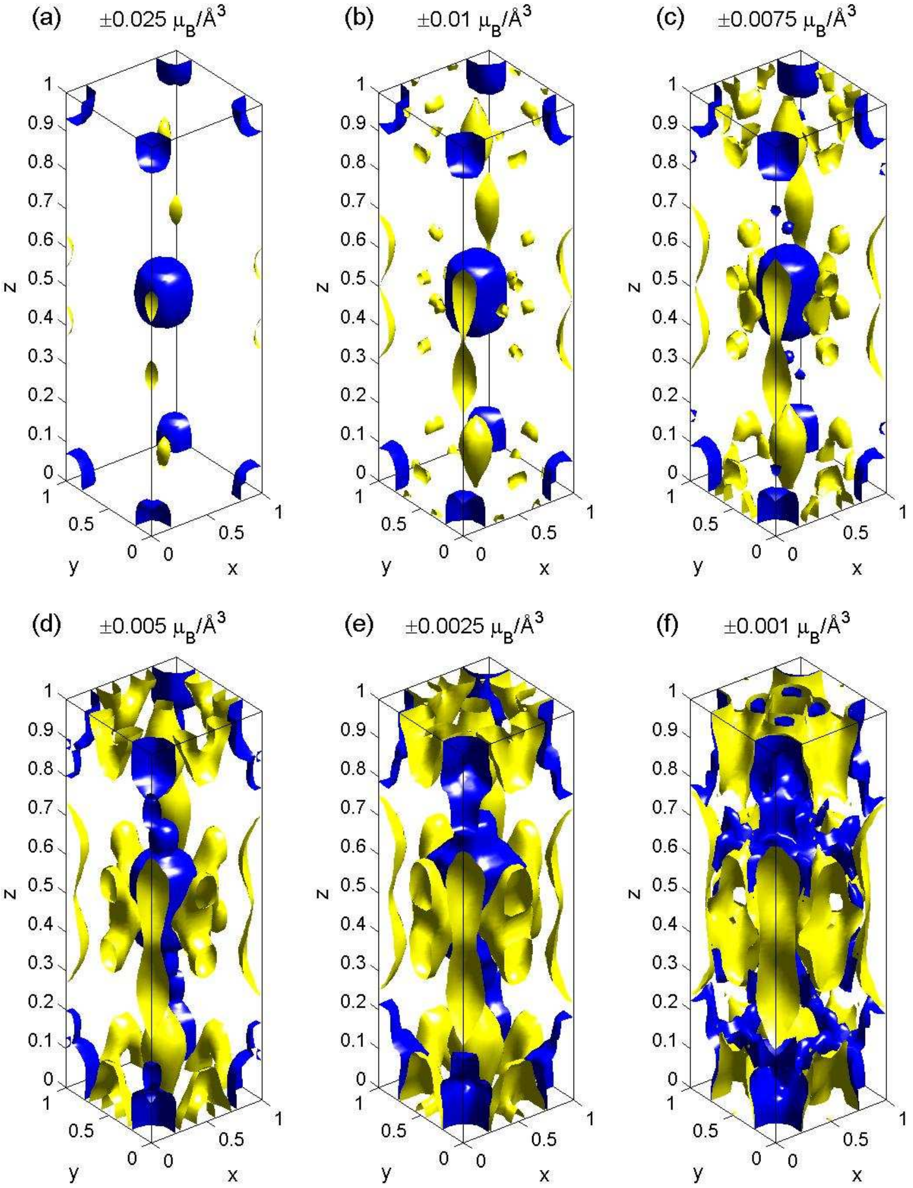

Figure 4.37: 3D contours of the magnetisation distribution in the structural unit cell of crystal B at 120K, with a magnetic field of 9T applied along the c-axis. The positive contour is shown in blue and the negative contour in yellow for each plot. The contours shown in each of the figures are as follows, (a) $\pm0.025\mu_\mathrm{B}/\mathrm{\AA}^3$, (b) $\pm0.01\mu_\mathrm{B}/\mathrm{\AA}^3$, (c) $\pm0.0075\mu_\mathrm{B}/\mathrm{\AA}^3$, (d) $\pm0.005\mu_\mathrm{B}/\mathrm{\AA}^3$, (e) $\pm0.0025\mu_\mathrm{B}/\mathrm{\AA}^3$ and (f) $\pm0.001\mu_\mathrm{B}/\mathrm{\AA}^3$.

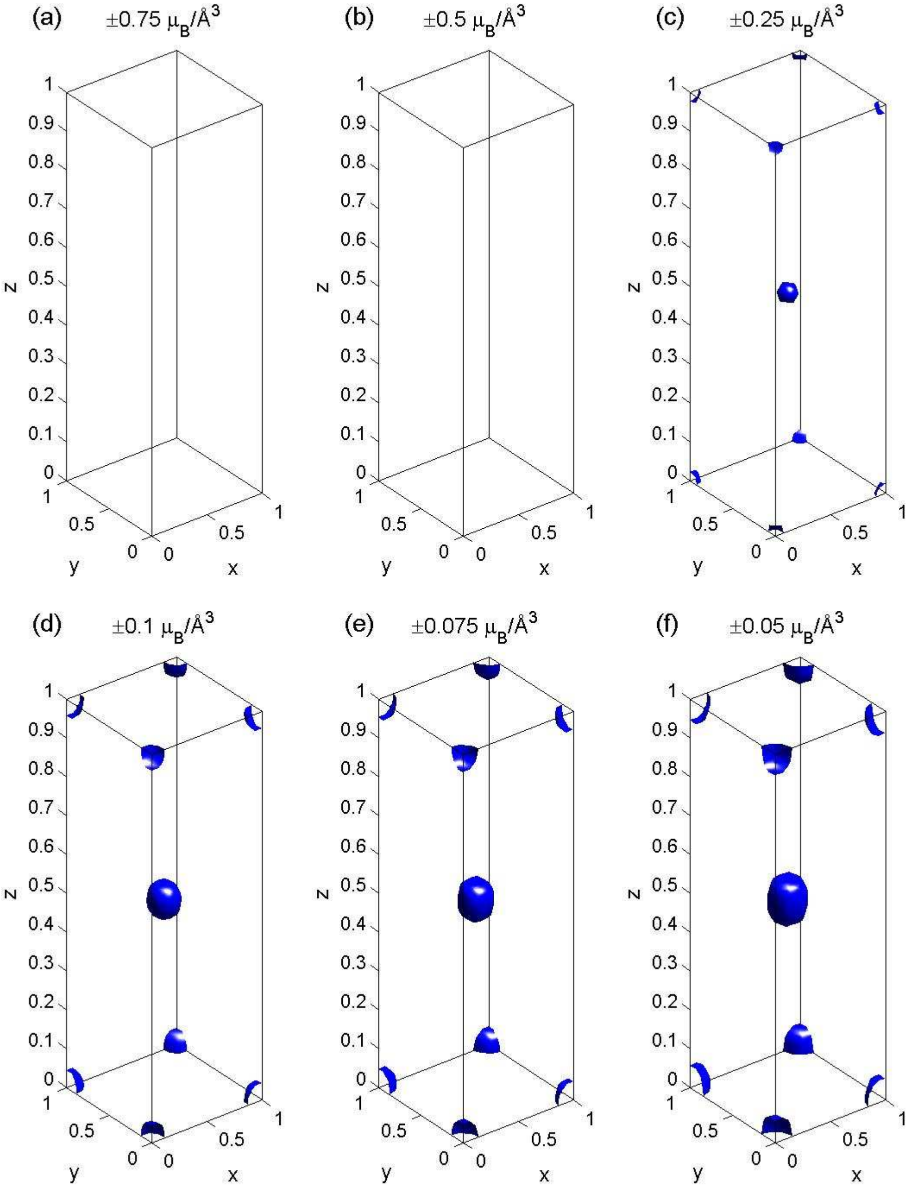

Figure 4.38: 3D contours of the magnetisation distribution in the structural unit cell of crystal B at 250K, with a magnetic field of 9T applied along the c-axis. The positive contour is shown in blue and the negative contour in yellow for each plot. The contours shown in each of the figures are as follows, (a) $\pm 0.75\mu_{\mathrm{B}}/\mathrm{\AA}^3$, (b) $\pm 0.5\mu_{\mathrm{B}}/\mathrm{\AA}^3$, (c) $\pm 0.25\mu_{\mathrm{B}}/\mathrm{\AA}^3$, (d) $\pm 0.1\mu_{\mathrm{B}}/\mathrm{\AA}^3$, (d) $\pm 0.075\mu_{\mathrm{B}}/\mathrm{\AA}^3$ and (f) $\pm 0.05\mu_{\mathrm{B}}/\mathrm{\AA}^3$.

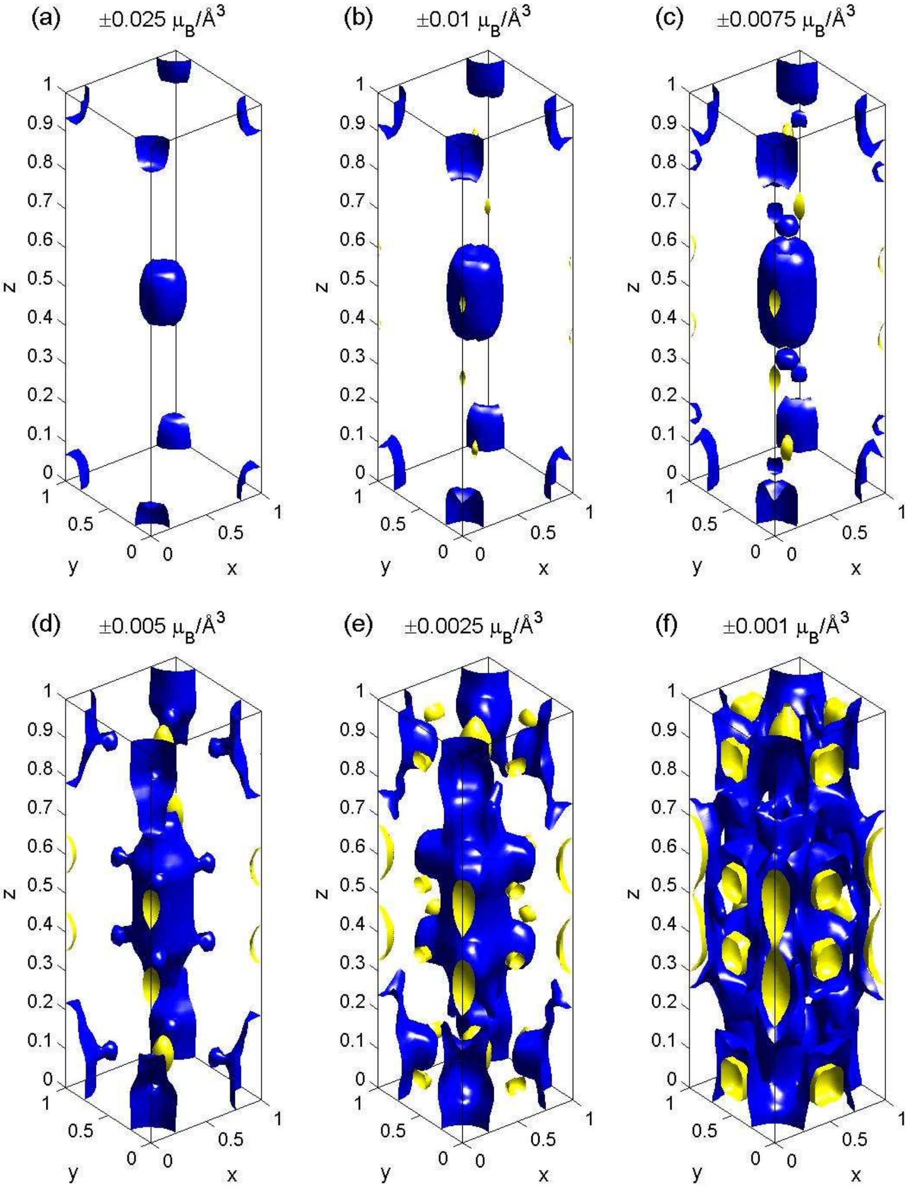

Figure 4.39: 3D contours of the magnetisation distribution in the structural unit cell of crystal B at 250K, with a magnetic field of 9T applied along the c-axis. The positive contour is shown in blue and the negative contour in yellow for each plot. The contours shown in each of the figures are as follows, (a) $\pm 0.025\mu_B/\text{Å}^3$, (b) $\pm 0.01\mu_B/\text{Å}^3$, (c) $\pm 0.0075\mu_B/\text{Å}^3$, (d) $\pm 0.005\mu_B/\text{Å}^3$, (e) $\pm 0.0025\mu_B/\text{Å}^3$ and (f) $\pm 0.001\mu_B/\text{Å}^3$.

the length of the *a*-axis.

To attempt to overcome these problems, two other ways of finding the moment at any site are introduced. The first method, is to centre a sphere on an ion position (or any position) and find the radius at which the moment reaches the maximum magnitude. Using this radius as opposed to the Shannon radii overcomes to a certain extent the problem of the maximum entropy method underestimating the moment by allowing for a sphere, but finding the maximum possible moment for a sphere on that site. This is called method α. The second method is to again centre a sphere on the desired site, but to only add up the positive or negative moments, depending on the site being investigated. This means that for an area that does not appear to have spherical character, a non spherical volume can be measured that has a shape of the positive or negative volume. This is referred to as method β. Both of these methods work better for negative moments in this analysis, because the unit cell is in total positive. An example comparing these two methods is given in Fig. 4.40 using the La/Sr (B) site in crystal A at 20K, with method α the moment is determined at the minimum value on the blue line and with method β the moment is determined at the Shannon radius. Method β gives the maximum possible moment expected for an ion.

The results of the different methods of calculating the moment at each site for both samples and all temperatures are given in the tables 4.6 and 4.7. Also presented is the total magnetic moment of the ions in the unit cell based on the results of measuring the magnetic moment using the Shannon radii. The total is calculated by simply adding the moment expected at a Mn site, two at the La/Sr sites, two moments at O(1) oxygen site and two at the O(2) oxygen site, then doubling this sum, i.e. all of the ions in the unit cell. The maxent total gives the total magnetic moment in the unit cell, regardless of whether the moment lies on an atomic site or

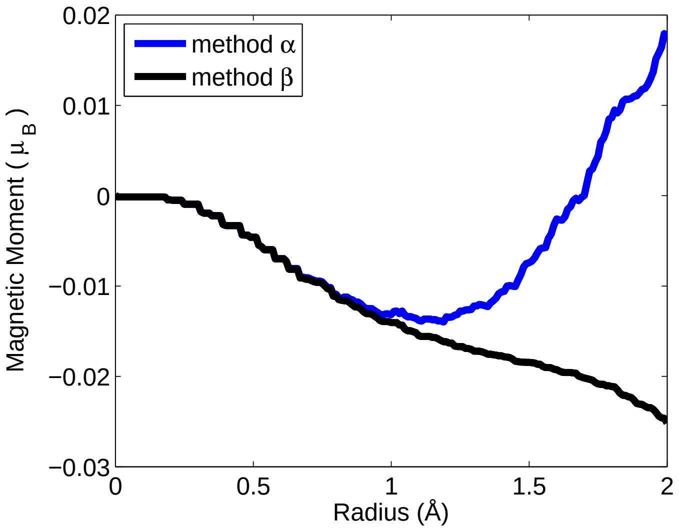

Figure 4.40: The total magnetic moment enclosed with in a sphere centred on the nominal La/Sr site of crystal A versus the radius of the sphere. Method α adds the magnetic moment in every pixel within the sphere whereas method β only considers the negative moment.

not.

4.9 Calculation of the Magnetic Structure Factor

Calculations of the magnetic structure factor in $La_{0.5}Sr_{1.5}MnO_4$ were performed using fullprof.[97] The calculations are performed by calculating the magnetic structure factor from from $La_{0.5}Sr_{1.5}MnO_4$ with only the moments entirely aligned along the *c*-axis. The unit cells are considered to be ferromagnetic to each and therefore the magnetic structure factor calculated should be entirely analogous to that determined in the D3 experiment. A few different calculations are presented in the first subsection and a maximum entropy analysis of these calculations is presented in the second subsection.

Table 4.6: Magnetic moment on various sites in crystal A at the temperatures 20K, 120K and 250K. The positions of each site are as follows, site A is the Mn ion, B the La/Sr ion, C the out of plane O(2) ion and E the in plane O(1) ion. The site D was observed to have a magnetic moment centred upon it but does not correspond to any ion that should be present in the material. The three methods of calculating the moment on each site use the Shannon radius (μ_S), method α (μ_α) with determined radius r_α and method β (μ_β). All three methods are discussed in the main body of the text. The row labeled "Total" sums the results for the Shannon radii measurements, giving an approximate total magnetisation due to the ions in crystal A. The "MaxEnt Total" row sums the magnetisation for the whole unit cell, as calculated using the maximum entropy method.

Temperature (K)	Position	μ_S (μ_B)	r_α(Å)	μ_α (μ_B)	μ_β (μ_B)
20K	A	0.3913	-	-	-
	B	-0.0106	1.19	-0.0140	-0.0179
	C	0.0433	-	-	-
	D	-	0.76	0.0056	-
	E	0.0039	1.18	-0.0110	-0.0146
	Total	0.929	-	-	-
	MaxEnt Total	1.0637	-	-	-
120K	A	0.3226	-	-	-
	B	-0.0099	1.19	-0.0109	-0.0130
	C	0.0525	-	-	-
	D	-	0.58	0.0003	-
	E	0.0021	1.2	-0.0050	-0.0113
	Total	0.8240	-	-	-
	MaxEnt Total	0.9211	-	-	-
250K	A	0.3034	-	-	-
	B	-0.0127	1.19	-0.0135	-0.0162
	C	0.0669	-	-	-
	D	-	-	-	-
	E	0.0041	1.2	-0.0018	-0.0069
	Total	0.8400	-	-	-
	MaxEnt Total	0.9267	-	-	-

Table 4.7: Magnetic moment on various sites in crystal B at the temperatures 20K, 120K and 250K. The positions of each site are as follows, site A is the Mn ion, B the La/Sr ion, C the out of plane O(2) ion and E the in plane O(1) ion. The site D was observed to have a magnetic moment centred upon it but does not correspond to any ion that should be present in the material. The three methods of calculating the moment on each site use the Shannon radius (μ_S), method α (μ_α) with determined radius r_α and method β (μ_β). All three methods are discussed in the main body of the text. The row labeled "Total" sums the results for the Shannon radii measurements, giving an approximate total magnetisation due to the ions in $La_{0.5}Sr_{1.5}MnO_4$. The "MaxEnt Total" row sums the magnetisation for the whole unit cell, as calculated using the maximum entropy method.

Temperature (K)	Position	μ_S (μ_B)	r_α(Å)	μ_α (μ_B)	μ_β (μ_B)
20K	A	0.5512	-	-	-
	B	0.0042	0.94	-0.0192	-0.0263
	C	0.0968	-	-	-
	D	-	-	-	-
	E	0.0329	0	-	-0.0068
	Total	1.6044	-	-	-
	MaxEnt Total	1.9050	-	-	-
120K	A	0.382	-	-	-
	B	-0.0267	1.22	-0.0281	-0.0307
	C	0.0333	-	-	-
	D	-	-	-	-
	E	-0.0226	1.22	-0.0279	-0.0316
	Total	0.7000	-	-	-
	MaxEnt Total	0.7664	-	-	-
250K	A	0.1653	-	-	-
	B	0.0068	0.85	-0.0041	-0.0054
	C	0.0503	-	-	-
	D	-	-	-	-
	E	0.0069	1.04	-0.0014	-0.0038
	Total	0.5322	-	-	-
	MaxEnt Total	0.6779	-	-	-

4.9.1 Fullprof Calculations

A number of different combinations of magnetic moments were calculated, but only a few particularly relevant ones are presented here. The first calculation (calculation 1) is of the magnetic structure factor from only the Mn ions. The magnitude of the Mn moments was set to be $2.1\mu_B$, which gave the correct scale for the magnetic structure factor, allowing it to be directly compared with that observed in the earlier experiments. The Mn ions are all treated as Mn^{3+}. This results of this calculation are shown in Fig. 4.41.

A calculation of the magnetic structure factor of the magnetisation distribution as predicted by Ferrari et al.[63] (calculation 2) is also shown in Fig. 4.41. A complication of this calculation was to choose a suitable form factor for the O ions, as this is not normally a magnetic ion. The oxygen ions were modeled as Mn^{2+} ions, making the moment distribution approximately spherical. The magnitude of the moment at the O(1) site was taken to be 17.5% of that at the Mn site, as determined by Ferrari et al.

The final calculation (calculation 3) presented here (Fig. 4.41) is based on the results of the maximum entropy method analysis, using the moment sizes presented in table 4.6. Here the O(2) site and La/Sr site are also modeled as Mn^{2+}. The results of the D3 experiment at 9.6T and 20K are also reproduced in Fig. 4.41.

Calculation 1 shows a smooth variation in the structure factor measured at different peaks, as expected for a magnetic structure of only ferromagnetic Mn ions. The effect of introducing magnetisation at the O site is to make the series of structure factors less smooth and the calculation looks qualitatively similar to the results of the D3 experiment. However, it appears that there are some significant differences in which peaks have a higher (or lower) than expected structure factor,

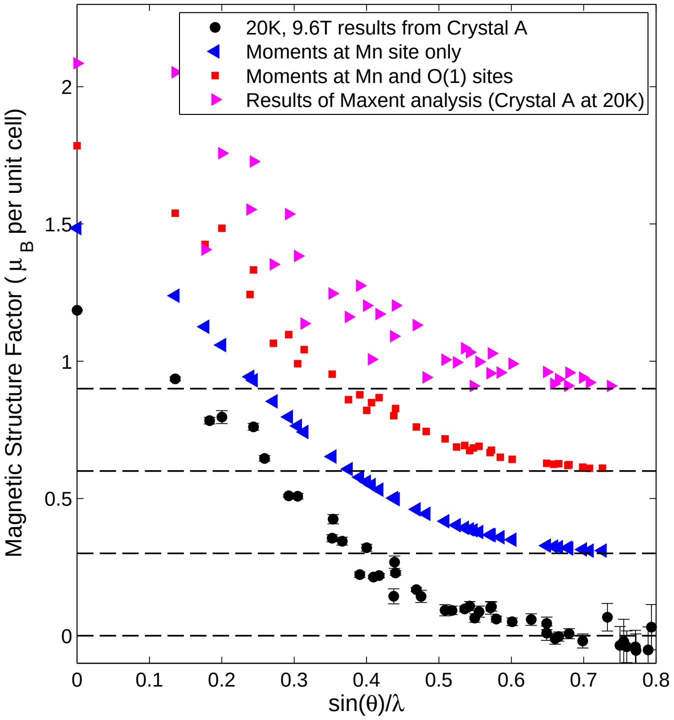

Figure 4.41: The measured and calculated magnetic structure factors for $La_{0.5}Sr_{1.5}MnO_4$ for various measured and calculated peaks. The results of the magnetic structure factor measurement on crystal A at 20K and 9.6T are reproduced in black circles. A calculation of the magnetic structure factor of $La_{0.5}Sr_{1.5}MnO_4$, with moment located solely on the Mn site is shown in blue triangles. The red squares show a calculation of the magnetic structure factor expected for the magnetisation distribution calculated by Ferrari et al.[63] A calculation of the magnetic structure factor based on the results of the maximum entropy method for crystal A at 20K and 9.6T is shown by the magenta triangles. The calculations are offset from zero on the $y-$axis for clarity.

i. e. whether they appear above or below the value expected for just Mn ions. These two observations might indicate that the quantity of the magnetic moment not located at the Mn site is approximately correct in this calculation, but that the distribution is not the same in both calculation 2 and the experiment. Calculation 3 shows a large variation in the structure factor from peak to peak, greater than that seen in the experiment. This is a further indication that the maximum entropy method is placing artifacts into the magnetisation distribution that are not present in the real material.

4.9.2 Maximum Entropy Analysis of the Fullprof Calculations

The maximum entropy analysis of the three calculations discussed in the previous subsection are shown in figures 4.42, 4.43 and 4.44 for calculations 1, 2 and 3, respectively. In each case a selection of 3D contours are presented.

The maximum entropy analysis of calculation 1 successfully reconstructs the unit cell of only Mn spheres down to below $0.01\mu_B/\text{Å}^3$, shown in Fig. 4.42. Below this level, Fig. 4.42(e) unwanted artifacts are introduced into the distribution. This gives a level below which the maximum entropy method is no longer entirely reliable. However, no artifacts are placed in the O(1) site, which is of most interest to this work.

The analysis of the calculation 2 results also show the expected distribution down to below $0.01\mu_B/\text{Å}^3$, in this case showing the Mn ion and a spherical negative moment at the O(1) site, shown in Fig. 4.43. Although unwanted artifacts are again introduced in this calculation, they are not located at the La/Sr site or the O(2) site, see Fig. 4.43(e). This suggests that the moments observed at these sites in the results are real.

This suggestion is reinforced by the results of the analysis of calculation 3, see Fig. 4.44. In this case the features observed in the maximum entropy analysis of the real data are reproduced at approximately similar contour levels, compare Fig. 4.44 with the results presented in figures 4.28-4.39. However, in the analysis of calculation 3, new artifacts are inserted, most noticeably a negative moment at (0.5,0.5,0). This is also observed in the analysis of the real data and any moment observed at this point maybe discarded as an artifact.

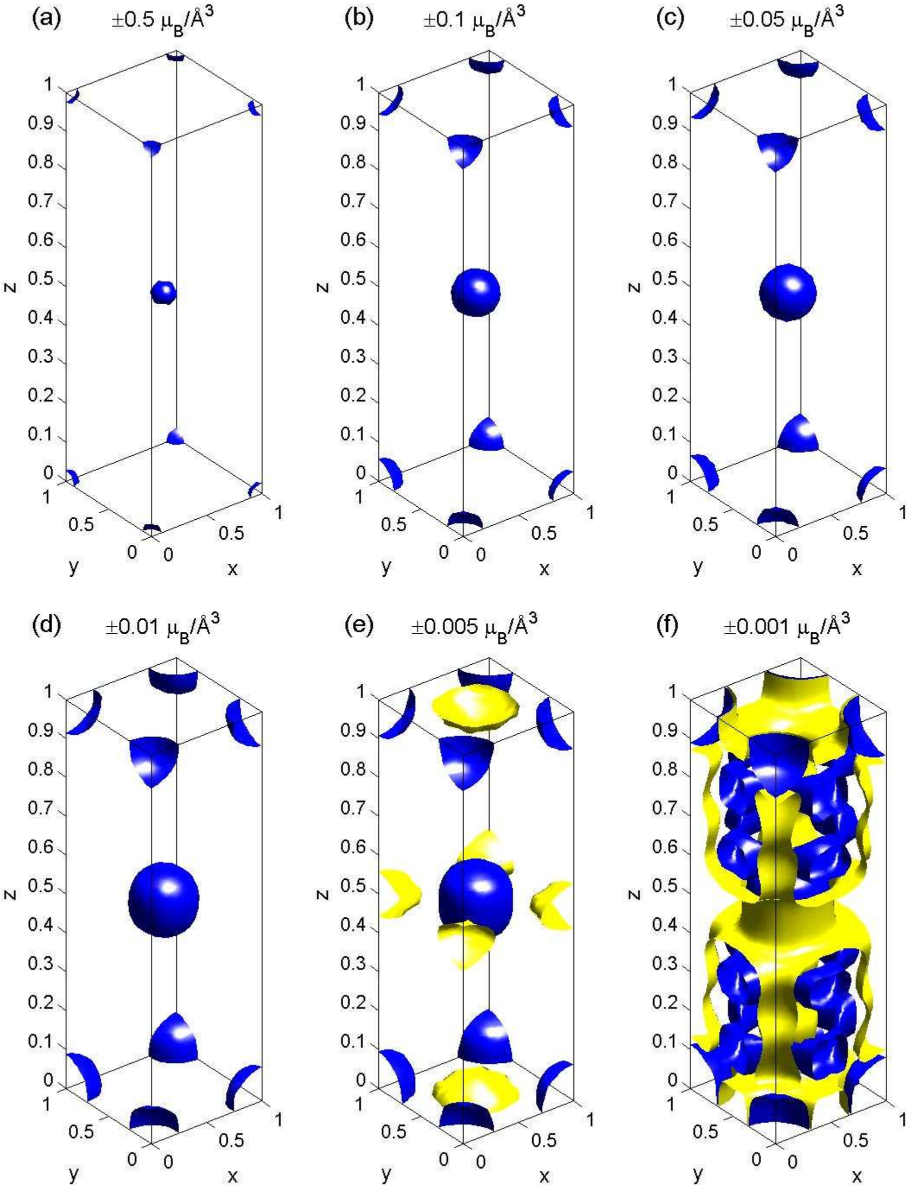

Figure 4.42: 3D contours of the magnetisation in the structural unit cell of La$_{0.5}$Sr$_{1.5}$MnO$_4$ based on the calculation 1, as discussed in the text. The positive contour is shown in blue and the negative contour in yellow for each plot. The contours shown in each of the figures are as follows, (a) $\pm 0.5\mu_{\mathrm{B}}/\mathrm{\AA}^3$, (b) $\pm 0.1\mu_{\mathrm{B}}/\mathrm{\AA}^3$, (c) $\pm 0.05\mu_{\mathrm{B}}/\mathrm{\AA}^3$, (d) $\pm 0.01\mu_{\mathrm{B}}/\mathrm{\AA}^3$, (e) $\pm 0.005\mu_{\mathrm{B}}/\mathrm{\AA}^3$ and (f) $\pm 0.001\mu_{\mathrm{B}}/\mathrm{\AA}^3$.

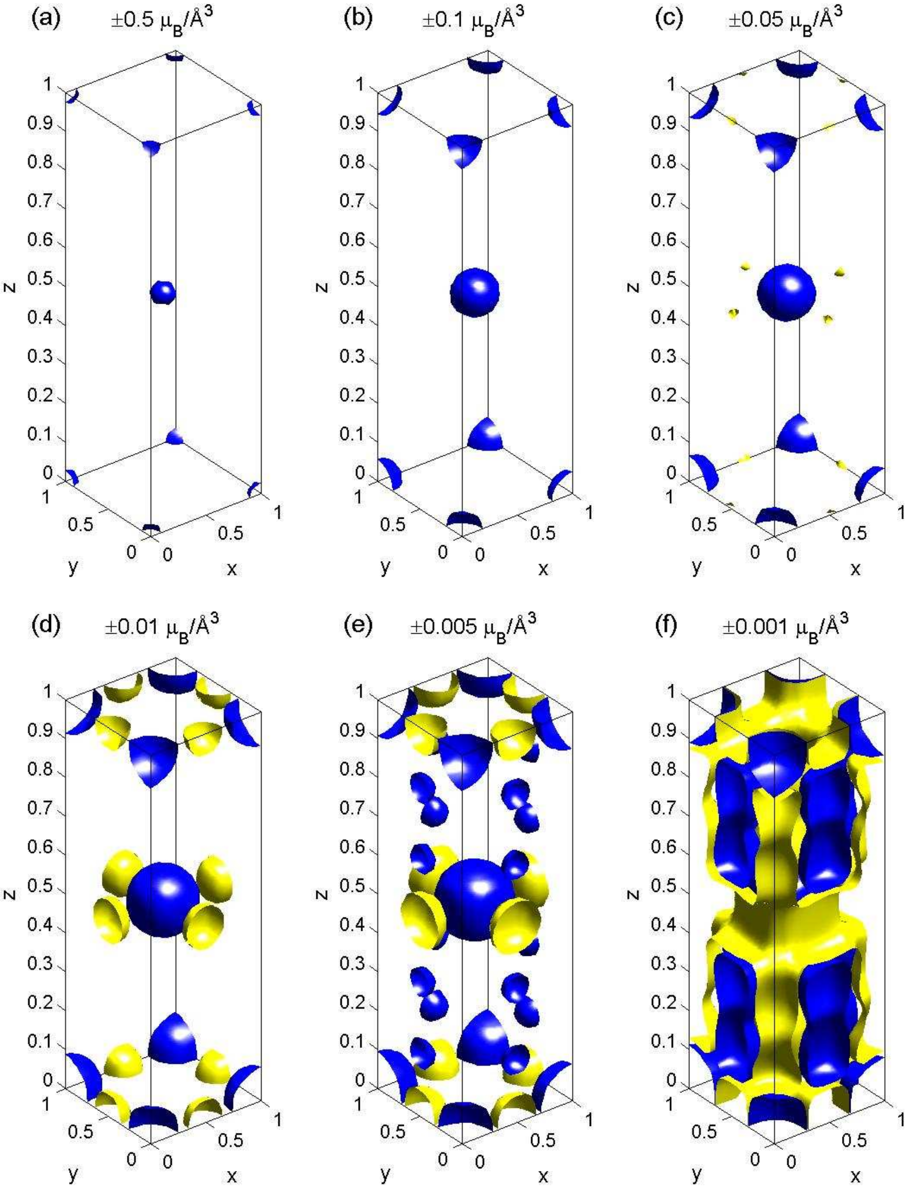

Figure 4.43: 3D contours of the magnetisation in the structural unit cell of La$_{0.5}$Sr$_{1.5}$MnO$_4$ based on the calculation 2, as discussed in the text. The positive contour is shown in blue and the negative contour in yellow for each plot. The contours shown in each of the figures are as follows, (a) $\pm 0.5\mu_{\rm B}/\text{Å}^3$, (b) $\pm 0.1\mu_{\rm B}/\text{Å}^3$, (c) $\pm 0.05\mu_{\rm B}/\text{Å}^3$, (d) $\pm 0.01\mu_{\rm B}/\text{Å}^3$, (e) $\pm 0.005\mu_{\rm B}/\text{Å}^3$ and (f) $\pm 0.001\mu_{\rm B}/\text{Å}^3$.

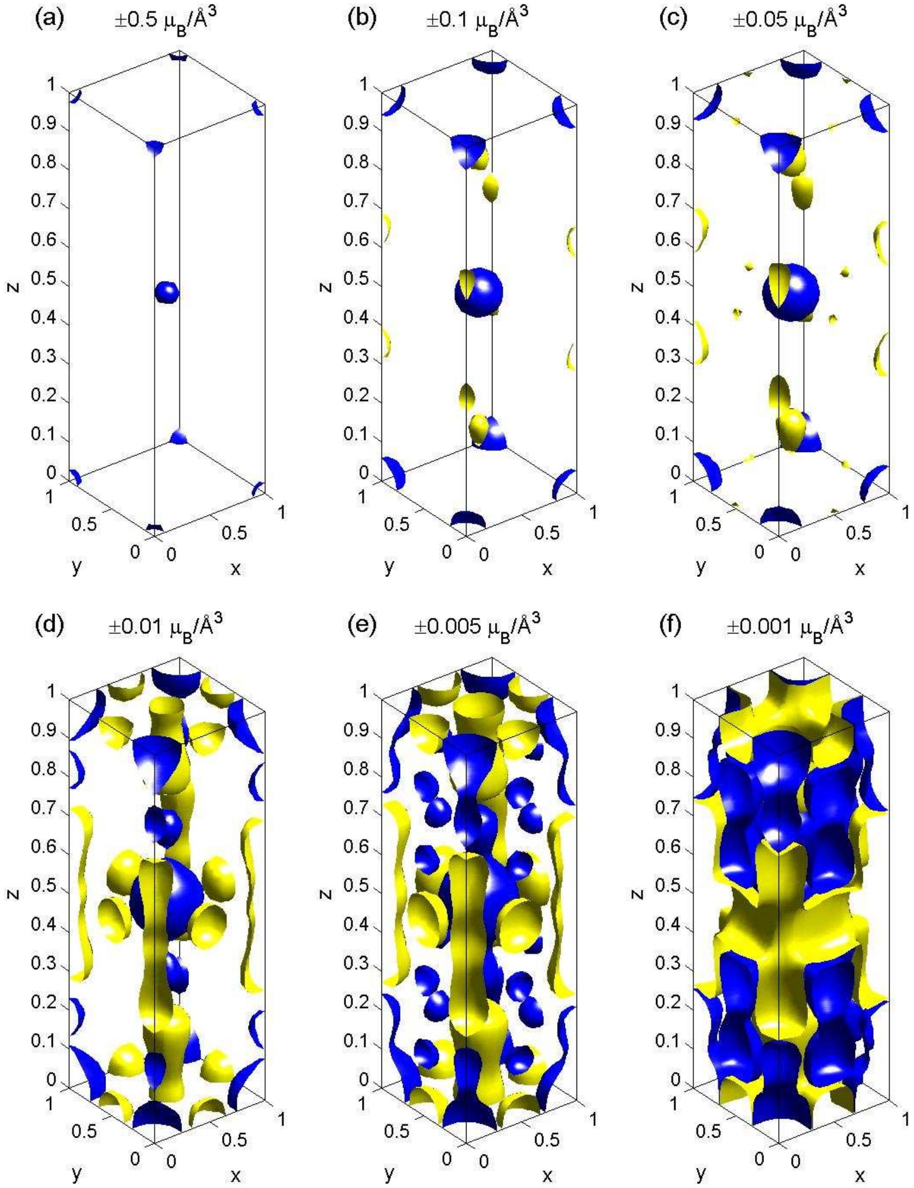

Figure 4.44: 3D contours of the magnetisation in the structural unit cell of $La_{0.5}Sr_{1.5}MnO_4$ based on the calculation 3, as discussed in the text. The positive contour is shown in blue and the negative contour in yellow for each plot. The contours shown in each of the figures are as follows, (a) $\pm 0.5\mu_B/\text{Å}^3$, (b) $\pm 0.1\mu_B/\text{Å}^3$, (c) $\pm 0.05\mu_B/\text{Å}^3$, (d) $\pm 0.01\mu_B/\text{Å}^3$, (e) $\pm 0.005\mu_B/\text{Å}^3$ and (f) $\pm 0.001\mu_B/\text{Å}^3$.

4.10 Discussion

The results for both crystal A and crystal B show the expected dominance of the magnetic moment at site A, the site of the Mn ion. However, some of the results of the observations at other sites are surprising, especially the features observed at sites where no ion should be located. The most important results for this study are the ones that directly probe the magnetic moment distribution in the CE magnetic phase, which are the results on crystal A at 20K. Most of the other experimental results and calculations are discussed in the context of those results.

To put the results in context, it is meaningful to initially examine the total magnetisation in the unit cell found from the maximum entropy method and compare it to the sum of the magnetic moments on the ionic sites. The sum of the magnetic moments on the ionic sites accounts for between 79% and 91% (depending on sample and temperature) of the total magnetic moment in the maximum entropy method results, showing that the calculation places a significant amount of the magnetic moment in what should be relatively empty parts of the unit cell.

Comparing the total magnetisation in the unit cell determined by the maximum entropy method with the corresponding magnetisation measurements presented in tables 4.3 and 4.4 illustrates one of the shortcomings of the maximum entropy method, the tendency to underestimate the magnetisation. For each sample and temperature, the calculation shows a lower magnetisation than that observed in the experiment. This means that all of the results presented here are likely to be lower than the actual values in the system. Although most of the calculated totals are approximately 10% lower than the measured values, the 120K results on crystal B show a reduction of about 50%. This is much lower than expected and is a further indication that there are significant problems with the results on crystal B at this temperature.

The magnetic moment at site A is due to the Mn ion. Mn is the only magnetic ion, being the only one with unpaired electrons. The only sensible way to measure the moment at the Mn site was to use the Shannon radii, since the magnetic moment for the unit cell is positive, the other two values lose there relevance. The proximity of the Mn site to the positive magnetic moment located along the *c*-axis from it means that any larger radii used would likely include some of the magnetic moment at this site. However, it appears from the analysis and by examining the 2D plots of the MnO_2 plane in Fig. 4.27 that the positive moment centred on this point extends beyond 0.7Å. Therefore, it is likely that the results for site A presented in tables 4.6 and 4.7 are a slight underestimate.

In crystal A at 20K the moment on the Mn site is 25 times greater than that observed on any other site of interest and the magnetic moment of the two Mn sites accounts for almost the entire magnetic moment of the unit cell, with the other positive and negative areas almost canceling each other out. With increasing temperature the size of the moment at the Mn site decreases, in agreement with the magnetisation data available on this sample, see Fig. 4.6. In crystal B the size of the moment does not change as much with temperature. This is a surprising result given the magnetisation data available from the two samples. The crystal B 3D plots at all temperatures show a depression in the moment distribution at the Mn site, located along the c-axis from the centre point, for example see Fig. 4.35(b). This feature suggests that the moment at the Mn site and the out-of-plane O(2) site are quite distinct, whereas in crystal A the two seem to overlap.

The next most significant feature in all of the results is the negative moment at site B, which is centred close to the location of the La/Sr ion in these materials. The feature is always approximately spherical and usually surrounded by a volume of positive moment and method α is probably the most accurate way of measuring the moment of this ion. In crystal A the magnitude of this feature does not vary much with temperature, regardless of the method of measuring the moment. The radius of the sphere that shows the minimum of the magnetic moment is also temperature independent. In crystal B there is an unusual temperature dependence of the magnitude, probably due to the poorer quality of the data than a real physical effect. This unusual temperature dependance is also seen in the radius of the ion in method α.

The La/Sr site is presumed to interact only weakly with the Mn-O layer and a mechanism to transfer electrons to this site and for them to be antiferromagnetically aligned with the Mn ions has not been discussed in the literature. La and Sr have the most electrons of any of the ions in this material and since the induced moment on this site is opposite to the applied magnetic field, it is possible that the observed feature could be due to diamagnetism. However, the magnetic moment expected from the diamagnetism of a free La ion (which has the larger atomic number of the two ions, but should only appear at 1/4 of the sites) is about two orders of magnitude smaller than the magnetic moment of the observed feature at the La/Sr site.

Site C is the location of an O ion, positioned directly along the c-axis from the Mn ion, referred to as the O(2) site in the literature.[86] As mentioned, this site has a magnetic feature that is aligned parallel to that on the Mn site and the two sites seem to overlap, making an accurate measurement of the magnetic moment on this site challenging. The magnetic moment on this site determined using the Shannon radii shows that this feature about half as large as the feature at the La/Sr site. In both crystal A and crystal B there is no obvious temperature dependence of the moment on this site.

As with the La/Sr site, a normal O^{2-} ion should have no unpaired electrons and should not have a magnetic moment. However, the theories of super-exchange and double-exchange rely on the ability of O ions bonded to metal ions to behave magnetically. A mechanism that would allow the O and Mn ions to be ferromagnetically aligned could involve a hybridisation between Mn and O states with similar energies,[17] although the Mn and O(2) ions are further from each other than the Mn and the in-plane O(1) ion, where a stronger interaction would therefore be expected. Another possibility is a magnetic interaction with the La/Sr site. The O(2) and La/Sr sites form a layer between the MnO_2 layers. Perhaps an interaction between these two ions causes the magnetic moment that appears on both of them. The link between these two ions for crystal A is supported by the magnetic moment on these sites not being temperature dependent, whereas there is a very similar temperature dependance of the magnitude of the magnetic moment on the other two ionic sites, the Mn and O(1) sites, discussed later.

There is also the possibility that the features at site B and C are artifacts of the maximum entropy method. The similarity of the two features at all temperatures is unusual when large variations are observed in the magnetisation. The calculations performed using fullprof seem to suggest that these are not entirely artifacts, as the maximum entropy analysis only places moment here at low contour levels in the calculations shown in section4.9.2. It should also be noted that the centres of these two features are not located precisely on the La/Sr and O(2) sites, they are slightly offset along the *c*-axis, raising the possibility that these two features appearing close to the ionic sites is merely a coincidence. Since it was not possible to measure peaks that were far from parallel to the $ab-$plane, the accuracy of the maximum entropy method reconstruction along the $z - axis$ is reduced which may explain why the features are not observed precisely on the ionic site.

The positive magnetic moment observed on site D in crystal A at 20K is unique to this set of results, all of the other sets of results that have a significant feature at this location show a negative moment, see Fig. 4.27. There should not be any ions located at this site and it would be an unlikely location for an excess ion of any of the species involved in this system. The maximum entropy method does not take into consideration the positions of the ions in the unit cell, it only places magnetic moments in the positions that give the best model. Therefore, if the calculation is putting a magnetic moment in what should be empty space, it might indicate that the calculation is no longer totally reliable at this level of detail. The only conclusion that can be drawn is that, for either a positive or negative moment, this is an artifact of the maximum entropy method that has no physical relevance. This is reinforced by the maximum entropy analysis determining that there should be a moment moment located here when analysing the fullprof calculations, where there was definitely no moment introduced. This shortcoming of the maximum entropy method is present because the method wants to have a smoothly varying distribution, this is not always a realistic goal and at a certain level of detail, the validity of the reconstruction comes into question.

The original purpose of this investigation was to measure the magnetic moment at the O(1) position (O site within the MnO_2 plane), located at site E. Although a moment is not observed centred on this position in any of the results, a negative magnetic feature is observed close to this point in all of them. In crystal A at 20K, there is a negative lobe located between site E and site A that bears a resemblance to the magnetic feature predicted by Ferrari et. al.[63], compare Fig. 4.2 and top left panel of Fig. 4.27. At 120K, a similar shape is observed, but a new feature with a larger moment is observed along the c-axis from site E. This new feature is the more prominent feature near site E in all of the other datasets from both crystal

A and crystal B. It is not a stretch to suggest that these lobes, either in the MnO_2 plane or located along the c-axis from the plane, bare a resemblance to a *p*-orbital with its long axis aligned in or perpendicular to the MnO_2 plane, respectively. These features are smaller than those observed at the other four sites, including the features at site D where there should be no ion present, but the observed shape of this feature is evidence that there is some magnetic moment observed at the O(1) site, anti-aligned with the moment on the neighbouring Mn sites.

The results of the maximum entropy analysis of the fullprof calculations suggests that the feature at site E is not an artifact. Magnetisation is only placed at this site when there is a moment expected there, such as in calculations two and three, but not in calculation one, at least down to very low contour levels.

The features near the O(1) site are all highly anisotropic and therefore a sphere would not give an accurate measurement of the magnetic moment at this position. Therefore, method β, which sums only the negative components within a sphere with the Shannon radius, gives an almost shape independent magnetic moment. In crystal A the magnitude of the magnetic moment on the O(1) site is proportional to that on the Mn site for varying temperatures. This points to the magnetic moment on this site being directly linked to that on the Mn site, similar to that discussed by Ferrari et al.[63] The values obtained from the results on crystal B do not show any correlation with the Mn ion and there is an unexpectedly large moment observed at this site in the 120K results and re-enforcing the idea that the results for crystal B should only really be considered in a qualitative way.

In this work the magnetic unit cell is folded into the high temperature structural unit cell. This means that care must be taken when comparing these results to the work by Ferrari et. al.[63]. Their calculation shows that not all O(1) sites have a magnetic moment on them. This means that in the results of this experiment the O(1) sites with a moment are averaged with the sites where no moment is expected, see Fig. 4.2. This of course means that if the results presented here were re-drawn in the structural unit cell, the magnetic moment on the magnetic O(1) sites shown in that calculation, would be approximately double the results measured here. Although it is difficult to decisively conclude that there is a magnetic moment on the O(1) site based on the results in this thesis, it is possible to give an upper value for such a moment. The field-induced moment located on the O(1) ion in the CE magnetic phase of $La_{0.5}Sr_{1.5}MnO_4$ (crystal A) is no larger than $0.0292\mu_B$, although this value comes with the caveat that the maximum entropy method typically underestimates the magnitude of magnetic moments in its attempt to have all of the features smoothly varying.

This means that the moment on the O(1) site has a magnitude of about 7.5% of the moment observed on the Mn site. The calculation by Ferrari et al.[63] suggested that the magnitude of the moment on the O(1) ion would be around 17.5% of that on the Mn site. This clearly shows some disagreement between this experiment and the earlier calculations. This study might have observed a lower moment due to the sample not being precisely $La_{0.5}Sr_{1.5}MnO_4$. It is possible that the applied magnetic field was not strong enough to fully align the moment on the O(1) site with the *c*-axis, meaning that the full magnetic moment was not observed by the neutron scattering, whereas the calculation by Ferrari et al. considers the full magnetic moment. It is apparent from the bulk magnetisation measurements that the sample is not saturated at these fields, suggesting precisely this issue. It is also worth remembering that the two studies were on slightly different materials, which could account for some small differences.

The similarity between the highest temperature dataset on both crystal A and crystal B is interesting. It suggests that both of these materials have a similar distribution of the magnetisation, which is unsurprising as these results are both at a higher temperature than any of the charge-ordered/orbital-ordered or magnetic transition temperatures.

4.11 Conclusion and Outlook

This investigation has shown tentative experimental evidence that there is a magnetic moment on the in-plane O ion in the CE-type antiferromagnetically ordered system $La_{0.5}Sr_{1.5}MnO_4$ and suggests that the charge on such O ions is not strictly 2-. Although the evidence presented here is not conclusive, the maximum observed moment on the O(1) site is expected to be less than 7.5% of moment on the Mn site, since a significantly larger moment than this would be observable in an experiment such as this one. This contrasts with the theoretical value of the moment being about 17.5% of the magnitude of the moment on the Mn site. If the charge of the O ions is not 2-, then it is likely that electrons are being lost from the O *p*-orbital that lies in the line between two Mn ions, due to the location of the lobes of negative magnetic moment observed in this investigation.

Magnetic features were also observed on the La/Sr site and on the out-of-plane O(2) site in all of the measurements in this investigation. These features are both more significant than the features observed on the in-plane O(1) site. The magnetisation of these features does not display a temperature dependence, whereas the other ions appear to have a common temperature dependence, suggesting that there is some magnetic interaction between the La/Sr ions and the O(2) ions in $La_{0.5}Sr_{1.5}MnO_4$. Although calculations of magnetic structure factors suggest that these features are real, it there is a possibility that these are artifacts of the analysis methods.

There are a number of further investigations that could give a better understanding of this system. The calculations performed in section 4.9 could be expanded into an entire research project. The calculations presented here could obviously be improved upon by using form factors that more accurately represent the magnetisation distribution observed at individual ion sites, for example, modeling an oxygen $p-$orbital instead of a sphere. It should also be possible to fit the magnetic structure factors observed to a magnetic dipole model. It would be useful to perform this experiment again with higher quality samples of $La_{0.5}Sr_{1.5}MnO_4$. Magnetisation temperature dependencies indicated that the sample of $La_{0.5}Sr_{1.5}MnO_4$ used here, did not consist entirely of $x = 0.5$ material.

Chapter 5

Study of the Multiferroic, $DyMn_2O_5$, Using Resonant Magnetic X-ray Scattering

---

5.1 Introduction

The link between electricity and magnetism that was established in the 19th century is well known and well understood. The Hall effect and magnetoresistance both show direct links between the two fundamental forces of nature within materials. However, materials that show both an electronic ordering (such as a net electrical polarisation in a ferroelectric) and a magnetic ordering (such as a ferromagnet), known as multiferroics, are relatively rare. There are a number of types of multiferroics, most of which show a weak coupling between the electronic and magnetic states of the material. However, there is a subset of materials that display the magnetoelectric effect, predicted by Pierre Curie at the turn of the 20th century,[98] which show a coupling between these two types of ordering. Not only do these materials involve interesting condensed matter physics, the possible applications of being able to control two different types of ordering in a material could be useful in a number of technologies.[99] An overview of multiferroics is presented in section

1.8 and further details can be found in a number of reviews.[100, 28, 2, 101]

Since Curie's original prediction of the magnetoelectric effect and its later discovery in a number of materials,[102, 103, 104, 105, 106, 107, 108, 109] the field of research has gradually fallen out of favour, largely because the coupling between the magnetism and the ferroelectric phases of these systems was always observed to be too small for useful applications. The research area has had a recent resurgence since the discovery of the magnetically induced ferroelectricity in $TbMnO_3$ [16] and in similar materials where Tb is replaced by another rare earth ion.[110] These materials and the related RMn_2O_5 series (where R is a rare earth, Y or Bi) display a large coupling between the magnetic and electrical properties of the system, although the electrical polarisation of the systems tends to be quite weak. The mechanism behind the multiferroicity in these systems is not completely understood, but theories based on symmetry considerations have provided important insights.[111, 112] To construct microscopic models that explain the physics in these systems, more information on the details of the various electronic and magnetic phases is required.

Ferroelectricity arises from electrical polarisation caused at the microscopic levels. In the RMn_2O_5 materials there are two models that would allow electrical polarisation. The first of these is ionic polarisation, where an ion moves to a different position in the unit cell, causing a polarisation by the separation of positive and negative ions in the material.[28, 2, 16, 113] A second possible method is that the ions themselves do not move significantly, but the valence electrons on the ions do move.[114, 115] This arises due to the covalency between a transition metal and its neighbouring oxygen ions and some experiments do show evidence of this type of polarisation.[116, 117]

The bulk magnetic and electronic properties of the many members of the RMn_2O_5 series are well documented through various studies going as far back as the 1960's

[118, 119]. Originally the complicated magnetic structures displayed by these materials provided the main reason of the interest, but the discovery of the ferroelectric properties of these materials [120, 113, 121, 122, 123] led to a large number of publications on RMn_2O_5 materials in the last few years. The details of the magnetic structure are believed to be important to establishing magnetically induced multiferroic phase and the magnetic structures for many members of the RMn_2O_5 series are well known, usually determined using neutron scattering [119, 124, 125, 126] or by resonant x-ray diffraction [45].

One of the less well understood structures is that of the material that displays the largest electrical polarisation of the RMn_2O_5 systems, $DyMn_2O_5$, see Fig. 5.1.[127] Although the magnetic properties of $DyMn_2O_5$ have been studied previously,[119, 124, 128, 129] the nature of the magnetic ordering has remained poorly understood, particularly in the multiferroic phase. These previous studies of the magnetism have examined the low temperature phase (which is not ferroelectric) and followed the magnetic ordering wavevector as a function of temperature, but crucially, the magnetic structure in the ferroelectric phase has not been fully determined. A better understanding of the magnetic structure of $DyMn_2O_5$ in the ferroelectric phase and how it changes as ferroelectric phases change could be of importance in establishing the reasons for why $DyMn_2O_5$ has the largest electrical polarisation in this series.

This chapter presents a study of the nature of the magnetism and electronic polarisation of $DyMn_2O_5$. In particular, a detailed study of the magnetic structure in the ferroelectric phase is presented.

5.1.1 Properties of $DyMn_2O_5$

The bulk properties of the other members of the RMn_2O_5 series are well documented.[120, 122, 123] These materials show a ferroelectric polarization along the b-axis, approximately in the temperature range $20 \leq T \leq 35$ K. The magnetic properties of the members of the series also show common features. There exists a transition $T_N \approx 40$ K into an incommensurate magnetic phase, just above the ferroelectric phase. Below the incommensurate magnetic phase, the magnetic structure becomes commensurate and the ferroelectric phase shows the largest polarisation when this commensurate magnetic phase is present. The electrical polarization exists parallel to the b-axis in all phases where it is apparent. A lower temperature incommensurate phase appears below 20 K. These are the higher temperature magnetic phases and only have magnetic ordering of the Mn ions. The lowest temperature magnetic phase shows spontaneous magnetic ordering of the rare earth ions (assuming that the rare earth ion is magnetic). A summary of the electronic polarisation behaviour in many RMn_2O_5 compounds at various temperatures is presented in Fig. 5.1.

The electronic and magnetic properties of $DyMn_2O_5$ are somewhat different from the other members of the RMn_2O_5 series [120, 113, 121, 122, 123]. In $DyMn_2O_5$ there is a high temperature incommensurate magnetic phase (HT-ICM), appearing at 44K on cooling, but below 42K, this phase is replaced by the commensurate magnetic ordering (CM), with the characteristic Bragg reflections at $(h + \frac{1}{2}, k, l \pm 1/4)$. Below 40K, $DyMn_2O_5$ enters an electrically polarised phase (FE), with polarisation along the b-axis. The ferroelectric phase exists down to 7K, where the material re-enters a paraelectric phase [122]. Where the ferroelectric and commensurate magnetic order coexist, the electronic polarisation is largest and this important phase is referred to as the CM-FE phase. The details of the ferroelectric phase

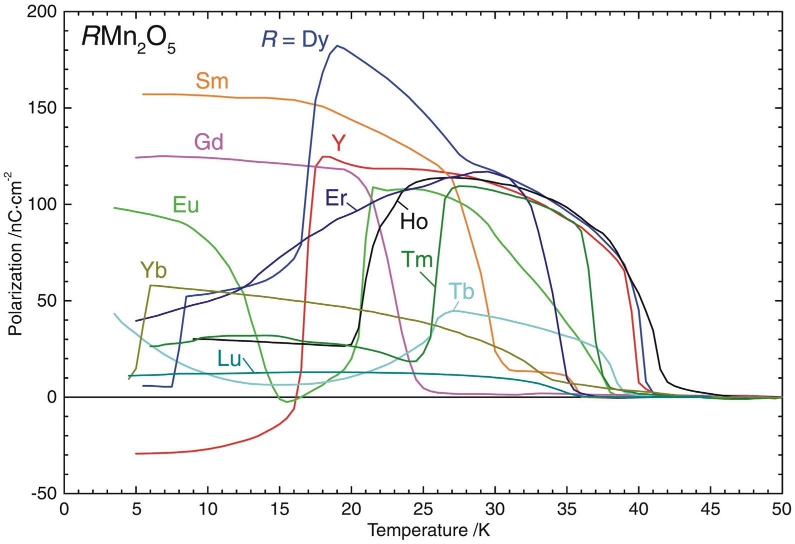

Figure 5.1: Measurement of the electrical polarisation along the *b*-axis for many members of the RMn$_2$O$_5$ series. Reprinted figure with permission from Fukunaga et al.[127] Copyright (2010) by the Physical Society of Japan.

change with temperature and an overview is shown in Fig. 5.2. This figure shows the overlap of the magnetism (marked by T_N) and the ferroelectric phases (various FE labels) and the transition temperatures marked by the dashed lines.

The high temperature phases are similar to those of the other RMn$_2$O$_5$ materials, apart from slightly different transition temperatures. It is at low temperatures that DyMn$_2$O$_5$ differs from the other members of the series. The commensurate magnetic structure (which is present throughout the ferroelectric phase) remains constant from 42K down to 18K where the magnetism enters a new incommensurate phase (LT-ICM) with magnetic Bragg peaks observed at $(h + \frac{1}{2} \pm \delta, k, l + \frac{1}{2} \pm \varepsilon)$ [129]. The LT-ICM and CM phases appear to coexist for a few degrees, with the CM finally disappearing at 12K. The HT-ICM, CM-FE and LT-ICM magnetic phases are all due solely to the ordering of the moments on the Mn ions and all have corresponding phases in the other RMn$_2$O$_5$ materials. Below 8K another commensurate magnetic ordering is observed with reflections at $(h+\frac{1}{2}, k, l)$, believed

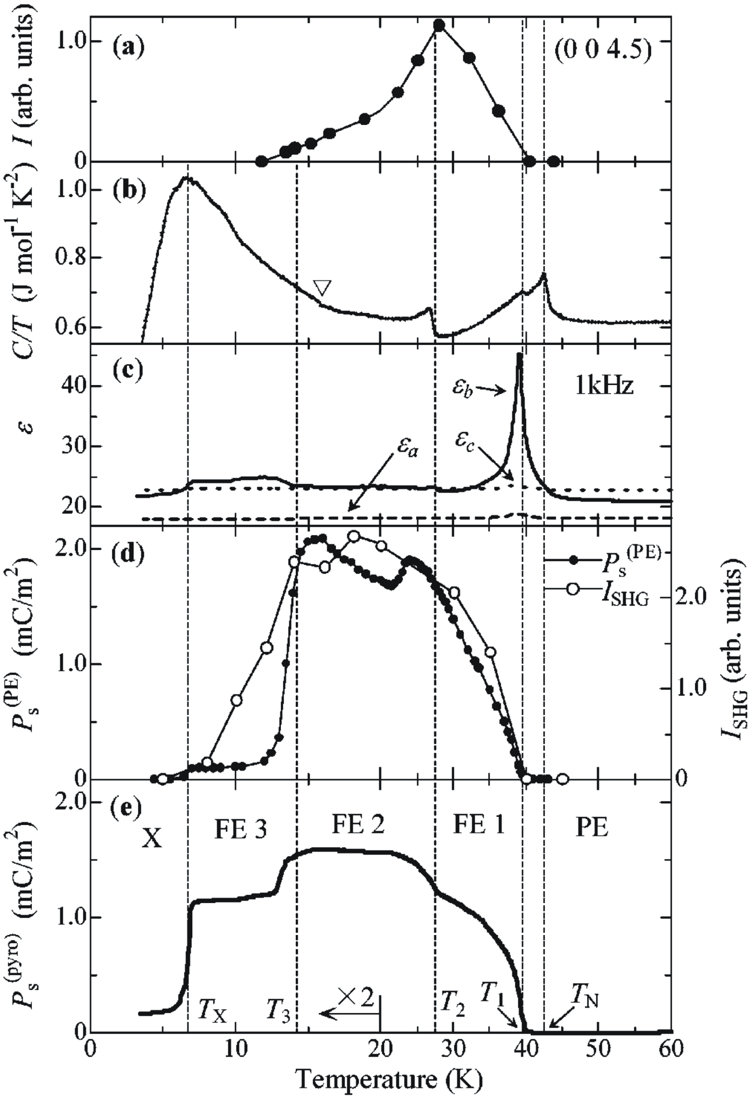

Figure 5.2: This figures shows measurements of many of the physical properties of DyMn$_2$O$_5$. (a) The integrated intensity of the x-ray superlattice peak at (004.5), (b) The specific heat (C) divided by the temperature, (c) dielectric constants (ε) for applied fields along the a, b and c axis, (d) the black dots show the spontaneous polarisation, obtained from polarisation vs electric field curves, white dots show the intensity of second-harmonic-light (I_{SHG}) and (e) the measurement of the polarisation along the b-axis by the measurement of the pyroelectric current. Reprinted figure with permission from Higashiyama et al.[122] Copyright (2004) by the American Physical Society.

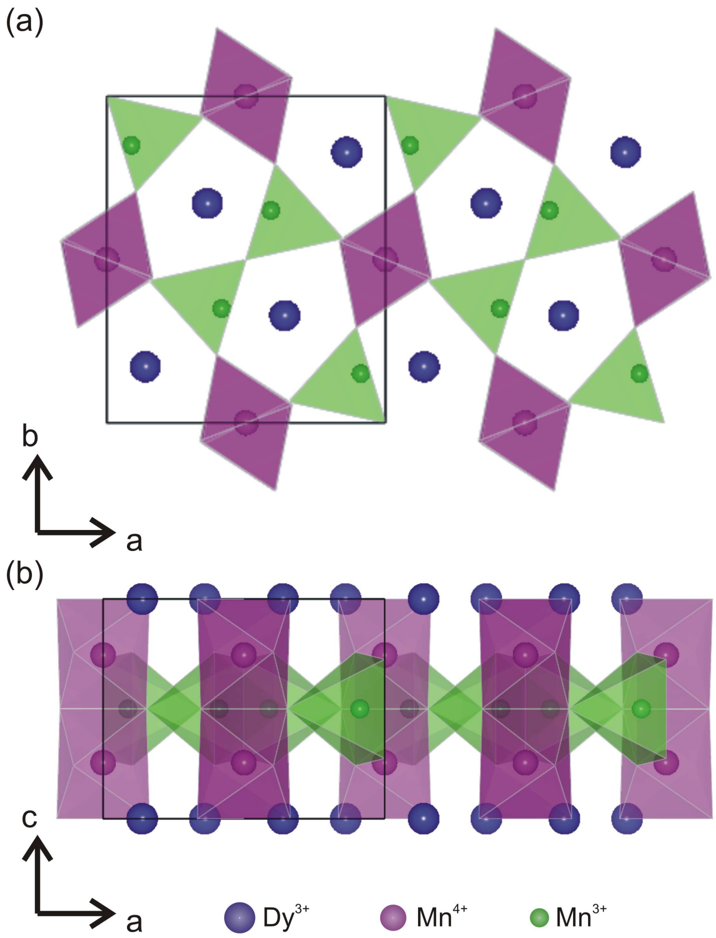

Figure 5.3: The crystal structure of $DyMn_2O_5$ observed as a projection along the (a) c-axis and (b) b-axis. Dy^{3+} is shown as the large blue circle, Mn^{4+} as the purple circle contained within an octahedra representing O ions and Mn^{3+} as the small green circle contained with in an O ion square-based pyramid.

to arise from the ordering of the Dy moments [128] and referred to here as the rare earth commensurate phase (RE-CM). This low temperature commensurate phase is unique to $DyMn_2O_5$ among the RMn_2O_5 compounds, as all of the other compounds that display rare earth ordering show incommensurate ordering in this phase.

$DyMn_2O_5$ has an orthorhombic structure, existing in the space group *Pbam*, with lattice parameters $a = 7.294$Å, $b = 8.551$Å and $c = 5.688$Å at room temperature [119]. The Mn and O form a structure of $Mn^{4+}O_6$ octahedra and $Mn^{3+}O_5$

square-based pyramids, with the Dy ions sitting in the gaps of the MnO structure, shown as a projection along the c-axis in Fig. 5.3(a) and along the b-axis in Fig. 5.3(b). This structure has ribbons of $Mn^{4+}O_6$ octahedra running parallel to the c-axis with the ribbons linked by layers of $Mn^{3+}O_5$ square-based pyramids. The Dy ions all sit in the same plane in the unit cell and form a layer that is as far from the Mn^{3+} layer as possible in the unit cell.

The magnetic structure of $DyMn_2O_5$ in the RE-CM phase has already been established [119, 124]. Neutron diffraction [128] and resonant magnetic x-ray scattering (RMXS)[129] experiments made in the CM-FE phase, have not yet determined the magnetic structure at this temperature. The main goal of this study is to remove this gap in the information known about $DyMn_2O_5$.

5.1.2 Experimental Overview

The high neutron absorption cross-section of ^{164}Dy, which accounts for about 28% of naturally occurring Dy, limits the information that can be obtained from a neutron scattering experiment to determine the magnetic structure of $DyMn_2O_5$. For this reason, RMXS has been used in this study. The x-ray signal from a magnetic structure is usually very weak, so using RMXS, an intense scattering signal can be observed due to the resonant enhancement.[43, 44] The other key advantage of using RMXS to determine the magnetic structure of $DyMn_2O_5$ is that by tuning to a resonance frequency, the x-rays are directly probing an electronic transition of one of the ion species in the material. The fact that the resonance directly probes an electronic transition of one of the ions in the material means that it can be used to decouple the magnetic effects of one magnetic ion species from that of the other one, making the signal somewhat ion dependent. An introduction to RMXS is presented in section 2.4.2.

This study involved a few separate experiments, one using a hard x-ray source ($E > 2$keV), another with a soft x-ray source ($E < 2$keV) and a measurement of the bulk electrical polarisation of $DyMn_2O_5$. This allowed access to most of the electronic transitions of interest in $DyMn_2O_5$. The details of these experiments will be covered in the next section. The results fall into three main areas of interest and these areas are each presented in separate sections. X-ray resonance spectra of $DyMn_2O_5$ are presented in section 5.3. Temperature dependent properties of $DyMn_2O_5$ are presented and discussed in section 5.4. The magnetic structure of $DyMn_2O_5$ was determined using results from the hard x-ray experiment only and is presented in section 5.5.

5.2 Experimental Procedure

The crystals used in these experiments were grown by Wanklyn et al.[130] at the University of Oxford in 1972. The crystal used for the two x-ray scattering measurements was a small crystal cut so that the $(0, 0, 1)$ scattering vector was perpendicular to the main flat surface of the sample. The electrical polarisation was measured on a crystal from the same growth, but in this case the sample had two opposite flat surfaces that were both perpendicular to the crystallographic b-axis, the direction of the electrical polarisation.

5.2.1 Resonant Magnetic X-ray Scattering Using Hard X-rays

The part of this experiment requiring high energy (hard, $E > 2$keV) x-rays was performed at the ESRF in Grenoble, France. The beamline used was ID20 [131], a high-intensity beamline specialising in magnetism, that has since been dismantled. The instrument used was a standard four-circle diffractometer in the vertical scattering geometry, i.e. the scattering plane was perpendicular to the plane of the synchrotron.

The crystal was polished before the experiment, to ensure that the x-rays could interact with a good scattering surface. The crystal was then mounted on the cold finger of a closed-cycle refrigerator, allowing cooling down to 12K. There was a problem with the power of the x-ray beam heating the sample out of the magnetic phase, but by attenuating the intensity of the beam by a factor of 7, the beam heating was reduced to a minimal amount. Attenuation was achieved using thin sheets of metal, used as standard on ID20.

The details of RMXS and the choice of energies used are discussed in section 2.4.2. The x-ray energies of interest in this hard x-ray scattering measurement on $DyMn_2O_5$ are the Dy L_{III}-edge and the Mn K-edge. The Dy L_{III}-edge is a transition from the 2p electron orbitals to the 5d electron orbitals in Dy and has an energy of 7.7901 keV. The Mn K-edge is a transition from the 1s electron orbitals to the 4p electron orbitals in Mn, at an energy of 6.5039 keV.

For all parts of this experiment, the polarisation of the x-ray beam had to be considered. This is based on the work by Blume et al. [43] and Hill et al. [44], who show how the resonant x-ray scattering signal is polarisation dependent. It is shown in these papers that the resonant x-ray diffraction signal in the $\sigma\sigma$ polarisation channel is non magnetic and that the $\sigma\pi'$ polarisation channel will show only magnetic scattering. The energy scans and the temperature dependencies presented here are all performed in these polarisation channels. The outgoing polarisation of the experiment was measured using the $(0, 0, 6)$ reflection of graphite as a polarisation analyser. Polarisation analysers are discussed in section 2.5.3.

5.2.2 Resonant Magnetic X-ray Scattering Using Soft X-rays

The soft x-ray part of this study was performed at the Diamond Light Source in Oxfordshire, UK. The experiment was performed on the beamline I10 (BLADE) using the RASOR end station. RASOR was used as a four circle diffractometer, with a vertical scattering geometry, but with only limited range in the χ circle. The limited χ-range is because the entire diffractometer must be enclosed within a high vacuum chamber, to stop the soft x-rays being absorbed in air, meaning that there is not enough space to include a full χ circle.

The sample used in this experiment, was the same one that was used for the hard x-ray experiment at ESRF, described in the previous section. The sample surface was polished prior to the experiment. The sample was mounted on the cold finger of a liquid helium cryostat that allowed cooling down to 20 K.

Soft x-rays cover an energy range of 0.4 to 2 keV and in this range there were two x-ray edges of interest for this measurement on $DyMn_2O_5$ that were accessible on RASOR. Measurements were performed at the Mn L_{III}-edge, the transition of $1s \to 3d$ electron orbitals in Mn, with an energy of 640 eV. The other edge used in this experiment was the O K-edge, the transition from $1s \to 2p$ electron orbitals in O, with an energy of 532 eV. For polarisation analysis of the diffraction signal at these wavelengths, a suitable multilayer analyser was used, with different layer depths for each edge. The Dy M_{V}-edge is also in this energy range, (the $3d \to 4f$ transition in Dy, with an energy of 1292 eV), but there was no suitable polarisation analyser available for this edge at the time of the experiment.

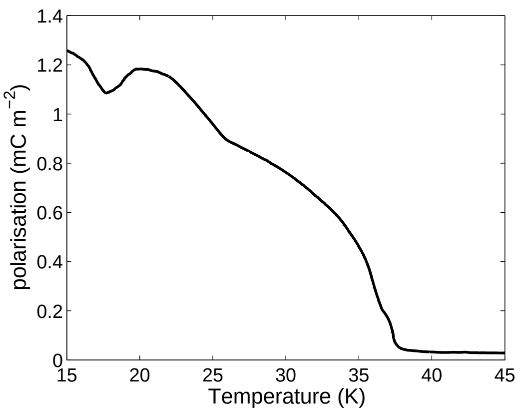

Figure 5.4: The temperature dependence of the electrical polarisation of $DyMn_2O_5$ along the b-axis, by the method of measuring the pyroelectric current.

5.2.3 Measurement of the Bulk Electrical Polarisation of $DyMn_2O_5$

The bulk electrical polarisation of $DyMn_2O_5$ was measured on a crystal from the same growth batch as the one used in the scattering experiments already mentioned. The crystal was cut to be plate like with the two opposite faces having the b-axis as surface normal (the polarisation in RMn_2O_5 materials has always been observed parallel to the b-axis). The method used to determine the polarisation was a measurement of the pyroelectric current under electrical field (section 2.6.2 for details). This measurement has previously been performed by Higashiyama et al. [122] (shown in Fig. 5.2) and the results presented here generally agree with those previously reported apart from small temperature shifts. However, a small drop in the polarisation is observed below 20K that has not been previously reported. The poling field used on this sample was 200V and the measurement was made over the temperature range of 15K to 45K. The results are presented in Fig. 5.4.

5.3 Energy Scans

Examination of the energy spectra around the various resonance edges can give valuable information on how to conduct further experiments at the edge, for example the azimuthal scans. They can also provide information about the magnetism and electronic structure of the material as well. This section will present the results of the various energy spectra that have been measured in this study. It will also cover a brief discussion of their contribution to the understanding of the magnetic and electronic properties of $DyMn_2O_5$.

5.3.1 Results

A number of energy spectra were measured across the relevant resonant edges in this experiment. A measurement of an energy spectrum around the Dy L_{III}-edge at the $(-0.5, 0, 4.25)$ peak in the $\sigma\sigma$ polarisation channel at 20K, is shown in Fig. 5.5, and another two in the $\sigma\pi'$ polarisation channel, at 20K (Fig. 5.6) and at 12K (Fig. 5.7). A fluorescence measurement was also performed around this energy, again at 20K, see Fig. 5.8. The fluorescence measurement is performed away from any Bragg peaks.

The $(-1.5, 0, 3.25)$ peak was studied around the Mn K-edge. A scan was made of the energy spectra in the $\sigma\sigma$ polarisation channel, Fig. 5.9 and in the $\sigma\pi'$ polarisation channel, Fig. 5.10. A fluorescence scan was also performed in the same energy range away from any Bragg peaks, Fig. 5.11.

Around the Mn L_{III}-edge an energy spectrum at the $(0.5, 0, 0.25)$ peak was measured at 22K, in both the $\sigma\sigma$ and $\sigma\pi'$ polarisation channels, Fig. 5.12 and Fig. 5.13 respectively. Measurements of the same peak were also performed at the O K-edge, the energy spectra at 22K in both the $\sigma\sigma$ and $\sigma\pi'$ polarisation channels,

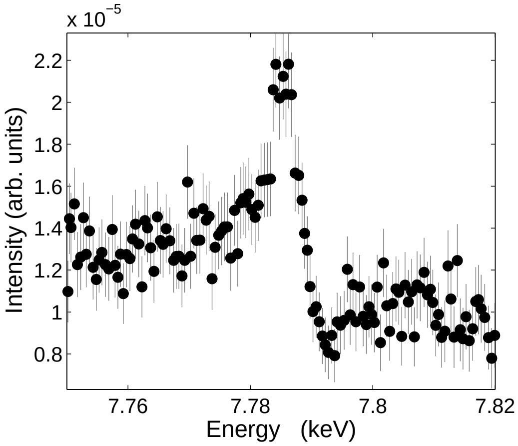

Figure 5.5: Energy resonance spectrum measured around the Dy L$_{\text{III}}$-edge, at the $(-0.5, 0, 4.25)$ peak, at 20K, in the $\sigma\sigma$-polarisation channel.

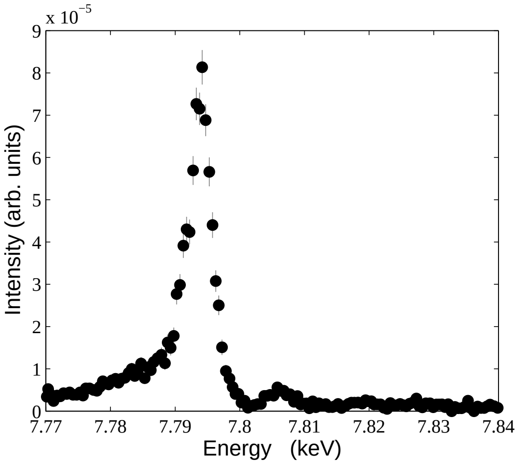

Figure 5.6: Energy resonance spectrum measured around the Dy L$_{\text{III}}$-edge, at the $(-0.5, 0, 4.25)$ peak, at 20K, in the $\sigma\pi'$-polarisation channel.

Fig. 5.14 and Fig. 5.15 respectively. A fluorescence was also measured at the O K-edge at 22K, shown in Fig. 5.16.

5.3.2 Analysis

The resonance scans around the Dy L$_{\text{III}}$-edge are perhaps the most important measured for this study as they are used to get the peak resonance enhancement at the edge where the majority of the information on the magnetic structure of DyMn$_2$O$_5$ is obtained. A direct comparison of the Dy L$_{\text{III}}$-edge measured at 20K on the

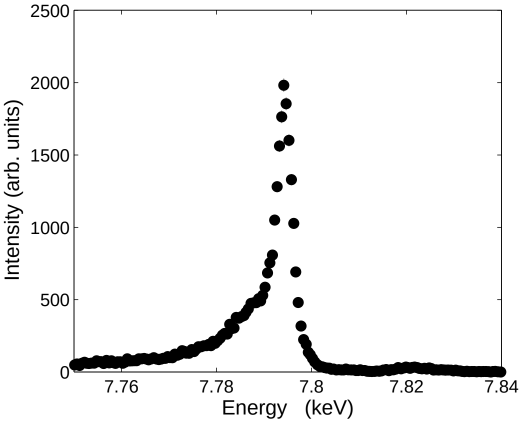

Figure 5.7: Energy resonance spectrum measured around the Dy L_{III}-edge, at the $(-0.5, 0, 4.25)$ peak, at 12K, in the $\sigma\pi'$-polarisation channel.

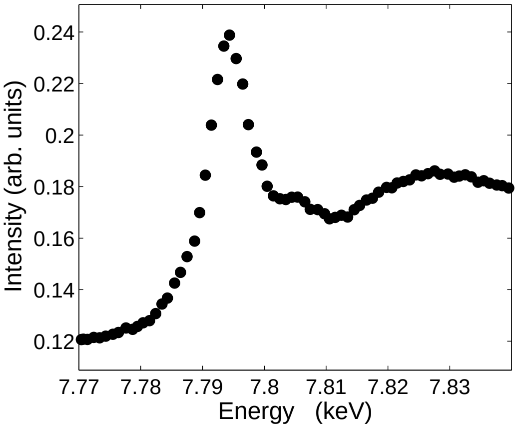

Figure 5.8: Fluorescence spectrum measured around the Dy L_{III}-edge, at 20K, in the $\sigma\pi'$-polarisation channel.

$(-0.5, 0, 4.25)$ in $\sigma\sigma$ channel with that measured in the $\sigma\pi'$ channel, Fig. 5.5 and Fig. 5.6 respectively, is revealing. The Dy L_{III}-edge is expected to be at a value of 7.79keV. In the $\sigma\sigma$-channel, there is a small peak, approximately double the intensity of the background, centred just below the expected value of the resonance peak. It is unclear what causes this peak, but it is not likely to be leakage from the other polarisation channel because of the change in energy. However, in the $\sigma\pi'$-channel (which is sensitive to the magnetic enhancement of the signal), this is completely obscured by the much higher intensity peak at ~ 7.794 keV. This is the maximum of the magnetically enhanced resonance signal and is the energy used for

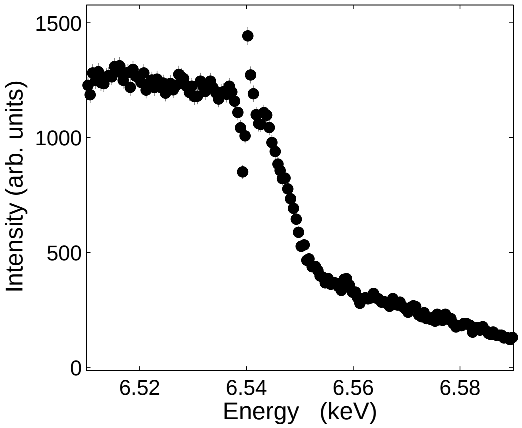

Figure 5.9: Energy resonance spectrum measured around the Mn K-edge, at the $(-1.5, 0, 3.25)$ peak, at 14K, in the $\sigma\sigma$-polarisation channel.

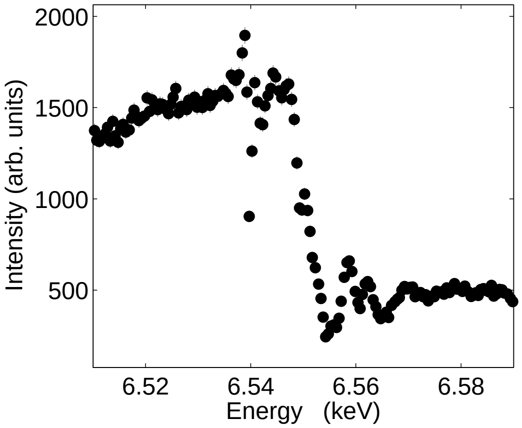

Figure 5.10: Energy resonance spectrum measured around the Mn K-edge, at the $(-1.5, 0, 3.25)$ peak, at 14K, in the $\sigma\pi'$-polarisation channel.

all subsequent measurements at the Dy L$_{\text{III}}$-edge. There is a small peak observed at $\sim$ 7.805 keV in the $\sigma\pi'$ channel at 20 K, which is not present in the scan at 12 K. The fluorescence measurement at this energy, Fig. 5.8, also shows a peak at 7.794 keV confirming that this signal is the Dy L$_{\text{III}}$-edge.

The further measurement made in the $\sigma\pi'$ channel, was the $(-0.5, 0, 4.25)$ peak at 12 K. It should be noted that this measurement was performed at the temperature where the maximum resonant enhancement was observed. However, the precise temperature is unclear as this measurement was made before the beam heating problem on this experiment was fully understood and the actual temperature is

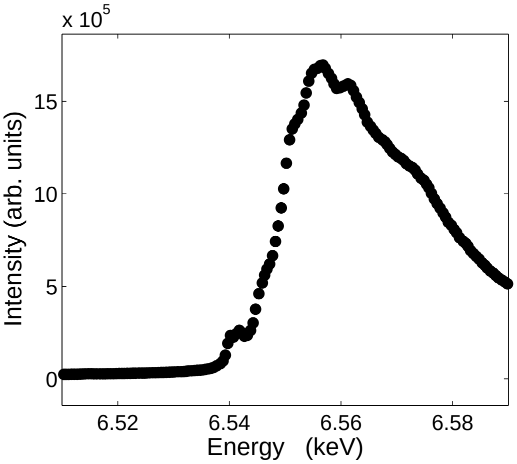

Figure 5.11: Fluorescence spectra measured around the Mn K-edge, at 14K.

expected to be a few degrees higher than the measured temperature, approximately in agreement with the previously observed maximum intensity for this peak observed at 15K by Ewings et al. [129]. The peak observed at ∼ 7.805 keV has disappeared at this temperature, but aside from this, the resonance lineshape and the energy of the maximum resonant enhancement remain the same at both 12 K and 20 K.

It is noted that there is no indication of the quadrupole transition ($2p \rightarrow 4f$, which allows direct examination of the magnetic ions in this material), expected at a slightly lower energy than the Dy L_{III}-edge (For example, in $TbMn_2O_5$ the quadrupole is 8 eV below the Tb L_{III}-edge). This transition is apparent in $TbMn_2O_5$ [45] and the reason for its appearance in that system but not $DyMn_2O_5$ is not well understood.

The energy spectra measured at the Mn K-edge are quite different in character from those at the Dy L_{III}-edge. Examining the two spectra measured at 14K on the $(-1.5, 0, 3.25)$ peak, in the $\sigma\sigma$-polarisation channel (Fig. 5.9) and the $\sigma\pi'$-polarisation channel (Fig. 5.10), it is clear that the magnetic resonance enhancement is smaller at this edge. The small peak just below 6.54 keV in the $\sigma\pi'$-polarisation channel is the Mn K-edge resonance peak, as it is not observed in the $\sigma\sigma$-polarisation

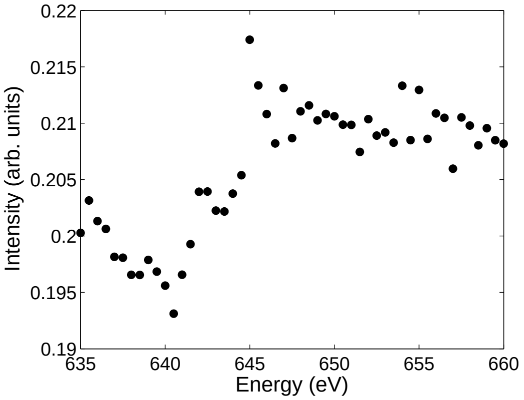

Figure 5.12: Energy resonance spectrum around the Mn L$_{\text{III}}$-edge, at the $(0.5, 0, 0.25)$ peak, at 22K in the $\sigma\sigma$-polarisation channel.

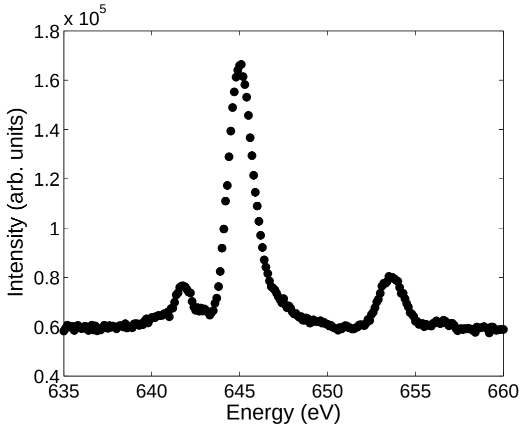

Figure 5.13: Energy resonance spectrum around the Mn L$_{\text{III}}$-edge, at the $(0.5, 0, 0.25)$ peak, at 22K in the $\sigma\pi'$-polarisation channel.

channel. This is the energy value used for other measurements at the Mn K-edge. The peak at the Mn K-edge has a very narrow lineshape in contrast to the resonance peaks found at the other measured edges. There are a few small peaks above the resonant edge in the $\sigma\pi'$-polarisation channel, which are not in the $\sigma\sigma$-polarisation channel, these are as yet unidentified, but presumably magnetic, features. The fluorescence scan, Fig. 5.11, shows a very small feature at 6.54 keV, again a signature of the resonance edge. The maximum resonance enhancement found just below 6.54 keV is used for all other measurements at the Mn K-edge.

The difference between the $\sigma\sigma$-polarisation channel (Fig. 5.12) and $\sigma\pi'$ polari-

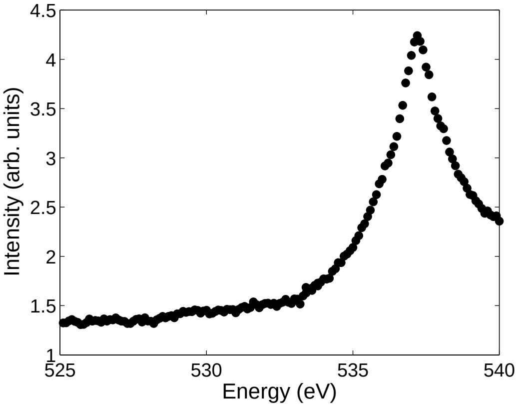

Figure 5.14: Energy resonance spectrum around the O K-edge, at the $(0.5, 0, 0.25)$ peak, at 22K in the $\sigma\sigma$-polarisation channel.

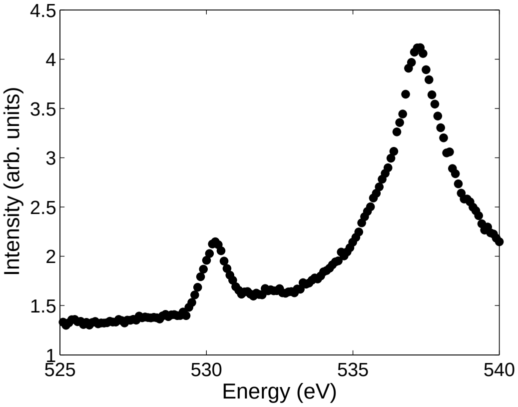

Figure 5.15: Energy resonance spectrum around the O K-edge, at the $(0.5, 0, 0.25)$ peak, at 22K in the $\sigma\pi'$-polarisation channel.

sation channel (Fig. 5.13) is most striking in the measurements at the Mn L_{III}-edge at the $(0.5, 0, 0.25)$ peak, at 22 K. In this case the $\sigma\sigma$-polarisation channel is almost featureless, whereas the $\sigma\pi'$-polarisation channel shows three distinct peaks. The large peak at 645 eV is the Mn L_{III}-edge and this value is used for all other measurements at the Mn L_{III}-edge. The smaller peak at a lower energy than the Mn L_{III}-edge is possibly a quadrupole signal. The other smaller peak above the Mn L_{III}-edge is the Mn L_{II}-edge, which should be at approximately 650 eV.

Finally the scans at the O K-edge are perhaps the simplest scans. The comparison between the $\sigma\sigma$-polarisation channel and $\sigma\pi'$-polarisation channel (Fig. 5.14

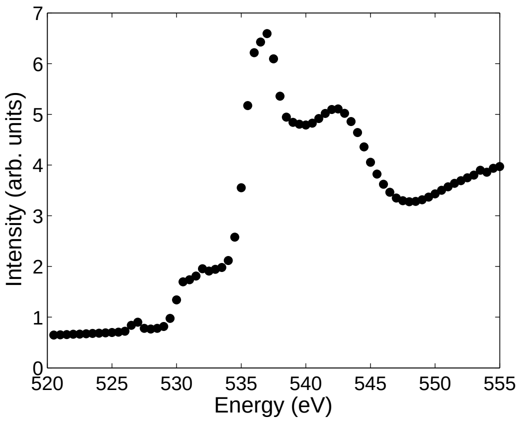

Figure 5.16: Fluorescence spectrum around the O K-edge, at 22K.

and Fig. 5.15), shows that the magnetic resonance feature is actually the lower intensity peak near 530eV, which is missing in the $\sigma\sigma$-polarisation channel. The fluorescence scan at the O K-edge shows a small feature at around 530eV and this energy is used for all other measurements at the O K-edge. The fact that a magnetic resonance has been observed at the O K-edge at all, suggests that the O ions are being magnetically polarised by the neighbouring Mn ions.[132, 117]

5.3.3 Discussion

The energy resonance scans presented in this section have two main uses. Firstly, the scans are vitally important for identifying the energy of the largest magnetic resonance enhancement to the x-ray scattering signal, which is necessary to establish for all of the other scans performed in this chapter. Secondly, these scans can be used to help analyse the magnetic structure of $DyMn_2O_5$ through monoelectronic, cluster-based multiple scattering calculations, using the program FDMNES. These calculations are covered in section 5.5.1, where the analysis of the magnetic structure of $DyMn_2O_5$ is presented. The observation of a magnetic signal at the O K-edge is also an interesting result of this investigation. Oxygen is not a magnetic

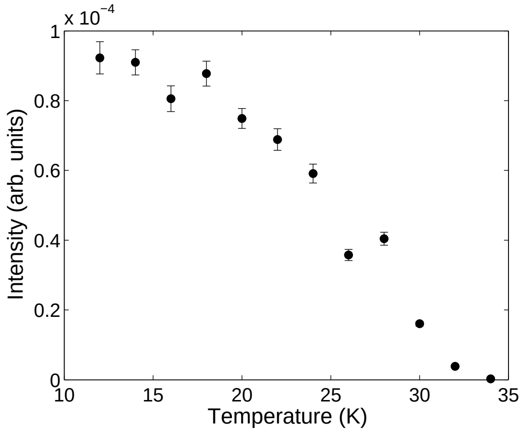

Figure 5.17: Temperature dependence of the intensity of the $(-0.5, 0, 4.25)$ magnetic peak at the resonant Dy L_{III}-edge in the $\sigma\pi'$ polarisation channel.

ion, therefore it was thought to be important to examine this effect further. A temperature dependence of the intensity of the signal at the O K-edge is presented in the next section.

5.4 Temperature Dependence

The four temperature dependencies measured in this study (three scattering measurements at different resonant edges and one measurement of the bulk polarisation) provide some interesting insight into how the physical properties of $DyMn_2O_5$ change with temperature. All of the temperature dependencies link into previous work by various authors and have been useful in performing this study.

5.4.1 Results

A temperature dependence of the integrated intensity was made at the Dy L_{III}-edge, on the $(-0.5, 0, 4.25)$ peak in the $\sigma\pi'$ polarisation channel, over a range of 15 K to 39 K. This shown in Fig. 5.17.

A temperature dependence of the integrated intensity of the $(0.5, 0, 0.25)$ diffraction peak was measured in the $\sigma\pi'$ polarisation channel for both the Mn L_{III}-edge and O K-edge. These are shown in Fig. 5.18 and Fig. 5.19 respectively.

5.4.2 Analysis and Discussion

The temperature dependence of the intensity of $(-0.5, 0, 4.25)$ reflection at the Dy $\mathrm{L_{III}}$-edge in the $\sigma\pi'$-polarisation channel, shown in Fig. 5.17, is in agreement with the earlier work by Ewings et al.[129]. The peak is still observed at temperatures below the transition temperature to LT-ICM phase ($T = 18$K), indeed the intensity of the peak is observed to be highest at the lowest available temperatures measured, 12K. As this measurement is made in the $\sigma\pi'$-channel, the signal is magnetic and therefore suitable for azimuthal scans and full linear polarisation analysis to determine the magnetic structure. For this reason, scans of this type (described in the following section) were performed near the temperature where there was maximum in the observed intensity. The peak is no longer observed above 34K, a few degrees lower than previously observed,[129] but this is probably connected to the beam heating problem with this experiment, as mentioned earlier.

The temperature dependencies of the x-ray scattering peaks in the soft x-ray regime are striking in their agreement with measurements of other physical properties of the system. The temperature dependence of the intensity of $(0.5, 0, 0.25)$ peak measured at the Mn $\mathrm{L_{III}}$-edge in the $\sigma\pi'$-channel appears to agree relatively well with the temperature dependence of the intensity of the neutron diffraction at the $(0.5, 1, 1)$ peak reported by Ratcliff et al. see Fig. 5.18.[128] On warming, both show a steady increase in intensity with temperature, followed by a plateau region spanning $\sim$ 5K and then a decrease in intensity until the temperature is above T_{N} and the signal has disappeared. This agreement between the magnetic x-ray scattering and the neutron diffraction of the similar magnetic reflections is

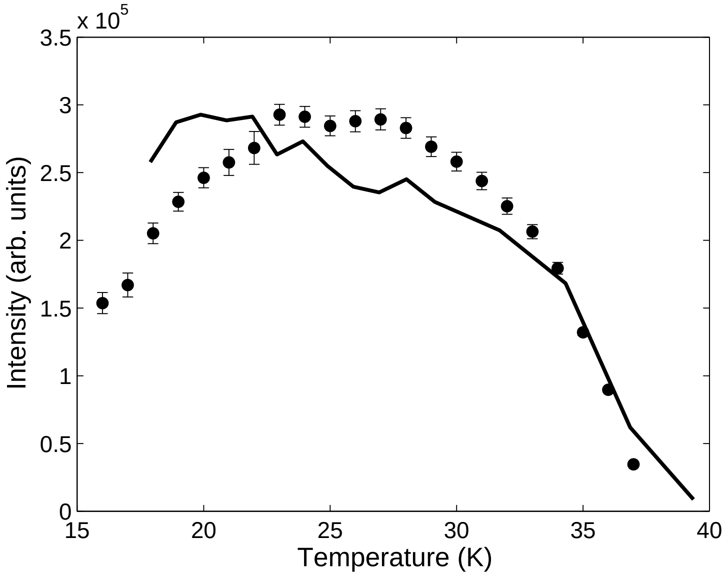

Figure 5.18: The markers show the temperature dependence of the intensity of $0.5, 0, 0.25$ magnetic peak at the Mn L_{III}-edge in $\sigma\pi'$ polarisation channel, offset by 5K from what was actually measured. The line shows the intensity of the neutron scattering from the $(0.5, 1, 1.25)$ peak of $DyMn_2O_5$ measured by Ratcliff et al.[128]

not surprising, but there is an obvious discrepancy ($\sim$ 5K) in the transition temperature and the temperature of the maximum intensity of the scattering in both cases. This is probably due to a systematic error in the thermometry of the experiment performed on RASOR, which was a very new instrument at the time of the experiment. The temperature discrepancy is corrected for in the plot, by simply shifting the x-ray data by 5K.

The temperature dependence of the O K-edge at the $(0.5, 0, 0.25)$ peak in the $\sigma\pi'$-polarisation channel also shows good agreement with a physical property of $DyMn_2O_5$, but in this case it is the ferroelectric polarisation. The agreement between the two can be seen in Fig. 5.19. The temperature of the x-ray scattering signal has been decreased by 5K in the plot, as the same temperature discrepancy arising from the systematic error in the thermometry, mentioned in the previous paragraph, was also present in this experiment. The difference in the temperature

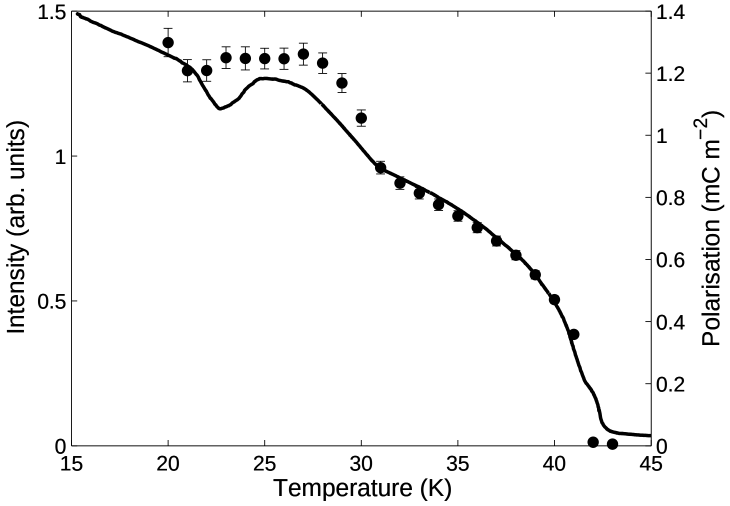

Figure 5.19: The markers show the temperature dependence of the intensity of $0.5, 0, 0.25$ magnetic peak at the O K-edge in $\sigma\pi'$ polarisation channel, offset by 5K from what was actually measured. The line shows the measurement of the electric polarisation measured along the b-axis, from measurements of the pyroelectric current.

dependencies at the different edges suggests that they arise for different reasons as discussed by Partzsch et al. for YMn_2O_5 [117]. The results presented here for the O K-edge appear to reinforce the conclusions of Partzsch et al, that there is an electronic component to the polarisation caused by the valence electrons moving from the Mn to O, rather than by a structural shift of ions, that is important to the ferroelectric moment observed in the RMn_2O_5 materials.

5.5 The Magnetic Structure of $DyMn_2O_5$

Determiniation of the magnetic structure of the commensurate phase in $DyMn_2O_5$ involved the combination of a variety of x-ray magnetic resonance scattering experiments, all from the hard x-ray experiment performed at ESRF, and analytical techniques. The magnetic ordering of the Dy^{3+} and Mn^{4+} sublattices was determined using data from azimuthal scans and full linear polarisation analysis (FLPA) performed at the Dy L_{III}-edge. The ordering of the Mn^{3+} sublattice is determined from an azimuthal scan at the Mn K-edge. These different techniques are all covered in section 2.4. The ordering of all magnetic ions is confirmed by *ab initio* calculations of the resonance spectrum around the Dy L_{III}-edge.

5.5.1 Results

To perform azimuthal scans the incoming polarization is kept constant, but the crystal is rotated around the scattering vector. Integrated intensity is then measured as a function of azimuthal angle. This technique has been used to determine details of the magnetic structure in the related materials $TbMnO_3$ [133, 47], $HoMn_2O_5$ [134] and $TbMn_2O_5$ [45].

All of the azimuthal scans were performed on the CM-FE phase magnetic structure, conducted at 15 K in the $\sigma\pi'$ x-ray polarization channel. Five azimuthal scans were measured, four at the Dy L_{III}-edge, at wavevectors $(-0.5, 0, 4.25)$, $(-1.5, 0, 3.25)$, $(0.5, 1, 4.25)$ and $(0.5, 2, 5.25)$, and one at the Mn K-edge (at wavevector $(0.5, 1, 3.25)$), giving a full picture of the magnetic scattering due to the different ion species in the system. The Dy L_{III}-edge scans are shown in Fig. 5.20–5.23 and the Mn K-edge is shown in Fig. 5.24.

In the azimuthal scans, it is important to have an accurate absorption correction. The signal is attenuated when the beam traverses the sample. Since the crystal is being rotated in the beam, the angles of the incident and outgoing x-ray beam are changing with respect to the crystal surface, and therefore the path length through the crystal is also changing. The absorption is calculated using the formula,

$$\mu = 1 + \frac{\sin(\alpha)}{\sin(\beta)}, \tag{5.1}$$

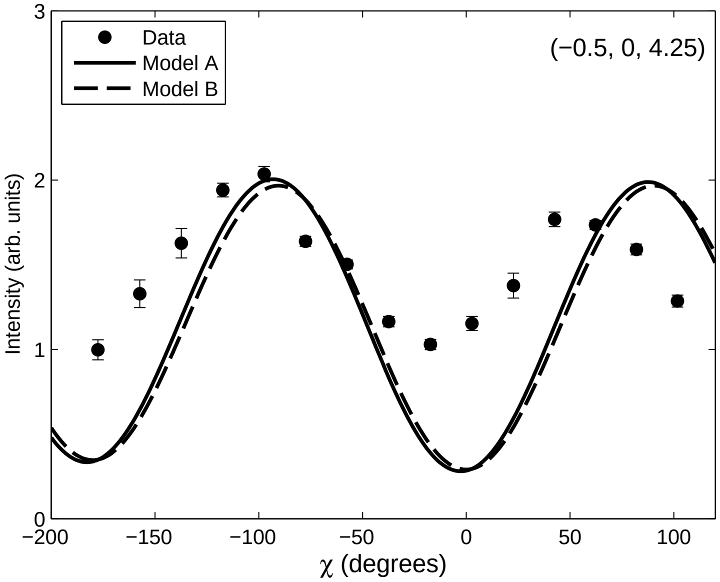

Figure 5.20: Azimuthal scan performed at the Dy L_{III}-edge, on the $(-0.5, 0, 4.25)$ peak, at 15K in the $\sigma\pi'$-polarisation channel

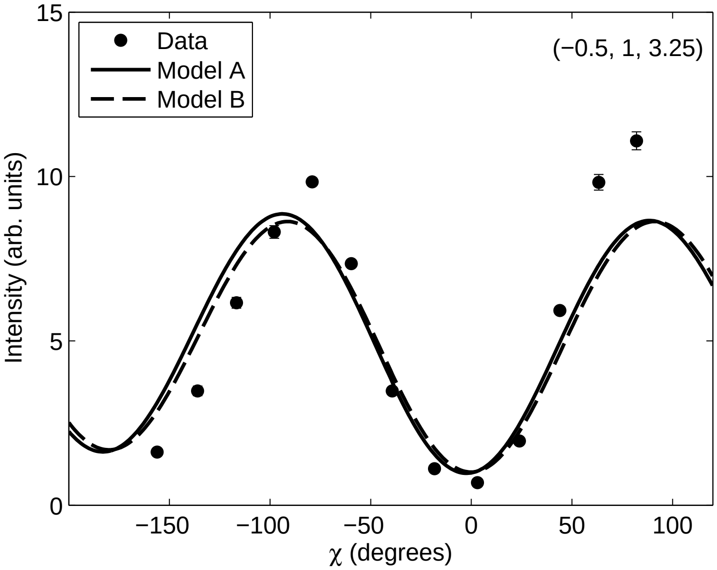

Figure 5.21: Azimuthal scan performed at the Dy L_{III}-edge, on the $(-1.5, 0, 3.25)$ peak, at 15K in the $\sigma\pi'$-polarisation channel

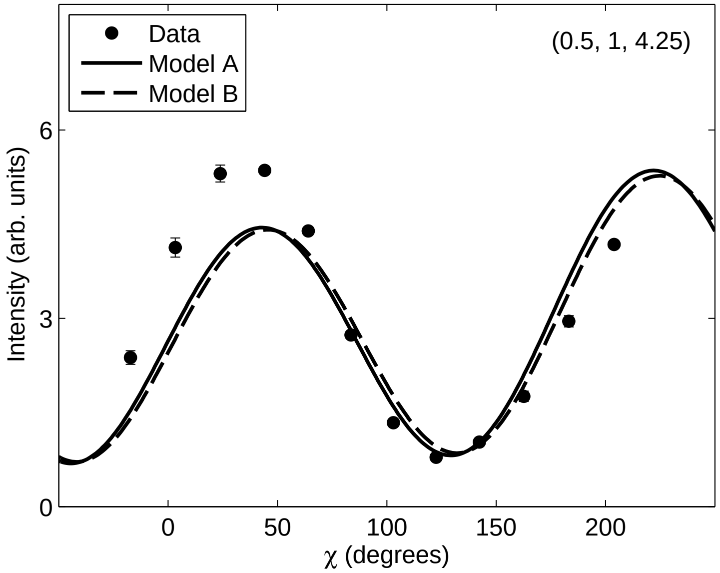

Figure 5.22: Azimuthal scan performed at the Dy L$_{\mathrm{III}}$-edge, on the $(0.5, 1, 4.25)$ peak, at 15K in the $\sigma\pi'$-polarisation channel

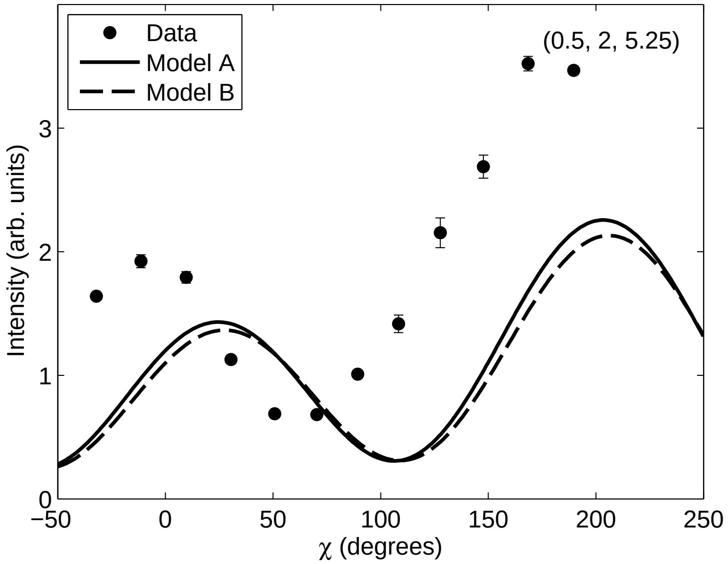

Figure 5.23: Azimuthal scan performed at the Dy L$_{\mathrm{III}}$-edge, on the $(0.5, 2, 5.25)$ peak, at 15K in the $\sigma\pi'$-polarisation channel

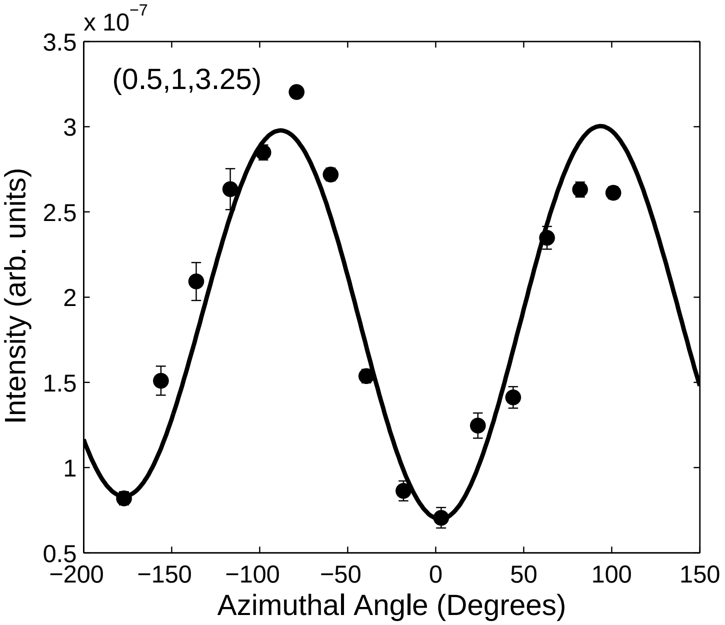

Figure 5.24: Azimuthal scan performed at the Mn K-edge, on the $(0.5, 1, 3.25)$ peak, at 15K in the $\sigma\pi'$-polarisation channel

where α is the angle of incidence of the incoming x-ray beam and β the angle of incidence for the outgoing beam,.

Another method used to determine the magnetic structure at 15K, is full linear polarisation analysis (FLPA). With this method the incoming polarization is varied by use of diamond phase-plates, while keeping the sample in a fixed position, discussed in Johnson et. al.[45] This has two advantages over the azimuthal scan. First the absorption does not vary during the measurement, and second, the sample does not move so the same part of the sample is always measured.

The FLPA in this experiment, was performed on the $(-0.5, 0, 4.25)$ reflection at 15K and was measured at the Dy L_{III}-edge. The angle of the incoming polarization, χ, is set so that $\chi = 0$ corresponds to σ polarised light (and therefore π polarised light is at $\chi = 90°$). For each value of incoming polarization measured, an analysis of the outgoing polarization was performed. The integrated intensity (I) of the

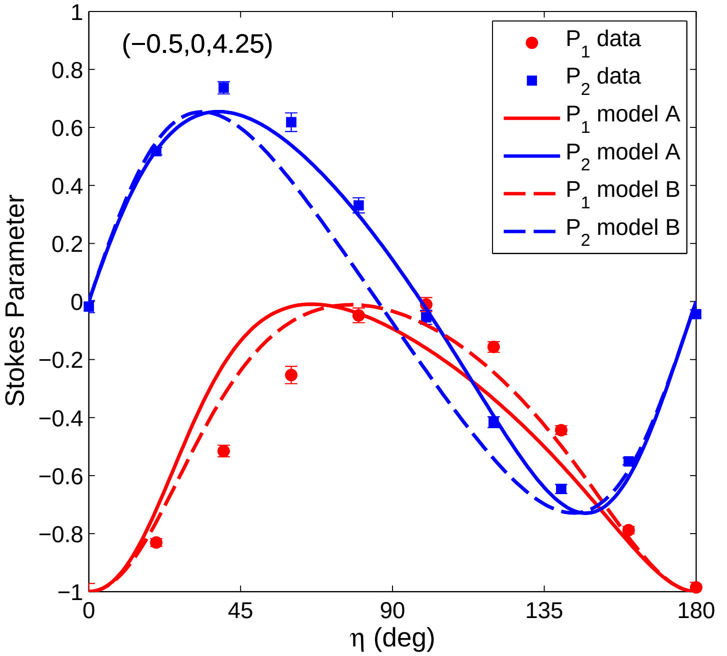

Figure 5.25: The first two Stokes parameters, shown as a function of the incident polarisation χ. These measurements are made at the Dy L_{III}-edge, on the $(-0.5, 0, 4.25)$ peak, at 15K

outgoing x-ray beam is measured at a range of analyser angles (η), which obeys the relationship,

$$I = \frac{I_0}{2}(1 + P_1 \cos(2\eta) + P_2 \sin(2\eta)), \tag{5.2}$$

where I_0 is the intensity of the incident beam and P_1 and P_2 are the first two Stokes parameters. For each angle of incident polarisation, χ, the first two Stokes parameters were calculated and are shown in Fig. 5.25. The relationship between the incoming polarization and the Stokes parameters is dependent on the magnetic structure of the sample.[45]

5.5.2 Analysis

To determine the magnetic ordering in $DyMn_2O_5$, the analysis is broken into three parts. The magnetic ordering on the Dy^{3+} and Mn^{4+} sites was determined from a fit to the four azimuthal scans and the FLPA χ scan performed at the Dy L_{III} edge. Having obtained the Mn^{4+} magnetic structure, the ordering on the Mn^{3+} ions was determined from a fit to the azimuthal scan at the Mn K edge. Finally, the validity of the results was confirmed by comparing the energy scans over the Dy L_{III} edge with *ab initio* calculations. These calculations were performed by Roger Johnson. The entire procedure is explained in this section.

X-ray magnetic scattering at the Dy L_{III} edge probes the empty Dy $5d$ states. The magnetic polarization of the $5d$ states arises not only from the localized Dy $4f$ moments but also from the Mn^{4+} moments due to the overlap between the extended Dy $5d$ states and the Mn^{4+} $3d$ orbitals. This contribution of the Mn^{4+} structure at a rare-earth metal $L-$edge was observed in the experiment on $TbMn_2O_5$ by Johnson et al.[45] This effect is discussed in section 2.4.2 The Mn^{3+} ions are thought to have a negligible contribution at the Dy L_{III} edge, as they are situated further from the Dy ions in the crystal structure.

The crystal structure of the RMn_2O_5 compounds is described by the space group *Pbam*. Previous work has shown that at low temperatures the spontaneous magnetic ordering of the R sublattice, does not always have the same symmetry as that of the Mn sublattice. Following work on $TbMn_2O_5$ and $HoMn_2O_5$ [125, 45], the direction of the Dy^{3+} moments on pairs of sites were constrained to be the same. Specifically, sites (1,2) have one moment direction and sites (3,4) have another moment direction (see Table 5.1 for the positions of the sites), and the size of all the Dy^{3+} moments is constrained to be the same. For the Mn magnetic order the same structure was assumed that has been found many times previously [126]. Initially, the component of the ordered moments along the c direction was neglected, which is reasonable given that the magnetic structures of other RMn_2O_5 compounds have only a small c-axis component. With these assumptions, the Dy^{3+}/Mn^{4+} magnetic structure is described by three free parameters, two in-plane angles for Dy^{3+} and one in-plane angle for Mn^{4+}. One more parameter must also be condisered, α, the ratio of contribution to the signal from Mn^{4+} and Dy^{3+} sublattices.

The fit to the data at the Dy $L_{\rm III}$-edge was performed simultaneously to the four azimuthal scans and the FLPA χ scan and the fit results are shown by the solid line (model A) in the figures Figs. 5.20–5.23 and 5.25. The free parameters in the fit were the three in-plane angles of the ordered moments (one for each of the inequivalent Dy sites, and one for the Mn^{4+}site) and the fraction α of the Mn^{4+} contribution to the signal (the remainder coming from the Dy^{3+}). The best fit was achieved with $\alpha = 0.64(7)$. It is noted that it is not possible to obtain a good fit to the Dy $L_{\rm III}$-edge data allowing only Dy^{3+} ions with this model ($\alpha = 0$), nor is it possible using only Mn^{4+}ions in the model ($\alpha = 1$).

At the Mn K-edge, the empty $4p$ states of the Mn ions are probed, but the magnetism is carried by the 3d electrons. The Mn K-edge scan is mainly sensitive to the Mn^{4+} and Mn^{3+} moments, and we assume the contribution from the Dy moments is negligible because the Dy $4f$ and Mn $4p$ states are highly localized. Mn K-edge azimuthal scan was fitted to a model for the magnetic ordering of the Mn^{3+} ions assuming the magnetic structure of the Mn^{4+} ions determined previously from the data at the Dy $L_{\rm III}$-edge. The process to determine the ratio β of the contribution to the signal from Mn^{3+} to Mn^{4+} was the same as that described in the previous paragraph for α. The best fit is shown in Fig. 5.24 and had $\beta = 0.55(2)$ as the fraction of the signal arising from the Mn^{3+} ions.

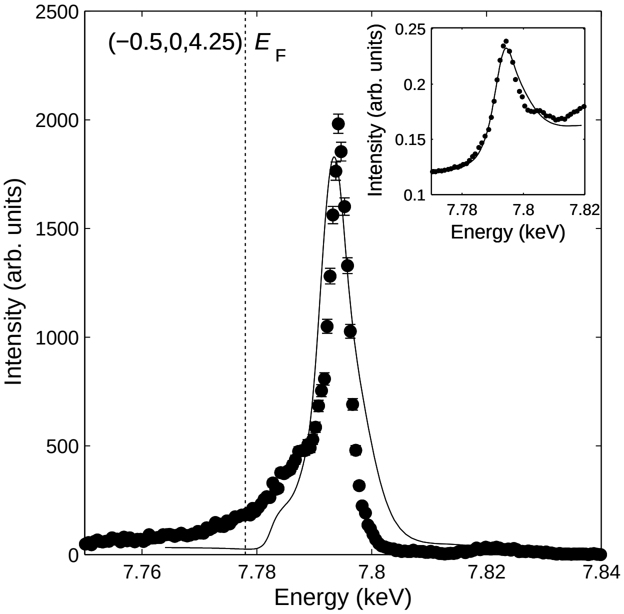

Figure 5.26: Energy resonance through the Dy L$_{\text{III}}$-edge (black circles) with the FDMNES calculation of model A (line). The inset shows the Dy L$_{\text{III}}$-edge fluorescence and the FDMNES calculation.

Using this method, several equally good fits of the azimuthal and FLPA χ scans were found. However, all but one of the models could be dismissed from analysis of Dy L_{III}-edge resonant energy spectrum. To differentiate between these magnetic structure models, *ab-initio* calculations of the Dy L_{III}-edge resonance at the $(-0.5, 0, 4.25)$ reflection were performed. The FDMNES code was employed,[135] which performs a monoelectronic, cluster-based multiple scattering calculation, well suited to the prediction of resonant spectra that involve excitations into delocalized (rare-earth 5d) states. A 256 atom, $2a \times b \times 4c$ supercell (the magnetic unit cell) was defined, containing 32 Dy atoms, located on 8 symmetry inequivalent sites. A cluster radius of 4.5 Å was selected, above which no improvement in the calculation accuracy was observed. First, the absolute energy scale was calibrated by calculating the Dy L_{III} absorption spectra and comparing to the experimentally measured fluorescence, shown in the inset of Fig. 5.26. The Fermi energy was then set at

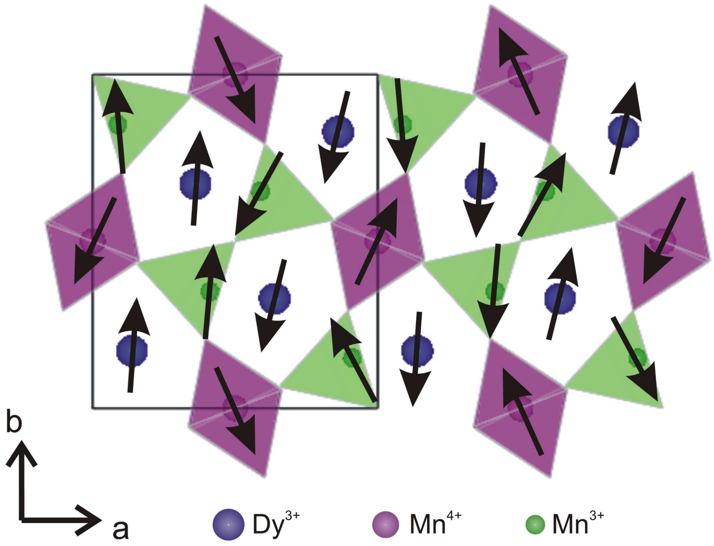

Figure 5.27: The *ab*-plane of model A magnetic structure of $DyMn_2O_5$ in the CM-FE phase.

$E_F = 7.778$ keV, giving a low energy cut-off. The resonance was then calculated with both E1–E1 and E2–E2 excitation channels allowed. The E2–E2 excitation, however, gave a negligible contribution to the resonant intensity and was therefore omitted from the final calculations. By comparing calculations based on the possible magnetic structure models it was clear that only one model properly reproduced the resonant energy spectrum, with this one shown in Fig. 5.26. Each of the other models were found to be unsuitable as the line shape did not match the measured resonance, the other models predicted either too narrow or too broad a peak at the resonance.

The most successful magnetic structure after modeling with FDMNES is referred to as model A, shown in the table 5.1 and is the magnetic structure superimposed upon the crystal structure in Fig. 5.27, viewed in the *ab*-plane. This magnetic structure shows only the component of the magnetic moments in the *ab*-plane and the results are presented as an angle in degrees measured from the *a*-axis. The

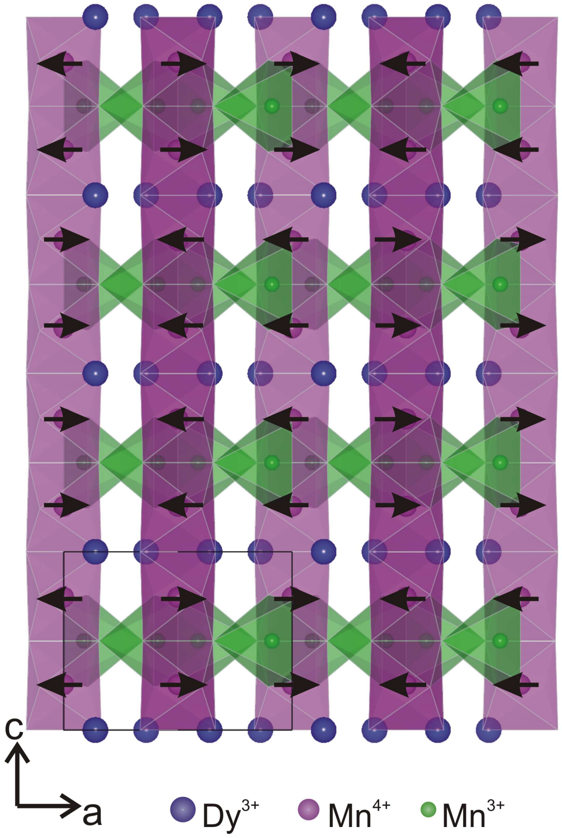

Figure 5.28: Magnetic structure of $DyMn_2O_5$ when observed parallel to the *b*-axis

layers stack with alternating ferromagnetic and antiferromagnetic coupling. This gives the ↑↓↓↑ magnetic ordering along the c-axis that is observed in other RMn_2O_5 materials. This ordering is seen in the side on view shown in Fig. 5.28, which shows one magnetic unit cell.

The fact that the temperature at which these experiments were performed (15 K) is above the spontaneous ordering temperature for Dy (8 K) suggests that any ordered magnetic moments on the Dy sites are induced by the magnetic order of the Mn sublattice. This should mean that ordering on the Dy sites has the same symmetry as the Mn magnetic structure. However, this symmetry constraint is not applied in model A. Therefore, a second model was tested (model B) with the moments on the Dy ions following the same symmetry as the Mn moments.

Table 5.1: The two possible models for the magnetic structure of DyMn$_2$O$_5$ at 15 K, in the commensurate antiferromagnetic and ferroelectric phase. The positions of the ions have been determined elsewhere [119]. The measured moment directions lie in the ab-plane and are specified by the angle from the a-axis, ϕ_A for model A and ϕ_B for model B.

Atom	x	y	z	ϕ_A (deg)	ϕ_B (deg)
Mn^{4+} (1)	0	0.5	0.2521	246(3)	246(3)
Mn^{4+} (2)	0	0.5	0.7479	246(3)	246(3)
Mn^{4+} (3)	0.5	0	0.2521	294(3)	294(3)
Mn^{4+} (4)	0.5	0	0.7479	294(3)	294(3)
Mn^{3+} (1)	0.0759	0.8447	0.5	95.2(0.7)	95.2(0.7)
Mn^{3+} (2)	0.4241	0.3447	0.5	85.8(0.7)	85.8(0.7)
Mn^{3+} (3)	0.5759	0.6553	0.5	241.2(0.2)	241.2(0.2)
Mn^{3+} (4)	0.9241	0.1553	0.5	118.8(0.2)	118.8(0.2)
Dy^{3+} (1)	0.1389	0.1729	0	86.3(10)	71(5)
Dy^{3+} (2)	0.3611	0.6729	0	86.3(10)	109(5)
Dy^{3+} (3)	0.6389	0.3271	0	256.2(10)	246(4)
Dy^{3+} (4)	0.8611	0.8271	0	256.2(10)	66(4)

In model B, the Dy moments are still considered in pairs, but rather than being parallel, as in model A, the moments in each pair are related by either a b-glide or a b'-glide. Under these constraints the best fit to the data at the Dy L$_{\mathrm{III}}$ edge is found when $\alpha = 0$, meaning that only the magnetic moments at the Dy sites contribute to the signal. The calculated azimuthal and FLPA χ scans for this fit are shown in Figs. 5.20–5.23 and 5.25 with a broken line. These are obviously very similar to the fits with model A also presented in these figures. The value of the reduced χ^2 is about 3% higher for the best fit to model B when compared to the best fit to model A. An FDMNES simulation (Fig. 5.29) assuming the best-fit model B structure is consistent with the measured Dy L_{III} edge resonance at the $(-0.5, 0, 4.25)$ reflection. Fig. 5.30 depicts the model B magnetic structure.

The experimental geometry used meant that there was limited sensitivity to the component of the magnetic moment parallel to the c-axis. Test models in which a c-axis component was added by hand confirmed this insensitivity. This insensitivity

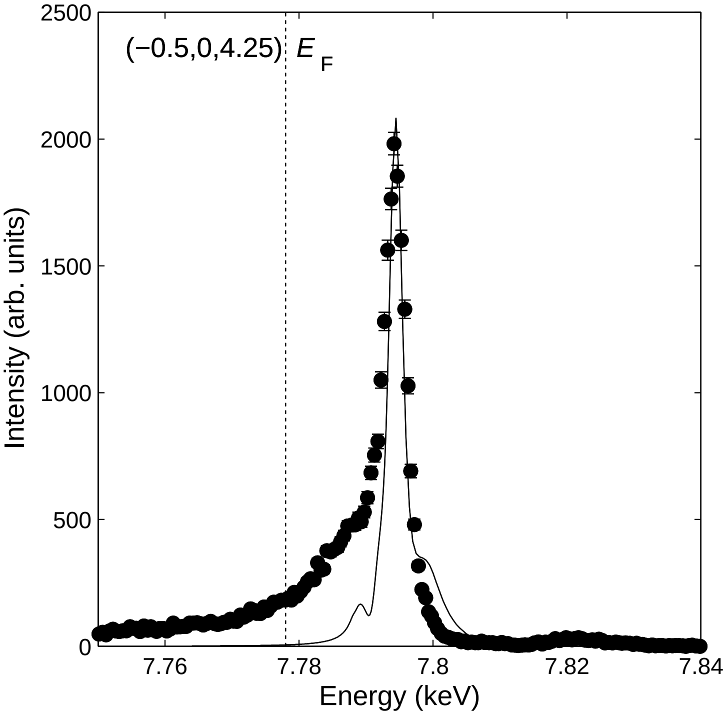

Figure 5.29: Energy resonance through the Dy L$_{\mathrm{III}}$-edge with FDMNES calculation of model B shown.

is caused by the relatively small angles that the chosen scattering vectors make with the *c*-axis. However, it is not possible to rule out a small *c*-axis component to the ordered moments, although as noted earlier, in other RMn$_2$O$_5$ compounds the moments lie predominantly in the *ab*-plane.

5.5.3 Discussion

The two models that have been identified are different. However, with the exception of one moment on a Dy site they have a similar overall character. The Dy ions are not spontaneously ordered at this temperature which may make it more difficult to determine the Dy structure in comparison to the Mn structure.

The magnetic structure of the Mn ions, found here for the ferroelectric phase,

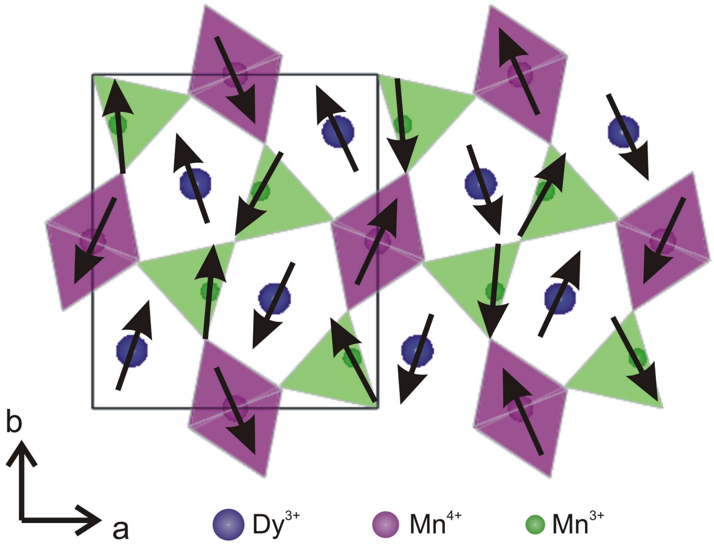

Figure 5.30: The *ab*-plane of model B magnetic structure of DyMn$_2$O$_5$ in the CM-FE phase.

is similar to the magnetic structure of the Mn ions found in DyMn$_2$O$_5$ in the Dy-ordered phase by previous studies [124, 119]. The structure shows approximately antiferromagnetic chains running parallel to the a-axis, a common feature of the RMn$_2$O$_5$ series that agrees with the magnetic exchanges discussed elsewhere [32, 124]. However, one distinct difference between DyMn$_2$O$_5$ and the other members of the RMn$_2$O$_5$ series is that in the ferroelectric phase measured here, the magnetic moments are aligned close to parallel with the *b*-axis. This is in contrast to the other members of the series which tend to have the magnetic moments approximately parallel to the *a*-axis.

The best fit model obtained (model A) breaks the space group symmetry on the Dy site. In this model, the Dy moments occur in ferromagnetically-aligned pairs. This is similar to the rare-earth magnetic ordering in TbMn$_2$O$_5$, [45], but in contrast to that in HoMn$_2$O$_5$ [125]. However, at 15 K, the material is above the spontaneous magnetic ordering transition temperature of the Dy ions, so at this temperature it would be expected that any static order of the Dy moments would be induced by coupling to the Mn sublattice and would therefore have the same symmetry as the Mn magnetic order. This is the case for model B (by construction) but not for model A. Therefore, if model A describes the correct structure, then the implication is that the Dy–Dy magnetic interactions remain a sufficiently strong influence at 15 K to prevent the Dy magnetic order from adopting the same symmetry as the Mn magnetic order.

The differences between the Dy magnetic structures of model A and model B are actually relatively small. In model A, the Dy moment on site 4 is parallel to that on site 3, whereas in model B the moments on sites 3 and 4 are approximately antiparallel (see Fig. 5.27 and Fig. 5.30). The other Dy moments are found to have only a slight difference in their angle to the a-axis between the two models. In both models the Dy moments are close to parallel with the b-axis, again in contrast to the observations of other members of the RMn_2O_5 series.

There are a few noteworthy features of the fit itself. The fit successfully describes three out of four of the Dy L_{III}-edge azimuthal scans, but does not adequately describe the azimuthal scan at $(0.5, 2, 5.25)$. When treating this scan independently of all other scans, there were no physically realistic model that could describe the observed azimuthal dependence. One possibility is that there is a systematic error due to sample absorption. Of the reflections studied, the wavevector $(0.5, 2, 5.25)$ is the furthest from the surface normal of the crystal, so the absorption of the photons in the sample will vary considerably throughout the scan. However, calculations indicate that the variation in absorption is not significantly greater than at the other reflections.

In the FLPA χ-scan, around the point $\chi = 90^\circ$, P_1^2 and P_1^2 both tend to zero. The parameter P_1 describes the polarization perpendicular and parallel to the scattering plane and P_2 the polarization at ±45° to the scattering plane. The two parameters therefore characterise the linear polarization, with $P_{lin} = \sqrt{P_1^2 + P_2^2}$. There is a third parameter, P_3, which is related to the circular polarization. The magnitude of the Stokes vector (P_1, P_2, P_3) should be equal to one for polarized light. It is obvious that at $\chi = 90°$, $P_{lin} \neq 1$ (Fig. 5.25). The data suggests that the beam is either depolarized or there is a circular component to the polarization. This effect has been observed before and was explained by a non-zero P_3, giving a circular component to the outgoing beam.[136, 137, 138]

5.6 Conclusions and Further Work

This work has investigated the magnetic and ferroelectric properties of the multiferroic $DyMn_2O_5$. Two alternative, but similar models for the magnetic structure in the ferroelectric phase of the material have been presented, that provide a good description of the experimental data. The symmetry of the rare-earth and Mn magnetic structure in $DyMn_2O_5$ is the same as that found in the other RMn_2O_5 compounds. A key difference between $DyMn_2O_5$ and the other RMn_2O_5 materials is the fact that the magnetic moments in $DyMn_2O_5$ are approximately aligned parallel to the *b*-axis, in contrast to the *a*-axis alignment observed in other RMn_2O_5 compounds. This study has gone some way to confirming that there is a contribution to the ferroelectric polarisation coming from a transfer of the valence electrons from the Mn sites to the O sites.

There are a few studies that could be performed to build upon this work. Another measurement of the azimuthal scan that agreed poorly with the model might determine whether this was a systematic experimental error. An experiment performed with a different crystal surface normal may be able to determine the *c*-axis component of the magnetic structure. Any further measurements could also lead to being able to distinguish between the two proposed magnetic models. The intensity of the $(0.5, 0, 0.25)$ reflection in O K-edge was measured only above ~ 15K. Extending this to lower temperatures would be of interest to observe how closely the agreement between the intensity and the polarisation holds as temperature decreases out of the ferroelectric phase.

Bibliography

[1] J. Orenstein and A. J. Millis. Advances in the physics of high-temperature superconductivity. *Science*, 288:468, 2000. (Cited on page 1.)

[2] D. Khomskii. Classifying multiferroics: Mechanisms and effects. *Phyiscs*, 2:20, 2009. (Cited on pages 1, 2, 18, 19 and 192.)

[3] L. X. Zheng, M. J. O'Connell, S. K. Doorn, X. Z. Liao, Y. H. Zhao, E. A. Akhadov, M. A. Hoff bauer, B. J. Roop, Q. X. Jia, R. C. Dye, D. E. Peterson, S. M. Huang, J. Liu, and Y. T. Zhu. Ultralong single-wall carbon nanotubes. *Nature Materials*, 3:673–676, 2004. (Cited on page 1.)

[4] J. G. Bednorz and K. A. Müller. Possible high t_c superconductivity in the ba-la-cu-o system. *Zeitschrift für Physik B Condensed Matter*, 64:189–193, 1986. (Cited on page 1.)

[5] A. P. Malozemoff. High t_C for the power grid. *Nature Materials*, 6:617–619, 2007. (Cited on page 2.)

[6] Aristotle. *De Anima*. Cosimo, Inc, 2008. (Cited on page 2.)

[7] A. P. Ramirez. Colossal magnetoresistance. *Journal of Physics: Condensed Matter*, 9:8171, 1997. (Cited on pages 2 and 17.)

[8] J. M. D. Coey, M. Viret, and S. von Molnár. Mixed-valence manganites. *Advances in Physics*, 48:167–293, 1999. (Cited on pages 2 and 17.)

[9] E. Chamlin, C. Vignaud, H. Salomon, F. Farges, J. Susini, and M. Menu. Minerals discovered in paleolithic black pigments by transmission electron

microscopy and micro-x-ray absorption near-edge structure. *Applied Physics A*, 83:213–218, 2006. (Cited on page 3.)

[10] Y. Tokura. Critical features of colossal magnetoresistive manganites. *Reports on Progress in Physics*, 69:3, 2006. (Cited on pages 3, 4, 17, 63 and 167.)

[11] E. Pollert, S. Krupička, and E. Kuzmičová. Structural study of $\mathrm{Pr}_(1-x)\mathrm{Ca}_x\mathrm{MnO}_3$ and $\mathrm{Y}_{1-x}\mathrm{Ca}_x\mathrm{MnO}_3$ perovskites. *Journal of Physics and Chemistry of Solids*, 43:1137, 1982. (Cited on page 3.)

[12] G-M. Zhao, K. Conder, H. Keller, and K. A. Müller. Giant oxygen isotope shift in the magnetoresistive perovskites $\mathrm{La}_{1-x}\mathrm{Ca}_x\mathrm{MnO}_{3+y}$. *Nature*, 381:676, 1996. (Cited on page 3.)

[13] C. Zener. Interaction between the d-shells in the transition metals. ii. ferromagnetic compounds of manganese with perovskite structure. *Physical Review*, 82:403–405, 1951. (Cited on pages 3 and 64.)

[14] C. Zener. Interaction between the d shells in the transtion metals. *Physical Review*, 81:440, 1951. (Cited on page 3.)

[15] E. O. Wollan and W. C. Koehler. The diffraction study of the magnetic properties of the series of perovskite-type compounds [(1-x)La, xCa]MnO_3. *Physical Review*, 100:545–563, 1955. (Cited on pages 3, 4, 14, 15, 63, 64, 66 and 119.)

[16] T. Kiruma, T. Goto, H. Shintani, K. Ishizaka, T. Arima, and Y. Tokura. Magnetic control of ferroelectric polarization. *Nature*, 426:55–58, 2003. (Cited on pages 3, 18, 19 and 192.)

[17] J. B. Goodenough. Theory of the role of covalence in the perovskite-type

manganites [La, M(II)]MnO_3. *Physical Review*, 100:564–573, 1955. (Cited on pages 4, 63, 64, 97, 119 and 185.)

[18] S. Blundell. *Magnetism in Condensed Matter*. Oxford University Press, 2001. (Cited on pages 6, 11 and 12.)

[19] K. W. H. Stevens. Matrix elements and operator equivalents comnnected with the magnetic properties of rare earth ions. *Proceedings of the Physical Society. Section A*, 65:209, 1952. (Cited on page 6.)

[20] H. A. Jahn and E. Teller. Stability of polyatomic molecules in degenerate electronic states. *Proceedings of the Royal Society A: Mathematical, Physical and Engineering Sciences*, 161:220–235, 1937. (Cited on page 8.)

[21] B. J. Sternlieb, J. P. Hill, U. C. Wildgruber, G. M. Luke, B. Nachumi, Y. Morimoto, and Y. Tokura. Charge and magnetic order in $La_{0.5}Sr_{1.5}MnO_4$. *Physical Review Letters*, 76:2169–2172, 1996. (Cited on pages 9, 64, 121, 123, 126, 130 and 131.)

[22] H. Ulbrich and M. Braden. Neutron scattering studies on stripe phases in non-cuprate materials, January 2012. (Cited on page 10.)

[23] Y. Tokunaga, T. Lottermoser, Y. Lee, R. Kumai, M. Uchida, T. Arima, and Y. Tokura. Rotation of orbital stripes and consequent charge-polarized state in bilayer manganites. *Nature Materials*, 5:937–941, 2006. (Cited on pages 10, 64, 65, 68, 69, 77 and 89.)

[24] Y. Tokura and N. Nagaosa. Orbital physics in transition-metal oxides. *Science*, 288:462–468, 2000. (Cited on page 10.)

[25] C. Kittel. *Introduction to Solid State Physics*. John Wiley and Sons, 1996. (Cited on page 16.)

[26] E. Dagotto, T. Hotta, and A. Moreo. Colossal magnetoresistant materials: The key role of phase seperation. *Physica Reports*, 344:1–153, 2000. (Cited on page 17.)

[27] M. B. Salamon and M. Jaime. The physics of manganites: Structure and transport. *Reviews of Modern Physics*, 73:583, 2001. (Cited on page 17.)

[28] S. W. Cheong and M. Mostovoy. Multiferroics: a magnetic twist for ferroelectricity. *Nature Materials*, 6:13, 2007. (Cited on pages 18, 19 and 192.)

[29] T. Katsufuji, S. Mori, M. Masaki, Y. Morimoto, N. Yamamoto, and H. Takagi. Dielectric and magnetic anomalies and spin frustration in hexagonal $r\mathrm{mno}_3$ (r=y, yb, and lu). *Physical Review B*, 64:104419, 2001. (Cited on page 19.)

[30] N. Ikeda, H Ohsummi, K. Ohwada, K. Ishii, T. Inami, K. Kakurai, Y. Murakami, K. Yoshii, S. Mori, and Y. Horibe. Ferroelectricity from iron valence ordering in the charge-frustrated system $\mathrm{lufe}_2\mathrm{o}_4$. *Nature*, 436:1136, 2005. (Cited on page 19.)

[31] I. E. Dzyaloshinskii. Magnetoelectricity in ferromagnets. *Europhysics Letters*, 83:67001, 2008. (Cited on page 19.)

[32] L. C. Chapon, G. R. Blake, M. J. Gutmann, S. Park, N. Hur, P. G. Radaelli, and S-W. Cheong. Structural anomalies and multiferroic behavior in magnetically frustrated $\mathrm{TbMn}_2\mathrm{O}_5$. *Phyiscal Review Letters*, 93:177402, 2004. (Cited on pages 19 and 227.)

[33] G. L. Squires. *Introduction to the Theory of Neutron Scattering*. Dover Publications, 1997. (Cited on pages 23, 24, 27 and 29.)

[34] B. T. M. Willis and C. J. Carlile. *Experimental Neutron Scattering*. Oxford University Press, 2009. (Cited on pages 23, 24, 35, 36, 37 and 42.)

[35] J. Als-Nielsen and D. McMorrow. *Elements of Modern X-ray Physics*. Wiley-Blackwell, 2000. (Cited on pages 23, 47 and 57.)

[36] J. Chadwick. The existence of a neutron. *Proceedings of the Royal Society*, A136:692–708, 1932. (Cited on page 24.)

[37] D. P. Mitchell and N. Powers. Bragg reflection of slow neutrons. *Physical Review*, 50:486–487, 1936. (Cited on page 24.)

[38] H. von Halban and P. Preiswerk. Preuve experimental de la diffraction des neutrons. *C. R. Acad. Sci. Paris*, 203:73–75, 1936. (Cited on page 24.)

[39] B. Roessli and P. Böni. *Scattering: Scattering and Inverse Scattering in Pure and Applied Science*. Academic Press, 2002. (Cited on page 28.)

[40] T. Chatterji, R. Ballou, B. Ouladdiaf, J. Schweizer, P. J. Brown, L. P. Regnault, C. F. Majkrzak, K. V. O'Donovan, N. F. Berk, A. Wiedenmann, C. Pappas, G. Ehlers, and F. Mezei. *Neutron Scattering from Magnetic Materials*. Elsevier, 2006. (Cited on pages 32, 125 and 151.)

[41] M. Altarelli. Resonant x-ray scattering: A theoretical introduction. *Lecture Notes in Physics*, 697:201–242, 2006. (Cited on pages 47 and 50.)

[42] F. de Bergevin and M. Brunel. Observation of magnetic superlattice peaks by x-ray diffraction on an antiferromagnetic NiO crystal. *Physics Letters A*, 39:141–142, 1972. (Cited on page 49.)

[43] M. Blume and D. Gibbs. Polarization dependence of magnetic x-ray scattering. *Physical Review B*, 37:1779, 1988. (Cited on pages 49, 54, 198 and 200.)

[44] J. P. Hill and D. F. McMorrow. X-ray resonant exchange scattering: Polarisation dependence and correlation functions. *Acta Crystallographica*, A52:236–244, 1996. (Cited on pages 49, 51, 54, 198 and 200.)

[45] R. D. Johnson, S. R. Bland, C. Mazzoli, T. A. W. Beale, C-H Du, C. Detlefs, S. B. Wilkins, and P. D. Hatton. Determination of magnetic order of the rare-earth ions in multiferroic $TbMn_2O_5$. *Physical Review B*, 78:104407, 2008. (Cited on pages 53, 54, 193, 207, 215, 218, 219, 220 and 227.)

[46] R. Caciuffo, L. Paolasini, A. Sollier, P. Ghinga, F. Pavarini, J. van den Brink, and M. Altarelli. Resonant x-ray scattering study of magnetic and orbital order in kcuf3. *Phyiscal Review B*, 65:174425, 2002. (Cited on page 54.)

[47] D. Mannix, D. F. McMorrow, R. A. Ewings, A. T. Boothroyd, D. Prabahakaran, Y. Joly, B. Janousova, C. Mazzoli, L. Paolasini, and S. B. Wilkins. X-ray scattering study of the order parameters in multiferroic $TbMnO_3$. *Physical Review B*, 76:184420, 2007. (Cited on pages 54 and 215.)

[48] E. Hecht. *Optics, 4th edition*. Addison-Wesley, 2002. (Cited on page 55.)

[49] J. Baruchel, J. L. Hodeau, M. S. Lehmann, J. R. Regnard, and C. Schlenker. *Neutron and Synchrotron Radiation for Condensed Matter Studies*. Springer-Verlag, 1994. (Cited on page 59.)

[50] S. N. Ruddlesden and P. Popper. New compunds of the K_2NiF_4 type. *Acta Crystallographica*, 11:54–58, 1957. (Cited on page 63.)

[51] S. N. Ruddlesden and P. Popper. The compound $Sr_3Ti_2O_7$ and its structure. *Acta Crystallographica*, 11:54–55, 1958. (Cited on page 63.)

[52] R. M. Kusters, J. Singleton, D. A. Keen, R. McGreevy, and W. Hayes. Magnetoresistance measurements on the magnetic semiconductor $Nd_{0.5}Pb_{0.5}MnO_3$. *Physica B*, 155:362–365, 1989. (Cited on page 63.)

[53] J. Kanamori. Superexchange interaction and symmetry properties of electron orbitals. *Journal of Physics and Chemistry of Solids*, 10:87–98, 1958. (Cited on pages 64 and 97.)

[54] D. V. Efremov, J. van der Brink, and D. I. Khomskii. Bond-versus site centred ordering and possible ferroelectricity in manganites. *Nature Materials*, 3:853–856, 2004. (Cited on page 65.)

[55] P. G. Radaelli, D. E. Cox, M. Marezio, and S-W. Cheong. Charge, orbital and magnetic ordering in $La_{0.5}Ca_{0.5}MnO_3$. *Physical Review B*, 55:3015–3023, 1997. (Cited on page 65.)

[56] S. B. Wilkins, P. D. Spencer, P. D. Hatton, S. P. Collins, M. D. Roper, D. Prabahakaran, and A. T. Boothroyd. Direct observation of orbital ordering in $La_{0.5}Sr_{1.5}MnO_4$ using soft x-ray diffraction. *Physical Review Letters*, 91:167205, 2003. (Cited on page 65.)

[57] R. J. Goff and J. P. Attfield. Charge ordering in half-doped manganites. *Physical Review B*, 70:140404, 2004. (Cited on pages 65 and 106.)

[58] S. Grenier, J. P. Hill, Doon Gibbs, K. J. Thomas, M. v. Zimmermann, C. S. Nelson, V. Kiryukhin, Y. Tokura, Y. Tomioka, D. Casa, T. Gog, and C. Venkataraman. Resonant x-ray diffraction of magnetoresistant perovskite

$Pr_{0.6}Ca_{0.4}MnO_3$. *Physical Review B*, 69:134419, 2004. (Cited on pages 65 and 106.)

[59] J. Rodríguez-Carvajal, A. Daoud-Aladine, L. Pinsard-Gaudart, M. T. Fernández-Díaz, and A. Revcolevschi. A new interpretation of the CO state in half-doped manganites: New results from neutron scattering and synchrotron radiation experiments. *Physica B*, 320:1–6, 2002. (Cited on pages 65 and 119.)

[60] A. Daoud-Aladine, J. Rodríguez-Carvajal, L. Pinsard-Gaudart, M. T. Fernández-Díaz, and A. Revcolevschi. Zener polaron ordering in half-doped manganites. *Physical Review Letters*, 89:097205, 2002. (Cited on pages 65 and 119.)

[61] K. J. Thomas, J. P. Hill, S. Grenier, Y-J Kim, P. Abbamonte, L. Venema, A. Rusydi, Y. Tomioka, Y.Tokura, D. F. McMorrow, G. Sawatzky, and M. van Veenendaal. Soft x-ray resonant diffraction study of magnetic and orbital correlations in a manganite near half doping. *Physical Review B*, 92:237204, 2004. (Cited on page 65.)

[62] J. C. Loudon, S. Cox, A. J. Williams, J. P. Attfield, P. B. Littlewood, P. A. Midgley, and N. D. Mathur. Weak charge-lattice coupling requires reinterpretation of stripes of charge order in $La_{1-x}Ca_xMnO_3$. *Physical Review Letters*, 94:097202, 2005. (Cited on page 65.)

[63] V. Ferrari and M. Towler an P. B. Littlewood. Oxygen stripes in $La_{0.5}Ca_{0.5}MnO_3$ from ab initio calculations. *Physical Review Letters*, 91:227202, 2003. (Cited on pages 65, 120, 121, 158, 176, 177, 186, 187 and 188.)

[64] P. Barone, S. Picozzi, and J. van der Brink. Buckling-induced zener polaron in-

stability in half-doped manganites. *Physical Review Letters*, 83:233103, 2011. (Cited on page 65.)

[65] D. Senff, F. Krüger, S. Scheidl, M. Benomar, Y. Sidis, F. Demmel, and M. Braden. Spin-wave dispersion in orbitally ordered $La_{1/2}Sr_{3/2}MnO_4$. *Physical Review Letters*, 96:257201, 2006. (Cited on pages 65, 92, 93 and 97.)

[66] M. García-Fernández, U. Staub, Y. Bodenthin, V. Scagnoli, V. Pomjakushin, S. W. Lovesey, A. Mirone, J. Herrero-Martín, C. Piamonteze, and E. Pomjakushina. Orbital order at Mn and O sites and absence of zener polaron formation in manganites. *Physical Review Letters*, 103:097205, 2009. (Cited on page 65.)

[67] O. Sikora and A. M. Oleś. Ordered phases and magnetic excitations in doped manganites. *Acta Physica Polonica A*, 106:659–664, 2004. (Cited on pages 66 and 102.)

[68] Y. Tokunaga, T. Sato, M. Uchida, R. Kumai, Y. Matsui, T. Arima, and Y. Tokura. Versatile and competing spin-charge-orbital orders in the bilayered manganite system $Pr(Sr_{1-y}Ca_y)_2Mn_2O_7$. *Physical Review B*, 77:064428, 2008. (Cited on pages 68, 69 and 81.)

[69] Y. Tokunaga, R. Kumai, N. Takeshida, Y. Kaneko, J. P. He, T. Arima, and Y. Tokura. Effect of uniaxial stress on orbital stripe direction in half-doped layered manganites: $Eu_{0.5}Ca_{1.5}MnO_4$ and $Pr(Sr,Ca)_2Mn_2O_7$. *Physical Review B*, 155105:78, 2008. (Cited on page 68.)

[70] Y. S. Lee, Y. Tokunaga, T. Arima, and Y. Tokura. Optical detection of the rotation of orbital stripes in a charge-orbital ordered bilayer manganite at half-doping. *Physica B*, 403:1579–1581, 2008. (Cited on page 69.)

[71] Z. A. Li, X. Li, Z. Wang, H. F. Tian, C. Ma, L. J. Zeng, and H. X. Yang. A ”checkerboard” orbital-stripe phase and charge ordering transitions in $Pr(Sr_xCa_{2-x})Mn_2O_7$. *EPL*, 86:67010, 2009. (Cited on page 69.)

[72] T. A. W. Beale, S. R. Bland, R. D. Johnson, P. D. Hatton, J. C. Cezar, S. S. Dhesi, M. V. Zimmermann, D. Prabhakaran, and A. T. Boothroyd. Thermally induced rotation of 3d orbital stripes in $Pr(Sr_{0.1}Ca_{0.9})_2Mn_2O_7$. *Physical Review B*, 79:054433, 2009. (Cited on page 69.)

[73] D. Prabhakaran and A. T. Boothroyd. Single-crystal growth of $la_{2-2x}sr_{1+2x}mn_2o_7$ under pressure. *Journal of Material Science: Materials in Electronics*, 14:587–589, 2003. (Cited on page 70.)

[74] D. Senff, O. Schumann, M. Benomar, M. Kriener, T. Lorenz, Y. Sidis, P. Link, and M. Braden. Melting of mangetic correlations in charge-orbital ordered $La_{1/2}Sr_{3/4}MnO_4$: Competition of ferromagnetic and antiferromagnetic states. *Physical Review B*, 77:184413, 2008. (Cited on pages 77, 94, 123, 125, 126, 128 and 129.)

[75] O. Sikora and A. M. Oleś. Magnetic order and excitations in half-doped manganites. *Physica B*, 359:1300–1302, 2005. (Cited on page 102.)

[76] T. G. Perring, D. T. Adroja, G. Chaboussant, G. Aeppli, T. Kiruma, and Y. Tokura. Spectacular doping dependence of interlayer exchange and other results on spin waves in bilayer manganites. *Phyiscal Review Letters*, 87:217201, 2001. (Cited on page 116.)

[77] R. Maezano, S. Ishihara, and N. Nagaosa. Orbital polarization in manganese oxides. *Physical Review B*, 57:13993, 1998. (Cited on page 119.)

[78] K. I. Kugel and D. Khomskii. *Soviet Physics JETP*, 37:725, 1973. (Cited on page 119.)

[79] H. L. Ju, H.-C. Sohn, and K. M. Krishnan. Evidence for O_{2p} hole-driven conductivity in $La_{1-x}Sr_xMnO_3$ ($0 \leq x \leq 0.7$) and $La_{0.7}Sr_{0.3}MnO_z$ thin films. *Physical Review Letters*, 79:3230, 1997. (Cited on page 120.)

[80] S. Grenier, K. J. Thomas, J. P. Hill, U. Staub, Y. Bodenthin, M. García-Fernández, V. Scagnoli, V. Kiryukhin, S-W. Cheong, B. G. Kim, and j. M. Tonnerre. Direct observation of oxygen superstructures in manganese. *Physical Review Letters*, 99:206403, 2007. (Cited on page 120.)

[81] R. Bastardis, C. de Graaf, and N. Guihéry. *Ab Initio* study of the ce magnetic phase in half-doped manganites: Purely magnetic versus double exchange description. *Physical Review B*, 77:054426, 2008. (Cited on page 120.)

[82] J. Herrero-Martín, A. Mirone, J. Fernández-Rodríguez, P. Glatzel, J. García, J. Blasco, and J. Geck. Hard x-ray probe to study doping-dependent electron redistribution and strong covalency in $La_{1-x}Sr_{1+x}MnO_4$. *Physical Review B*, 82:075112, 2010. (Cited on page 120.)

[83] R. Kraus, M. Scharde, R. Schuster, and M. Knupfer. Signatures of electronic polarons in $La_{1-x}Sr_{1+x}MnO_4$ observed by electron energy-loss spectra. *Physical Review B*, 83:165130, 2011. (Cited on page 120.)

[84] R. J. Papoular and B. Gillon. Maximum-entropy reconstruction of spin-density maps in crystals from polarised neutron-diffraction data. *Europhysics Letters*, 13:429, 1990. (Cited on pages 121, 125 and 152.)

[85] M. Tokunaga, N. Miura, Y. Tomioka, and Y. Tokura. High-magnetic-field

study of the phase transitions of $r_{1-x}ca_xmno_3$ (r =pr, nd). *Physical Review B*, 57:5259, 1998. (Cited on page 122.)

[86] D. Senff, P.Reutler, M. Braden, O. Freidt, D. Bruns, A. Cousson, F. Bouree, M. Merz, B. Buchner, and A. Revcolevschi. Crystal and magnetic structure of $La_{1-x}Sr_{1+x}MnO_4$: Role of orbital degrees of freedom. *Physical Review B*, 71:024425, 2005. (Cited on pages 122, 126 and 184.)

[87] Y. Moritomo, Y. Tomioka, A. Asamitsu, Y. Tokura, and Y. Matsui. Magnetic and electronic properties in hole-doped manganese oxides with layered structures: $La_{1-x}Sr_{1+x}MnO_4$. *Physical Review B*, 51:3297, 1995. (Cited on pages 123, 124, 126, 128 and 130.)

[88] M. Arao, Y. Inoue, K. Toyoda, and Y. Koyama. Transverse and longitudinal lattice modulations in the charge-orbital-ordered manganite $Sr_{2-x}La(_xMnO_4$ around x=0.5. *Physical Review B*, 84:014102, 2011. (Cited on page 123.)

[89] D. Prabhakaran, A. I. Coldea, A. T. Boothroyd, and S. J. Blundell. Growth of large $la_{1-x}sr_xmno_3$ single crystals under argon pressure by the floating-zone technique. *Journal of Crystal Growth*, 237:806, 2002. (Cited on page 125.)

[90] C. Wilkinson, H. W. Khamis, R. F. D. Stansfield, and G. J. McIntyre. Integration of single-crystal reflections using area multidetectors. *Journal of Applied Crystallography*, 21:471, 1988. (Cited on pages 127 and 133.)

[91] P. J. Becker and P. Coppens. Extinction within the limit of validity of the darwin transfer equations. i. general formalism for primary and secondary extinction and their applications to spherical crystals. *Acta Crystallographica A*, 30:127, 1974. (Cited on pages 138 and 139.)

[92] C. G. Shull and Y. Yamada. *Journal of the Physical Society of Japan*, 17 (Supplement BIII):1, 1962. (Cited on page 150.)

[93] S. F. Gull and J. Skilling. Maximum entropy method in image-processing. *IEE Proceedings-F Radar and Signal Processing*, 131:6, 1984. (Cited on page 152.)

[94] A. J. Markvardsen. *Polarised neutron diffraction measurements of $PrBa_2Cu_3O_{6+x}$ and Bayesian statistical analysis of the such data*. PhD thesis, University of Oxford, 2000. (Cited on page 152.)

[95] A. J. Markvardsen, A. T. Boothroyd, B. Buck, G. J. McIntyre, and Th. Wolf. Magnetisation density in single-crystal $\mathrm{PrBa_2Cu_3O_{6+x}}$. *Journal of Magnetism and Magnetic Materials*, 177:502, 1998. (Cited on page 152.)

[96] R. D. Shannon and C. T. Prewitt. Effective inonic radii in oxides and fluorides. *Acta Crystallographica*, B25:925, 1969. (Cited on page 167.)

[97] J. Rodríguez-Carvajal. Recent advances in magnetic structure determination by neutron powder diffraction. *Physica B*, 192:55, 1993. (Cited on page 173.)

[98] P. Curie. Sur la symétrie dans les phénomènes physiques, symétrie d'un champ électrique et d'un champ magnétique. *Journal de Physique Théorique et Appliquée*, 3:393, 1894. (Cited on page 191.)

[99] W. Eerenstein, N. D. Mathur, and J. F. Scott. Multiferroic and magnetoelectric materials. *Nature*, 442:759–765, 2006. (Cited on page 191.)

[100] M. Fiebig. Revival of the magnetoelectric effect. *Journal of Physcis D: Applied Physcis*, 38:123, 2005. (Cited on page 192.)

[101] K. F. Wang, J. M. Liu, and Z. F. Ren. Multiferroicity: the coupling between

mangnetic and polarization orders. *Advances in Physics*, 58:321, 2009. (Cited on page 192.)

[102] E. F. Bertaut and M. Mercier. Magnetoelectricity in theory and experiment. *Materials Research Bulletin*, 6:907–921, 1971. (Cited on page 192.)

[103] I. E. Dzyaloshinskii. On the magneto-electrical effect in antiferromagnets. *Soviet Physics JETP*, 10:628–629, 1960. (Cited on page 192.)

[104] D. N. Astrov. The magnetoelectric effect in antiferromagnets. *Soviet Physics JETP*, 11:708–709, 1960. (Cited on page 192.)

[105] G. T. Rado and V. J. Folen. Observation of magnetically induced magnetoelectric effect and evidence for antiferromagnetic domains. *Physical Review Letters*, 7:310–313, 1961. (Cited on page 192.)

[106] B. I. Alshin and D. N. Astrov. Magnetoelectric effect in titanium oxide Ti_2O_3. *Soviet Physics JETP*, 17:809–811, 1963. (Cited on page 192.)

[107] G. T. Rado. Observation + possible mechanisms of magnetoelectric effects in ferromagnet. *Physical Review Letters*, 13:335–338, 1964. (Cited on page 192.)

[108] E. Fischer, G. Gorodets, and R. M. Hornreic. A new family of magnetoelectric materials: $A_2M_4O_9$ (A=Ta, Nb; M=Mn, Co). *Solid State Communications*, 10:1127–1132, 1972. (Cited on page 192.)

[109] L. W. Holmes, L. G. Vanutier, and G. W. Hull. Magnetoelectric effect and critical behavior in ising-like antiferromagnet, $DyAlO_3$. *Solid State Communications*, 9:1373, 1971. (Cited on page 192.)

[110] T. Goto, T. Kiruma, G. Lawes, A. P. Ramirez, and Y. Tokura. Ferroelectricty

and giant magnetocapcaitance in perovskite rare-earth manganites. *Physical Review Letters*, 92:257201–257204, 2004. (Cited on page 192.)

[111] M. Mostovoy. Ferroelectricity in spiral magnets. *Physical Review Letters*, 96:067601–067604, 2006. (Cited on page 192.)

[112] J. J. Bertouras, G. Giovanetti, and J. van der Brink. Multiferroicity induced by dislocated spin density waves. *Physical Review Letters*, 98:257602–257605, 2007. (Cited on page 192.)

[113] N. Hur, S. Park, P. A. Sharma, J. S. Ahn, S. Guha, and S. W. Cheong. Electric polarization reversal and memory in a multiferroic material induced by magnetic fields. *nature*, 429:392–395, 2004. (Cited on pages 192, 193 and 194.)

[114] A. S. Moskvin and R. V. Pisarev. Charge-transfer transitions in mixed-valent multiferroic $TbMn_2O_5$. *Physical Review B*, 77:060102, 2008. (Cited on page 192.)

[115] G. Giovannetti and Jeroen van den Brink. Electronic correlations decimate the ferroelctric polarization of multiferroic $HoMn_2O_5$. *Phyiscal Review Letters*, 100:227603, 2008. (Cited on page 192.)

[116] Th. Lottermoser, D. Meier, R. V. Pisarev, and M. Fiebig. Giant coupling of second-harmonic generation to a multiferroic polarization. *Phyiscal Review B*, 80:100101, 2009. (Cited on page 192.)

[117] S. Partzsch, S. B. Wilkins, J. P. Hill, E. Schierle, E. Weschke, D. Souptel, B. Büchner, and J. Geck. Observation of electronic ferroelectric polarization in multiferroic YMn_2O_5. *Physical Review Letters*, 107:057201, 2011. (Cited on pages 192, 210 and 214.)

[118] G. Buisson. Sinusoid and helicoid magnetic structures of rare-earth in TMn_2O_5. *Physica Status Solidi A-Applied Research*, 17:191–198, 1973. (Cited on page 193.)

[119] C. Wilkinson, F. Sinclair, P. Gardner, J. B. Forsyth, and B. M. R. Wanklyn. The antiferromagnetic structure of $DyMn_2O_5$ at 4.2k. *Journal of Physics C: Solid State Physics*, 14:1671–1683, 1981. (Cited on pages 193, 197, 198, 225 and 227.)

[120] A. Inomata and K. Kohn. Pyroelectric effect and possible ferroelectric transition of helimagnetic $GdMn_2O_5$, $TbMn_2O_5$ and YMn_2O_5. *Journal of Physics-Condensed Matter*, 8:2673–2678, 1996. (Cited on pages 193 and 194.)

[121] N. Hur, S. Park, P. A. Sharma, S. Guha, and S. W. Cheong. Colossal magnetodielectric effects in $DyMn_2o_5$. *Physical Review Letters*, 93:107207–107210, 2004. (Cited on pages 193 and 194.)

[122] D. Higashiyama, S. Miyasaka, N. Kida, T. Arima, and Y. Tokura. Control of the ferroelectric properties of $DyMn_2O_5$ by magnetic fields. *Physical Review B*, 70:174405, 2004. (Cited on pages 193, 194, 196 and 202.)

[123] D. Higashiyama, S. Miyasaka, and Y. Tokura. Magnetic-field-induced polarization and depolarization in $HoMn_2O_5$ and $ErMn_2o_5$. *Physical Review B*, 72:064421, 2005. (Cited on pages 193 and 194.)

[124] G. R. Blake, L. C. Chapon, P. G. Radaelli, S. Park, N. Hur, S-W. Cheong, and J. Rodriguez-Carvajal. Spin structure an magnetic frustration in mulitferroic RMn_2O_5 (R=Tb, Ho, Dy). *Physical Review B*, 71:214402, 2005. (Cited on pages 193, 198 and 227.)

[125] C. Vecchini, L. C. Chapon, P. J. Brown, T. Chatterji, S. Park, S-W. Cheong, and P. G. Radaelli. Commensurate magnetic structures of $\mathrm{RMn}_(2)\mathrm{O}_5$ (R=Y, Ho, Bi) determined by single-crystal neutron diffraction. *Physical Review B*, 77:134434, 2008. (Cited on pages 193, 220 and 227.)

[126] P. G. Radaelli and L. C. Chapon. A neutron diffraction study of $\mathrm{RMn}_(2)\mathrm{O}_5$ multiferroics. *Journal of Physics-Condensed Matter*, 20:434213, 2008. (Cited on pages 193 and 221.)

[127] M. Fukunaga and Y. Noda. Classification and interpretation of the polarization of mulitferroic $\mathrm{RMn}_2\mathrm{O}_5$. *Journal of the Physical Society of Japan*, 79:054705, 2010. (Cited on pages 193 and 195.)

[128] W. Ratcliff II, V. Kiryukin, M. Kenzelmann, S.-H. Lee, R. Erwin abnd J. Schefer, N. Hur, S. Park, and S-W. Cheong. Magnetic phase diagram if the colossal magnetoelectric $\mathrm{DyMn}_2\mathrm{O}_5$. *Physical Review B*, 72:060407(R), 2005. (Cited on pages 193, 197, 198, 212 and 213.)

[129] R. A. Ewings, A. T. Boothroyd, D. F. McMorrow, D. Mannix, H. C. Walker, and B. M. R. Wanklyn. X-ray resonant diffraction study of multiferroic $\mathrm{DyMn}_2\mathrm{O}_5$. *Physical Review B*, 77:104415, 2008. (Cited on pages 193, 195, 198, 207 and 212.)

[130] B. M. Wanklyn. Flux growth of some complex materials. *journal of Material Science*, 7:813, 1972. (Cited on page 199.)

[131] L. Paolasini, C. Detlefs, C. Mazzoli, S. Wilkins, P. P. Deen, A. Bombardi, N. Kernavanois, F. de Bergevin, F. Yakhou, J. P. Valade, I. Breslavetz, A. Fondacaro, G. Pepellin, and P. Bernard. ID20: a beamline for magnetic and

resonant x-ray scattering investigations under extreme conditions. *Journal of Synchrotron Radiation*, 14:301–312, 2007. (Cited on page 199.)

[132] T. A. W. Beale, S. B. Wilkins, R. D. Johnson, S. R. Bland, Y. Joly, T. R. Forrest, D. F. McMorrow, F. Yakhou, D. Prabahakaran, A. T. Boothroyd, and P. D. Hatton. Antiferromagnetically spin polarized oxygen observed in magnetoelectric $TbMn_2O_5$. *Physical Review Letters*, 105:087203, 2010. (Cited on page 210.)

[133] J. Voigt, J. Persson, J. W. Kim, Bihlmayer, and Th. Brückel. Strong coupling between the spin polarization of Mn and Tb in multiferroic $TbMnO_3$ determined by x-ray resonance exchange scattering. *Physical Review B*, 76:104431, 2007. (Cited on page 215.)

[134] G. Beutier, A. Bombardi, C. Vecchini, P. G. Radaelli, S. Park, S-W. Cheong, and L. C. Chapon. Commensurate phase of multiferroic $HoMn_2O_5$ studied by x-ray magnetic scattering. *Physical Review B*, 77:172408, 2008. (Cited on page 215.)

[135] Y. Joly. X-ray absorption near edge structure calculations beyond the muffin-tin appoximation. *Phyiscal Review B*, 63:125120–125129, 2001. (Cited on page 222.)

[136] C. Mazzoli, S. B. Wilkins, S. Di Matteo, B. Detlefs, C. Detlefs, V. Scagnoli, L. Pao;asini, and P. Ghinga. Disentangling multipole resonances through a full x-ray polarization analysis. *Physical Review B*, 76:195118, 2007. (Cited on page 229.)

[137] S. R. Bland, B. Detlefs, S. B. Wilkins, T. A. W. Beale, C. Mazzoli, Y. Joly, P. D. Hatton, J. E. Lorenzo, and V. A. M. Brabers. Full polarization analysis

of resonant superlattice and forbidden x-ray reflections in magnetite. *Journal of Physics: Condensed Matter*, 21:485601, 2009. (Cited on page 229.)

[138] S. R. Bland, M. Angst, S. Adiga, V. Scagnoli, R. D. Johnson, J. Herrero-Martin, and P. D. Hatton. Symmetry and charge order in Fe_2OBO_3 studied through polarized resonant x-ray diffraction. *Physical Review B*, 82:115110, 2010. (Cited on page 229.)